JAEA-Conf 2024-002
INDC(JPN)-0211
DOI:10.11484/jaea-conf-2024-002

JAEA-Conf

Proceedings of the Joint Symposium on Nuclear Data and PHITS in 2023 November 15-17, 2023, Tokai Industry and Information Plaza "iVil", Tokai-mura, Ibaraki, Japan

(Eds.) Nobuhiro SHIGYO, Takuya FURUTA and Yosuke IWAMOTO

Nuclear Science and Engineering Center
Nuclear Science Research Institute

November 2024

Japan Atomic Energy Agency

日本原子力研究開発機構

国立研究開発法人日本原子力研究開発機構　研究開発推進部　科学技術情報課
〒 319-1112　茨城県那珂郡東海村大字村松 4 番地 49
E-mail: ird-support@jaea.go.jp

JAEA-Conf 2024-002
INDC(JPN)-0211

Proceedings of the Joint Symposium on Nuclear Data and PHITS in 2023
November 15-17, 2023,
Tokai Industry and Information Plaza "iVil",
Tokai-mura, Ibaraki, Japan

(Eds.) Nobuhiro SHIGYO*[1], Takuya FURUTA and Yosuke IWAMOTO

Nuclear Science and Engineering Center, Nuclear Science Research Institute
Japan Atomic Energy Agency
Tokai-mura, Naka-gun, Ibaraki-ken

(Received July 12, 2024)

The 2023 Symposium on Nuclear Data was held at Tokai Industry and Information Plaza "iVil" on November 15-17, 2023. The symposium was organized by the Nuclear Data Division of the Atomic Energy Society of Japan (AESJ) in cooperation with Radiation Engineering Division of AESJ, North Kanto Branch of AESJ, Investigation Committee on Nuclear Data in AESJ, Nuclear Science and Engineering Center of Japan Atomic Energy Agency, and High Energy Accelerator Research Organization.

In the symposium, tutorials " Overview of the nuclear data processing code, FRENDY version 2 " was proposed and held. two sessions of lectures and discussions were held: "Recent Topics on Nuclear Data and Particle and Heavy Ion Transport code System (PHITS)". In addition, recent research progress on experiments, nuclear theory, evaluation, benchmark, and applications were presented in the poster session. The total number of participants was 108 participants. Each oral and poster presentation was followed by an active question and answer session. This report consists of a total of 36 papers including 17 oral and 19 poster presentations.

Keywords: Nuclear Data Symposium 2023, Experiments, Nuclear Theory, Nuclear Data Evaluation, Benchmark Test, Nuclear Data Applications, PHITS

---

* [1] Kyushu University

Organizers: Yosuke IWAMOTO (Chair, JAEA), Jun-ichi HORI (Vice-chair, Kyoto Univ.), Atsushi KIMURA (JAEA), Cheol Ho Pyeon (Kyoto Univ.), Shin-ichiro MEIGO (JAEA), Hideaki OTSU (RIKEN), Takanori KITADA (Osaka Univ.), Masayuki AIKAWA (Hokkaido Univ.), Toshiya SANAMI (KEK), Chikako ISHIZUKA (Tokyo Tech.), Nobuhiro SHIGYO (Kyushu Univ.), Tatsuhiko Sato (JAEA), So KAMADA (NMRI)

JAEA-Conf 2024-002
INDC(JPN)-0211

2023 年度核データ＋PHITS 合同研究会報告集

2023 年 11 月 15 日～17 日
東海村産業・情報プラザ「アイヴィル(iVil)」

日本原子力研究開発機構　原子力科学研究所　原子力基礎工学研究センター

（編）執行　信寛*、古田　琢哉、岩元　洋介

(2024 年 7 月 12 日受理)

2023 年度核データ研究会は、2023 年 11 月 15 日～17 日に、東海村にある東海村産業・情報プラザ「アイヴィル(iVil)」にて開催された。本研究会は、日本原子力学会核データ部会が主催、日本原子力学会放射線工学部会、日本原子力学会北関東支部、日本原子力学会「シグマ」調査専門委員会、日本原子力研究開発機構原子力基礎工学研究センター、高エネルギー加速器研究機構が共催した。

チュートリアルとして、「核データ処理コード FRENDY 第二版の概要」を、講演・議論のセッションとして、「核データに関する最近の話題と粒子・重イオン輸送計算コード PHITS」の 2 セッションを実施した。さらにポスターセッションでは実験、理論、評価、ベンチマーク、応用など幅広い内容について発表が行われた。参加者数は 108 名で、それぞれの口頭発表およびポスター発表では活発な質疑応答が行われた。本報告書は、本研究会における口頭発表 17 件、ポスター発表 19 件の合計 36 の論文を掲載している。

キーワード: 2023 年度核データ研究会、実験、原子核理論、核データ評価、ベンチマークテスト、核データ応用、PHITS

原子力科学研究所：〒319-1195　茨城県那珂郡東海村大字白方 2-4
*[1] 九州大学

Contents

Papers presented at Poster Session

目次

ポスター発表論文

1. Joint Symposium on Nuclear Data and PHITS in 2023 - Programme

November 15 - 17, 2023

Wednesday, November 15

Opening Address (13:30 - 13:40) Jun-ichi HORI (Kyoto University)

(13:40 - 15:50) Convener: Shin-ichiro MEIGO (JAEA)

13:40 Relationship with JENDL and Expectations for Possibilities of Opening up Nuclear Data
Tokio FUKAHORI (JAEA)

14:20 Reactor physics for innovative reactor development and applications in space, medical and planetary science
Naoyuki TAKAGI (Tokyo City University)

14:50 Experiences of HTTR Critical Approach Calculation and Nuclear Data
Nozomu FUJIMOTO (Kyushu University)

15:20 Measurement of photoneutron production cross section for mono-energetic linearly polarized photon
Toshiya SANAMI (KEK/SOKENDAI)

Break (15:50 - 16:00)

(16:00 - 17:00) Convener: Atsushi KIMURA (JAEA)

16:00 Nuclear data generation by combining machine learning and nuclear reaction models
Shoto WATANABE (Hokkaido University)

16:30 Crucial importance of correlation between cross sections and angular distributions in nuclear data of ^{28}Si on estimation of uncertainty of neutron dose penetrating a thick concrete
Naoki YAMANO (Tokyo Institute of Technology)

Thursday, November 16

(09:30 - 12:00) Convener: Yosuke IWAMOTO (JAEA)

09:30 Overview of FRENDY version 2
Kenichi TADA (JAEA)

10:30 Nuclear data measurement by surrogate reactions using ion beam
Katsuhisa NISHIO (JAEA)

11:00 Muon Nuclear Data
Megumi NIIKURA (RIKEN)

11:30 Research and Development on Recycling of Radioactive Waste in JAEA
Takanori SUGAWARA (JAEA)

Lunch break (12:00 - 13:00)

(13:00 - 14:50) Convener: Chikako ISHIZUKA (Tokyo Institute of Technology)

13:00 Features of the Supercritical Water-cooled Reactor (SCWR) and the Reactor Physics Issues
Akinori YAMAJI (Waseda University)

13:30 Overview and Future of JENDL-5
Osamu IWAMOTO (JAEA)

14:00 Experiments for Nuclear Data Using RCS at J-PARC and HiRadMat at CERN
Shin-ichiro MEIGO (JAEA)

14:30 Activities of Investigation Committee on Nuclear Data of AESJ
Nobuhiro SHIGYO (Kyushu University)

Break (14:30 - 15:00)

Poster Session (15:00 - 17:00)

Improving Accuracy of Fission Product Yields by Bayesian Neural Network
Jingde CHEN (Tokyo Institute of Technology)

4-D Langevin Trajectory Analysis Using Machine Learning
Yuta MUKOBARA (Tokyo Institute of Technology)

Study of INC Model for alpha-Induced Reaction at 230 MeV/u
Toshimasa FURUTA (Kyushu University)

Calculation of Fission Fragment Yields for thermal neutron reaction of ^{239}Pu
Futoshi MINATO (Kyushu University)

Development of a New Web Services and RESTful APIs for Experimental Nuclear Reaction Database (EXFOR)
Shin OKUMURA (IAEA)

Neutron Total and Capture Cross Section Measurements of ^{nat}Er at ANNRI
Gerard ROVIRA (JAEA)

Measurement of the Very-forward-angle Neutron Elastic Scattering and PHITS Simulation for Neutron Shielding
Tomoya NAKADA (Kyoto University)

Evaluation of Photonuclear Reaction Data ^{209}Bi at 13 and 17 MeV Photon Energy
Thuong Thi Hong NGUYEN (SOKENDAI)

Measurement of Double Differential Cross Sections of Charged Particles Produced by 100 MeV/u ^{12}C Beam Nuclear Reactions
Ryota IKOMA (Kyushu University)

Friday, November 17

Opening Address and recent status of PHITS (13:30 - 13:40) Tatsuhiko SATO (JAEA)

(09:50 - 10:50) Convener: Shintaro HASHIMOTO (JAEA)

09:50 Current Development Status of Simulation Code for Physical and Chemical Processes in PHITS
Yusuke MATSUYA (Hokkaido University)

10:10 Details of the PHIG-3D's Visualization Functions
Seiki OHNISHI (National Marine Research Institute)

10:30 Geometry Design of Complex Entities into the PHITS Computational Space by using 3D-CAD/CG and Solid Meshing
Minoru SAKAMA (Tokushima University)

Break (10:50 - 11:00)

(11:00 - 12:00) Convener: Takuya FURUTA (JAEA)

11:00 A Proposal for the Development of Boron Neutron Capture Therapy Agents based on Simulation Studies using PHITS Microdosimetry
Takafumi SHIGEHIRA (Okayama University)

11:20 Simulation Analysis of Cosmic Ray Muon Penetrating Subsurface of Huge Mountain
Shoichi NAKAMURA (University of Yamanashi)

11:40 Fundamental study on responsiveness of gel dosimeters to carbon-ion beams and applicability of measurement of three dimensional dose distribution
Masumitsu TOYOHARA (Toshiba Energy Systems & Solutions Corporations)

Lunch break (12:00 - 13:00)

(13:00 - 15:00) Convener: Tatsuhiko OGAWA (JAEA)

13:00 Nuclear heating and damage data in JENDL-5 neutron ACE file
Chikara KONNO (JAEA)

13:20 Simulation of aluminum activation experiment at CERN/CHARM
Tsuyoshi KAJIMOTO (Hiroshima University)

13:40 Test of ^{107}Pd transmutation with macroscopic quantities
Yasuto MIYAKE (RIKEN)

14:00 Design of radiation shield for RI production beam line by PHITS
Atsuko AKASHIO (RIKEN)

14:20 Calculation of the Skyshine Radiation Measurement Experiment in Kansas by PHITS
Yusuke YASUNO (Mitsubishi Nuclear Fuel Co. Ltd.)

14:40 Introduction to PHITS-UDM (User Defined Model)
Yasuhito SAKAKI (KEK/SOKENDAI)

Poster Award Ceremony and Closing Remarks (15:00 – 15:20)
Yosuke IWAMOTO (JAEA), Jun-ichi HORI (Kyoto University)

2. Relationship with JENDL and Expectations for Possibilities of Opening up Nuclear Data

Tokio FUKAHORI
Japan Atomic Energy Agency
fukahori.tokio@jaea.go.jp

abstract

The author has been keeping relationship with Japanese Evaluated Nuclear Data Library for around 38 years. During this period, he has been contributing code developments, for example, Preequilibrium Nuclear Reaction Calculation Code (ALICE-F) and Particle and Heavy Ion Transport Code System (PHITS). The author has also been assisting for EXFOR activities, and promoting Evaluated Nuclear Data Processing Code (FRENDY) and Multiphase Multicomponent Detailed Thermal Fluid Analysis Code (JUPITER). In this paper, introduced are the outline of the author's works. Also reported are the author's perspective and challenge for the future form of nuclear data.

1. Introduction

The author has been keeping relationship with nuclear data activities including Japanese Evaluated Nuclear Data Library (JENDL)[1-11] for around 38 years. During this period, He has been contributing code developments, for example, Preequilibrium Nuclear Reaction Calculation Code (ALICE-F)[12] for intermediate energy nuclear data evaluation and Particle and Heavy Ion Transport Code System (PHITS)[13] following the study on the quantum molecular dynamics (QMD). The author has also been assisting for EXFOR activities as an adviser and data implementation, promoting Evaluated Nuclear Data Processing Code (FRENDY)[14] for contribution as a bridge between evaluated nuclear data files and reactor physics applications, and also promoting Multiphase Multicomponent Detailed Thermal Fluid Analysis Code (JUPITER)[15] for an analysis on the accident progress of TEPCO Fukushima Daiichi Nuclear Power Station. In this paper, introduced are the outline of the author's work topics. Also reported are his perspective and challenge for consideration on the future form of nuclear data supply.

2. Works at JAERI and JAEA

2.1 Research on nuclear data evaluation and file production

The first work at the nuclear data center was improvement of optical and statistical nuclear reaction calculation code, CASTHY[16]. Measurements and analyses of double-differential cross section (DDX) have been done for JENDL Fusion File[6]. Activation cross sections have been also measured.

Relating to intermediate nuclear data, improvement of ALICE-F code and study on high-energy fission reaction have been carried out for JENDL High Energy File[7-9,12]. The ALICE-F code was also used for photonuclear data evaluation for JENDL Photonuclear Data File[10,11]. The method for direct calculation of primary knock-on atom (PKA) from nuclear data files was proposed for JENDL PKA/KERMA File whose application was radiation damage of reactor structural materials. This work also contributed for the standard enacted by International Organization for Standardization (ISO). Results studied on QMD, photonuclear reaction and PKA/KERMA were used in PHITS code. Expansion of fission yields into the intermediate energy also performed by using the 5 Gaussian model.

2.2 International Collaboration

In 1989, the author was dispatched to the National Nuclear Data Center (NNDC) at Brookhaven National Laboratory (BNL) in US for 1.5 years, to investigate on intermediate nuclear data evaluation. It was the first time to visit abroad by business trip and was the start of the JENDL High Energy File.

For the collaboration through the international organization, the author visited International Atomic Energy Agency (IAEA), OECD Nuclear Energy Agency (NEA) and the International Science and Technology Center (ISTC). At IAEA, he joined to the Coordinated Research Projects (CRP) on the Reference Input Parameter Library (RIPL 1-3), the photonuclear data evaluation, the fission product yields, etc. He also attended the international nuclear data committee (INDC) and the Nuclear Reaction Data Center (NRDC) meetings, and the advisory group, consultants and technical meetings. At OECD/NEA, the author contributed to the Nuclear Science Committee (NSC), especially to the Working Party on International Nuclear Evaluation Cooperation (WPEC). The author contributed to ISTC as the collaborator for the projects with the Petersburg Nuclear Physics Institute (PNPI) and the Institute of Physics and Power Engineering (IPPE), and the chair of Science Advisory Committee (SAC).

As the collaborator on JAEA-CEA bilateral collaboration, the author coordinate in the fields of Nuclear Science and Fukushima. As the research exchange program (1992-2000), the author visited to Korea, People Republic of China, Vietnam, Thailand, Malesia, Indonesia and Bangladesh, where he made lecture about nuclear data activities. He also worked as the secretariat of International Conference, for example, ND1988, ND2001, ICRS1999 and PHYISOR2014.

2.3 Domestic Collaboration

Domestic collaboration has been done mainly through Atomic Society of Japan (AESJ). The nuclear data collaboration through Sigma Committee, which official name has been changed several times, has been done for over 35 years, especially as a chair (2019-2022). It through the Nuclear Data Subcommittee is also still continuing, and the author appointed its chair during 2015-2018. Other contributions for AESJ were as a member of the Editorial Board, the Public Information, Subcommittee Administration Committee, etc. Secretariat of the Symposium on Nuclear Data was done in 1993-2004

as JAERI meetings and in 2006-2007 as AESJ ones.

The author also collaborated with the Japanese Atomic Power Company on decommissioning and dismantling of nuclear power plants, with Tokyo Tech. and Hokkaido U. by J-PARC/ANNRI construction and experiments and with RIKEN in the nuclear physics fields. The author made lectures as a guest professor at universities, Hokkaido, Tohoku, Ibaraki, Tsukuba, Tokyo, Tokyo Tech., Waseda, Tokyo City, Fukui, Kyoto (KUR), Osaka, Konan, Kyushu, etc.

3. Future Appearance of Nuclear Data

3.1 Perspective for Future Evaluated Nuclear Data Service

"Is it OK to use the current library format?" is long-term question to producer of evaluated nuclear data files. What form should it take, if change? What is the feedback from applied fields? The author thinks two of important subjects are considered as expansion of applicable fields and reduce response time (timely delivery).

For above purpose, the author was thinking about Collaborative International Evaluated Library Organization (CIELO, WPEC/SG-40), Generalized Nuclear Data (GND, WPEC/EG-B) and TENDL[17] approaches. The CIELO approach can solve resource shortage. However, the property is strongly depended on the base evaluated file. The GND approach says the file is human readable, but who wants to see covariance data from text files. In addition, files like ENDF, ENSDF, EXFOR, etc. could not be unified. The TENDL approach can storage as many as data so as to include infinite combination of projectile and target nucleus by keeping model parameters. The author thinks the TENDL approach is close to the ideal appearance and good for an artificial interagency application. Unfortunately, however, this is not always given good data accuracy.

3.2 What is Advanced Nuclear Data File?

In the real world, evaluated nuclear data files should have good cost (resource) performance, effectiveness and needs matching. The producers always think "Seeds see needs", for everything, anywhere, anytime.

For this, calculated results by nuclear data evaluation codes must increase its utilization rate of reproducibility of the files, expand of applicable fields and reduce response time. It should also be needed high precision theory and models with reducing parameters and/or comprehensive maintenance of parameters.

In addition, the relation between nuclear data and their applications is important. For example, it with reactor physics fields is shown in **Fig.1**. Theory/model of nuclear physics is applied for nuclear data evaluation with experimental data, evaluators give the results into files, the libraries is processed from the files and served to end users. In this process, many of experimental facility and codes can used for production, verification and validation. However, feedback loops both between nuclear physics and nuclear data evaluation, and between nuclear data producers and reactor physicists are closed in their

small cycles, at this moment. The author thinks enlarging the loop size and related tool development are necessary. In the next chapter, proposal by the author is introduced as trial activity.

4. CCOne-driven Nuclear Data Library (CCONDL) Project

Figure 2 shows the basic concept of nuclear data evaluation scheme. In general, the nuclear evaluation is performed through model calculation code with the verification by differential (nuclear physics) experimental data. The calculated results are summarized into evaluated nuclear data file and validated by integral (reactor physics) experiments. The models are integrated into the code and evaluation can be done by adjusting model parameters to reproduce experimental data. However, the calculated results do not always reproduce all experimental data. The author defines this "reproducibility". He also estimates the reproducibility is achieved about 30% at most currently.

For giving evaluated nuclear data by only evaluation codes, it could be necessary that the reproducibility be achieved more than 80%. So, the author proposes the "CCONDL Project" so that evaluated code can produce evaluated file. The CCONDL is based on CCONE, the best model parameters and precise theory/models. The CCONDL can serve timely nuclear data. After accumulation of individual nuclear data, the integral nuclear data can be released as evaluated nuclear data file, like as snap shot. For this purpose, the first step is improvement of the CCONE code and its model parameters so as to reproduce JENDL-5 more than 80%.

5. Summary

Have you heard about the Business Continuation Plan (BCP)? It is necessary for the certain organization to be sustainable. Probably we already know the resources are not increased here after, rather decreased. How about the nuclear data continuation plan (NDCP). Please consider it.

Acknowledgements

The author would like to thank for the organizing committee of Nuclear Data + PHITS Symposium, giving the opportunity to introduce his experiences as a final-lecture-like presentation. The author also appreciates for long-term support to relating committee members, staffs of the JAEA/JAERI nuclear data center and all friends.

References

[1] Nakagawa T., Shibata K., Chiba S., Fukahori T., Nakajima Y., Kikuchi Y., Kawano T., Kanda Y., Ohsawa T., Matsunobu H., Kawai M., Zukeran A., Watanabe T., Igarasi S., Kosako K. and Asami T.: "Japanese evaluated nuclear data library, version 3 revision-2; JENDL-3.2," J. Nucl. Sci. Technol. 32, 1259 (1995).

[2] Shibata K., Kawano T., Nakagawa T., Iwamoto O., Katakura J., Fukahori T., Chiba S., Hasegawa A., Murata T., Matsunobu H., Ohsawa T., Nakajima Y., Yoshida T., Zukeran A., Kawai M., Baba

M., Ishikawa M., Asami T., Watanabe T., Watanabe Y., Igashira M., Yamamuro N., Kitazawa H., Yamano N. and Takano H.: “Japanese Evaluated Nuclear Data Library Version 3 Revision-3: JENDL-3.3,” J. Nucl. Sci. Technol. 39, 1125 (2002).

[3] Shibata K., Iwamoto O., Nakagawa T., Iwamoto N., Ichihara A., Kunieda S., Chiba S., Furutaka K., Otuka N., Ohsawa T., Murata T., Matsunobu H., Zukeran A., Kamada S. and Katakura J.: “JENDL-4.0: A New Library for Nuclear Science and Engineering,” J. Nucl. Sci. Technol. 48(1), 1-30 (2011).

[4] Iwamoto O., Iwamoto N., Kunieda S., Minato F., Nakayama S., Abe Y., et al.: “Japanese evaluated nuclear data library version 5: JENDL-5”, J. Nucl. Sci. Technol., 60(1), 1-60 (2023).

[5] Shibata K., Iwamoto N., Kunieda S., Minato F., Iwamoto O.: “Activation Cross-section File for Decommissioning of LWRs”, JAEA-Conf 2016-004, 47-52.

[6] Chiba S. et al.: “JENDL Fusion File 99”, J. Nucl. Sci. Technol. 39(2), 187-194 (Feb 2002).

[7] Watanabe Y. et al.: “Nuclear Data Evaluation for JENDL High-Energy File”, Proceedings of International Conference on Nuclear Data for Science and Technology, Santa Fe, New Mexico, USA, Sep. 26 - Oct. 1, 2004, Vol. 1, pp.326 (2004).

[8] Watanabe Y. et al.: “Status of JENDL High Energy File”, Journal of the Korean Physical Society, 59(2), 1040-1045 (2011).

[9] Kunieda S. et al.: “Overview of JENDL-4.0/HE and benchmark calculation”, JAEA-Conf 2016-004, pp.41-46 (2016).

[10] Kishida N. et al.: “JENDL Photonuclear Data File”, Proceedings of International Conference on Nuclear Data for Science and Technology, Santa Fe, New Mexico, USA, Sep. 26 - Oct. 1, 2004, Vol. 1, pp.199 (2004).

[11] Iwamoto N., Kosako K., Fukahori T.: “JENDL photonuclear data file 2016”, J. Nucl. Sci. Technol., 60(8), 911-922 (2023).

[12] Fukahori T.: “ALICE-F Calculation of Nuclear Data up to 1 GeV”, Proc. of the Specialists' Meeting on High Energy Nuclear Data, 3-4 October 1991, JAERI Tokai, Japan, JAERI-M 92-039, pp.114 (1992).

[13] Sato T., Iwamoto Y., Hashimoto S. et al.: “Features of Particle and Heavy Ion Transport Code System (PHITS) version 3.02”, J. Nucl. Sci. Technol. 55(5-6), 684-690 (2018).

[14] Tada K., Nagaya Y., Kunieda S., Suyama K., Fukahori T.: “Development and verification of a new nuclear data processing system FRENDY”, J. Nucl. Sci. Technol., 54, 806-817 (2017).

[15] Yamashita S., Ina T., Idomura Y., Yoshida H.: “A numerical simulation method for molten material behavior in nuclear reactors”, Nucl. Eng. and Design, 322, 301-312 (2017).

[16] Igarasi S., and Fukahori T.: “Program CASTHY: Statistical Model Calculation for Neutron Cross Sections and Gamma Ray Spectrum”, JAERI 1321 (1991).

[17] Koning A.J., et al.: “TENDL: Complete Nuclear Data Library for Innovative Nuclear Science and Technology”, Nucl. Data Sheets, 155, 1-55 (2019).

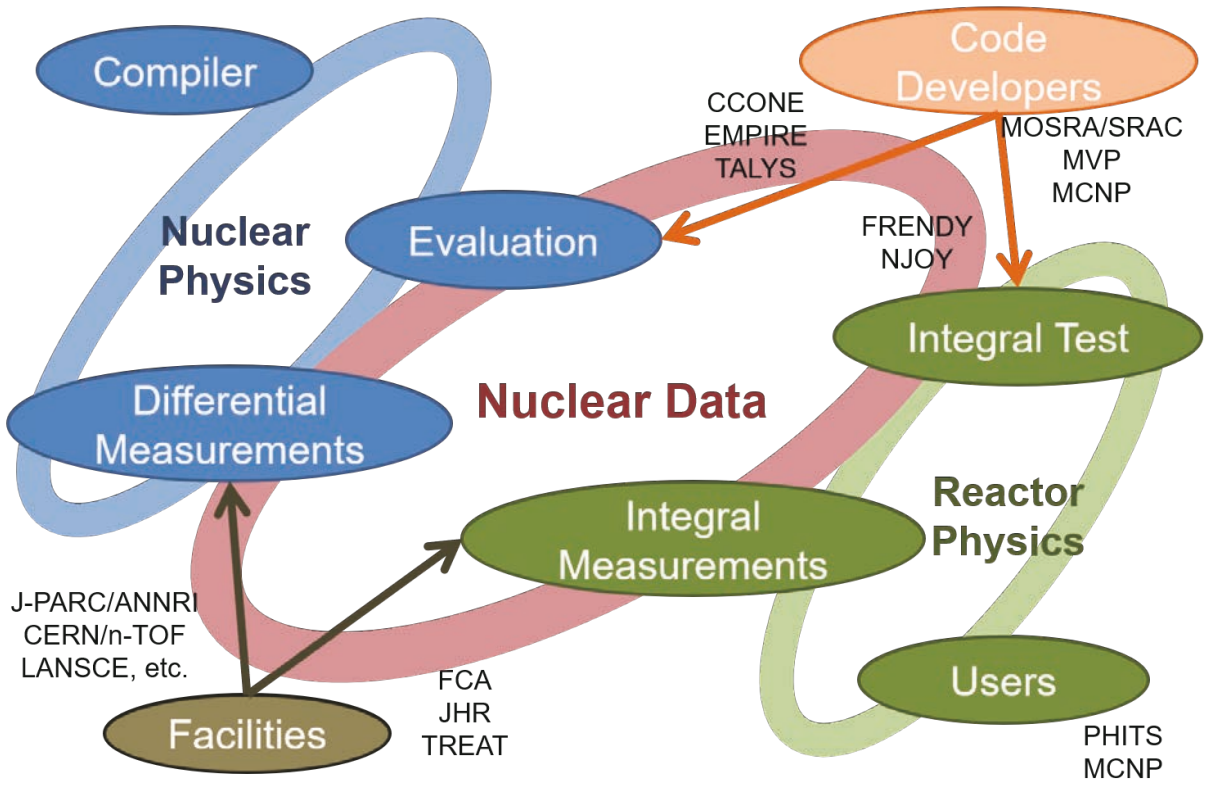

Figure 1 Relation between nuclear data and reactor physics

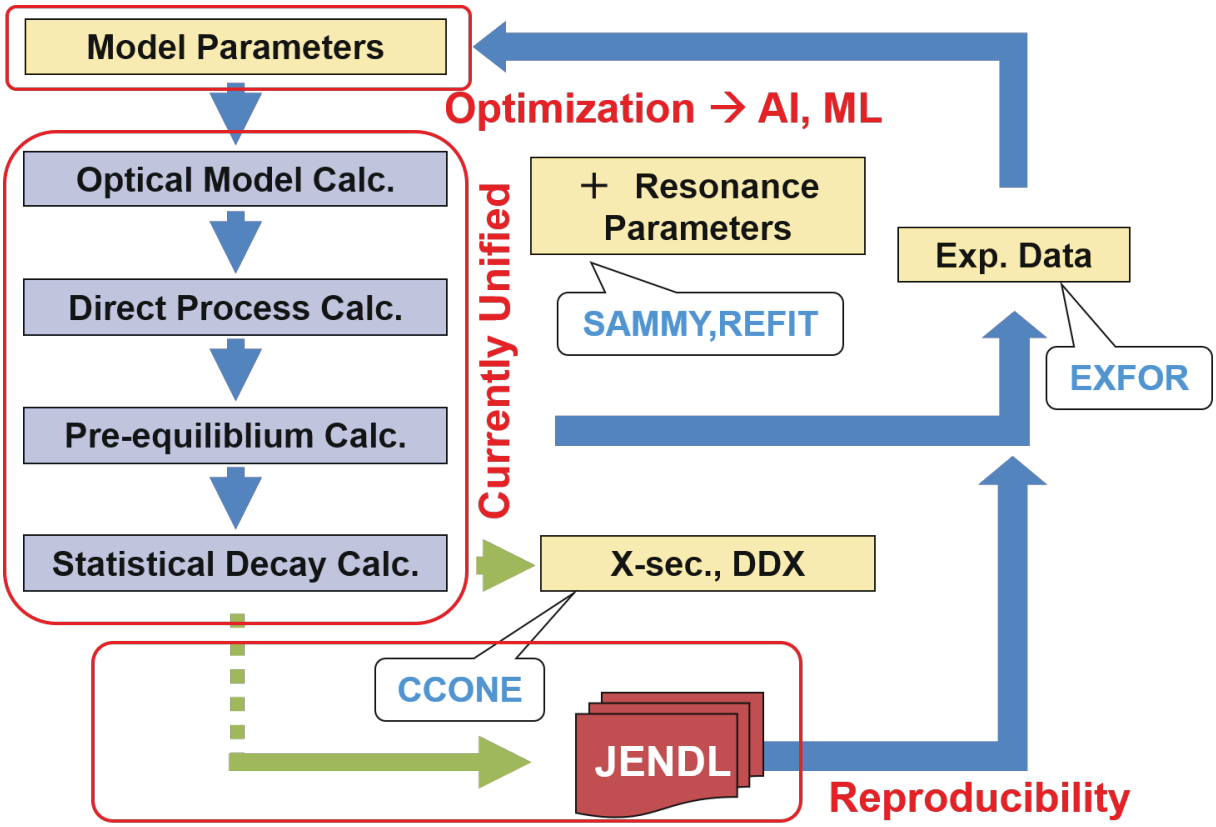

Figure 2 Concept of nuclear data evaluation scheme

3. Crucial importance of correlation between cross sections and angular distributions in nuclear data of ^{28}Si on estimation of uncertainty of neutron dose penetrating a thick concrete

Naoki YAMANO [1*], Tsunenori INAKURA [1], Chikako ISHIZUKA [1] and Satoshi CHIBA [1]
[1]Institute of Innovative Research, Tokyo Institute of Technology
2-12-1 Ookayama, Meguro-ku, Tokyo 152-8550, Japan
[*]Email: yamano@zc.iir.titech.ac.jp

Accurate estimation of uncertainties, induced by those of nuclear data through error propagation, of quantities calculated by neutron transport calculation is crucially important for Verification and Validation (V&V) of design and safety analysis of nuclear systems. In this paper, uncertainty in neutron dose after penetrating a 3-m-thick concrete with ^{235}U thermal fission neutron source was estimated based on three different kinds of Total Monte Carlo methods under random sampling methodology. A thousand random nuclear data files were generated for ^{28}Si by T6 by perturbing underlying model parameters. In the first method, these files were used directly to yield processed library preserving all the correlations among different physical quantities. In the second method, a covariance file in the ENDF-6 format was generated and 1000 random files were produced based on the covariance file. In the third method, the random files populated by T6 were used but the angular distribution data were kept fixed to non-perturbed nominal ones. It was found that the second and third methods gave equivalent variance of the neutron dose after deep penetration of a concrete, and this uncertainty was larger than the uncertainty given by the first method. It shows that the positive correlation between total cross section and angular distribution of elastic scattering, which stems from Wick's inequality derived from the optical theorem affects uncertainty of the calculated neutron dose. The correlation of uncertainties of such different quantities is not represented properly in the ENDF-6 format, hence this correlation is normally ignored. It could be concluded that the uncertainty obtained by using the covariance files given in the ENDF-6 format may not give correct results for the uncertainty of deep neutron penetration calculation.

1. Introduction

Accurate estimation of uncertainty in the propagation of errors in the reactor physics quantities obtained from neutron transport calculations due to nuclear data uncertainty is of great importance for the Verification and Validation (V&V) of nuclear system design and safety analysis. Typically, such an error propagation is calculated through a covariance file specified for nuclear data in ENDF-6 format [1].

In the field of reactor physics, the generalized perturbation method using the transport equation and its adjoint equation and cross section covariance is applied to sensitivity analysis such as effective multiplication factor.

Although its application to shielding and activation analyses has been attempted, several problems exist in accurately evaluating error propagation in neutron current fields because the ENDF-6 format cannot represent all possible correlations of uncertainties that may exist in nuclear data. The treatment of incomplete data, i.e., correlations between different reactions (including correlations between the angular distribution of elastic scattering and the total cross section), is a challenging task.

From the perspective of utilizing nuclear data covariance, we have developed a new uncertainty analysis method which can solve this problem. In this paper, we will discuss the importance of the correlation between cross section and angular distribution while showing an application example of the evaluation of neutron dose uncertainty for ^{28}Si nuclear data in a thick concrete penetration problem [2].

2. Treatment of nuclear data errors

Needless to say, the evaluated nuclear data contain the most probable evaluation data, but the evaluator also evaluates errors in the experimental values and uncertainties in the theoretical calculation, and stores the error data in covariance files (MF30-40) of the ENDF-6 format. Using this covariance files and the generalized perturbation method, it is possible to calculate the error propagation from the cross section error to the reactor physics quantity of interest.

However, the evaluated nuclear data libraries of JENDL-4.0 [3] and JENDL-5 [4] do not contain covariance files for all nuclides, and even for nuclides that are stored, only some data are stored as shown in **Table 1**, and not all covariance data have been evaluated. The treatment of these incomplete data is an issue to be addressed in the future. For ^{28}Si, which is the focus of this study, there is no covariance data in JENDL-4.0 or JENDL-5.

Table 1. ENDF-6 format and covariance data stored in the evaluated nuclear data library.

MF number	Types of covariance data
30	Data covariances obtained from parameter covariances and sensitivities (not applicable)
31	Covariances of average number of neutrons per fission $\bar{\nu}$
32	Covariances of resonance parameters
33	Covariances of neutron cross sections (no correlation between different reactions)
34	Covariances for angular distributions of secondary neutrons (MT=2, only P_1)
35	Covariances for energy distributions of secondary neutrons (only MT=18)
40	Covariances for production of radioactive nuclei (not applicable)

3. Uncertainty analysis method

To evaluate the uncertainty of the cross section even when no error data are stored in the evaluated nuclear data, and to evaluate the error propagation to the reactor physics by considering the correlation between different reactions and the angular and energy distribution of secondary neutrons, a method combining T6 [5] and the Total Monte Carlo (TMC) method [6], which follows the flow shown in **Figure 1** was developed. If covariance data are stored in the evaluated nuclear data library, SANDY [7] can be used to connect to the TMC method.

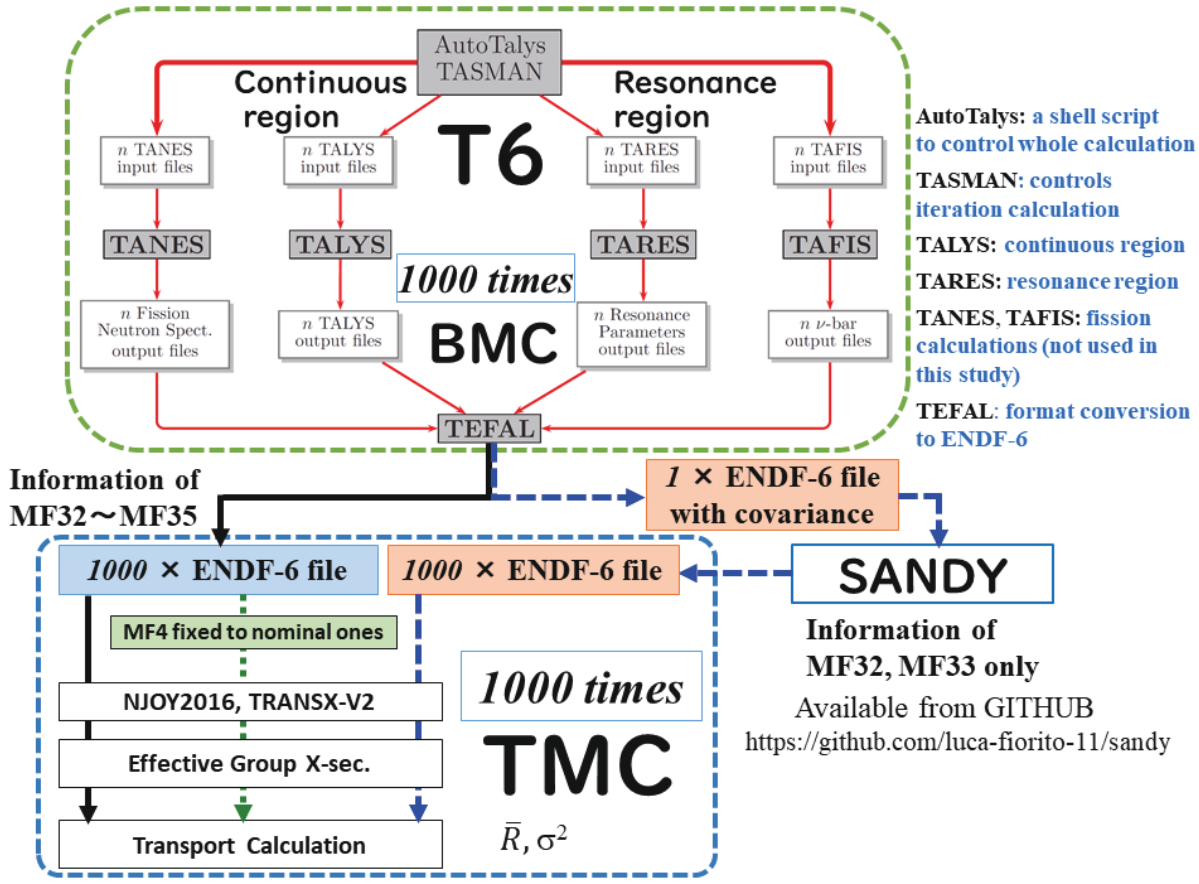

Figure 1. Flow of uncertainty analysis method. [2]

(1) After reproducing cross sections of evaluated nuclear data (JENDL-4.0 was adopted as the reference library in this study) using T6, 1,000 random nuclear data files were generated by randomly perturbed various model parameters (solid line in Fig. 1). T6 is a set of cross section calculation modules, and the reason for using it is that it can be obtained complement information on correlations between different reactions and correlations between angular and energy distributions of secondary neutrons for which covariance data do not exist in evaluated nuclear data. Even in the absence of any covariance data, it is possible to produce error data consistent with the evaluated cross sections by reproducing the evaluated cross sections as much as possible. In the field of reactor physics, there are sometimes cases where other covariance data such as ENDF/B-VIII [8] are used for nuclides for which there is no covariance in JENDL-4.0. However, the use of error data with different evaluation policies and cross section values is not physically and logically consistent. In addition, the TEFAL module of T6 can create covariance files using data from 1,000 random files.

(2) Second, we performed TMC calculation using 1,000 random files generated from nuclear data with covariance using SANDY (dashed line in Fig. 1). SANDY is a code developed at MOL in Belgium that can generate arbitrary multiple random files from nuclear data with covariance using a modified Cholesky decomposition. However, SANDY adopts NJOY [9] as an external engine, covariance data processing is limited to the processing functions of ERRORR in NJOY.

(3) Third, for comparison, we generated 1,000 random nuclear data files based on the 1,000 random nuclear data files generated in (1) above, without considering the perturbation of the angular distribution of secondary neutrons for elastic scattering (MF4, MT2) and fixed to the nominal data, and performed the TMC calculation (as indicated “MF4 no perturbed”) (dotted line in Fig. 1).

(4) Using each of the 1,000 random files, we calculated the expected value and variance (standard

deviation) of the physical quantity of interest. The solver used in TMC is configured by the user by combining the calculation codes that yield the physical quantity of interest. In other words, the user can select the solver best suited for the analysis of interest.

The basic idea of obtaining covariance (error) in T6 is to consider that the input parameters used by TALYS for calculations and the resonance parameters of the nuclear data read by TARES each have uncertainty. The values of the input parameters and resonance parameters are each randomly perturbed within a certain distribution, a number of slightly different cross sections (random files) are calculated, and these many random files are statistically processed to calculate the covariance. The authors used the convergence of the correlation matrix as a criterion for determining the total number of random files. Generally, the convergence of the variance was faster than the convergence of the correlation matrix, and the convergence of the correlation matrix was almost satisfied with 500 random files, but 1,000 was set as the standard in consideration of statistical errors. The convergence of this correlation matrix was confirmed for each reaction.

Figure 2 shows a comparison of the ^{28}Si total cross sections generated by the random calculation of T6 (gray line) with the reference JENDL-4.0 (red line). **Figure 3** shows the correlation matrix of the ^{28}Si cross sections generated by the random calculation of T6 for each reaction. The conventional covariance file does not store correlations between different reactions. By using T6, the correlation matrices between different reactions can be estimated, and TMC can directly reflects these correlations in transport calculations.

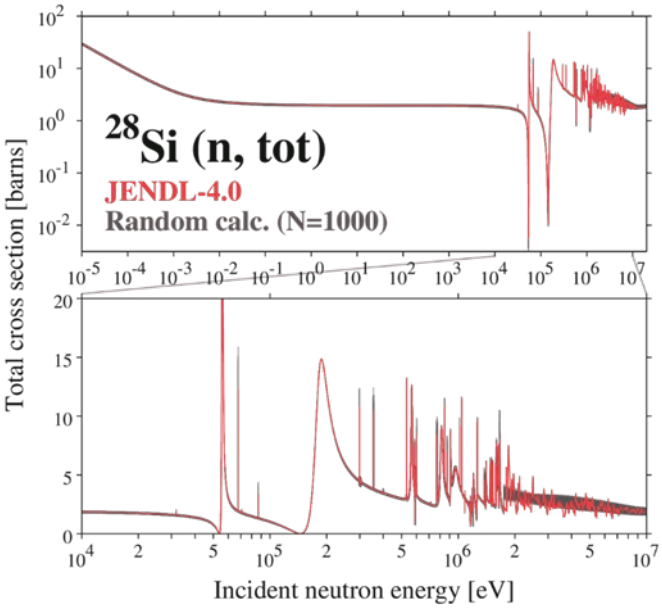

Figure 2. Comparison of ^{28}Si total cross section (gray line) generated by random calculation of T6 and JENDL-4.0 (red line) [2]. The lower figure is an enlarged partial view of the upper part.

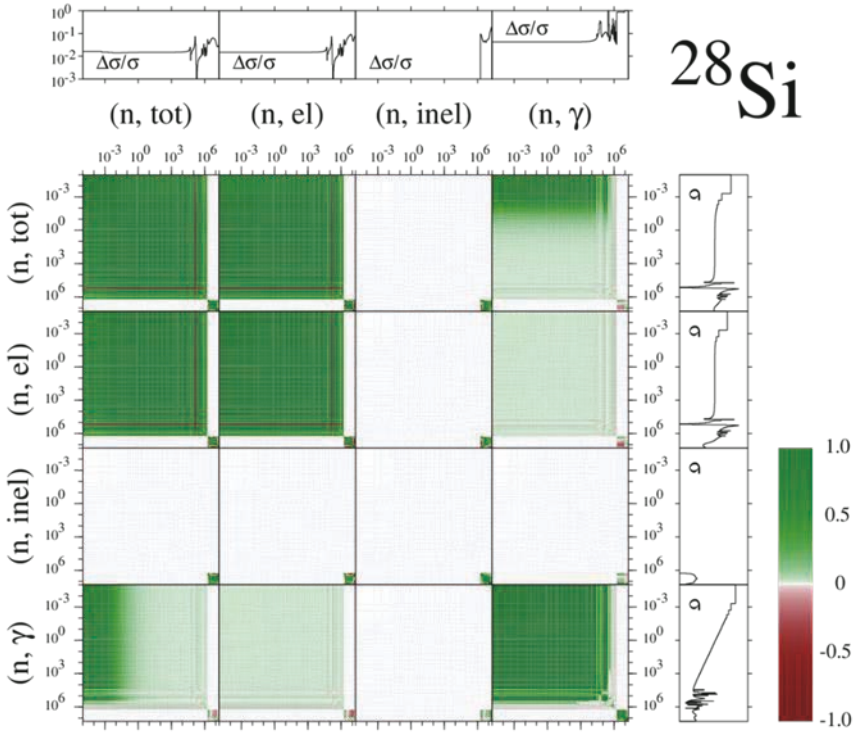

Figure 3. Correlation matrix and relative standard deviation for each reaction of the ^{28}Si cross section generated with T6 [2]. The 199 energy group structure in VITAMIN-B6 [10] was adopted.

4. Application to deep neutron penetration problem containing ^{28}Si

Error evaluation due to cross section uncertainty in neutron transmission problems is important for shielding safety analysis and evaluation of activation activity for decommissioning. Here, the error propagation due to the uncertainty of the ^{28}Si cross section to the neutron dose from the deep penetration of concrete was calculated using a one-dimensional spherical model shown in **Figure 4**. The left boundary is the reflection condition and the right boundary is the vacuum condition. The source is a U-235 fission neutron spectrum uniformly distributed in the first 100 cm air layer.

The group constants of the VITAMIN-B6 199 energy group structure [10] for each of the three types of 1,000 sets were generated using NJOY2016 [11] and TRANSX-V2 [12], and the neutron transmission problem was calculated with the one-dimensional Sn transport code ANISN [13] (P_5S_{16}) to compare the expected neutron dose and the standard deviation obtained from the variance.

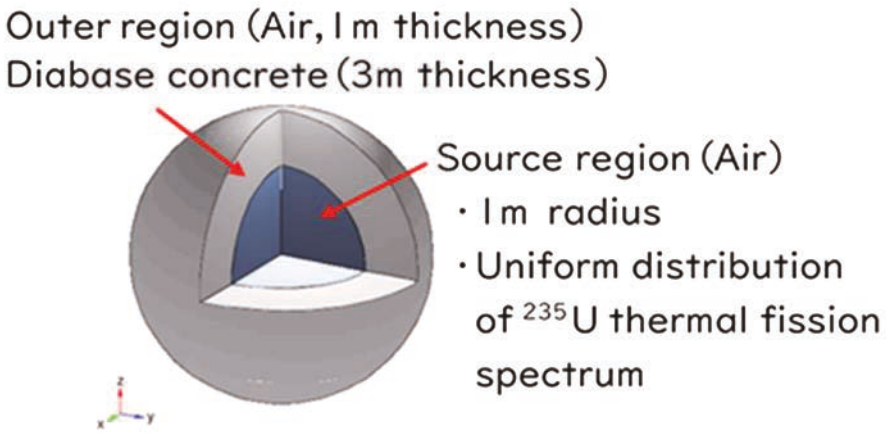

Figure 4. ANISN neutron transport calculation geometry.

The results are shown in **Figure 5**, which compares the neutron dose distributions of T6, SANDY, and MF4 no-perturbed obtained by TMC. The expected dose values were almost the same for the three, but the standard deviations were different. **Figure 6** shows an enlarged image of the standard deviation distribution. The result of fixing the angular distribution of elastic scattering (MF4, MT2) to the nominal data without considering the perturbation (MF4 no perturbed) gave almost the same results with SANDY. SANDY basically refers to the information in covariance files MF32, MF33 and MF34 created in T6, but covariance data processing uses ERRORR in NJOY. In other words, since ERRORR cannot process the higher-order moments of the angular distribution of secondary neutrons in MF34, the result was similar to that obtained by fixing the angular distribution of secondary neutrons to the nominal data (MF4 no perturbed). On the other hand, TMC, which directly uses the random file generated by T6, takes into account all perturbations in the angular distribution of secondary neutrons.

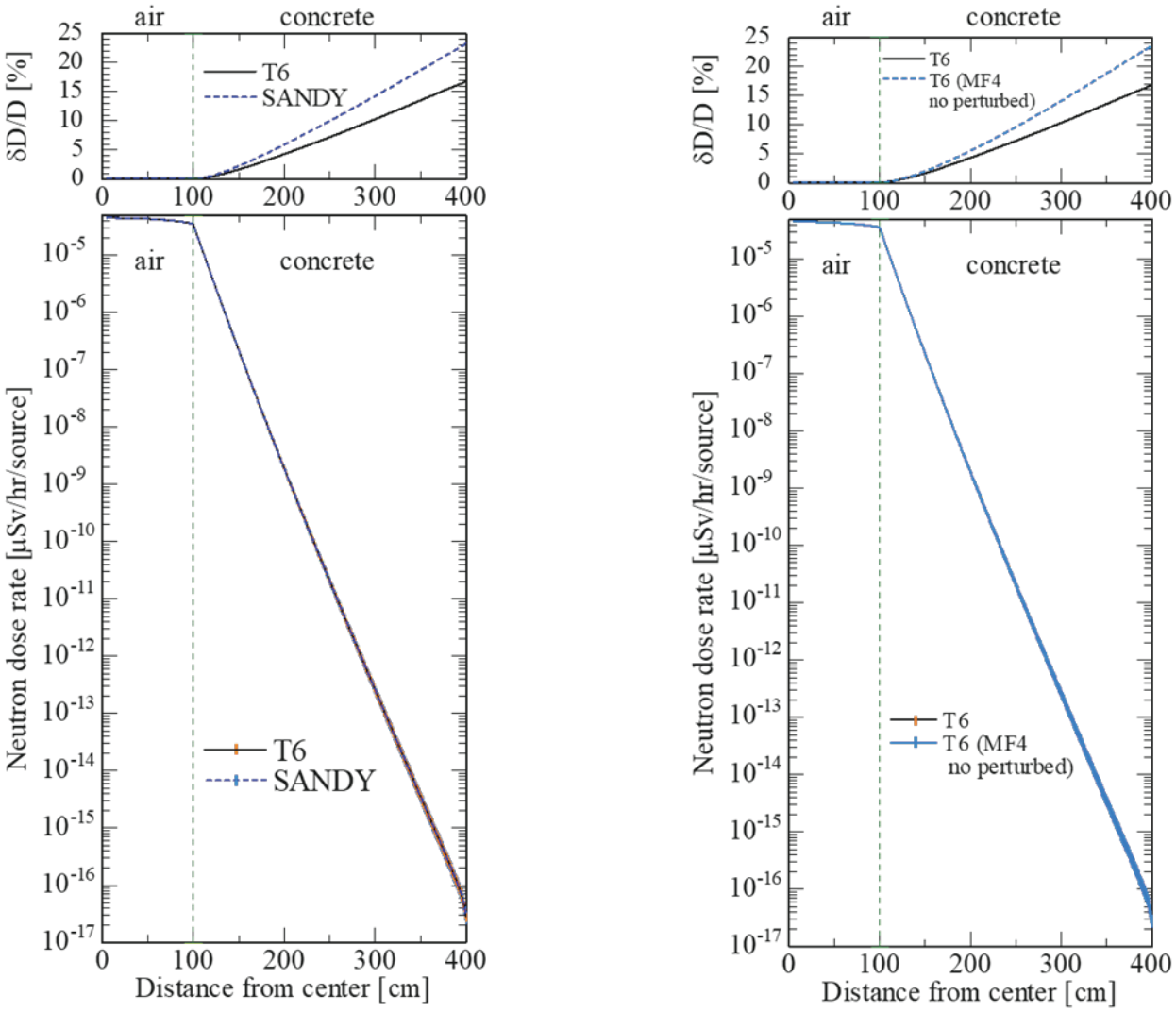

Figure 5. Results of neutron dose rate and standard deviation for T6, SANDY and MF4 no perturbed. [2]

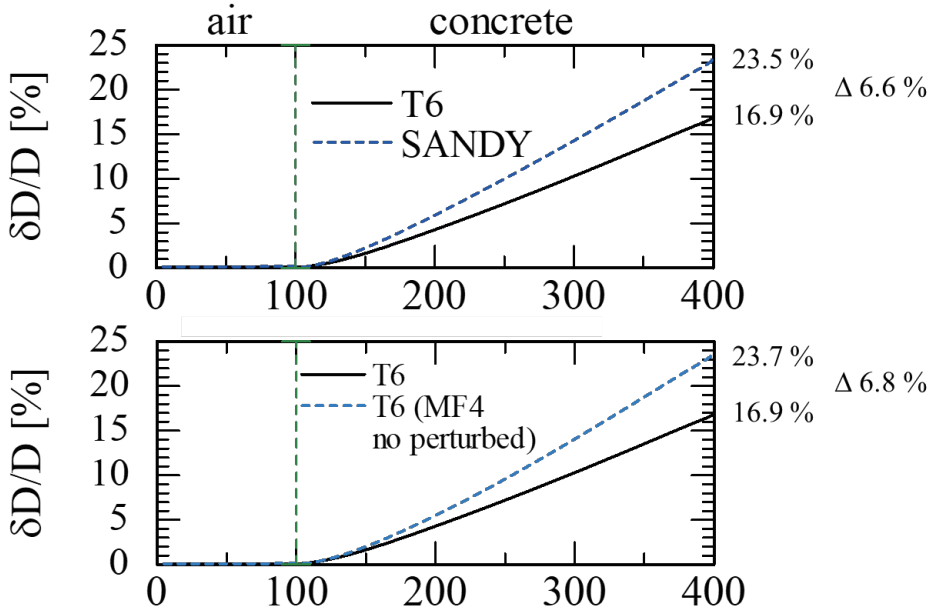

Figure 6. Standard deviation of neutron dose rate for T6, SANDY and MF4 no perturbed. (enlarged image)

As the optical theorem clearly shows, there is a positive correlation between the total cross section and the forward elastic scattering cross section, which is expressed by Wick's inequality (also called Wick's limit) [14] shown in the following equation.

$$\text{Optical theorem: } Imf(0) = \frac{k}{4\pi}\sigma_t \quad \rightarrow \quad \sigma_{el}(0) = |f(0)|^2 \geq \left(\frac{k}{4\pi}\sigma_t\right)^2 \qquad (1)$$

where $\sigma_{el}(0)$, σ_t and k denote elastic scattering cross section at 0 degree, total cross section and wave number of incident neutron, respectively.

Figure 7 shows the correlation between total cross sections and elastic scattering cross sections in the 0-degree direction from 1,000 random files generated by T6. The incident neutron energies are 2.2 MeV and 14 MeV. The black dots are for the T6 random data, and the red dots show the result of neglecting the correlation of the angular distribution of elastic scattering (MF4 no perturbed). It is clear from this figure that there is a strong positive correlation between the total cross section and the elastic scattering cross section at 0 degrees, but this correlation is reduced when the perturbation of the angular distribution of secondary neutrons is ignored. At the incident neutron energy of 14 MeV, the latter correlation almost disappears.

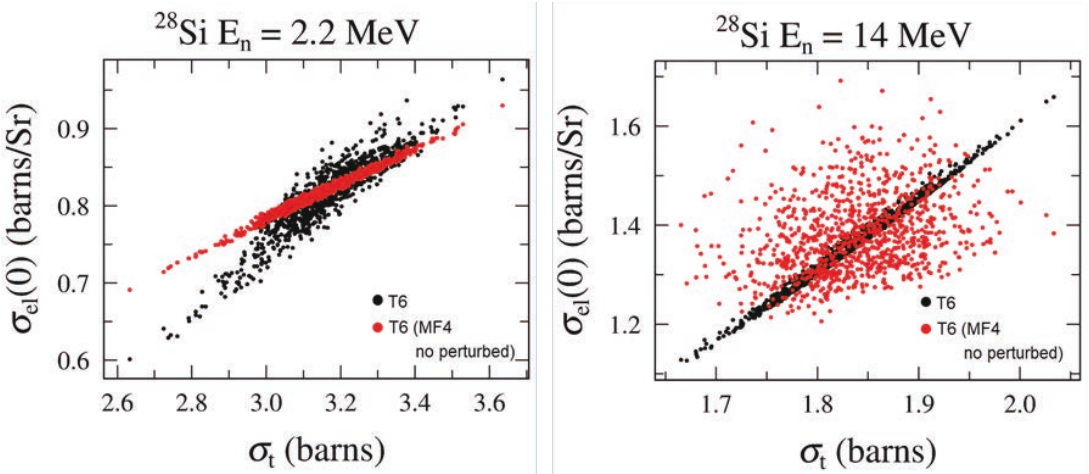

Figure 7. Correlation between the total cross section and the elastic scattering cross section in the 0 degree direction of 1,000 random data generated by T6. [2]

As shown in **Figure 8**, the forward elastic scattering cross section changes to cancel out the change in neutron transmission due to the change in the total cross section due to parameter perturbation, so the perturbations in the total cross section and the differential scattering cross section cancel each other out. It was shown that the standard deviation of the neutron dose rate decreases when this is taken into account. It has become clear that uncertainty in the angular distribution of secondary neutrons must be taken into account for accurate error evaluation of neutron current fields such as deep penetration problems.

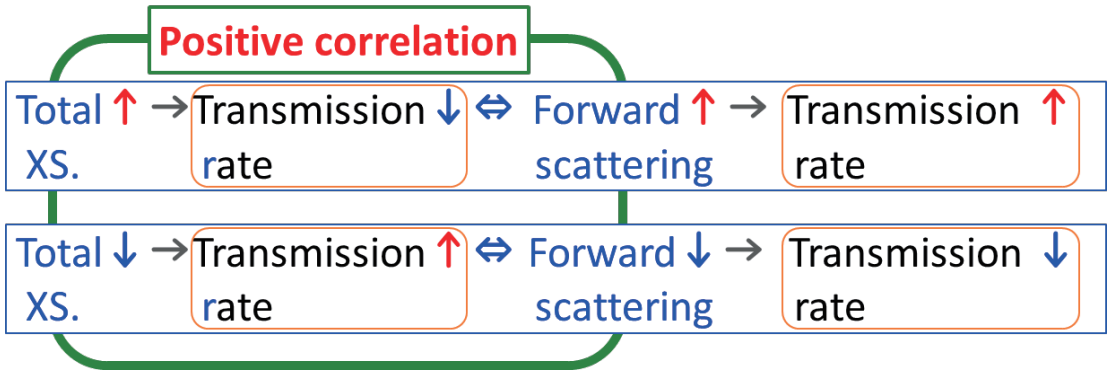

Figure 8. Relationship between total cross section, forward elastic scattering cross section, and neutron transmission rate.

5. Conclusion

The newly developed uncertainty analysis method is a combination of the T6 and the TMC method, and it is possible to consider the correlation between the angular distribution of elastic scattering and the total cross section, which is difficult to process with the current ENDF-6 format. This method is able to build a model and evaluate the propagation of errors of reactor physics quantities due to uncertainties in nuclear data. An example of application to the problem of deep penetration of concrete containing ^{28}Si was presented, and it was found that the uncertainty in dose rate can be reduced by considering the correlation between the angular distribution of elastic scattering and the total cross section. In the near future, it is expected to be applied to many fields such as shielding analysis of space reactors, fusion reactors and accelerator-driven systems (ADS).

References

1) Trkov A, Herman M, Brown DA, Eds. ENDF-6 formats manual, data formats and procedures for the evaluated nuclear data file ENDF/B-VI, ENDF/B-VII and ENDF/B-VIII. Brookhaven National Laboratory (US); 2018. doi: 10.2172/1425114 (BNL report BNL-203218-2018-INRE)
2) Yamano N, Inakura T, Ishizuka C, Chiba S. Crucial importance of correlation between cross sections and angular distributions in nuclear data of ^{28}Si on estimation of uncertainty of neutron dose penetrating a thick concrete. J Nucl Sci Technol. 2022; 59(5): 641-646. doi: 10.1080/00223131.2021.1997665.
3) Shibata K, Iwamoto O, Nakagawa T, et al. JENDL-4.0: a new library for nuclear science and engineering. J Nucl Sci Technol. 2011; 48(1): 1–30. doi:10.1080/18811248.2011.9711675.
4) Iwamoto O, Iwamoto N, Kunieda S, et al. Japanese evaluated nuclear data library version 5: JENDL-5. J Nucl Sci Technol. 2023; 60(1): 1-60. doi: 10.1080/00223131.2022.2141903.

5) Koning AJ, Rochman D, Sublet JC, et al. TENDL: complete nuclear data library for innovative nuclear Science and technology. Nucl Data Sheets. 2019; 155: 1–55. doi: 10.1016/j.nds.2019.01.002.
6) Koning AJ, Rochman D, Towards sustainable nuclear energy: putting nuclear physics to work. Ann Nucl Energy. 2008; 35(11): 2024–2030. doi: 10.1016/j.anucene.2008.06.004.
7) Fiorito L, Žerovnik G, Stankovskiy A, et al. Nuclear data uncertainty propagation to integral responses using SANDY. Ann Nucl Energy. 2017; 101: 359–366. doi: 10.1016/j.anucene.2016.11.026.
8) Brown DA, Chadwick MB, Capote R, et al. ENDF/B-VIII.0: the 8th major release of the nuclear reaction data library with CIELO-project cross sections, New standards and thermal scattering data. Nucl Data Sheets. 2018; 148: 1–142. doi: 10.1016/j.nds.2018.02.001.
9) MacFarlane RE, Kahler AC. Methods for processing ENDF/B-VII with NJOY. Nucl Data Sheets. 2010; 111(12): 2739–2890. doi: 10.1016/j.nds.2010.11.001.
10) Ingersoll DT, White JE, Wright RQ, et al. Production and testing of the VITAMIN-B6 fine group and the BUGLE-93 broad-group neutron/photon cross-section libraries derived from ENDF/B-VI nuclear data. NUREG/CR-6214 (US); 1995. (ORNL report ORNL– 6795).
11) MacFarlane RE, Muir DW, Boicourt RM, et al. The NJOY nuclear data processing system, version 2016. Los Alamos National Laboratory (US); 2016. (LANL report LA-UR–17–20093).
12) MacFarlane RE. TRANSX 2: a code for interfacing MATXS cross-section libraries to nuclear transport codes. Los Alamos National Laboratory (US); 1993. (LANL report LA-12312-MS).
13) Engle WW Jr. ANISN, a one-dimensional discrete ordinates transport code with anisotropic scattering. Oak Ridge National Laboratory (US); 1967. (ORNL report K–1693).
14) Wick GC. A theorem on cross sections. Phys Rev. 1949; 75(9): 1459. doi: 10.1103/PhysRev.75.1456.

4. Overview of FRENDY Version 2

Kenichi TADA[1*]
[1]Japan Atomic Energy Agency
2-4 Shirakata, Tokai-mura, Naka-gun, Ibaraki-ken 319-1195, Japan
[*]Email: tada.kenichi@jaea.go.jp

This paper explains the overview of the nuclear data processing code FRENDY version 2.

1. Overview of FRENDY 2

Nuclear data processing has an important role to connect evaluated nuclear data libraries and neutronics calculation codes. JAEA has developed the nuclear data processing code FRENDY since 2013 to generate a cross section file from an evaluated nuclear data file with a simple input file. FRENDY version 1 was released in 2019[1]. It only generates an ACE formatted cross section file[2] for the continuous energy Monte Carlo calculation codes such as PHITS[3], MCNP[4], Serpent[5], and OpenMC[6]. After we released FRENDY version 1, many functions were implemented such as multi-group cross section file generation function[7], adaptive setting of background cross section[8], resonance upscattering correction[9], ACE file perturbation[10], statistical uncertainty quantification of probability table[11], and modification of ENDF-6[12] formatted files[13]. We released FRENDY version 2 including these new functions in 2022[13,14].

2. How to use FRENDY?

FRENDY is an open-source software under 2-clause BSD license[15]. Everyone can freely use FRENDY and implement the modules of FRENDY in their code without any restriction. It can be downloaded from the JAEA website[16]. The references, manual[13], and presentation materials of FRENDY are available on the JAEA website. If you are interested in FRENDY or nuclear data processing, please visit the JAEA website. There are many materials to use FRENDY and study overview of nuclear data processing.

3. Input format of FRENDY

FRENDY can treat two input formats. One is the FRENDY's original input format. It is very simple and it does not require expert knowledge of nuclear data processing. For example, FRENDY can generate a cross section file with an evaluated nuclear data file name and processing mode. The other is the NJOY[17] compatible input format. The available NJOY input is MODER, RECONR, BROADR, PURR, UNRESR, THERMR, ACER, GROUPR, and MATXSR.

FRENDY version 2 has original functions to generate a multi-group cross section file, *e.g.*, explicit consideration of the resonance interference effect of the compound of different isotopes such as UO_2[7], automatic background cross section set with the minimum number of background cross section[8], and

resonance upscattering correction[9]. These functions are only available for the FRENDY's original input format. The sample inputs to use these functions are found in the manual of FRENDY[13]. These functions will improve the prediction accuracy of multi-group neutronics calculation codes.

4. Future work

We are now developing the heat production cross section calculation function, multi-group covariance matrices function, and treatment of the GNDS format[18]. FRENDY version 3 will be released including these functions in the future.

References

1) Tada K, Nagaya Y, Kunieda S, et al., Development and verification of a new nuclear data processing system FRENDY, J. Nucl. Sci. Technol., 54, 2017, pp.806–817.
2) Conlin JL, editor. A compact ENDF (ACE) format specification, LA-UR-19-29016, 2019.
3) T. Sato, Y. Iwamoto, S. Hashimoto, et al., Recent improvements of the Particle and Heavy Ion Transport code System - PHITS version 3.33, J. Nucl. Sci. Technol., 61(1), 2024, pp.127–135.
4) Werner CJ, editor. MCNP user's manual code version 6.2, LA-UR–17–29981, 2017.
5) Leppänen J, Pusa M, Viitanen T, et al. The Serpent Monte Carlo code: status, development and applications in 2013, Ann. Nucl. Energy, 82, 2015, pp.142–150.
6) Romano PK, Horelik NE, Herman BR, et al., OpenMC: a state-of-the-art Monte Carlo code for research and development, Ann. Nucl. Energy, 82, 2015, pp.90–97.
7) Yamamoto A, Tada K, Chiba G, et al., Multi-group neutron cross section generation capability for FRENDY nuclear data processing code, J. Nucl. Sci. Technol., 58, 2021, pp.1165–1183.
8) Yamamoto A, Endo T, Tada K., Adaptive setting of background cross sections for generation of effective multi-group cross sections in FRENDY nuclear data processing code, J. Nucl. Sci. Technol., 58, 2021, pp.1343–1350.
9) Yamamoto A, Endo T, Chiba G, et al., Implementation of resonance upscattering treatment in FRENDY nuclear data processing System, Nucl. Sci. Eng., 196, 2022, pp.1267–1279.
10) Tada K, Kondo R, Endo T, et al., Development of ACE file perturbation tool using FRENDY, J. Nucl. Sci. Technol., 60, 2023, pp.624–631.
11) Tada K, Endo T., Convergence behavior of statistical uncertainty in probability table for cross section in unresolved resonance region, J. Nucl. Sci. Technol., 60, 2023, pp.1397–1405.
12) Trkov A, Herman M, Brown DA., ENDF-6 format manual, BNL-203218-2018-INRE, 2018.
13) Tada K, Yamamoto A, Kunieda S, et al., Nuclear data processing code FRENDY version 2, JAEA-Data/Code 2022-009, 2023, 208p.
14) Tada K, Yamamoto A, Kunieda S, et al., Development of nuclear data processing code FRENDY version 2, J. Nucl. Sci. Technol., 61(6), 2024, pp. 830–839.
15) https://opensource.org/license/bsd-2-clause/ (accessed 2024/9/9).
16) https://rpg.jaea.go.jp/main/en/program_frendy/ (accessed 2024/9/9).
17) Kahler AC, editor., The NJOY nuclear data processing system, version 2016, LA-UR–17–20093, 2016.
18) OECD/NEA, Specifications for the generalised nuclear data structure (GNDS) version 2.0, NEA No. 7647, 2023.

5. Nuclear data measurement by surrogate reactions using ion beams

Katsuhisa NISHIO[†1]

[1]Advanced Science Research Center, Japan Atomic Energy Agency
[†]Email: nishio.katsuhisa@jaea.go.jp

Abstract

Surrogate reaction is a method to take neutron-induced nuclear data by populating the same compound nucleus of interest by nucleon transfer and/or multinucleon transfer (MNT) reactions using accelerated ion beams. In this approach we can take data for nuclei which are difficult and/or practically impossible using a neutron beam. In this report, we show results of fission data using MNT reactions. Among several fission data obtained in our setup, we introduce fission-fragment mass distributions (FFMDs). In this approach, data for many fissioning nuclei can be obtained in one measurement, including neutron-rich nuclei. Taking advantage of the property of MNT reactions which widely distribute excitation-energy in the compound nucleus, excitation-energy dependence of FFMDs is taken. The results of FFMDs indicate a strong effects of multichance fission.

1 Introduction

An accelerator-driven subcritical reactor system is one of the method to reduce the amount of long-lived minor actinides, produced in atomic power plants, by nuclear fission. In this system, many actinide niclides are produced in neutron-induced reactions and radioactive decay. The neutron-energy also distributes widely to high energies. In order to realize such a system, neutron-induced nuclear data for nuclides, including short-lived one, up to high-neutron energies are required. For short-lived nuclei, taking data using a neutron beam is practically impossible due to difficulty to prepare target material. Also, the experiments are difficult when one cannot prepare enough amount of target material with high purity. A surrogate reaction using ion-beam and available target material is the method to derive neutron-induced nuclear data.

In JAEA we are promoting surrogate reaction study to take neutron-induced fission data using multinucleon transfer (MNT) reactions [1]. The idea of measurement is shown in Fig. 1. The accelerated ion beam is bombarded to the target nuclei. The MNT channel, thus the compound nuclide, is identified by detecting the ejectile nucleus. The excitation energy, correspondingly incident neutron energy in surrogate reaction, is determined by measuring kinetic energy of ejectile. The fission fragments are detected by fission-fragment detector. In this setup, we can take fission cross sections, fission-fragment mass distribution (FFMD) and fission-barrier height. By mounting neutron-detectors, we can obtain neutron multiplicity accompanied in fission. In this report experimental data of FFMDs are highlighted.

2 Experimental setup

The setup for MNT-induced fission at the tandem accelerator facility in Tokai is shown in Fig. 2 [2, 3]. The setup consists of a silicon ΔE-E telescope located at forward angle to identify

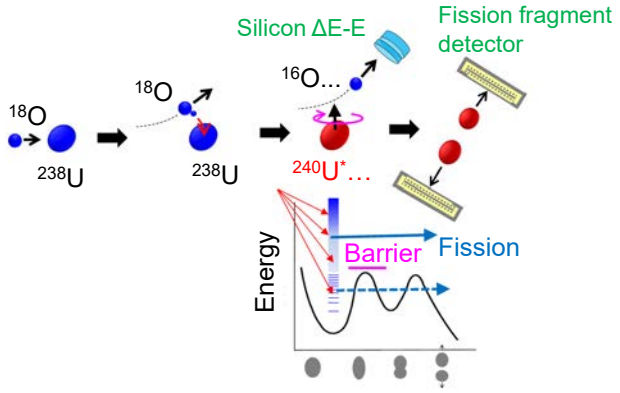

Figure 1: (Color online) Principle of MNT-induced fission measurement.

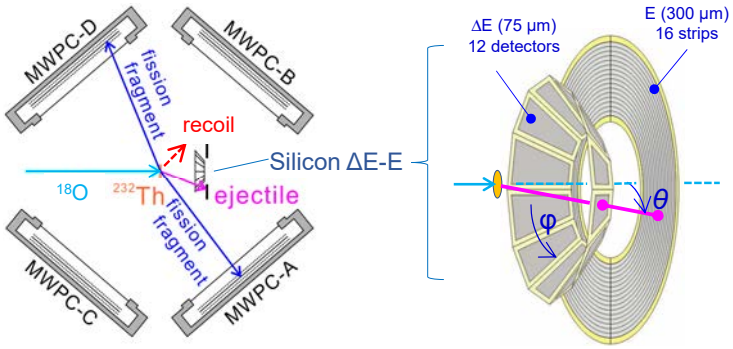

Figure 2: (Color online) Schematic detection set-up (left), and expanded view of the silicon ΔE-E telescope (right).

transfer channel, surrounded by MWPC detectors to detect fission fragments. The ΔE part of the telescope consists of 12 detectors, where each detector describes an azimuthal sector φ around the beam axis. Typical thickness of the ΔE detectors is 50–75 μm. The E detector is an annular-type, and the ring-shaped strip number defines the scattering angle θ with respect to the beam direction. Total energy of the ejectile particle is calculated as $E_{\rm sum} = \Delta E + E$. The energy resolution to determine $E_{\rm sum}$ is ∼1.0 MeV FHWM, which corresponds to the uncertainty in determining the excitation energy of the CN. Figure 3 shows the result of particle identification in this setup, obtained in the ^{18}O+^{237}Np reaction [4] at a beam energy 80% higher than the Coulomb barrier. It is found that more than 20 ejectile nuclides can be identified. From the information of ejectile species, kinetic energy and trajectory (θ, φ), the momentum of the recoil nucleus and its direction are determined. We assume that the most of the total excitation energy $E^*_{\rm tot}$ is taken by the fissioning CN.

To obtain fission data for each compound nucleus, the ΔE-E telescope is combined with fission detectors. Two fragments are detected in coincidence by either of the two pairs of MWPCs, and the time difference Δt(A-D) or Δt(B-C) are recorded to derive the fragment masses. The MWPCs also record the incident position (X,Y) of the fragments. Fission-fragment mass and kinetic energies are determined through the conservation of momentum with respect to the momentum vector determined for the recoiling CN.

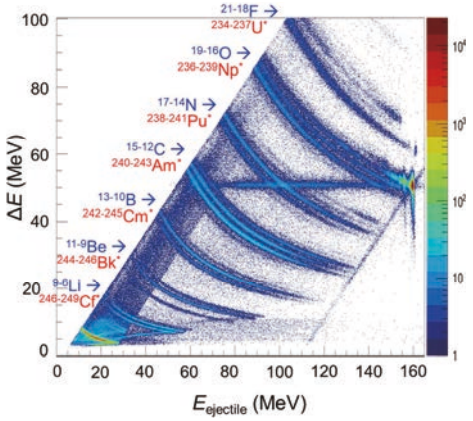

Figure 3: (Color online) An example of identification of ejectile nuclei (labeled in blue) by the silicon ΔE-E telescope obtained in the ^{18}O+^{237}Np reaction at the beam energy of 162 MeV [4]. The corresponding fissioning compound nuclei are shown (in red).

3 Results and discussion

Figure 4 shows the FFMDs for $^{234-237}$U, $^{236-239}$Np, and $^{238-241}$Pu obtained from MNT reaction of ^{18}O+^{238}Np [4]. The excitation-energy dependence of the FFMDs are shown for each fissioning nucleus. In this reaction, data for CN with larger atomic and mass numbers ($^{240-243}$Am, $^{242-245}$Cm, $^{244-246}$Bk) are also obtained. The lowest excitaion-energy data in Fig. 4, below E^* =20 MeV exhibit a prominent double peak structure due to the shells. Toward high excitation energies, the two-peak structure of FFMD disappears due to smearing of the shells.

In MNT induced fission, a nuclide to be studied can be populated by different MNT channels, starting from different projectile-target combinations. In Fig. 5, FFMDs of low-energy fissions with average excitation energy E^*=15 MeV for $^{235-237}$U*, ^{239}Np*, and ^{241}Pu*, ^{242,243}Am*, ^{247}Cm*, and ^{249,250}Bk* from different MNT reactions are compared. For all the nuclei, the general shape of the FFMD remains apparently insensitive to the number of transferred nucleons, i.e., insensitive to the way the CN is produced. In particular, a good agreement of the light- and heavy-fragment peak positions can be noticed. With regards to excitation-energy dependence, it has been shown that, in the excitation energy range of 13−45MeV, FFMDs from fission of ^{239}U produced in the ^{238}U(^{18}O,^{17}O)^{239}U reaction agree with those from the neutron-induced fission of ^{238}U [3]. Also, it is confirmed in the fission from highly excited states of $^{235-237}$U*, ^{239}Np*, and ^{241}Pu*, that obtained FFMDs from different MNT channels are essentially the same as one another up to E^* =60 MeV [4].

3.1 Multichance fission

Multichance fission is obverved as a step-like structure in fission cross sections when viewed as a function of excitation energy, in which intermittent steps appear as excitation energy exceed each neutron-emission threshold [5]. The effects of this so-called multichance fission (MCF) on FFMDs are schematically explained in Fig. 6(a). The compound nucleus ^{240}U* in this example can decay either via "first-chance fission", or single neutron emission, leading to a less excited ^{239}U*. The daughter nucleus can then decay again, either by fission (thus, "second-chance fission") or by further neutron evaporation; the competition between fission and neutron emission continues, until the excitation energy of the corresponding daughter nucleus (or residual nucleus) drops below neutron-evaporation threshold. The shape of the FFMD for each fission chance is

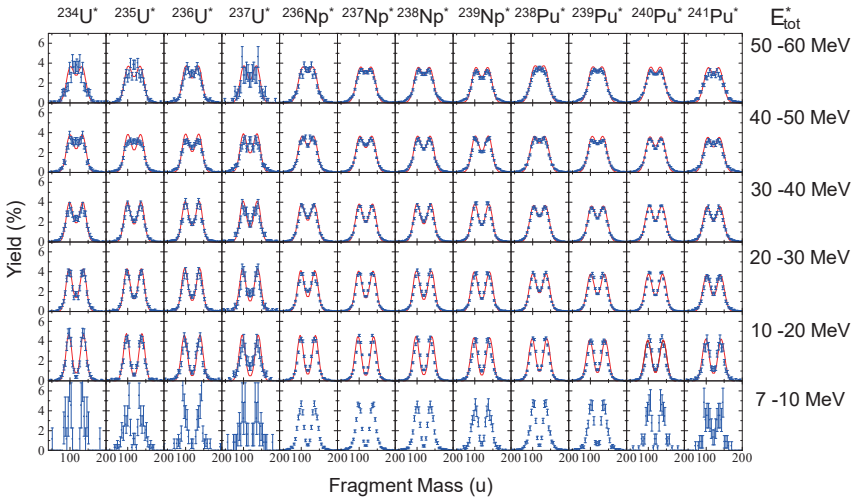

Figure 4: (Color online) Fission-fragment mass distribution for nuclei ($^{234-237}$U, $^{236-239}$Np, $^{238-241}$Pu) produced in the multinucleon transfer channels of ^{18}O+^{237}Np [4]. Curves are Langevin calculations which takes into account multichance fission.

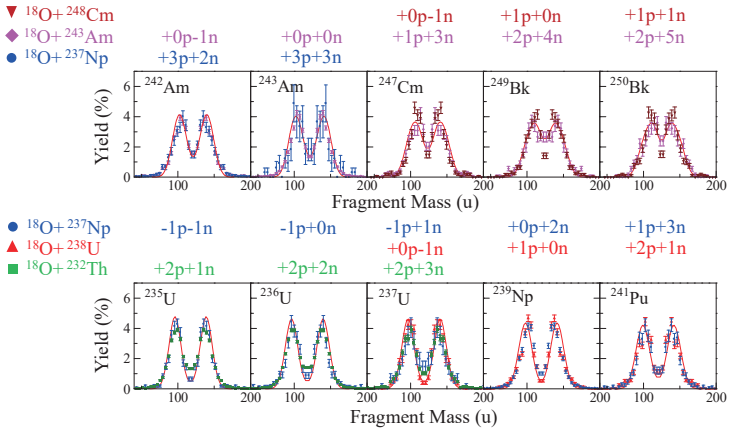

Figure 5: (Color online) Fission-fragment mass distribution at low-excitation energy of $E^*_{\rm tot}$=10−20 MeV for $^{235-237}$U*, ^{239}Np*, ^{241}Pu*, ^{242,243}Am*, ^{247}Cm*, and ^{249,250}Bk*, obtained in multinucleon transfer reactions of ^{18}O+^{232}Th [2], ^{18}O+^{238}U [3], ^{18}O+^{237}Np [4], ^{18}O+^{243}Am, and ^{18}O+^{248}Cm (unpublished). The number of transferred neutrons and protons is shown for each CN, where positive sign means the movement of nucleon from the projectile to the target nucleus and the negative sign represents the opposite direction. Solid curves are Langevin calculation.

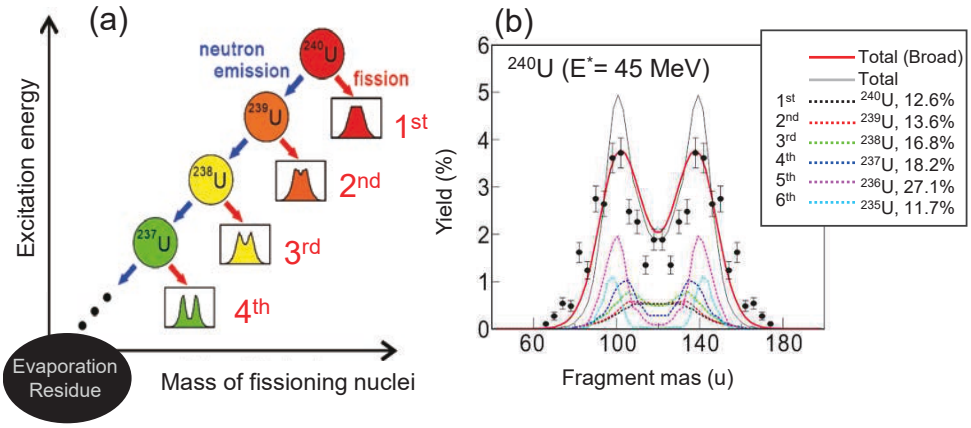

Figure 6: (Color online) (a) A conceptual view of MCF for the case of the initial compound nucleus ^{240}U; see detail in the text. (b) Calculated FFMDs for all the MCF steps up to sixth-chance fission (dashed curves) are shown for the initial compound nucleus ^{240}U at excitation energies of 40−50 MeV [3]. Their sum is given by the thin solid line. For comparison with the experimental data (solid circles with error bars), the calculated sum of the FFMDs was broadened by the experimental mass resolution, and the resulting FFMD is shown by the red thick curve.

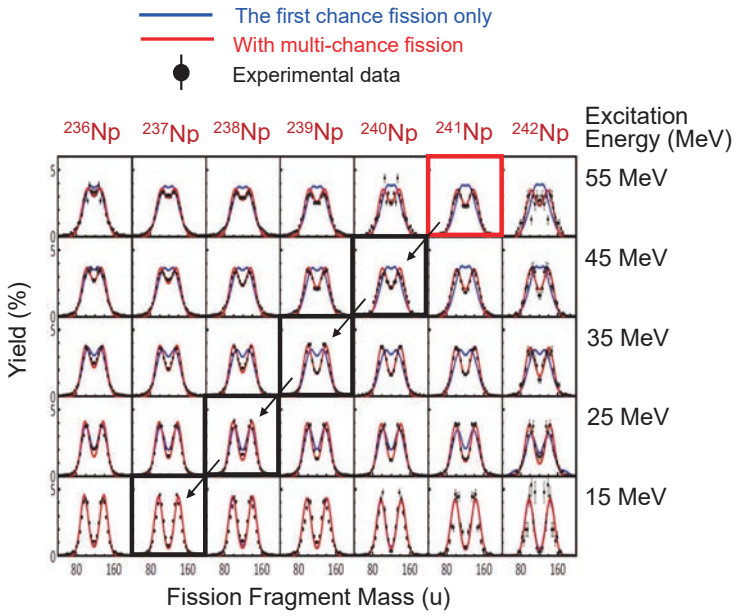

Figure 7: (Color online) Comparison of the measured fission-fragment mass distributions for neptunium isotopes (solid circles) [3, 4] with the Langevin calculations. The red and blue curves are the calculation respectively with and without taking into account the MCF concept. The average excitation-energy for each 10-MeV excitation-energy bin is shown on the right-hand side.

also shown schematically in this figure, with predominantly symmetric fission for the initial compound nucleus $^{240}U^{*}$, and dominant asymmetric fission for subsequent higher-order fission chances, due to the revival of the shell effects responsible for mass asymmetry in fission. This effect is particularly evident for $^{237}U^{*}$ (fourth-chance fission) in this example. The application of this process to the calculation of FFMDs for $^{240}U^{*}$ at 45 MeV is demonstrated in Fig. 6(b) [3]. The calculated FFMDs by the Langevin approach [6] for successive fission chances are shown by the dashed curves with different colors, where the fraction (probability) of each fission chance is determined using the GEF code [7]. The sum of all the FFMDs obtained from each fission chance (up to sixth-chance fission) is shown by the thin black curve. After taking into account the experimental mass resolution (red thick curve), the calculation well reproduces the experimental data. The key finding from Fig. 6(b) is that the apparent mass-asymmetric fission observed in the data, even at high excitation energies, originates from the lower-energy fourth-, fifth-, and sixth chance fissions (^{237,236,235}U). On the contrary, the first- and second-chance fissions lead to predominantly symmetric mass splits, as they occur at high excitation energy.

The same calculation, including the MCF, is applied to the FFMDs for neptunium isotopes obtained in the ^{18}O+^{237}Np ($^{236-239}$Np) and ^{18}O+^{238}U ($^{240-242}$Np) reactions [8]. The results are shown in Fig. 7. Although the FFMDs for the lowest average excitation energy (15 MeV) exhibit almost the same peak-to-valley ratio for all the isotopes, the spectra above 35 MeV clearly show a systematic variation of the FFMDs. By comparing the FFMDs across isotopes for each of the higher excitation-energy ranges, it is observed that the heavier isotopes have larger peak-to-valley ratio. In Fig. 7, the experimental data are compared with a pair of Lagevin calculation, carried out by imposing two apposing assumptions. One is obtained without introducing neutron emission before fission (without MCF). This calculation apparently overestimates the symmetric fission yields at $E^{*} \geq$30 MeV and cannot explain the measured double-peak structure. Whereas the other calculation, which takes into account the MCF, well explains the FFMDs, including the enhanced peak-to-valley ratio toward heavier neptunium isotopes. This is due to a smaller neutron binding energy for heavier neptunium isotopes, which enhances the neutron-emission probability before fission. The Langevin calculation with MCF is also compared with experimental data in Fig. 4 and Fig. 5, where good agreement is found.

Starting from the initial nucleus ^{241}Np at 55 MeV (red box) of Fig. 7, the blue curves in Fig. 7 shown in the bold-boxes can be interpreted as the FFMDs for each stage of fission chance, similar to the FFMDs shown in Fig. 6(a), as these nuclides are successively populated by neutron emission. Having established the predictive power of the calculations in matching the experimental data, the blue FFMD curves from the Langevin calculation show the pure picure of fission at each excitation energy, and the results indicates that the shell effects for fission disappear at $E^{*} \approx$40 MeV.

References

[1] Nishio, K. *Multinucleon-transfer induced fission*, Handbook of Nuclear Physics, Springer Nature, p.91 (2023).

[2] Léguillon, R. et al., Phys. Lett. B, vol. 761, 125 (2016).

[3] Hirose, K. et al., Phys. Rev. Lett., vol. 119, 222501 (2017).

[4] Vermeulen, M.J. et al., Phys. Rev. C, vol. 102, 054610 (2020).

[5] Lestone, K.P. Nucl. Data Sheets, vol. 112, 3120 (2011).

[6] Aritomo, Y. and Chiba, S. Phys. Rev. C, vol. 88, 044614 (2013).

[7] Schmidt, K.-H., Nucl. Data Sheet vol. 131, 107 (2016).

[8] Tanaka, S. et al., Phys. Rev. C, vol. 100, 064605 (2019).

6. Muon Nuclear Data

Megumi NIIKURA[1*], Shinichiro ABE[2], Shoichiro KAWASE[3], Teiichiro MATSUZAKI[1],
Futoshi MINATO[4], Rurie MIZUNO[5], Yukinobu WATANABE[3], Yuji YAMAGUCHI[2]
[1]RIKEN Nishina Center, 2-1 Hirosawa, Wako-shi, Saitama 351-0198, Japan
[2]Japan Atomic Energy Agency,
2-4 Shirane, Shirakata, Tokai-mura, Naka-gun, Ibaraki 319-1195, Japan
[3]Faculty of Engineering Sciences, Kyushu University
6-1 Kasugakoen, Kasuga-shi, Fukuoka 816-8580, Japan
[4]Faculty of Science, Kyushu University, 744 Motooka, Nishi-ku, Fukuoka 819-0395, Japan
[5]Faculty of Science, the University of Tokyo, 7-3-1 Hongo, Bunkyo-ku, Tokyo 113-0033, Japan
[*]Email: niikura@ribf.riken.jp

We plan to develop a new nuclear database for muon-induced nuclear reactions (muon nuclear data). The database will consist of (1) energies and intensities of the muonic X rays, (2) lifetimes of the muonic atom, (3) production branching ratio of the residual nuclei by muon capture, (4) emission probabilities of the particles after muon capture, and (5) energy spectra of the emitted particles after muon capture. In this paper, we review the present status and current investigations for the muon nuclear data.

1. Introduction

The muon is a second-generation charged lepton with a mass of 105.658 MeV/c^2 and a lifetime of approximately 2.2 μs in the vacuum. When a negatively charged muon[1] stops in the matter, it forms a highly excited atomic state with the nucleus, the so-called muonic atom. The excited muonic atom promptly cascades down to the atomic ground (1s) state by emitting Auger electrons and muonic X-rays. Because the muon's wave function in the muonic atom largely overlaps with that of the nucleus, the energies of the muonic X-rays are affected by the finite size of the nuclear charge distribution and thus provide a determination of an absolute charge radius of the nucleus [1–4]. The energies of the muonic K_α X-rays for various nuclei are summarized in Ref. [1] as a table of nuclear charge radii.

The muon in the muonic atom at the 1s state decays via two processes: free muon decay and muon capture. The free muon decay is the same decay process as the muon in the vacuum as follows:

$$\mu^- \rightarrow e^- + \nu_\mu + \nu_e, \quad (1)$$

and muon capture is a process which is the capture of the muon by a proton in the nuclear medium via the charged current of the weak interaction as follows [5]:

$$\mu^- + p \rightarrow n + \nu_\mu. \quad (2)$$

The partial lifetime of the free muon decay is approximately the same as the lifetime of the negative

[1] Though there are two muons, the positive and negative muons, we discuss only the negative muon in this paper, and hereafter "muon" represents the negatively charged muon.

muon in the vacuum, and that of muon capture depends on the overlap of the wave functions of the muon and the nucleus. Because the size of the muonic atom (Bohr radius) is approximately inversely proportional to the element number (Z) of the nucleus, the lifetime of the muonic atom is shorter for the heavy muonic atom. The typical lifetime of the muonic atom with $Z < 10$ is 2 μs, corresponding to the free decay branch of more than 90%. In contrast, the typical lifetime for the heavier muonic atom with $Z > 40$ is about 100 ns, corresponding to the free decay branch of less than 5% (see Fig.1 in Ref. [5]). Most of the published data for measured lifetimes of the muonic atom is listed in Ref. [6].

Muon capture is an analogous reaction to electron capture; the main difference between them is in their energy transfer. The energy released by muon capture is 104.3 MeV, corresponding primarily to the mass of the muon. If the proton is at rest, as expressed in Equation (2), the recoiling neutron takes only 5.2 MeV of kinetic energy, whereas the neutrino takes away 99.1 MeV. Muon capture for the general nucleus of (A, Z), where A is the mass number of the nucleus, produces a compound nucleus of $(A, Z-1)^*$ as follows:

$$\mu^- + (A, Z) \rightarrow (A, Z-1)^* + \nu_\mu. \quad (3)$$

Because the nucleus is a many-body system, the excitation energy of the compound nucleus is distributed around 10–50 MeV. The energy and angular-momentum (spin) distributions of the compound states populated by muon capture are of interest in an understanding of the reaction mechanism; however, experimental data are sparse and require improvements.

The importance of the interactions between the muon and the nucleus, namely spectroscopic information of the muonic atom and muon capture, has recently been focused in the many fields of the natural sciences and applications, such as nuclear physics, nuclear transmutation for nuclear waste [7], muon-induced radioactive isotope production for medical use [8], radiation safety data in the muon facilities [], cosmic muon-induced soft error in modern semiconductor devices [9,10], cosmogenic production of radioactive nuclides for geological studies, and non-destractive element analysis by muon-induced X-ray emission (MIXE) [11-13]. Despite those demands, nuclear data for muon-induced nuclear reactions (muon nuclear data) has not existed thus far.

2. Muon nuclear data

We here propose to develop muon nuclear data. The database will consist of the following five sublibraries:

(1) The energies and intensities of the muonic X-rays,
(2) Lifetimes of the muonic atom (muon capture probability),
(3) The production branching ratio of the residual nuclei by muon capture,
(4) Emission probabilities and multiplicities of the evaporation particles by muon capture,
(5) Energy distribution of the emission particles by muon capture.

Important note that the “cross-section” is not an objective of muon nuclear data because the formation probability of the muonic atom is unity, and the reactions occur only when the muon stops in the matter.

3. Current status of muon nuclear data

The muonic X-ray energies only for the Lyman series (Kα) are summarized in Ref. [1], and measured X-ray energy spectra for various samples are uploaded on the website by the Joint Institute for Nuclear Research (JINR) [14]; however, energies for other higher-order X-ray series and muonic

X-ray intensities are rarely found in the publication. For the theoretical model calculation, the muonic X-ray energies can be calculated by Mudirac [15]. Mudirac reproduced measured muonic X-ray energy rather well, within approximately 1-keV accuracy, while the calculation for the X-ray intensity is under development.

Most of the published data for measured lifetimes of the muonic atom is listed in Ref. [6]. For the theoretical model calculation, Primakoff proposed an empirical formula to estimate the lifetime of the muonic atom [16]. The Primakoff formula well reproduced experimentally measured lifetime with some exceptions (see Fig. 6 in Ref. [6]).

The production branching ratios of the residual nuclei by muon capture have been measured in the past, and most of them are summarized in the review article by Measday [17]. The production branching ratios of reaction residues of muon capture were estimated from the known experimental data, for example, as shown in Table 5.5 in Ref. [17] for a case of muon capture on ^{28}Si. Because of several inconsistencies in the different experiments, Measday “gives no error because of the inconsistencies” and states this compilation as a “suggestion”.

The production branching ratio of the residual nuclei and emission probabilities and multiplicities of the evaporation particles by muon capture is complemental information. In medium and heavy nuclei, the particles emitted from muon capture are primarily neutrons because the emission of charged particles is suppressed by the Coulomb barrier. Neutron multiplicity has been measured in the past neutron measurement using a large liquid scintillator tank [18], γ-ray measurement [19], and activation measurement [20]. The neutron multiplicities for 0, 1, 2, and 3 neutron emissions were estimated at 15-30%, 50-60%, 10-20%, and 0.2-10%, respectively [20]. Because of the large error propagation in the folding analysis for the neutron measurement and the incomplete data for the activation, only roughly estimated values without uncertainty for the neutron multiplicity are known so far.

The energy distribution of the emission particles (neutron, proton, deuteron, alpha, etc…) by muon capture was also measured for some nuclei. The energy spectra of neutrons have been measured for the heavy nuclei of Tl, Pb, Bi [21], and Pd isotopes [22]. The low-energy component of the neutron energy spectrum below 5 MeV can be understood by the statistical evaporation from the compound nucleus; however, the spectrum extends to higher energies. The high-energy component of the neutron energy spectrum is interpreted as due to direct and pre-equilibrium processes, in which the neutron is emitted immediately at the time of muon capture before reaching the thermal equilibrium of the compound states. The energy spectra for the charged particles were also measured for some nuclei; however, the experimental data is limited.

4. Recent investigations for muon nuclear data

In this section, we introduce our recent theoretical and experimental investigations and developments related to muon nuclear data.

4.1. Theoretical models

For the theoretical model calculation, muon interaction models have recently been implemented in the Monte Carlo simulation code of the particle and heavy ions transport code system (PHITS) [23,24]. In this model, the neutron energy produced by muon capture, as expressed in Equation (2) and (3), was sampled from the excitation function proposed by Singer [25]. The time evolution of the

initial neutron energy to the compound nucleus was calculated using JAERI Quantum Molecular Dynamics (JQMD) [26,27], and the sequential evaporation process was calculated using the Generalized Evaporation Model (GEM) [28].

There is another attempt to calculate the muon capture reaction by the microscopic theoretical model [29,30]. In the model, the muon capture rates are estimated by the second Tamm-Dancoff approximation with the two-component exciton model, which describes particle emission from the pre-equilibrium state [31,32]. For particle evaporation from the compound state, the Hauser-Feshbach statistical models were applied [33].

Due to the lack of muon nuclear data, particularly related to the muon capture reaction, the model calculation requires further experimental data for benchmarking and improvements.

4.2. Developments of experimental methods and detectors

The activation method is the most reliable and sensitive technique for determining the production rate of radioactive nuclei by muon beam irradiation. In classical activation measurements, only production ratios of long-lived radioactive isotopes can be obtained because the decay measurements usually take place separately at the time and location of beam irradiation to avoid the beam background. We have recently developed a novel method called the in-beam activation method, which enables us to measure the activities of short-lived states [34]. The combination of in-beam and ordinary offline activation methods enables the measurement of most of the β-decaying states with a wide range of half-lives from a few milliseconds to years.

Recently, we have also developed detectors for muonic X-ray spectroscopy [35,36] and for the measurements of neutrons and charged particles from muon capture [37,38]. The wide-range photon detection system for muonic X-ray spectroscopy was developed using a germanium detector with Compton suppressors. The system was demonstrated at the muon facility in the Paul Scherrer Institute, and complete data of muonic X-ray energies and intensities for ^{197}Au and ^{209}Bi was obtained [38]. For the neutron measurement, a new solid-state scintillator with neutron-gamma discrimination capability (EJ-276) is under development [37]. The charged particle detector array was also constructed. The detector has a particle discrimination capability based on digital waveform analysis techniques for neutron transmutation-doped silicon (nTD-Si) detectors [38]. In 2023, charged particle measurement from muon capture of ^{28}Si at the RIEKN-RAL facility in the Rutherford Appleton Laboratory was performed, the data analysis of which is ongoing.

5. Summary and outlook

We plan to develop the muon nuclear data, which will consist of the following five sublibraries. The importance of the interactions between the muon and the nucleus, namely spectroscopic information of the muonic atom and muon capture, has recently been focused in the many fields of the natural sciences and applications. Although some of the sublibraries measured in the past are already summarized in the publication [1,6], there is no complete database, and it needs compilation and improvements. Several theoretical and experimental investigations for muon nuclear data are currently ongoing.

References

1) G. Fricke et al., “Nuclear Ground State Charge Radii from Electromagnetic Interactions”,

At. Data Nucl. Data Tables **60**, 177 (1995).
2) I. Angeli and K. P. Marinova, “Table of experimental nuclear ground state charge radii: An update”, At. Data Nucl. Data Tables **99**, 69 (2013).
3) P. Bergem et al., “Nuclear polarization and charge moments of ^{208}Pb from muonic x rays”, Phys. Rev. C Nucl. Phys. **37**, 2821 (1988).
4) T. Y. Saito et al., “Muonic X-Ray Measurement for the Nuclear Charge Distribution: the Case of Stable Palladium Isotopes”, arXiv:2204.03233 [nucl-ex] (2022).
5) T. Yamazaki et al., “Negative Moun Spin Rotation”, Phys. Scr. **11**, 133 (1975).
6) T. Suzuki et al., “Total nuclear capture rates for negative muons”, Phys. Rev. C Nucl. Phys. **35**, 2212 (1987).
7) R. Fujita et al., Patent JP6106892
8) T. Matsuzaki, Patent JP6288694; and T. Matsuzaki et al., Patent JP6873484.
9) S. Manabe et al., “Negative and Positive Muon-Induced Single Event Upsets in 65-nm UTBB SOI SRAMs”, IEEE Trans. Nucl. Sci. **65**, 1742 (2018).
10) T. Mahara et al., “Irradiation Test of 65-nm Bulk SRAMs With DC Muon Beam at RCNP-MuSIC Facility”, IEEE Trans. Nucl. Sci. **67**, 1555 (2019).
11) K. Terada et al., “A new X-ray fluorescence spectroscopy for extraterrestrial materials using a muon beam”, Sci. Rep. **4**, 5072 (2014).
12) K. Ninomiya et al., “Nondestructive Elemental Depth-Profiling Analysis by Muonic X-ray Measurement”, Anal. Chem. **87**, 4597 (2015).
13) S. Biswas et al., “Characterization of a Continuous Muon Source for the Non-Destructive and Depth-Selective Elemental Composition Analysis by Muon Induced X- and Gamma-rays”, Appl. Sci. **12**, 2541 (2022).
14) Joint Institute for Nuclear Research (JINR), Mesoroentgen Spectra Catalogue, https://muxrays.jinr.ru/ (accessed 2024-1-10).
15) S. Sturniolo and A. Hillier, “Mudirac: A Dirac equation solver for elemental analysis with muonic X-rays“, X-ray Spectrom. **50**, 180 (2021).
16) H. Primakoff, “Theory of Muon Capture”, Rev. Mod. Phys. **31**, 802 (1959).
17) D. F. Measday, “The nuclear physics of muon capture”, Phys. Rep. **354**, 243 (2001).
18) B. Macdonald, J. A. Diaz, S. N. Kaplan, and R. V. Pyle, “Neutrons from Negative-Muon Capture”, Phys. Rev. **139**, B1253 (1965).
19) G. Backenstoss et al., “Nuclear γ-rays following muon capture”, Nucl. Phys. A **162**, 541 (1971).
20) G. Heusser and T. Kirsten, “Radioisotope production rates by muon capture”, Nucl. Phys. A **195**, 369 (1972).
21) W. U. Schröder et al., “Spectra of neutrons from μ capture in thallium, lead and bismuth”, Z. Phys. 268, 57 (1974).
22) T. Y. Saito, Ph.D. thesis, Univ. Tokyo (2023).
23) T. Sato et al., “Particle and Heavy Ion Transport code System, PHITS, version 2.52”, J. Nucl. Sci. Technol. **50**, 913 (2013).
24) S. Abe and T. Sato, “Implementation of muon interaction models in PHITS”, J. Nucl. Sci. Technol. **54**, 101 (2017).
25) P. Singer, “Neutron emission following muon capture in heavy nuclei”, Il Nuovo Cimento

(1955-1965) **23**, 669 (1962).
26) H. Iwase, K. Niita, and T. Nakamura, “Development of General-Purpose Particle and Heavy Ion Transport Monte Carlo Code”, J. Nucl. Sci. Technol. **39**, 1142 (2002).
27) K. Niita et al., “PHITS—a particle and heavy ion transport code system”, Radiat. Meas. **41**, 1080 (2006).
28) S. Furihata, in *Advanced Monte Carlo for Radiation Physics, Particle Transport Simulation and Applications* (Springer Berlin Heidelberg, 2001), pp. 1045–1050.
29) M. Ciccarelli, F. Minato, and T. Naito, “Theoretical study of Nb isotope productions by muon capture reaction on ^{100}Mo“, Phys. Rev. C Nucl. Phys. **102**, 034306 (2020).
30) F. Minato, T. Naito, and O. Iwamoto, “Nuclear many-body effects on particle emission following muon capture on ^{28}Si and ^{40}Ca”, Phys. Rev. C Nucl. Phys. **107**, 054314 (2023).
31) J. Da Providência, “Variational approach to the many-body problem”, Phys. Rev. C Nucl. Phys. **61**, 87 (1965).
32) F. Minato, “Estimation of a 2p2h effect on Gamow-Teller transitions within the second Tamm-Dancoff approximation“, Phys. Rev. C Nucl. Phys. **93**, 044319 (2016).
33) W. Hauser and H. Feshbach, “The inelastic Scattering of Neutrons”, Phys. Rev. **87**, 366 (1952).
34) M. Niikura et al., “Measurement of the production branching ratios following nuclear muon capture for palladium isotopes using the in-beam activation method”, Phys. Rev. C Nucl. Phys. **109**, 014328 (2024).
35) R. Mizuno et al., “Response of germanium detectors for high-energy γ-rays by ^{27}Al(p,γ)^{28}Si at E_p=992 keV”, Prog Theor Exp Phys **2023**, (2023).
36) R. Mizuno et al., “Development of wide range photon detection system for muonic X-ray spectroscopy”, Nucl. Instrum. Methods Phys. Res. A **1060**, 169029 (2024).
37) T. Kawata et al., in this proceedings.
38) S. Kawase et al., “Effect of large-angle incidence on particle identification performance for light-charged (Z≤2) particles by pulse shape analysis with a pad-type nTD silicon detector”, Nucl. Instrum. Methods Phys. Res. A **1059**, 168984 (2024).

7. Typical and Newly Identified Reactor Physics Issues of the Supercritical Water-cooled Reactor (SCWR)

Akifumi YAMAJI[1*]
[1]Cooperative Major in Nuclear Energy, Waseda University
3-4-1, Okubo, Shinjuku-ku, Tokyo 169-8555, Japan
*Email: akifumi.yamaji@waseda.jp

Supercritical Water-cooled Reactor (SCWR) is the only water-cooled reactor among the six Generation IV reactor concepts. The SCWR plant concept may be characterized by low capital cost and high flexibility. The single-phase cooling nature of SCWR realizes the once-through direct cycle plant system, which has the potential to dramatically reduce capital (construction) cost of the plant by simplification and elimination of components. Moreover, the large temperature and density changes of the coolant allow designing of flexible cores with outlet temperature ranging from 500 to over 600 ℃ and neutron spectrum ranging from thermal to fast. The existing SCWR design concepts include both the pressure vessel type (China, the EU, Japan, Russia) and pressure tube type (Canada) reactors, and all the design concepts assume operation pressure of about 25 MPa.

Generally, the thermal and fast reactors are loaded with enriched uranium and plutonium fuels, respectively. The fuel enrichments tend to be higher than those of the current Light Water Reactors (LWRs), because of larger neutron absorption cross sections of candidate cladding materials. The major reactor physics issues may include, but not limited to accurate evaluations of the core power distributions and the coolant density reactivity feedbacks. The core power distribution directly influences the core average outlet temperature, while the coolant density changes by about ten times from the core inlet to the outlet. Such issues may be more important for the fast reactors, which have the following characteristics: the pseudo-fast neutron spectrum; the large heterogeneity with the seed and blanket fuels; and use of solid moderator (ZrH) in some designs to achieve negative void reactivity characteristics.

Currently, at Waseda University, the concept of fast reactor concept of SCWR is further being developed with multi-level physics modeling, which covers from the core design (including fuel performance modeling), transient and accident plant behavior, and severe accident management. The unique and challenging issue of the water-cooled fast reactor is preventing re-criticality of the fuel debris, when total loss of coolant must be assumed.

1. Features of Supercritical Water-cooled Reactor (SCWR)

Supercritical Water-cooled Reactor (SCWR) is the only water-cooled reactor among the six Generation IV reactor concepts. It is the logical evolution of the current Light Water-cooled Reactor (LWR) as it follows the historical development of fossil fuel-fired power plant, which has been operating at the supercritical pressure of water since 1970s. Under supercritical pressure, the boiling phenomenon

disappears, and thermos-physical properties of the water continuously changes from liquid-like to gas-like state without phase changes. Due to such nature of the coolant, the SCWR plant concept may be characterized by low capital cost and high flexibility [1]. The single-phase cooling nature of SCWR realizes the once-through direct cycle plant system without any water / steam separation as described in Figure 1. Such plant system has the potential to dramatically reduce capital (construction) cost by simplification and elimination of components. Moreover, the large temperature and density changes of the coolant allow designing of flexible cores with outlet temperature ranging from 500 to 625 ℃ [2] and neutron spectrum ranging from thermal to fast [1].

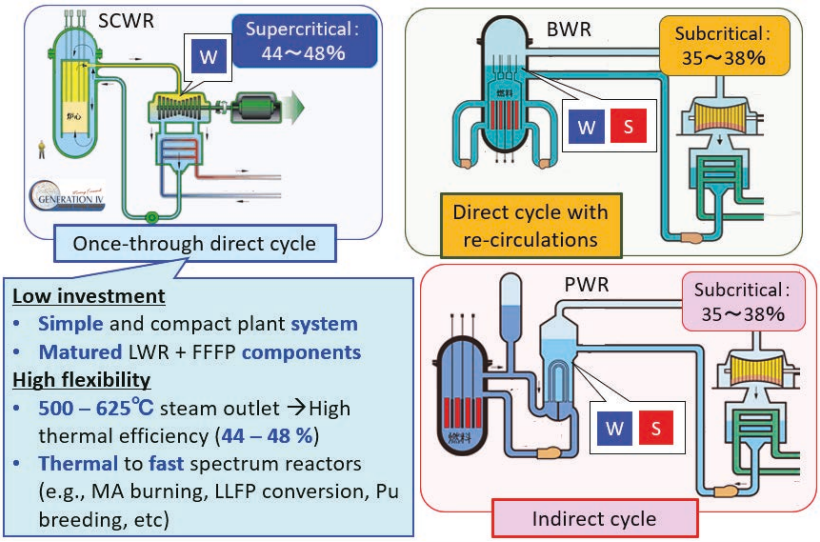

Figure 1: Features of the once-through direct cycle plant system of SCWR.

The existing SCWR design concepts include both the pressure vessel type (China, the EU, Japan, Russia) and pressure tube type (Canada) reactors, and all the design concepts assume operation pressure of about 25 MPa. For the pressure vessel type, most design concepts adopt the PWR-like Reactor Pressure Vessel (RPV) and control rod drive mechanism. The Primary Containment Vessel (PCV) design is similar to that of a BWR with suppression chamber and safety systems [3]. Passive safety systems [4] and Small Modular Reactor (SMR) design concepts have also been proposed and analyzed [5].

Overall, the Research and Development (R&D) issues of SCWR are found in three fields: the reactor concept development, the core thermal-hydraulics and the core materials development. The R&D relevant to reactor physics are often addressed together with the conceptual development studies. Currently, international collaborations are active in the Joint European Canadian Chinese development of Small Modular Reactor (ECC-SMART) running from September 2020 to August 2024 [6]. The four year Coordinated Research Project (CRP) on “Advancing Thermal-Hydraulic Models and Predictive Tools for Design and Operation of SCWR Prototypes” is also managed by IAEA [7].

2. Core Design Features and Typical Issues Relevant to Reactor Physics

2.1. Core Design Features

Generally, the thermal and fast reactors are loaded with enriched uranium and plutonium fuels, respectively. The fuel enrichments tend to be higher than those of the current LWRs, because of larger neutron absorption cross sections of candidate cladding materials compared with the current Zr based

alloys (e.g., advanced stainless steels, Ni-based alloys, etc). The fuel lattice is such that the gap size between fuel rods is small (typically, about 1 mm) to increase heat transfer with high coolant velocity for a given low coolant mass flux.

As shown in Figures 2 (a) and (b), the fuel assemblies of both the thermal and fast reactors are equipped with inlet orifices so that power to flow ratio can be appropriately assigned to each fuel assembly, which is important for attaining high average coolant outlet temperature of about 500 ℃ at the operation pressure of 25 MPa. The fuel assembly for the thermal reactor has water rods regularly arranged within the fuel lattice to gain sufficient neutron moderation. The typical neutron spectrum of the thermal reactor is like those of the current LWRs. In the meantime, the spectrum of the fast reactor is somewhat in between those of the current LWRs and that of the Sodium-cooled Fast Reactor (SFR) as shown in Figure 2 (c).

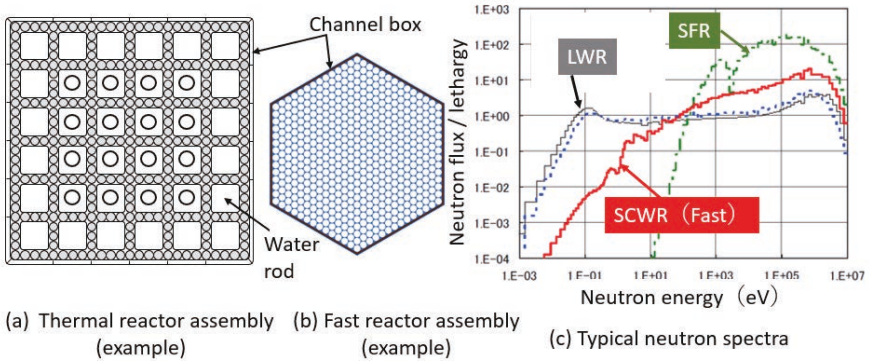

Figure 2: Examples of the fuel assembly designs and comparison of typical neutron spectra.

2.2. Issues Relevant to Reactor Physics

The major reactor physics issues may include, but not limited to accurate evaluations of the core power distributions and the coolant density reactivity feedbacks. It may be worth noting that power to cooling mismatch in the current LWR deteriorates the thermal safety margin (critical heat flux ratio) but does not directly affect the plant thermal performance, because the turbine inlet is saturated steam. However, in SCWR designs, the power to cooling mismatch directly deteriorates the core average coolant outlet temperature, because of the single-phase coolant, which is directly fed to the turbine. Such issues may be more important for the fast reactors, which have the following characteristics. Namely, the pseudo-fast neutron spectrum (as shown in Figure 2(c)); the large heterogeneity with the seed and blanket fuels; use of solid moderator (ZrH) in some designs to achieve negative void reactivity characteristics.

Figure 3 shows some examples of the heterogeneous core configurations of the fast reactor concepts. To attain high efficiency for converting fertile ^{238}U to fissile ^{239}Pu with pseudo-fast neutron spectrum, large heterogeneity with seed and blanket fuels is required. In the meantime, negative void reactivity characteristics should also be attained, because the coolant density greatly changes with enthalpy (temperature). It varies by almost 10 times from the core inlet to the outlet. Attaining negative void reactivity characteristics is more challenging than that of the current LWR, because of use of highly enriched ^{239}Pu. To overcome such issue, the concept of the blanket assembly with ZrH was developed as illustrated in Figure 3(a). Under a voided condition (when the coolant density is reduced), the streaming fast neutrons from the seed assembly is moderated by the solid moderator to enhance capture reactions of the fertile ^{238}U, which results in negative reactivity insertion [8].

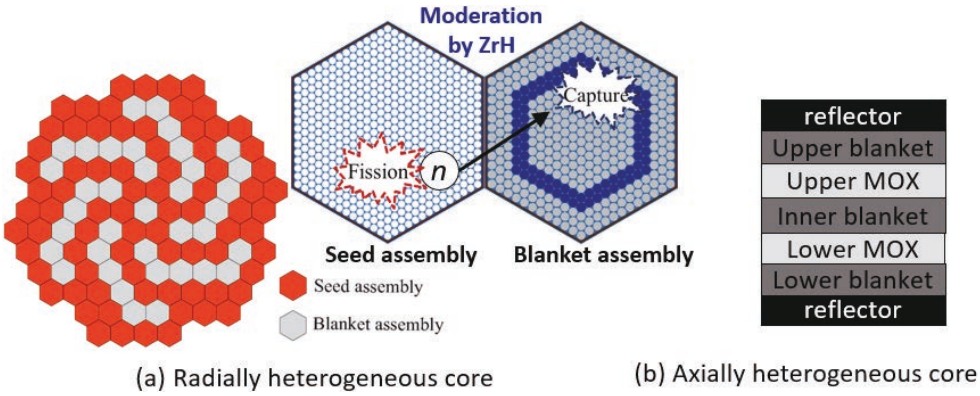

Figure 3: Examples of the heterogeneous core configurations of the fast reactor.

Accurate evaluations of power distributions and coolant void reactivities may also be important for designing heterogeneous cores for not only U to Pu conversions, but also for other purposes, such as Minor Actinide (MA) burning and long-lived fission product (LLFP) conversions, because the coolant void reactivity characteristics generally deteriorate with higher contents of MAs and LLFPs. According to one of the preceding studies, MA burning performance of SCWR may be improved by raising the core inlet temperature (reducing the core average coolant density), which suppresses neutron penalty due to loading of MAs into the core. Consequently, controlling the core power distribution becomes another issue as such change has large impact on the reactivity changes of the loaded fuels [9].

3. Newly Identified Issues Relevant to Reactor Physics

Recently, the lifespan extension of the currently operating reactors is becoming increasingly common across the world. In Japan, it typically took about 20 years from the time of planning a new reactor build to reaching the commercial operation. In USA, the maximum lifespan of 80 years is under consideration. Thus, any new nuclear reactor to be planned today may be in use 80 – 100 years ahead in the future. It may be long enough to realize technological breakthrough in retrieving effectively unlimited resources of uranium from the sea water, or clean and cost-effective hydrogen production without needing extremely high temperatures. SCWR, especially the fast reactor version, has the potential to meet various needs by modifying the core design with the same plant system.

However, The Fukushima Daiichi Nuclear Power Station (1F) accidents revealed potential severe accident risk of water-cooled reactors. Any innovative reactors, including SCWR, are expected to be better managed under severe accident conditions. In the meantime, lessons being learnt from the current 1F decommissioning effort may also be valuable for development of new innovative water-cooled reactors, such as SCWR. The 1F decommissioning may take as long as 30 – 40 years, because of the heavily contaminated PCV with radioactivity, which is preventing human access to the reactor. Alternatively, if the severe accident could be managed in such a way that the PCV internal contamination was dramatically reduced, then the post-accident management should be dramatically improved. Such technological readiness should give additional value to the innovative water-cooled reactors.

Thus, a newly identified reactor physics issue of SCWR is flexible core management and severe accident management with a focus on improving post-accident management. Figure 4 summarizes the needs for further innovation of SCWR. Due to the nature of supercritical water-cooling, SCWR is expected to be able to respond to various needs (e.g., Pu conversion, MA burning, attaining high

temperature for hydrogen production) by accepting different core designs with the same plant system. In the meantime, severe accident management should be well incorporated from the beginning of the conceptual development. In-Vessel Retention combined with suppression chamber type containment may be one of the possible solutions to limit the reactor internal contamination.

For development of such innovative concept, possible issue relevant to reactor physics is criticality control of the collapsing core under severe accident conditions. Unlike sodium-cooled fast reactor, SCWR cannot retain coolant once the system has depressurized, because of the low boiling point of water. Controlling reactivity under such extreme condition may be a new challenge for reactor physics.

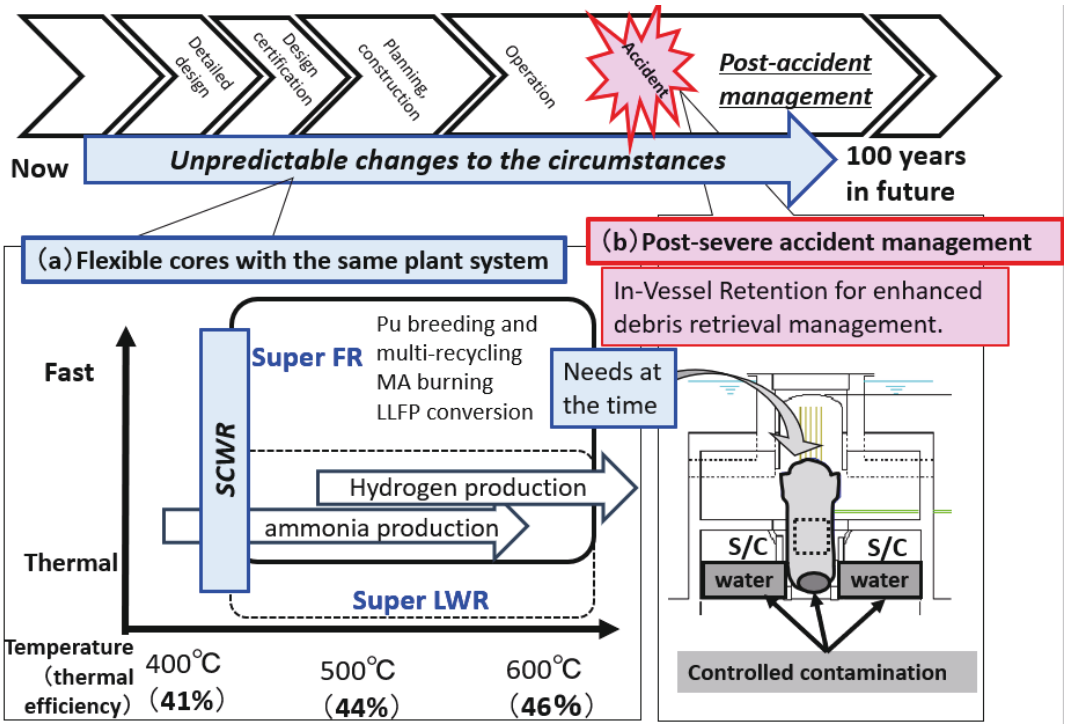

Figure 4: Needs for further innovation of SCWR.

4. Conclusions

The SCWR is the only water-cooled reactor among the six Generation IV reactor concepts. Both the thermal and fast reactor concepts can be developed with the same plant system. Accurate evaluations of the core power distributions and the coolant void reactivity characteristics have been the main reactor physics issues, especially for fast reactor designs with large heterogeneities with seed and blanket fuels. Newly identified issue may be criticality control of the collapsing fast reactor core during severe accidents.

References

1) Oka, Y, Koshizuka, S, Ishiwatari Y, Yamaji A. Super Light Water Reactors and Super Fast Reactors, ISBN: 978-1-4419-6035-1, Springer 2010.
2) Edwards G, Leung L, GIF Supercritical Water-cooled Reactor, Proliferation Resistance and Physical Protection White Paper, GIF/PRPPWG/2022/001, February 2022.
3) Ishiwatari Y, Oka Y, Koshizuka S, Yamaji A, Liu J. Safety of Super LWR, (I) safety system design, J Nucl Sci Technol. 2005; 42 (11), 927–934.

4) Sutanto, Oka Y. Passive safety system of a Super Fast Reactor, Nucl Eng Design. 2015; 289, 117-125.
5) Uchimura K, Yamaji A. Preliminary core design study of small Supercritical Fast Reactor with single-pass cooling, J. Nucl. Eng. 2020; Vol.1 46-53.
6) Joint European Canadian Chinese Development of Small Modular Reactor Technology, https://ecc-smart.eu/ (accessed 2023-09-16).
7) New CRP: Advancing Thermal-Hydraulic Models and Predictive Tools for Design and Operation of SCWR Prototypes (I31034), https://www.iaea.org/newscenter/news/new-crp-advancing-thermal-hydraulic-models-and-predictive-tools-for-design-and-operation-of-scwr-prototypes-i31034 (accessed 2023-09-16).
8) Oka Y, Jevremovic T. Negative void reactivity in large fast breeder reactors with hydrogeneous moderator layer, Ann. Nucl. Energy. 1996; 23(14), 1105–1115.
9) Fukuda F, Yamaji A. Conceptual design of Super FR for MA transmutation with axially heterogeneous core, Nucl Eng Design. 2020; 363: 110619.

Acknowledgements

This work was partly supported by JSPS KAKENHI Grant Number 20H02669. A part of this study is the result of “Understanding Mechanisms of Severe Accidents and Improving Safety of Nuclear Reactors by Computer Science” of Waseda Research Institute for Science and Engineering and the authors acknowledge support of the Institute for Advanced Theoretical and Experimental Physics, Waseda University.

8. Overview and future of JENDL-5

Osamu IWAMOTO
Nuclear Data Center, Japan Atomic Energy Agency
2-4 Shirakata, Tokai-mura, Naka-gun, Ibaraki-ken 319-1195, Japan
Email: iwamoto.osamu@jaea.go.jp

The latest version of the JENDL general-purpose file JENDL-5 released in 2021 are summarized and some examples of the evaluations are shown. JENDL-5 aims to meet the needs of expanding application area of radiation. The future plan of the next version of JENDL-5 is mentioned.

1. Introduction

The latest Japanese Evaluated Nuclear Data Library, JENDL-5 [1], was released in 2021. JENDL-5 was developed aiming at providing nuclear data to a wide range of application fields by providing many kinds of reaction data such as neutron, proton, deuteron, alpha-particle, and photon as well as thermal neutron scattering, fission product yields, and nuclear decay. The energy region of neutron was extended up to 200 MeV for 73 % of storing 795 target nuclei. The charged particle and photon induced reaction data were based on the data of the JENDL special purpose files [2] released so far with revisions. JENDL-5 is expected to be applicable for large parts of computer simulations for radiations.

JENDL-5 updates a lot of data important for nuclear reactors, but large part of them is not described in this report. This report rather focuses the data for non-energy applications used in the radiation transport codes such as PHITS [3]. One can find the full description of JENDL-5 and results of benchmark tests for nuclear reactors and shielding elsewhere [1, 4, 5].

2. JENDL-5

2.1. Sublibraries

JENDL-5 consists of 11 sublibraries: the data of neutron, thermal neutron scattering law, fission product yield, decay data, proton, deuteron, alpha-particle, photo-nuclear, photo-atomic, electro-atomic and atomic relaxation. The neutron sublibrary containing neutron induced reaction data is intensively updated from the previous version JENDL-4.0 [6] with increasing the number of target nuclei and the upper limit of the neutron incident energy. Regarding the thermal neutron scattering law library, original evaluations with the molecular dynamics simulations were performed for the light and heavy water [7, 8], and 7 organic molecules such as methane and benzene for the first time; other materials data were complemented by the data of ENDF/B-VIII.0 and JEFF-3.3. While the fission product yields of JENDL-4.0 are basically adopted the data of ENDF/B-VII.0, JENDL-5 includes the original evaluation for neutron induced fission and spontaneous one using the least square method with available experimental data and theoretical modeling [9]. The decay data were updated from JENDL/DDF-2015 with the up-to-date

ENSDF data [10] as of 2019, total absorption gamma-ray spectroscopy data, theoretical calculations, etc. For the sublibraries of charged particles and photon induced reactions, JENDL-5 adopts a large amount of data released in the special purpose files such as JENDL-4.0/HE, JENDL/DEU-2020, and JENDL/PD-2016.1 with adding and updating by new evaluations. The atomic related data were taken from ENDF/B-VIII.0 [11].

Some of the derived data from the neutron sublibrary are available for the user convenience: the pointwise data at 0K and 300K whose resonance parameters processed, the data up to 20 MeV of neutron incident energy, and activation data that give the activation cross sections and produced nuclides information only.

2.2. Neutron induced reaction

The neutron reaction data, which are the main parts of the general-purpose file, were intensively revised from JENDL-4.0. Figure 1 shows the number of nuclides and size of neutron data in JENDL-1 to JENDL-5. The number of nuclides is steadily increasing form 72 of the first version JENDL-1 to 406 of the previous version JENDL-4.0. JENDL-5 contains 795 nuclides which are almost double of JENDL-4.0 and more than 10 times of JENDL-1. This increase is mainly due to the effort to integrate the activation data to JENDL-5, which is traditionally separated in the activation files released as the special purpose files. In addition, the naturally existing nuclides were completed to meet needs to simulate the radiation transports in various materials in a variety of application fields. As shown in Fig. 1, the increase of the data size is more drastic because the stored data types are increasing with increasing the version of library. JENDL-1 mainly consists of the data of cross section, angular distribution, and energy spectrum. The later added ones such as of double differential cross sections (DDX) for particle emission and covariance contributes the increase of the data size from 10 Mbyte of JENDL-1 to 500 Mbyte of JENDL-

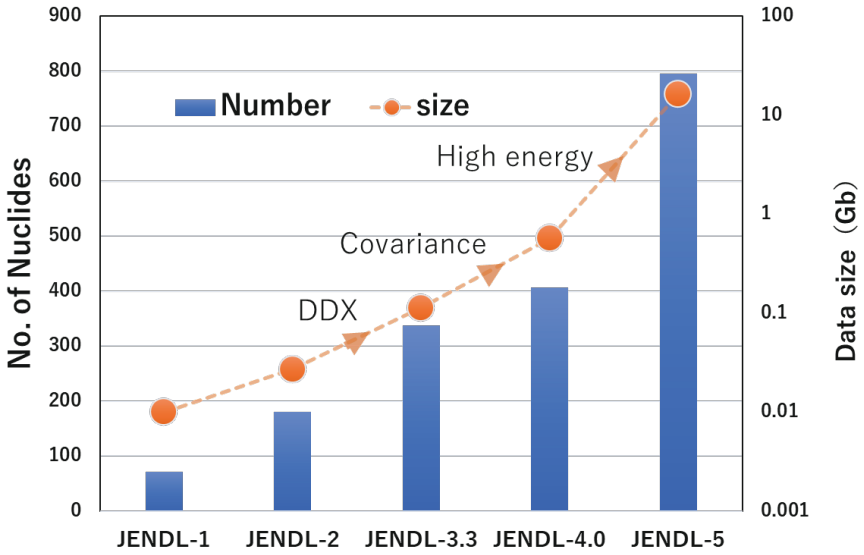

Fig.1 The number of nuclides and data size of neutron data of JENDL general purpose files

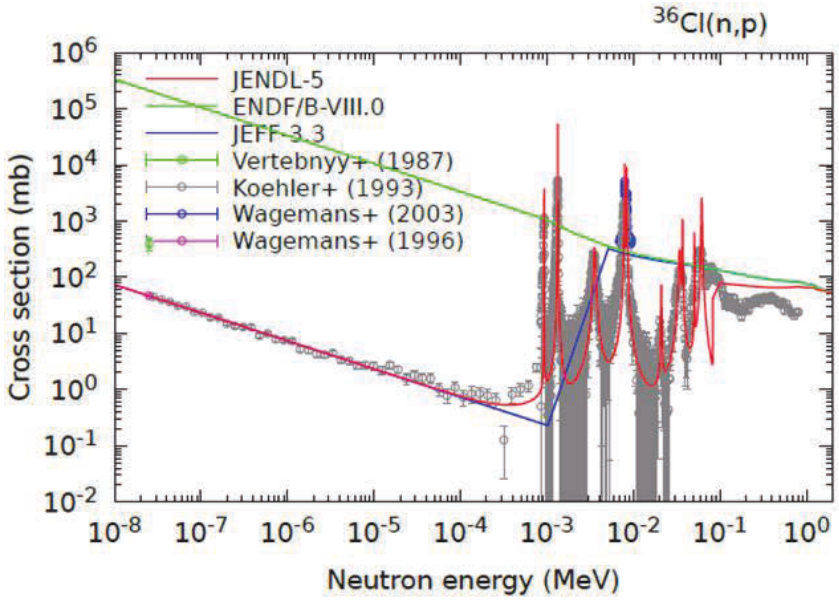

Fig.2 Cross section of ^{36}Cl(n,p) reaction

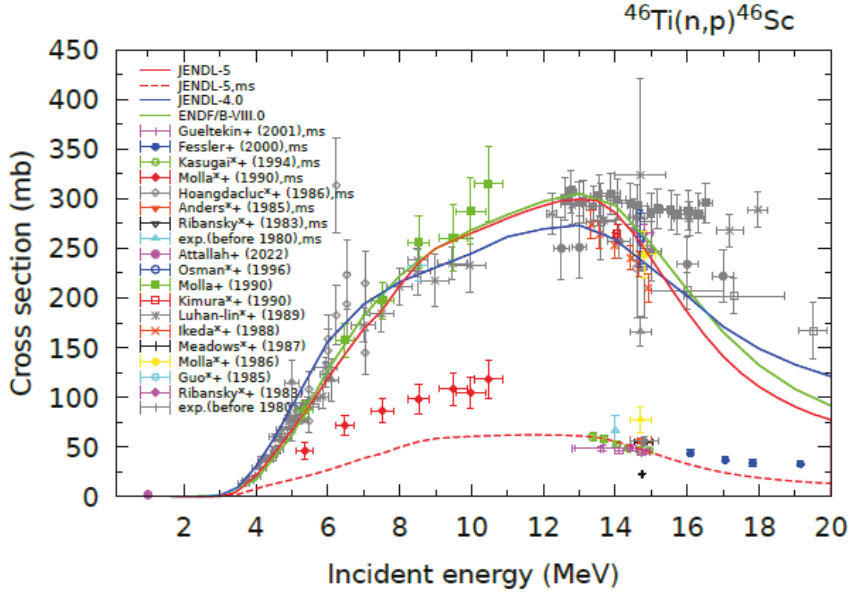

Fig.3 Cross section of ^{46}Ti(n,p)^{46}Sc

4.0. The expansion of the data size of JENDL-5 (larger than 10 Gbyte) is mainly due to the increase of the upper limit of the incident energy from 20 MeV to 200 MeV.

In JENDL-5, so many nuclides are revised and added from light to heavy nuclides. The revision covers the important nuclides in nuclear reactors such as major and minor actinides, structure materials, sodium, oxygen etc. In this paper, only some examples of evaluated results are shown, but details of the JENDL-5 can be seen elsewhere [1].

As an example of the newly evaluated nuclide for JENDL-5, the cross section of ^{36}Cl(n,p) is shown in Fig. 2; ^{36}Cl with the half live of around 0.3 million year would be produced in molten salt reactors with chlorine. The evaluation of JENDL-5 reproduces experimental data of Koehler et al. [12] better than the other libraries from the thermal to resonance energy region.

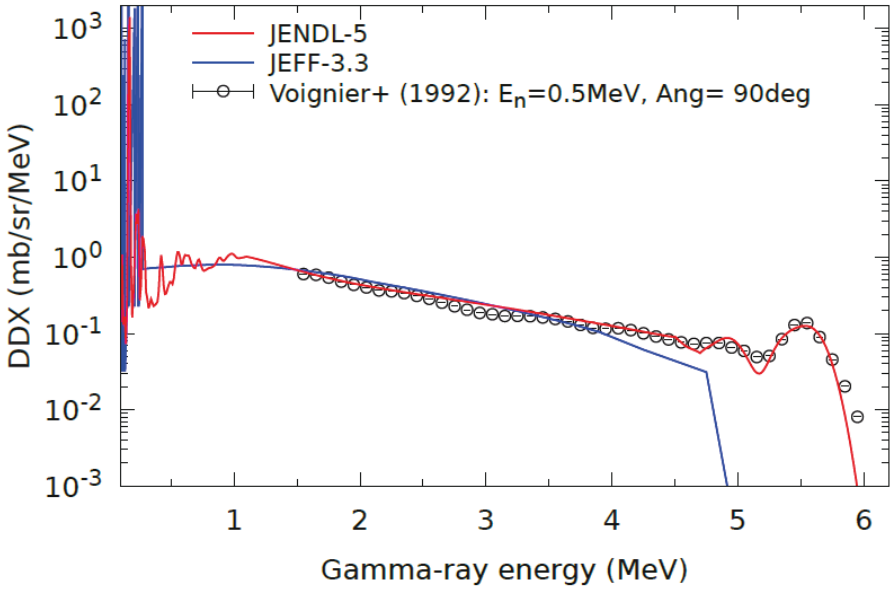

Fig.4 DDX of gamma-ray production of neutron induced reaction on ^{139}La. The discrete gamma-rays are broadened according to the experimental resolution.

Figure 3 shows the ^{46}Ti(n,p)^{46}Sc cross section with the isomer production. Among the experimental data rather scattered, the evaluated cross sections of both total and isomer production show good consistency with recent experimental data. According to the strategy to increase the completeness within the single library, this kind of isomer production cross section data included in JENDL-5; they had not been given in the general-purpose files up to JENDL-4.0 and had been separated to the special purpose files such as JENDL/A-96 and JENDL/AD-2017.

The secondary gamma-ray data are important in the evaluation of radiation shielding. JENDL-1 and JENDL-2 don't include these data, but many efforts were made to increase them resulting in having gamma-ray data for 87% nuclides in JENDL-4.0. The efforts were continued for JENDl-5 resulting in the coverage of 99 %. Figure 4 shows the DDX of the gamma-ray production for ^{139}La, for which the data are missing in JENDL-4.0. At the neutron energy 0.5 MeV in the figure, the most of gamma-rays are produced via neutron capture reaction. The JENDL-5 evaluation reproduces the experimental data well including peaks at high energy sides that is produced by the transition from the neutron capture state to low-lying levels of ^{140}La.

2.3. Deuteron induced reaction

The data of deuteron induced reaction were rather recently released as a special-purpose file JENDL/DEU-2020. Because the library was dedicated to development of neutron sources using deuteron induced reactions, the target nuclides were limited to the light nuclides that are candidates of the neutron source target, i.e. isotopes of Li, Be and C. However, the deuteron would interact not only the neutron source targets but also other accelerator materials and required for the computer simulations. The deuteron data of the isotopes of Al, Cu and Nb, which would be contained in beam dumps and superconducting cavities of the accelerator, were evaluated, and included in JENDL-5. Because the deuteron is a weakly bound particle consisting of proton and neutron, its reaction shows characteristic behavior arisen by breakup of deuteron. The most remarkable feature is enhancement of the neutron

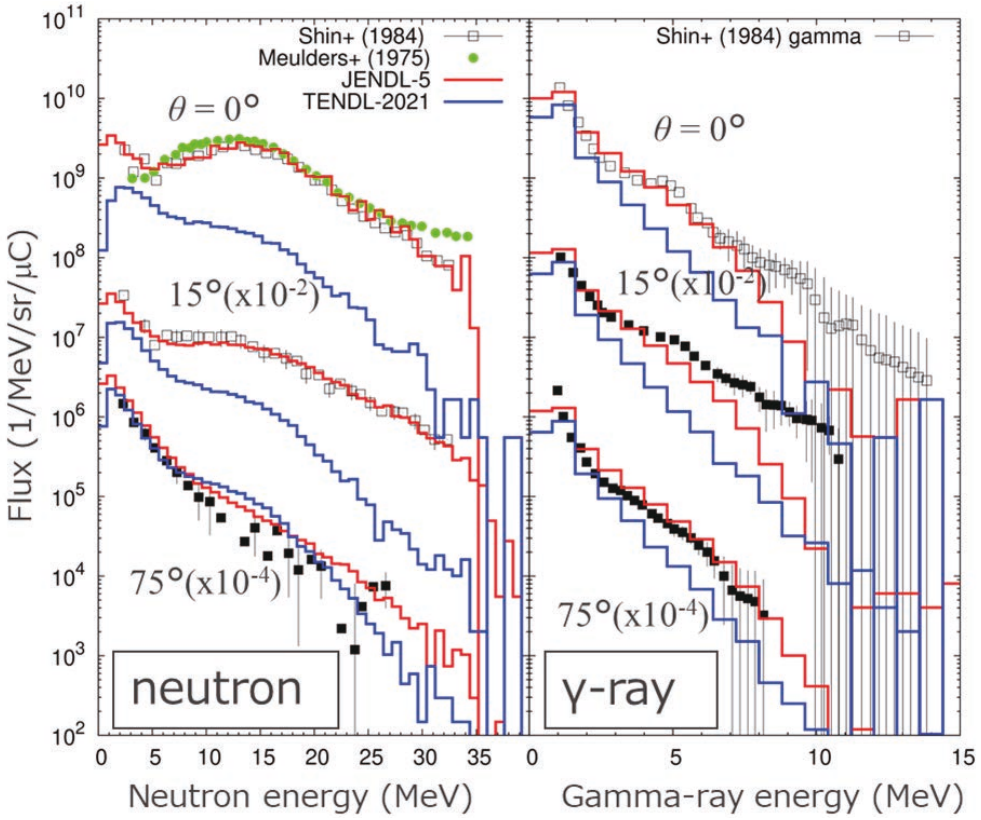

Fig.5 Thick target yields of neutron and gamma-ray for deuteron induced reaction on Cu at 33 MeV

emission at forward angle. The nuclear model calculation is quite important to evaluate the nuclear data for particle emission spectrum because of difficulty to measure the emission spectra covering wide emission angle for wide incident energies required in simulation calculations. Because the nuclear reaction model codes for nuclear data so far were developed mainly for nucleon induced reaction and it would fail to reproduce the deuteron reaction feature, the deuteron reaction model code DEURACS was newly developed and applied to the evaluation of JENDL/DEU-2020 and JENDL5. Figure 5 shows thick target yield of neutron and gamma-ray for deuteron induced reaction on Cu at 33 MeV. The JENDL-5 data given by DEURACS well reproduce the peak of neutron emission spectra at 0 and 15 degrees, which would be produced by the deuteron breakup. The gamma-ray spectra in right panel good exhibit good consistency between JENDL-5 and the experimental data. These results indicate the modeling in DEURACS reasonably well describes the nuclear reaction processes induced by deuterons.

3. Future plan and related activities

The uncertainty of the nuclear data is important to estimate reliability of computer simulations. It would be crucial for the development of new systems for which experimental knowledges are limited. Because the evaluation efforts of covariance data are limited in developing JENDL-5, the coverage of covariance data is still low. Therefore, the enhancement of the covariance data is urgent task and is a main target of the next release of JENDL. To achieve it, the development of the covariance evaluation system is undergoing. In addition, increase of the number of target nuclei for

charged particle reaction is another target of the next JENDL, because those data are significantly limited comparing with the neutron data.

Discussions about the future developments of JENDL are in progress under Nuclear Data Division of Atomic Energy Society of Japan. In this framework, several workshops were planed and held on the topics of muon nuclear data, nuclear regulation, fission product yield, and medical isotope production.

In the current situation, the next release of JENDL would be in FY 2027 or 2028.

References

[1] Iwamoto, O. et al., Japanese evaluated nuclear data library version 5: JENDL-5, J. Nucl. Sci. Technol., vol. 60, no.1, 2023, pp.1-60.

[2] Shibata, K., JENDL: Nuclear databases for science and technology, J. Nucl. Sci. Technol., vol. 50, no.5, 2013, pp.449-469.

[3] Sato, T., Recent improvements of the Particle and Heavy Ion Transport code System - PHITS version 3.33, J. Nucl. Sci. Technol., vol. 61, 2024, pp.127-135.

[4] Tada, K. et al., JENDL-5 benchmark test for shielding applications, J. Nucl. Sci. Technol., vol. 61, no.1, 2024, pp.2-22.

[5] Konno, C. et al., JENDL-5 benchmarking for fission reactor applications, J. Nucl. Sci. Technol., vol. 60, no.9, 2023, pp.1046-1069.

[6] Shibata, K. et al., JENDL-4.0: A New Library for Nuclear Science and Engineering, J. Nucl. Sci. Technol.. vol. 48, no. 1, 2011, pp.1-30.

[7] Abe, Y. et al., Evaluation of the neutron scattering cross-section for light water by molecular dynamics, Nucl Instrum Methods Phys Res A. vol. 735, 2014, pp. 568–573.

[8] Ichihara A, Abe Y. Theoretical evaluation of neutron thermal scattering laws of heavy water for JENDL-5, 2022. JAEA-Conf 2022-001, 2022, pp.175–180.

[9] Tsubakihara, K. et al., Evaluation of fission product yields and associated covariance matrices, J. Nucl. Sci. Technol., vol. 58, no.2, 2021, pp.151-165.

[10] Brookhaven National Laboratory, Evaluated nuclear structure data file; 2000. https://www.nndc.bnl.gov/ensdf/ (accessed 9 Sep. 2024)

[11] Brown, D.A. et al., ENDF/B-VIII.0: The 8th Major Release of the Nuclear Reaction Data Library with CIELO-project Cross Sections, New Standards and Thermal Scattering Data, Nuclear Data Sheets, vol. 148, 2018, pp. 1-142.

[12] Koehler, P.E. et al. ^{36}Cl(n,p)^{36}S cross section from 25 meV to 800 keV and the nucleosynthesis of the rare isotope ^{36}S, Phys. Rev. C 47, 1993, pp.2107-2112.

Acknowledgements

The author is grateful to all the member involved in the JENDL-5 development for their efforts and would like to thank Drs. N. Iwamoto and S. Nakayama for provision of figures used in the presentation and this report.

9. Experiments for nuclear data using RCS at J-PARC and HiRadMat at CERN

Shin-ichiro MEIGO[†1]

[1]J-PARC Center, Japan Atomic Energy Agency, Shirakata 2-4, Tokai, Ibaraki, 319-1195, Japan
[†]Email: meigo.shinichiro@jaea.go.jp

Abstract

To decrease the toxic waste produced at the nuclear reactors, studies of the Accelerator Driven System (ADS) are developing worldwide. Since the neutron production target based on the spallation neutron is designed to be irradiated by protons in several GeV kinetic energy, a study in the kinetic energy region about GeV is essential. Using the 3-GeV proton synchrotron (RCS) at J-PARC, some studies are going to obtain nuclear data, especially for ADS. In this paper, the experiments using RCS are explained, such as nuclide production cross section induced by proton and displacement cross section, being essential to understand the material damage by the beam irradiation. For understanding of material damage in the high-energy region using 440-GeV protons, the experiment planned at CERN HiRadMat is introduced, as well.

1 Introduction

To reduce the hazards associated with the radioactive waste produced in a nuclear reactor, Japan Atomic Energy Agency (JAEA) proposed an accelerator-driven system (ADS) that comprises extremely high-power accelerators (30 MW) with proton kinetic energy of 1.5 GeV [1]. In ADS, Lead–bismuth eutectic (LBE) is used as a target material to produce spallation neutrons, and it simultaneously plays the role of a coolant. Since the neutron production target using spallation is designed to be irradiated by protons in several GeV kinetic energy, a study with the high-energy particles in the kinetic energy region $\sim$ GeV is essential for the research and development of spallation neutron source. In Japan, J-PARC can only provide the protons in the energy range for spallation neutron. Some studies of nuclear data for spallation neutron source were and are going to be conducted at J-PARC using the 3-GeV proton synchrotron (RCS) and the beam transport called 3NBT. For the accelerator facilities not only ADS but also high-intensity accelerators, it is crucial to understand the damage of materials under beam irradiation. The material damage is widely characterized by displacement per atom, which is given by the displacement cross section. To understand the displacement in the high-energy region, an experiment is planned at CERN using 440-GeV protons. In this paper, some experiments for the nuclear data conducted at J-PARC using several GeV-protons are introduced, such as nuclide production cross section induced by protons and displacement cross section. Also, the experiment planned at HiRadMat CERN is explained.

2 Nuclide production cross section induced by protons

To estimate the residual nuclei in the target and the beam window, nuclide production cross sections are required. However, the data are not enough to validate the calculation models. For validation of the calculation model, we have carried out the production cross section using several GeV-protons. For the experiment, sample changers with sample holders were installed at 3NBT. At the RCS, the kinetic energy of the extracted proton can be varied from 0.4 to 3 GeV, altering the acceleration duration. With the change in the rigidity of the following magnets, the beam was introduced to the sample. After irradiation, the sample was observed by the high-pure Ge detector. With the gamma spectrometry, the production cross section was derived.

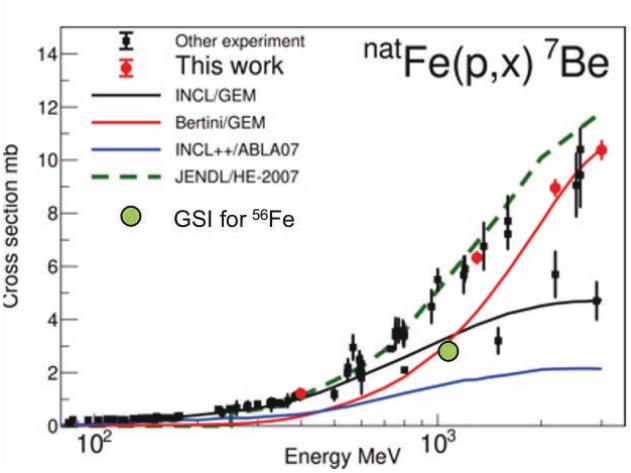

Figure 1: Cross section of ^{nat}Fe(p,x)^{7}Be as a function of kinetic energy of projectile protons.

So far, measurements with many target elements of Be [2], C [2], Al [3–5], Ti [6], Fe [7], Ni [8, 9], Zr [8, 9], Nb [6], Mn [10], Co [10], Sc [2], V [2], Pb [5], and Bi [5, 11] were conducted. Here, the cross section of ^{nat}Fe(p,x)^{7}Be reaction [7] is explained. The experimental results of ^{nat}Fe(p,x)^{7}Be are shown in **Fig. 1** compared with the various calculation models based on intra-nuclear cascade model (INC) and the evaluatied data of JENDL/HE-2007. It is shown that INCL-4.6 [12]/GEM and INCL++/ABLA07 show remarkable underestimation for the kinetic energy range above 1 GeV. The nuclide of ^{7}Be is mainly produced by the statistical decay and partially produced by the multi-fragmentation. On the other hand, the previous calculation INC model of Bertini/GEM shows good agreement in the energy range above 2 GeV. This tendency appears for light and light-heavy target nuclides. By the future study, the underestimation of ^{7}Be production based on INC will be improved.

Although JENDL/HE-2007 shows a good agreement with the experimental results, it shows a slight overestimation for energies above 2 GeV. At GSI, the same cross section for ^{56}Fe was measured with the inverse-kinematics [13], as shown in **Fig. 1**. The disagreement of the data obtained at GSI was pointed out by the other study [14]. With accumulated experimental results, the evaluated data will be improved. By applying machine learning, such as Gaussian Process Regression (GPR) [15], the prediction of cross section was improved with experimental data obtained at J-PARC using RCS.

3 Displacement cross section

At the Material and Life Science Experimental Facility (MLF) in J-PARC, an aluminum alloy is utilized as a beam window [16] to separate the vacuum in the accelerator and He-filled area at the target station. For high-intensity accelerators, the damage to the beam-intercepting material is one of the critical issues while it plays an essential roles. To operate a high-power accelerator confidently, damage estimation of the target material is essential. For quantitative estimation of the damage to the target material, the displacement per atom (dpa) index is generally employed. The dpa is estimated using the particle fluence multiplied with displacement cross section.

The cross section is usually obtained using the Norgertt–Robinson–Torrens (NRT) model [17]. The calculation method for the displacement cross section has been established for the low-energy regions where nuclear reactions produce no particles. For the protons in the high-energy region above 20 MeV, the experimental data of the displacement cross section are scarce. The displacement cross section has not been adequately studied. Since many reaction channels open (above 20 MeV), a calculation based on INC is used to obtain the cross section. For validation and improvement of the dpa evaluation, the experimental data are crucial. To obtain the data, the displacement cross-section measurements were conducted in J-PARC [18–20].

To obtain the displacement cross section, a vacuum chamber with a cryocooler was installed at the front of the beam dump of RCS with a similar scheme to the experiment of the production cross section. For observation of the damage in the sample, the sample is required to be cooled at a cryogenic temperature ($\sim$ 10 K), where the recombination of Frenkel pairs is well suppressed owing to thermal motion. With the observation of the resistivity change due to the irradiation at the cryogenic temperature, the experimental displacement cross section was obtained. A vacuum chamber was installed in front of the 3-GeV beam dump. The chamber was equipped with a Gifford–McMahon (GM) cryocooler, which cooled the sample , as shown in **Fig. 2**. The assembly of the GM cryocooler and a sample wire was placed on a movable stage to control the irradiation. Before installation, the sample was annealed just less than the melting point to eliminate the defect of the lattice. Each sample was sandwiched between electrical insulation sheets of an aluminum nitride ceramic and held by a holder made of aluminum. The resistance of the sample was measured using a voltmeter and current source. The sample wire was connected through terminals to both the current source and voltmeter for the compensation of the cable resistance between the sample and instruments.

During the experiment, the beam position given by the profile monitor was confirmed to be the center of the wire with the observation of the change in resistivity during the scan, owing to the precise beam control developed at J-PARC [21, 22]. The resistance of the iron sample was observed with the temperature of the sample holder determined using the attached thermometer during the beam irradiation. Although the sample temperature was not directly observed, it can be thought to be kept less than 20 K. The observed temperature of the holder increased by 0.2 K during the irradiation. The sample resistance was increased by about 0.2 $\mu\Omega$ from the start of the beam irradiation, which was produced due to the displacement by the protons.

The present displacement cross section of iron is shown in **Fig. 3** with the previous experimental data. The calculation with PHITS [23] using cascade model of INCL-4.6 [12] and the evaluated data given by the Karlsruhe Institute of Technology (KIT) [24] are also shown in this figure. For PHITS calculation and KIT evalulation, two displacement models were applied. The first one was NRT model, which is widely utilized for evaluation of dpa. The second one was the athermal–recombination–corrected dpa (arc-dpa) model based on molecular dynamics. For the arc-dpa, the parameters given by Nordlund [25] were applied to PHITS. It is found that the NRT model underestimates by about a factor of 2 in the energy region of GeV. It should be noted the arc-model calculation shows remarkably good agreement with the experimental data.

4 Experiment of displacement cross section at HiRadMat

In J-PARC, the data were obtained in the energy region below 30 GeV. As shown in **Fig. 3**, the cross section in the high-energy region above 1 GeV showed saturated to a certain value. In terms of the theoretical view, due to the relativistic, the stopping power given by projectiles increases as the energy, which was not shown in the observed displacement cross section. To confirm this, measurements of displacement cross sections were made using 120-GeV protons at Fermilab in 2023 in a similar manner at J-PARC. The experiment was performed at the

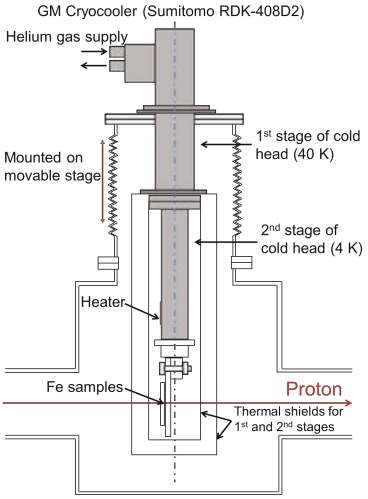

Figure 2: Schematic of the sample, vacuum chamber, and GM cryocooler used for the present experiment.

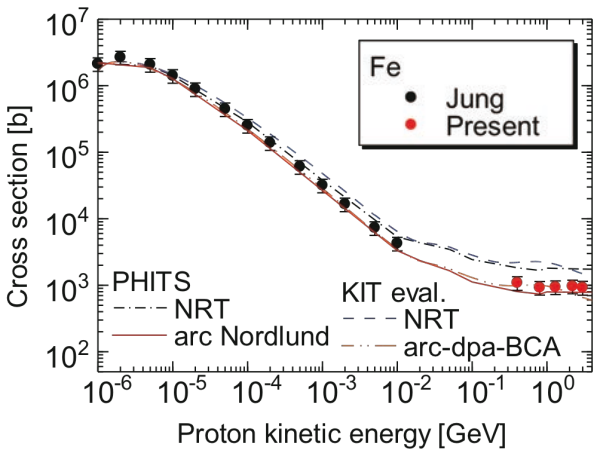

Figure 3: Comparison of the present experimental data for iron with previous experimental data [26], calculation data using PHITS [23] and KIT evaluations [24].

Fermilab Test Beam Facility using slow beam extraction. The data were successfully obtained and showed the conserving of the cross section regardless of the energy up to 120 GeV.

To expand the energy region, an experiment was planned at CERN to use 440-GeV protons. Already, the proposal for the experiment was approved by the program committee of HiRadMat. The experimental setup is shown in **Fig. 4**. At HiRadMat [27], many tests and examinations have been performed. One of those is to observe the impact on the cryogenic system used at Large Hadron Collider (LHC). One of the experimental groups has been performed with cryogenic using the vacuum vessel, which allowed us to use it for the measurement of the displacement. The experiment is planned to be conducted in May 2025.

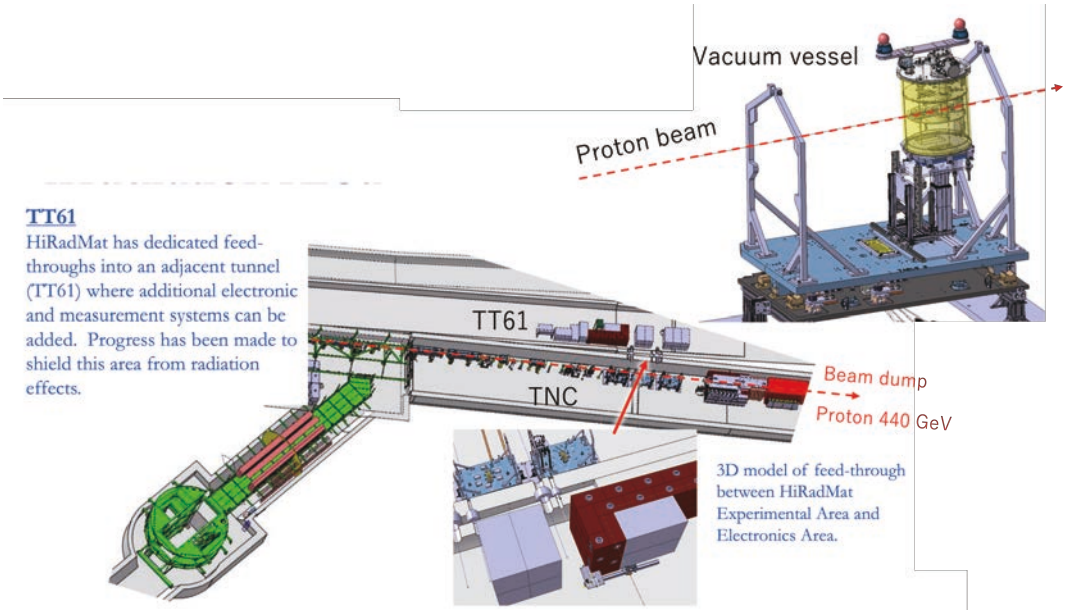

Figure 4: Schematic of the experimental setup at HiRadMat CERN for 440-GeV protons.

5 Summary

To evaluate the target materials used in high-intensity proton accelerators, particularly in ADS, experiments for the measurements of displacement and nuclei production cross sections were carried out at J-PARC using RCS. Some of the experimental data were obtained as the first one in the world. Due the the limited space, some studies, such as measurement of spallation neutron spectrum with the mercury target, are skipped in this paper. In the future, the data will be obtained at HiRadMat CERN using 440-GeV protons to solve the puzzle of the displacement cross section.

Acknowledgment

This paper partially contains the results of "Measurement of displacement cross section at J-PARC for structural material utilized at ADS" entrusted to JAEA by the MEXT. This work was supported by JSPS KAKENHI Grant Number 22K04992. This project has received funding from the European Unions Horizon Europe research and innovation program under grant agreement No 101057511.

References

[1] Tsujimoto K, et al. Research and development program on accelerator-driven subcritical system in JAEA. J. Nuc. Sci. and Technol., 2007;44(3):483 – 490.

[2] Nakano K, et al. Measurement of nuclide production cross-sections in high-energy proton-induced spallation reactions at J-PARC, JAEA-Research 2021-014,25p. 2022. (in Japanese).

[3] Meigo S, et al. Measurement of aluminum activation cross section and gas production cross section for 0.4 and 3-Gev protons. EPJ Web Conf. 2017;146:11039.

[4] Matsuda H, Meigo S, Iwamoto H. Proton-induced activation cross section measurement for aluminum with proton energy range from 0.4 to 3 GeV at J-PARC. J. Nucl. Sci. and Technol. 2018;55(8):955 – 961.

[5] Matsuda H, et al. Measurement of nuclide production cross section for lead and bismuth with proton in energy range from 0.4 GeV to 3.0 GeV. EPJ Web Conf. 2020;239:06004.

[6] Sugihara K, et al. Measurement of nuclide production cross sections for proton-induced reactions on ^{nat}Ti and ^{93}Nb at 0.8 and 3.0 GeV Nucl. Instr. and Meth. in Phys. Res. Sect. B 2023;545:165153.

[7] Matsuda H, et al. Measurement of nuclide production cross sections of ^{nat}Fe for 0.4 – 3.0 GeV protons in J-PARC. JPS Conf. 2021;33:011047.

[8] Takeshita H, et al. Nuclide Production Cross Sections of Ni and Zr Irradiated with 0.4-, 1.3-, 2.2-, and 3.0-GeV Protons. JPS Conf. 2021;33:011045.

[9] Takeshita H, et al. Measurement of nuclide production cross sections for proton-induced reactions on ^{nat}Ni and ^{nat}Zr at 0.4, 1.3, 2.2, and 3.0 GeV Nucl. Instr. and Meth. in Phys. Res. Sect. B 2022;527:17 – 27.

[10] Takeshita H, et al. Measurement of nuclide production cross sections for proton-induced reactions on Mn and Co at 1.3, 2.2, and 3.0 GeV Nucl. Instr. and Meth. in Phys. Res. Sect. B 2022;511:30 – 41.

[11] Iwamoto H, et al. Nuclide production cross sections in proton-induced reactions on Bi at GeV energies EPJ Web Conf. 2023;284:01033.

[12] Boudard A, et al. New potentialities of the liège intranuclear cascade model for reactions induced by nucleons and light charged particles. Phys. Rev. C. 2013 Jan;87:014606.

[13] Napolitani P, et al. High-resolution velocity measurements on fully identified light nuclides produced in ^{56}Fe + hydrogen and ^{56}Fe+titanium systems. Phys. Rev. C. 2004 Nov; 70:054607.

[14] Titarenko Y E, et al. Cross sections for nuclide production in a ^{56}Fe target irradiated by 300, 500, 750, 1000, 1500, and 2600 MeV protons compared with data on a hydrogen target irradiated by 300, 500, 750, 1000, and 1500 MeV/nucleon ^{56}Fe ions. Phys. Rev. C. 2008 Sep;78:034615.

[15] Iwamoto H. Generation of nuclear data using Gaussian process regression. J. Nucl. Sci. and Technol. 2020;57(8):932 – 938.

[16] Meigo S, et al. Radiation damage and lifetime estimation of the proton beam window at the Japan Spallation Neutron Source. J. Nucl. Mat. 2014;450(1):141 – 146.

[17] Norgett M, Robinson M, Torrens I. A proposed method of calculating displacement dose rates. Nucl. Eng. and Design. 1975;33(1):50 – 54.

[18] Meigo S, et al. Measurement of displacement cross section of structural materials utilized in the proton accelerator facilities with the kinematic energy above 400 MeV. JPS Conf. Proc. 2020;28:061004.

[19] Matsuda H, et al. Measurement of displacement cross-sections of copper and iron for proton with kinetic energies in the range 0.4 – 3 GeV. J. Nucl. Sci. and Technol. 2020;57(10):1141 – 1151.

[20] Meigo S, et al. Measurement of displacement cross-sections of Nb irradiated by protons with kinetic energy range between 0.4 and 3 GeV. EPS Web of Conf. 2023;284:05001.

[21] Meigo S, et al. Beam commissioning for neutron and muon facility at J-PARC. Nucl. Inst. and Meth. in Phys. Res. Sect. A 2009;600(1):41 – 43.

[22] Meigo S, Ooi M, Fujimori H. Two-parameter model for optimizing target beam distribution with an octupole magnet. Phys. Rev. Accel. Beams. 2020 Jun;23:062802.

[23] Iwamoto Y, et al. Improvement of radiation damage calculation in PHITS and tests for copper and tungsten irradiated with protons and heavy-ions over a wide energy range. Nucl. Instr. and Meth. in Phys. Res. Sect. B 2012;274:57 – 64.

[24] Konobeyev A, Fischer U, Simakov S. Improved atomic displacement cross-sections for proton irradiation of aluminium, iron, copper, and tungsten at energies up to 10 GeV. Nuc. Inst. and Meth. in Phys. Res. Sect. B 2018;431:55 – 58.

[25] Nordlund K, Zinkle SJ, Sand AE, et al. Improving atomic displacement and replacement calculations with physically realistic damage models. Nature Comm. 2018;9(1):1084.

[26] Jung P. Atomic displacement functions of cubic metals. J. Nucl. Mat. 1983;117:70 – 77.

[27] Harden F., et al. Targetry Challenges and HiRadMat JPS Conf. Proc 2021;33:011149.

10. Details of the PHIG-3D's visualization functions

Seiki OHNISHI[1*]
[1]National Maritime Research Institute, Japan
1-8-1 Shinkawa, Mitaka-shi, Tokyo 181-0004, Japan
Email: ohnishi@m.mpat.go.jp

PHIG-3D, a three-dimensional visualization tool designed for PHITS input data, realized a modernized appearance and user-friendly interface. However, there are limitations caused by its internal structure. The most significant limitation is the increased memory usage associated with the polygon construction process. This increase in memory usage comes from the Marching Cubes method. Another limitation is the character encoding. PHIG-3D supports only UTF-8 in input files because automatic encoding detection is complicated and UTF-8 can be easily handled in common by the cross-platform libraries used in PHIG-3D. This work provides such auxiliary knowledge to better use.

1. Background

1.1. Motivation

In recent years, the multi-purpose three-dimensional continuous energy Monte Carlo radiation transport code (MC code) PHITS [1] has been used in various fields. One of the advantages of MC codes is that they can handle three-dimensional complex geometries without discretization. However, the built-in visualization functions in PHITS can create only sliced images or overview images by ray-tracing, and it does not allow users to change viewpoints in real time.

In general, it is difficult to reconstruct a three-dimensional object from multiple two-dimensional images. Therefore, a tool with 3D rendering and real-time manipulation capabilities would be remarkably useful for spatial perception of geometries. For instance, Figure 1 shows the three-dimensional picture and sliced images of an input model. These pictures illustrate that it is difficult to reconstruct a 3D image from 2D images.

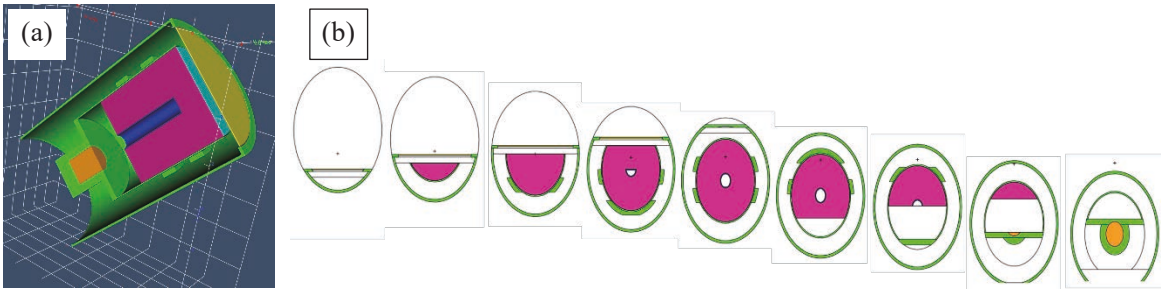

Figure 1 HPGe head model, (a) 3D overview, (b) sliced images at 1 cm intervals.

1.2. History

The prototype of the PHITS code, the NMTC code [2], was created in 1970, and the basic geometric features were completed in the modified version, NMTC/JAERI [3]. The later upgraded NMTC/JAERI97 [4] allowed the use of tori, and it became possible to input almost the same geometry as the current version of PHITS. After that, NMTC/JAM [5] extended the applicable energy ranges, and then the first version of PHITS [6] was released in 2002. Thus, by the end of the 1980s, the input syntax to define three-dimensional geometries was established, and there has been a demand for interactive 3D viewers since then. Focusing on 3D visualization APIs, OpenGL2.0 [7] was released in 2004, and consumer GPUs supporting it appeared almost at the same time. In other words, it has been more than 20 years since the technology stack which enables the development of 3D viewers was available. PHIG-3D (PHITS Interactive Geometry viewer in 3D) was developed to solve this problem. PHIG-3D has been developed based on Gxsview [8] as a prototype to minimize the development period. This paper describes the goals, internal structure, and constraints of PHIG-3D.

2. Goal of PHIG-3D

PHIG-3D has the following goals: real-time operation with a mouse, multi-threading, multi-language support, and displaying scalable fonts. Any situation in which these goals are not achieved is considered a bug.

2.1. Realtime operation with a mouse

The most important functionality in PHIG-3D is the ability to change viewpoints in real-time using the mouse and keyboard. To achieve it, Qt [9] and VTK [10] are adopted for the GUI widgets and the three-dimensional viewport respectively. Figure 2 is the screenshot of PHIG-3D. The screen consists of panes on the left side and a viewport on the right side. The panes are used to select visible cells, set the number of sampling points, and configure the rendering volume. The cell construction starts after pushing the “Draw” button at the bottom of the panes. A left-mouse-button-click on a cell in the viewport switches to the wireframe view, and a right-mouse-button-click allows the user to select menu options such as hide cell, center cell, and set opacity.

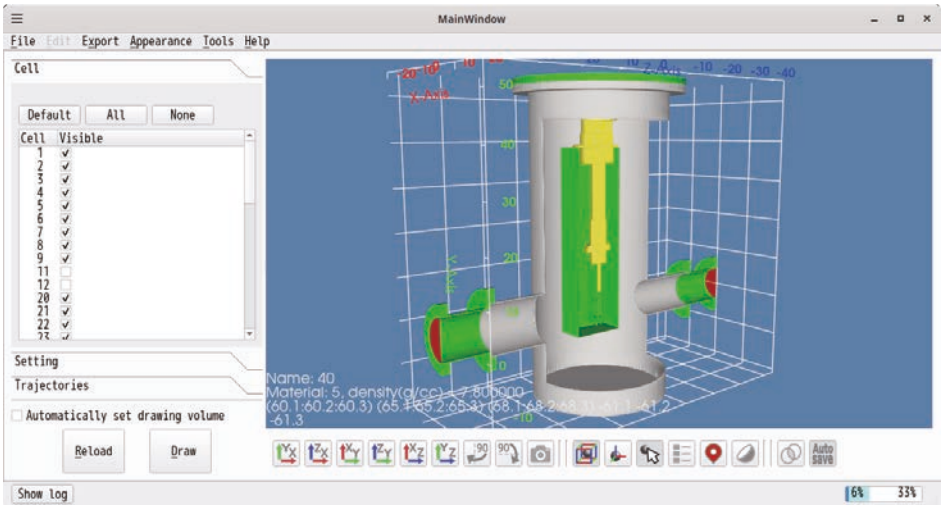

Figure 2 PHIG-3D displaying vacuum chamber[11].

2.2. Multithreading

PHIG-3D is developed using C++17, and it is parallelized by using the std::thread class to allocate a CPU core for each cell during polygon generation. In addition, the VTK libraries included in the official PHIG-3D distribution package are parallelized with Thread Building Block [12], which can achieve more effective parallel processing.

2.3. Multilingualization

The mixing of character encodings makes multilingual support difficult. Table 1 summarizes the encoding support status of major OSs and libraries used by PHIG-3D. On Linux and macOS, it is sufficient to unify the encoding to UTF-8. By contrast, three encodings, the system encoding (SJIS for Japanese Windows), UTF-8, and UTF-16, are used on Windows. Multilingual support would be simpler if Windows were not supported. However, this option cannot be taken, considering the number of PHITS users who use Windows OS. To minimize the development effort, PHIG-3D supports only UTF-8 input files. UTF-8 strings are used internally, and then they are converted to system encoding only when accessing files in need. The font can be changed by selecting the "Change font" submenu from the Appearance menu at the top of the window.

Table 1 Encoding in major environments.

Environments	System	C++ runtime libraries	Qt	VTK
Linux	UTF-8	UTF-8	UTF-8	Selectable[c]
macOS	UTF-8	UTF-8	UTF-8	Selectable[c]
Windows(ja)	SJIS, UTF-16[a]	SJIS	UTF-8/SJIS[b]	Selectable[c]

a: The system uses SJIS, and its Registry uses UTF-16

b: Qt commonly uses UTF-8, but some classes use SJIS by default on Windows.

c: VTK can treat both SJIS and UTF-8 but does not have multibyte character fonts.

3. Internal structure

In PHIG-3D, independent processes are carried out sequentially in the cell visualization process. Specifically, the flow is configured to be unidirectional and is executed in the following order: pre-processing, creation of implicit functions of surfaces, and creation of implicit functions of cells. Finally, the Marching Cubes method [13] is used to generate the polygons of the cells. Such a configuration is useful to avoid the "critical mass problem" in the software as described in the Jargon File [14].

3.1. Critical mass in software engineering

The Jargon File says about the critical mass, "*In physics, the minimum amount of fissionable material required to sustain a chain reaction. Of a software product, describes a condition of the software such that fixing one bug introduces one plus epsilon bugs. …*". Bugs are likely to occur in proportion to the amount of source code, and additional functionality increases the amount of source code. In addition, bug fixing is also a kind of programming process. Hence, software reaches critical mass in the long run. For programs that have exceeded critical mass, bugs are expected to increase exponentially (like the neutron flux in a nuclear reactor). To prevent super-criticality (the same as nuclear engineering), it is effective to reduce the amount of source material and then split it into a weakly coupled or independent state.

3.2. Processing flow

PHIG-3D processes input files in independent steps: input lexical analysis, instantiation of surface objects, instantiation of cell objects, and creation of 3D models. Figure 3 shows this processing flow. To simplify the complex visualization and GUI processes as much as possible, a pre-process is first performed to replace complex PHITS inputs with simple ones during lexical analysis of the input text. For example, meta cards such as infl: and set: are parsed first, and then input file concatenation and constants substitution are performed first. Subsequently, macrobody replacement with normal surfaces, cell interdependency resolution, element filling of lattice cells, and TRCL execution are performed. It should be noted that the TRCL parameter, although named after "Transform CeLl," is practically a surface transformation, so it is necessary to perform a coordinate transformation on the surface card. Since there is no input parameter in PHITS to specify the affine transformation matrix on the surface card, PHIG-3D introduces a TRSF parameter to transform a surface as an original extension.

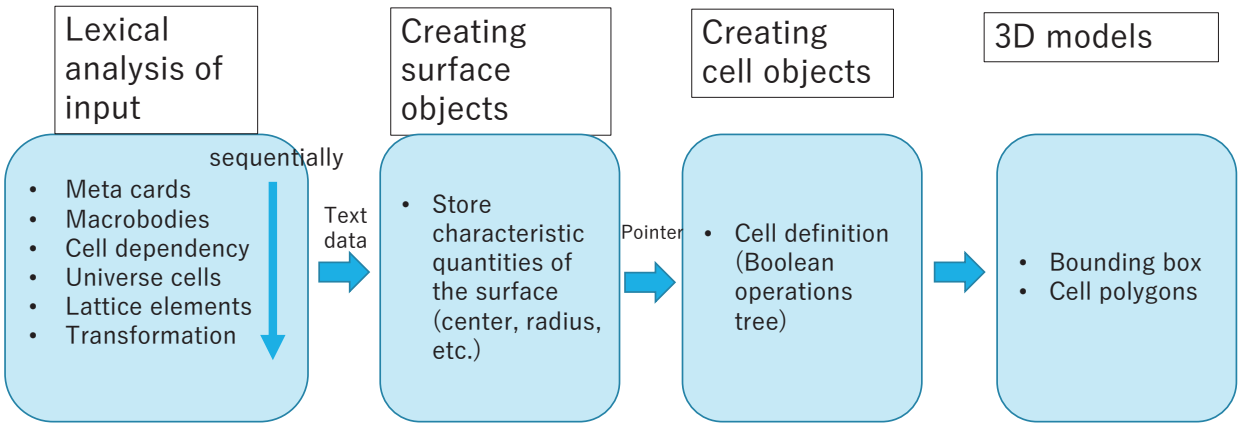

Figure 3 Input file processing flow.

3.3. Polygon creation

Cell implicit functions are created by combining surface implicit functions with Boolean operations. PHIG-3D uses the Marching Cubes method to generate polygons from the implicit functions of cells. Although this method can render complex shapes, it cannot render objects smaller than the grid size because the space is divided into a 3D grid and polygons are created by checking the inside or outside of the cell at each grid point. To improve this disadvantage, PHIG-3D uses axis-aligned bounding boxes (AABBs). If the AABB is calculated and set successfully, even extremely small cells (e.g., activation foil or HPGe detector window) can be rendered by generating grid points only within the AABB. This improvement is limited for non-axis-parallel cells because tight bounding boxes cannot be generated for them. Figure 4 compares the AABBs of the axis-aligned cells and none-axis-aligned cells.

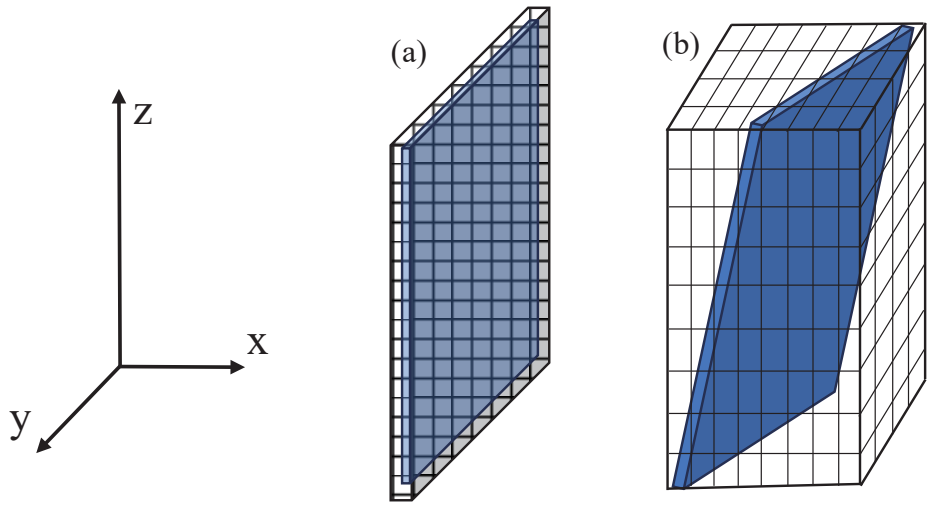

Figure 4 Thin cells and bounding boxes. An axis-aligned cell (a) fits a tight AABB, but a tight AABB cannot be created for a non-axis-aligned cell (b).

4. Conclusion

The internal structure of PHIG-3D and the features derived from them are described. Users can enhance their use of PHIG-3D by taking note of the following considerations: (1) UTF-8 or ASCII encoding is preferable for the input file, (2) The extended parameter (TRSF) is not recommended because PHITS cannot be executed, (3) Increase the number of samples with caution due to high memory consumption, (4) Thin non-axis-aligned cells are difficult to draw by the Marching Cubes method.

If the Marching Cubes method is used for precise drawing with small lattice sizes, a huge amount of memory is required. Thus, the amount of memory severely limits the drawing quality. In future work, the polygon Boolean method used in the web version of Gxsview [15] is planned to be adopted. This new method is expected to reduce memory consumption to 1/100.

References

1) Sato T, Iwamoto Y, Hashimoto S, et al. Recent improvements of the Particle and Heavy Ion Transport Code System – PHITS version 3.33. J. Nucl. Sci. Technol. 61(1), 2024, pp.127-135. doi: 10.1080/00223131.2023.2275736.
2) Coleman WA, Armstrong TW. The Nucleon-Meson Transport Code NMTC, Oakridge: Oak Ridge National Laboratory;1970. (ORNL-4606).
3) Nakahara Y, Tsutsui T., A Simulation Code System for High Energy Nuclear Reactions and Nucleon-Meson Transport Processes, 1982. JAERI-M 82-198. (In Japanese).
4) Takada H, Yoshizawa N, Kosako K, et al. An Upgraded Version of the Nucleon Meson Transport Code: NMTC/JAERI97, 1998. JAERI-Data/Code 98-005.
5) Niita K, Takada H, Meigo S, et al. High-energy particle transport code NMTC/JAM. Nucl. Instrum. Methods. 2001;184(3): 406-420. doi: 10.1016/S0168-583X(01)00784-4.
6) Iwase H, Niita K, Nakamura T. Development of general-purpose particle and heavy ion transport Monte Carlo code. J. Nucl. Sci. Technol. 2002;39(11):1142–1151. doi: 10.1080/18811248.2002.9715305.
7) History of OpenGL – OpenGL Wiki [Internet]. OpenGL Wiki contributors; Available from: https://www.khronos.org/opengl/wiki/History_of_OpenGL [cited 2023 Dec 5].

8) Ohnishi S. Gxsview: Geometry and cross section viewer for calculating radiation transport. SoftwareX. 2021;14:100681. doi: 10.1016/j.softx.2021.100681.
9) Qt | Tools For each Stage of Software Development Lifecycle [Internet]. Qt company and Qt project; Available from: https://www.qt.io/ [cited 2023 Dec 5].
10) VTK – The Visualization Toolkit [Internet]. Kitware, Inc.; Available from: https://vtk.org/ [cited 2023 Dec 5].
11) Iwamoto Y, Yoshida M, Meigo S, et al. Experimental plan for displacement damage cross sections using 120-GeV protons at Fermi National Accelerator Laboratory. Proceedings of the 2020 Symposium on Nuclear Data; 2020 Nov 26-27; Saitama, Japan. Naka-gun (Japan): Japan Atomic Energy Agency; 2021. JAEA-Conf 2021-001.
12) GitHub - oneapi-src/oneTBB: oneAPI Threading Building Blocks (oneTBB) [Internet]. Intel Corporation; Available from: https://github.com/oneapi-src/oneTBB [cited 2023 Dec 5].
13) Lorensen WE, Cline HE. Marching cubes: A high resolution 3D surface construction algorithm. ACM SIGGRAPH Computer Graphics. 1987; 21(4):163-169. doi: 10.1145/37402.37422.
14) Jargon File Resources [Internet]. Raymond ES, editor; Available from: http://jargon.org [cited 2023 Dec 5].
15) Ohnishi S. Virtual Reality System for Monte Carlo Transport Simulation Codes Using Web Technology and Commodity Devices. Nucl. Sci. Eng. 2023; ICRS 14/RPSD 2022 special issue. doi: 10.1080/00295639.2023.2177078.

Acknowledgments

I sincerely appreciate the PHITS developer team for their invaluable support in gathering user needs and providing insightful advice on the detailed functionalities of PHITS. Without their help, this work could not have been accomplished.

11. Geometry Design of Complex Entities into the PHITS Computational Space by using 3D-CAD/CG and Solid Meshing

Minoru SAKAMA[†1], Takuya SAZE [2], Shunki YANO[3], and Kento YOKOTA[4]

[1]Department of Radiation Science and Technology, Division of Radiological Sciences, Institute of Biomedical Sciences, Tokushima University Graduate School, 3-18-15 Kuramoto-cho, Tokushima 770-8503, Japan
[2]National Institute for Fusion Science (NIFS), National Institutes of Natural Sciences, 322-6 Oroshi-cho, Toki city, Gifu Prefecture 509-5292, Japan
[3]Graduate School of Health Science, Tokushima University, 3-18-15 Kuramoto-cho, Tokushima 770-8503, Japan
[4]National Cancer Center Hospital East, 6-5-1 Kashiwanoha, Kashiwa-shi Chiba 277-8577, Japan
[†]Email: minorusakama@tokushima-u.ac.jp

Abstract

Recently, while we have understood that PHITS code is positioned as a solver processing for radiation and particle transport behavior, it has been now possible to export Nastran bulk data (.bdf format as solid meshing typical in use) corresponding to the PHITS code by integrating the latest methods for pre-post processing of complex entities (human body, structures, etc.). We have examined the suitability of MSC Apex modeler as the best method for this pre=post processing. The MSC Apex modeler is responsible for the tetrahedral meshing design on the integrating MSC Apex software, and its powerful coupling with 3D-CAD and 3D-CG softwares has made it possible to precisely set up various complex entities, such as next-generation fusion reactors, HESTIA (Helical Fusion Co., Ltd. JAPAN) in this study, in the PHITS computational space. we have developed these technical workflows providing beneficial geometry designs for PHITS code. And also, we have presented that the results of exporting the T-track data obtained from the PHITS calculation to openFOAM format and using the data to create a 3D display of the tetrahedral discrete mesh bins in Paraview.

1 Introduction

Radiation and particle transport calculations based on the Monte Carlo method have been effectively used in various fields and are also now indispensable tools for the researchers and engineers involved. We have utilized the PHITS code [1] mainly for medical applications, radiation protection, radiation activation evaluation for medical accelerator, and next generation fusion reactor development. In recent years, a number of start-up companies have come forward worldwide in the field of fusion reactor development, including KYOTO FUSIONEERING [2], EX-fusion [3], and Helical Fusion [4] in Japan. One of the most important issues of Monte Carlo simulation calculations, including PHITS, is to set up a highly accurate and precise model of human bodies and structures equivalent to a real entity in a three-dimensional virtual space,

i.e.,a complex topology in which the real entities do not have to be actually constructed (manufactured or built). To fulfill this issues, it had been impossible to reproduce such complex topology groups in the 3D virtual calculation space due to very low software performance associated with older computer hardware performance (poor CPU and GPU performance and data transfer hardware) and insufficient 3D-CAD processing performance such as pre-post processing and solver processing using the finite element method, which is essential for 3D processing, and algorithms with slow code compilation processing. Recently, however, the drastic improvement in computer performance combined with the growing needs of general-purpose industries in the automotive, aerospace, shipbuilding, and creator industries has led to remarkable technological progress in 3D-CG production, an integrated simulation environment that includes pre-post processing, solver processing, and 3D-CAD (Computer Aided Design)/CAE (Computer Aided Engineering). In the course of this innovative technological advancement, we have been able to obtain MSC Apex modeler [5], an industry-established modeler for meshing structures to be reproduced in the PHITS computational space. The MSC Apex modeler belongs to MSC, the developer of the industry standard Nastran Bulk data (.bdf format) generally used for meshing, and is recognized for its influence on the quality of meshing in structural design using the finite element method (FEM), which is commonly used in structural analysis simulations in industry. There exists that radiation transport simulation calculations require the accurate reproduction of highly detailed and complex entities designed by 3D-CAD/CG in the calculation space. In this study, we have demonstrated the usefulness of the finite element meshing software MSC Apex modeler as a pre-post process that also serves as a smooth coupled execution to PHITS, a solver for radiation transport analysis, and we present some examples of its application and describe the workflow we have established.

2 Materials and Method

MSC Apex modeler is utilized for tetrahedral element structure meshing by finite element method modeling in this study. This modeling software of MSC Apex modeler has generated Nastran Bulk data (.bdf format) as automatically and accurately as possible, and has several sufficient editing tools to easily deal with errors such as self-intersections of tetrahedral structures caused by technial problems that are originated in the CAD production process. The presentation will also outline Fusion360 (3D-CAD) and Blender (3D-CG), both of which are necessary for designing complex entities.

2.1 On the finite element (FEM) method as a basis for tetrahedral element structure modeling

The finite element method (FEM) [6] is one of the core analytical methods used to numerically solve engineering problems that cannot be solved exactly. In the field of structural mechanics, it has been developed for stress analysis of structures, etc., and has now been extended to a variety of fields. In radiation behavior analysis, it is also focused on as nuclear thermal coupled analysis, and recently its application has been progressing in PHITS. The FEM method divides the structure into small simple geometries (elements with nodes, meshes such as tetrahedral) and formulates mathematical expressions for each of them. The behavior of the entire structure is analyzed and reproduced by solving simultaneous equations that link these formulas together. In the case of radiation analysis, we only need to know the meshed material information and its location which mesh it is, so basically we only apply meshing up to the FEM method.

2.2 MSC Apex modeler as a finite element modeling software

MSC Apex modeler is one of the CAE integration environments provided by MSC software corporation, a subsidiary of HEXAGON, and is comprised of MSC Apex Generative Design and MSC Apex Structures. Nastran bulk data format has the .bdf extension and is the data format handled by the NASTRAN program which is a finite element analysis and was originally developed for NASA in the late 1960s under United States government funding for the aerospace industry. The MSC (MacNeal-Schwendler Corporation) software corporation was the principal and original developer of the Nastran bulk data format. The MSC Apex modeler is a CAE specific direct and powerful modeling and meshing solution that streamlines CAD clean-up, simplification and meshing workflow, and can also import and deal with 3D surface polygon data of interest captured by a 3D scanner or is easily obtainable through e.g. Thingiverse that is one of the major websites in the 3D printer industry. One of the best features of this modeling software is that it should enable us to quickly find defects in an imported CAD data and automatically correct them during data import to reduce the occurrence of meshing errors during generating mesh modeling. Furthermore, when performing tetrahedral meshing, the continuous repairing with direct modeling and meshing allows for our easy GUI operations to correct error locations and immediately perform proper meshing as soon as the correction should have been implemented.

2.3 Autodesk Fusion 360 (3D-CAD) and Blender (3D-CG)

Technological breakthroughs in recent years on tetrahedral structure meshing and technological innovations such as the 3D-CAD/CG softwares, Fusion 360 (3D-CAD) [7, 8] and Blender (3D-CG), provided an incentive for scientists and engineers in the radiation transport simulation to design complex entities into the calculation space of their interests.

The design of the next-generation fusion reactor of HESTIA involved to this study was carried out primarily by Helical Fusion, Co. Ltd., using Fusion360. This cloud-based 3D CAD/CAM/CAE integration platform software of Fusion 360 from Autodesk, Inc. was released in 2013. It has been similar in operation to Autodesk's Inventor 3D-CAD software, with slightly less advanced functionality. Hybrid modeling, design, engineering, and fabrication, not at the industry level of high quality standards, but at a level of quality that can follow or even rise to the level of industry. Model design, sculpting (also known as form modeling, creating curved surface designs similar to computer graphics), meshing, rendering, animation, simulation (thermal analysis, etc.), CAM (object machining), sheet metal processing, drawing creation.

Blender (the latest version is 3.6.2 on November 2023) [9] is an open source integrated 3D-CG software and has been developed and presented by Ton Roosendaal in 1998. This software is equipped with a wide variety of functions necessary for 3D production, including modeling (mesh, NURBS, and sculpting), rendering, and video editing functions. The industry standard AUTODESK Maya and its rise to prominence is remarkable.

3 Results and Discussion

In order to evaluate radiation transports including neutron and photon so on in advance with accuracy, it is especially important to accurately represent the target structure in the computational domain in radiation transport analysis in advance. High resolution representing the design of the next-generation helical-type nuclear fusion reactor of HESTIA by Helical Fusion is inevitable. However, it is extremely difficult to accurately represent complex design structures like a helical structure in PHITS calculation space. There is, we have provided an example workflow of addressing the MSC Apex Modeler to generate MSC Nastran input data (.bdf format)

to be imported into PHITS from the 3D CAD data of the next-generation helical-type nuclear fusion reactor of HESTIA.

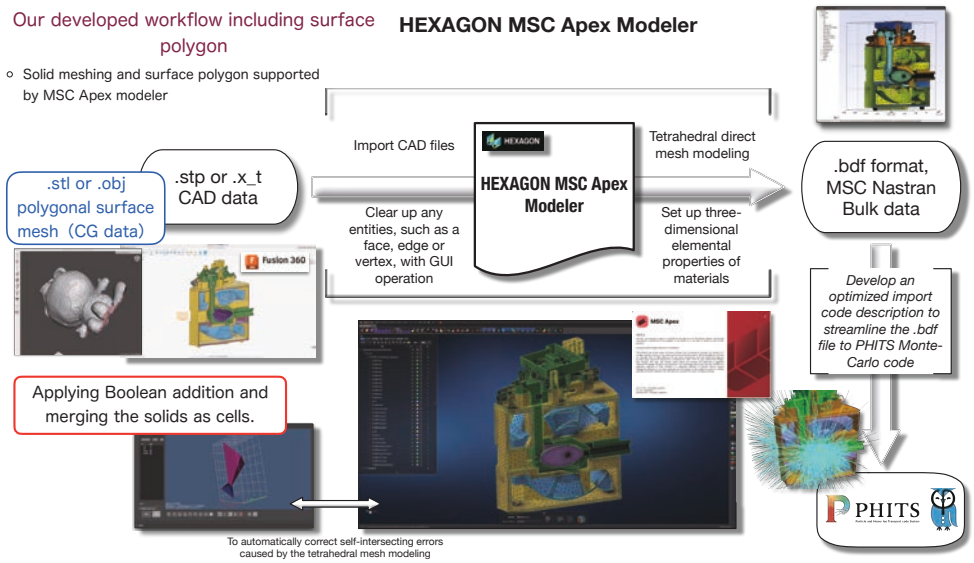

Figure 1: The technical workflow of MSC Apex modeler which we have developed in this study, from MSC Apex modeler for pre-post processing with solid finite element meshing to PHITS for solver processing in the geometric design of complex topologies.

Figure 1 shows the technical workflow of MSC Apex modeler which we have developed in this work. In this workflow, 3D CAD data was imported into MSC Apex Modeler, geometries were edited, and solid mesh was generated to obtain the input data in MSC Nastran input data format. Then, the file output from MSC Apex was loaded in the PHITS calculation code and the calculation was performed successful. The procedure orders for this work flow are as follows: 1) define the materials used for each parts designed by CAD/CG-designed part, 2) assign material number to each part number, which corresponds to a cell number in PHITS, 3) execute solid meshing (tetrahedral direct mesh modeling). If errors such as self-interactions have been made during the solid meshing operations, various geometry editing and solid meshing functions in MSC Apex allow us to detect those intersections and other errors in the GUI and to visually edit geometries with advanced tools such as “Vertex/Edge Drag”, 4) export the bdf file and verify the drawing with the Gmsh software for accuracy of the geometric entities obtained by the solid mesh modeling and for the proper correspondence with the material number of each part. Whenever this drawing is unsuccessful, we have proved that PHITS will not execute using the exported bdf file. 5) Finally, we identify that when the shape of the entire part of our interest is reproduced correctly or not in PHITS, and if we detect any areas where no material is assigned (indicated by white drawing), the booleans in the face-sharing part of the tetrahedral mesh shape are not working properly, so we return to the meshing edit window and implement repeatedly the direct mesh modeling to improve the focusing tetrahedral groups on the entire part. The present solid mesh modeling results of the next-generation nuclear fusion reactor of HESTIA revealed that for one (36-degree unit) of the ten units of the circumferential 360-degree helical structure on HESTIA, the number of nodes was 999,662 (of which the internal nodes were 604,899 and the surface ones were 394,763), and the number of elements was 4,797,001, and the size of this obtained bdf file was approximately 320 MB. Obviously, the number of those nodes and elements in a higher-resolution tetrahedral mesh structure (i.e., with almost no tolerance between the real object and the tetrahedral meshed one) would be enormous, and the file size

would be huge.

Figures 2 and 3 show the results of preliminary two-dimensional neutron (source setting is 14 MeV neutron primary energy) transport calculation distributions on HESTIA, with Fig. 2 representing cross sections of some transverse planes and Fig. 3 representing cross sections of some coronal planes. The number of histories for each calculation is 50,000,000. The total calculation time for this output was about 5 hours with the memory-sharing parallel of openMP-PHITS calculation. The calculation time for the tetrahedral structure mesh modeling with a bdf file is shorter than that for the calculations written in the input files with the usual geometry settings inside PHITS, due to the advantage that the PHITS calculation program can easily determine the coordinate positions of the materials comprising the object in the radiation transport calculation.

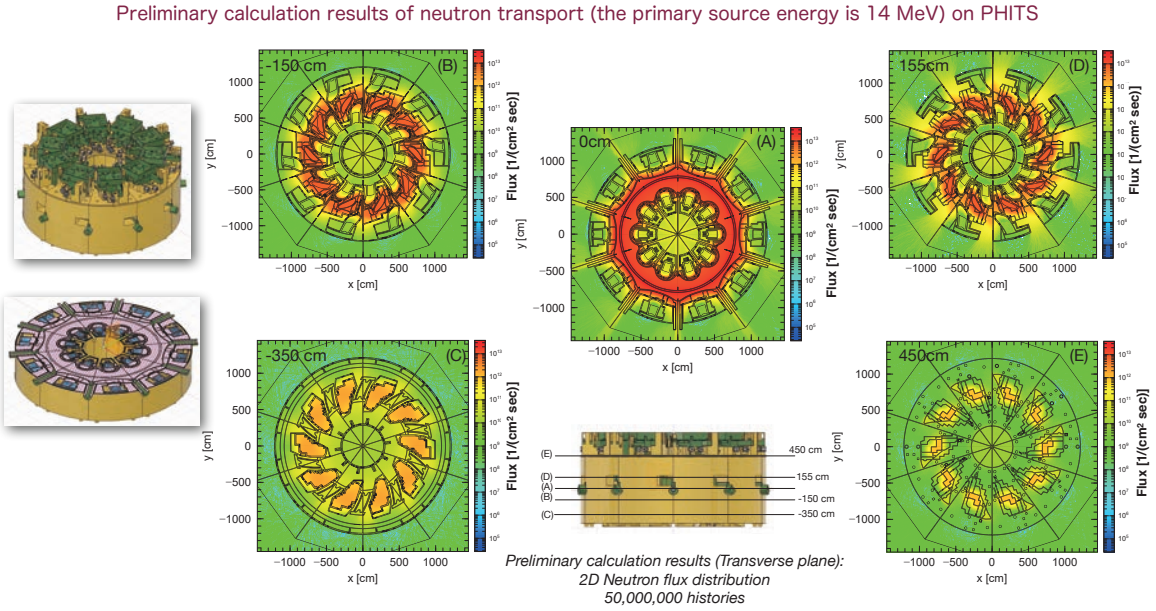

Figure 2: Preliminary results of 2D neutron transport calculations in the cross sections of transverse planes on HESTIA.

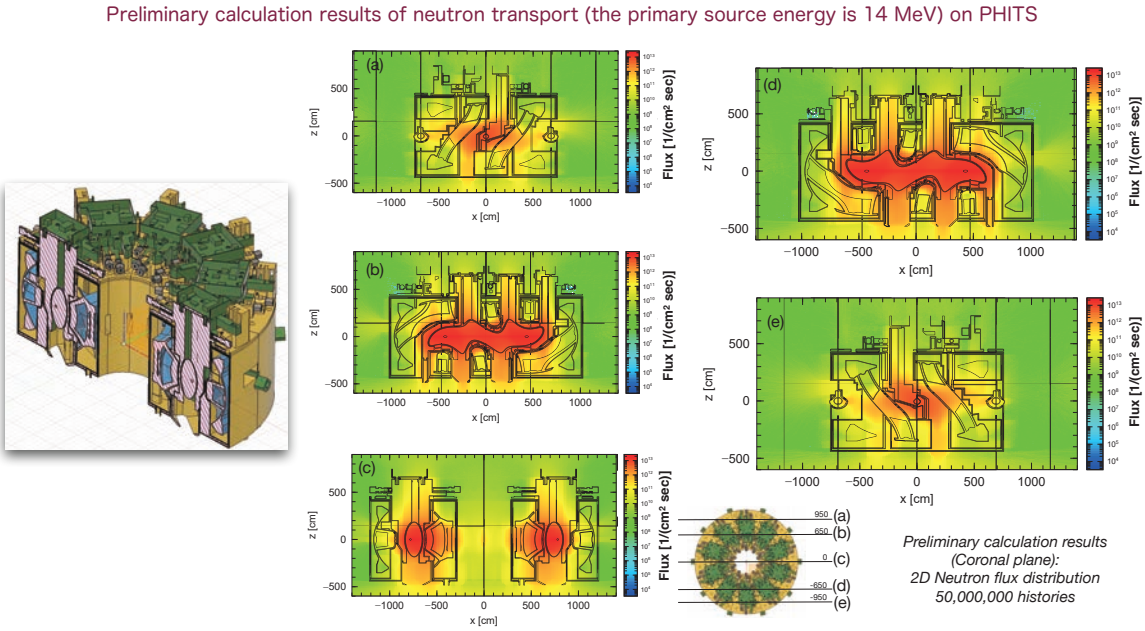

Figure 3: Preliminary results of 2D neutron transport calculations in the cross sections of coronal planes on HESTIA.

Figure 4 shows the focused workflow from capturing the 3D-CG outer complex entities (such as surface polygon) with a 3D scanner to building them into Nastran bulk data (.bdf format). In addition, Figure 5 presents the results of exporting the T-track data obtained from the PHITS calculation to openFOAM format and then using the data to create a 3D display of the tetrahedral discrete mesh bins in Paraview. The advantage of this openFOAM format make it for us possible to understand that the calculation time is much shorter and the size of the output data is much smaller than that of the vtk output, which has been explained by default on the PHITS. Furthermore, the obtained drawing through the openFOAM format can be displayed in Paraview, which improves the visibility and comprehension of the radiation tally distribution (in this case, neutron flux distribution) in terms of handling of the 3D display.

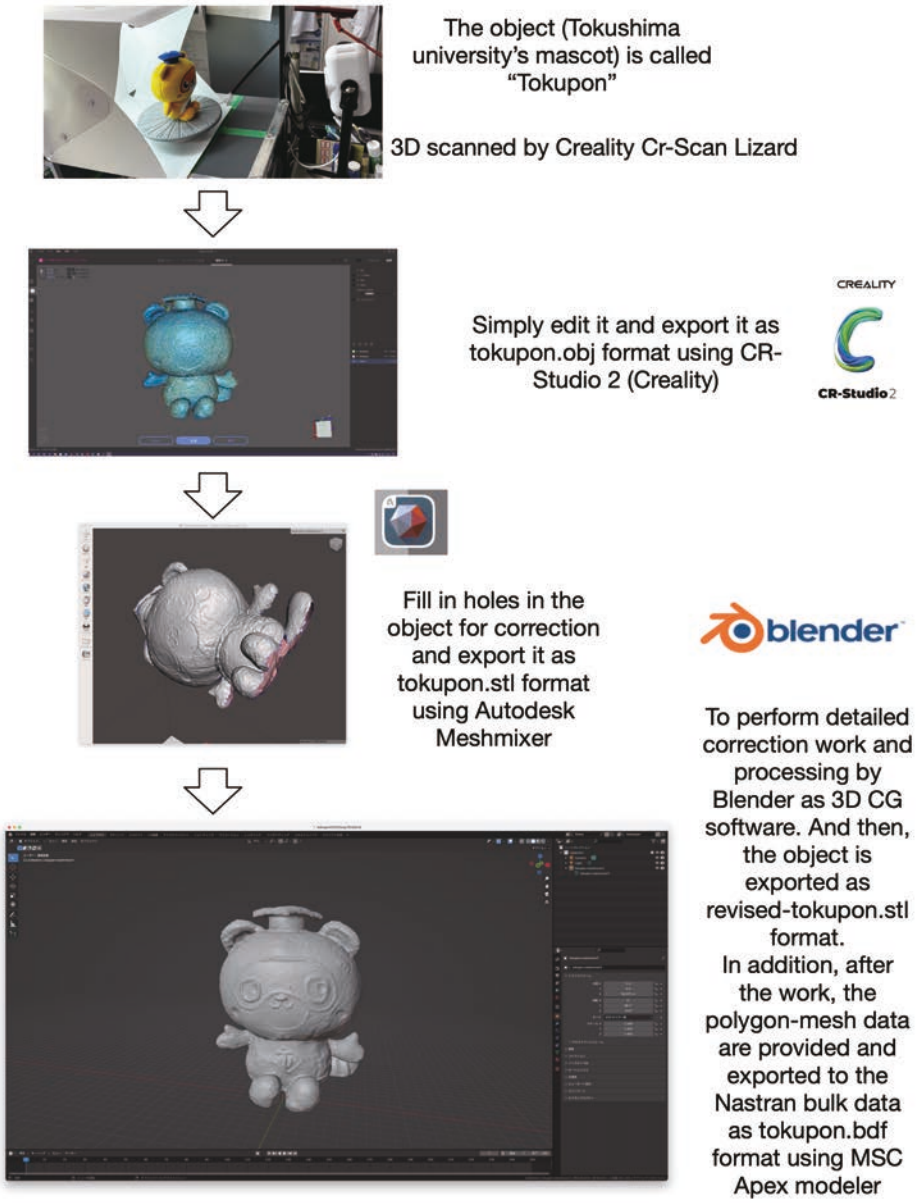

Figure 4: Example of the workflow to PHITS calculation space from capturing a 3D-CG outer complex entity with a surface polygon obtained from a 3D scanner of consumer use.

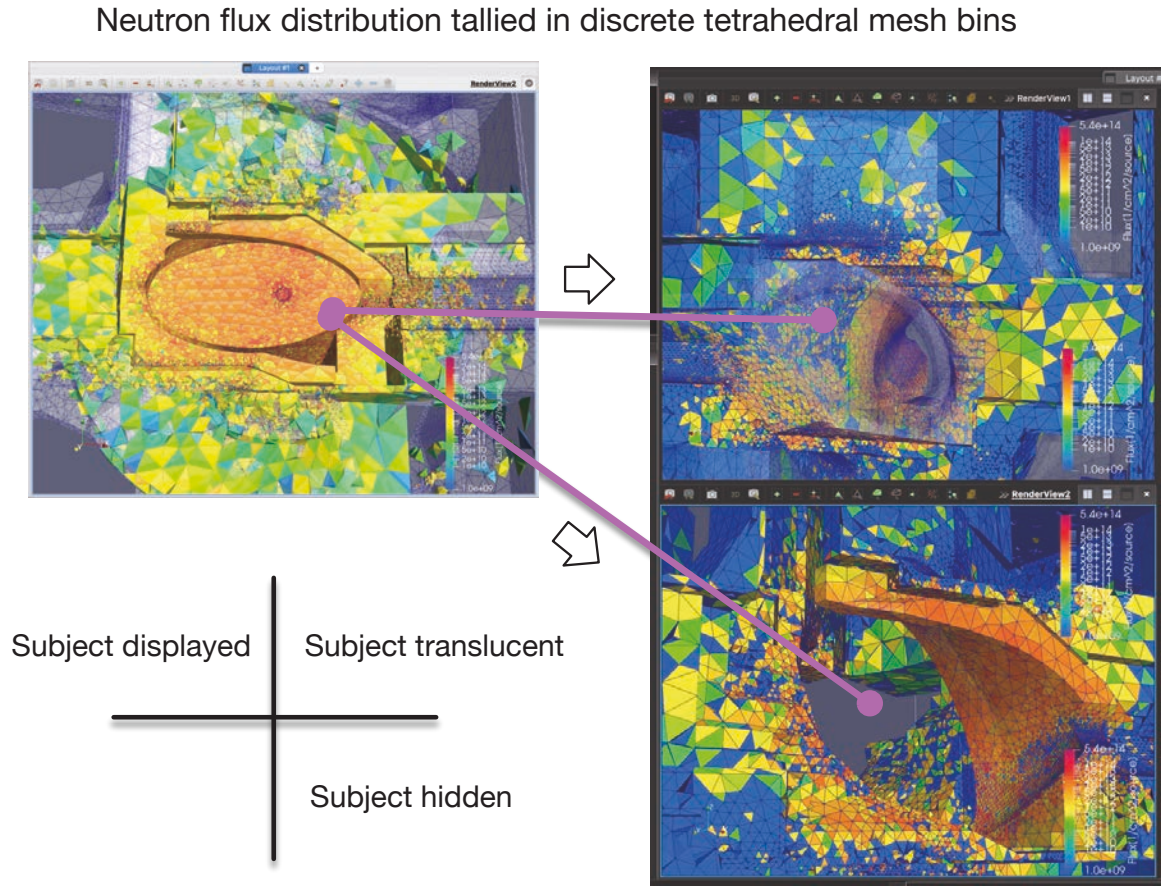

Figure 5: Neutron flux tallied in tetrahedral discrete mesh bins on the next generation of nuclear fusion reactor.

4 Conclusion

For real-world accurate and precise human bodies and structures in the PHITS computational space, MSC Apex Modeler, a solid meshing software that has been developed in the industry-standard integrated pre-post processing, solver processing, and 3D-CAD/CAE simulation computing environment, supports error correction function (e.g., cleanup) on advanced CAD design and exports high-quality Nastran bulk data (tetrahedral structural meshed modeling). The workflow for designing a complex topology is extremely useful and, once incorporated into the PHITS computational space, allows for the creation of a variety of PHITS tally results, 2D and 3D displays of radiation transport conditions, time lapses, and more. The 3D-CG (Blender) software facilitates the capture of the topology by the 3D scanner and the modification of surface polygons, and by using MSC Apex Modeler to capture and modify this data, even more complex topologies can be incorporated into the PHITS calculation space. The system design of the next generation helical fusion reactor HESTIA (Helical Fusion Co., Ltd.) has been completed, and the neutron transport calculation results in PHITS have reached the stage of providing basic data on neutron flux distribution and service life of the blanket, which are important in a fusion reactor. Finally, any real-world system can now be reproduced in high-resolution in PHITS by MSC Apex modeler.

References

[1] Sato, T, Iwamoto, Y., Hashimoto, S., Ogawa, T., Furuta, T., Abe, S., Kai, T., Matsuya, Y., Matsuda, N., Hirata, Y., Sekikawa, T., Yao, L., Tsai, P.E., Hunter, H.N., Iwase, H., Sakaki, Y., Sugihara, K., Shigyo, N., Sihver L., and Niita, K., Recent improvements of the Particle and Heavy Ion Transport code System – PHITS version 3.33, J. Nucl. Sci. Technol. 61(1), 2024, pp 127-135 DOI: 10.1080/00223131.2023.2275736

[2] KYOTO FUSIONEERING, `https://kyotofusioneering.com/` (accessed 2024-01-30) .

[3] EX-Fusion, `https://ex-fusion.com/` (accessed 2024-01-30) .

[4] Helical Fusion, `https://www.helicalfusion.com/`(accessed 2024-01-30) .

[5] MSC Apex modeler, `https://hexagon.com/ja/products/msc-apex-modeler` (accessed 2024-01-30) .

[6] Brenner, S.C. and Scott, L.R., The mathematical theory of finite element methods, Second Edition. Springer Science & Business Media., 2002.

[7] AUTODESK, Autodesk Fusion 360, `https://www.autodesk.co.jp/products/fusion-360/overview?term=1-YEAR&tab=subscription&plc=F360` (accessed 2024-01-30) .

[8] Song, P.P., Qi, Y.M., and Cai, D.C., Research and Application of Autodesk Fusion360 in Industrial Design, IOP Conf. Ser.: Mater. Sci. Eng. 359, 012037 (2018).

[9] Community, B. O. (2018). Blender - a 3D modelling and rendering package. Stichting Blender Foundation, Amsterdam. Retrieved from `http://www.blender.org` (accessed 2024-01-30) .

Acknowledgments

We greatly thank Dr. Junichi MIYAZAWA (Co-Founder, Co-CEO), Dr. Takuya GOTO (Co-Founder, Board Member), Dr. Akio SAGARA (Science Advisor), ann Takaya TAGUCHI (Co-Founder, Co-CEO) on Helical Fusion, Co., Ltd.(Japan) for supporting the present work. Without their financial support, our research would not have been possible and absolutely will continue to require their support in future.

12. A Proposal for the Development of Boron Neutron Capture Therapy Agents Based on Simulation Studies Using PHITS Microdosimetry

Takafumi SHIGEHIRA[1], Tadashi HANAFUSA[2], Kazuyo IGAWA[2], Tomonari KASAI[2], Shuichi FURUYA[3], Hisakazu NISHIMORI[4], Yoshinobu MAEDA[4], Hiroyuki MICHIUE[2], and Atsushi FUJIMURA[1,2]

[1]Department of Cellular Physiology
Okayama University Graduate School of Medicine, Dentistry and Pharmaceutical Sciences
Okayama, Okayama 700–8558, Japan

[2]Neutron Therapy Research Center
Okayama University
Okayama, Okayama 700–8558, Japan

[3]Research Laboratory of Accelerator-Based BNCT system
Graduate School of Engineering Nagoya University
Nagoya, Aichi 464–8603, Japan

[4]Department of Hematology and Oncology
Okayama University Hospital
Okayama, Okayama 700–8558, Japan

E-mail: atsushi.fujimura@okayama-u.ac.jp

Boron Neutron Capture Therapy (BNCT) is a radiation methodology utilizing the Boron Neutron Capture Reaction (BNCR) mechanism, depicted by $^{10}B(n.\alpha)^{7}Li$, to accurately target and eradicate tumor cells. The required ^{10}B level for its therapeutic effect in Boronophenylalanine (BPA)-BNCT is usually between 15-40 ppm. While this concentration serves as a standard for several boron derivatives, the precise ^{10}B demand for alternative boron compounds, with their distinct accumulation patterns, remains unclear. To examine this, we crafted a virtual cell model with organelles. Using the particle and heavy ion transport system, we calculated the BPA equivalent dose concentration for the cell nucleus. Additionally, we presented the idea of the Intranuclear Minimal Region (IMR), referring to the domain in the microdosimetric kinetic model, and projected the BPA's equivalence dose concentration to the IMR. The findings suggest that the required boron dosage can change markedly based on how boron molecules settle within cell components. It appears important to consider the BNCR's impact, emphasizing the individual accumulation profiles, rather than strictly using the 15-40 ppm as a reference.

1. Introduction

Boron Neutron Capture Therapy (BNCT) is a radiation treatment method. First, boron is incorporated into cancer cells. Subsequently, neutron irradiation is performed, inducing the Boron Neutron Capture Reaction (BNCR) within the target cells, resulting in radiation therapy [1]. The BNCR is expressed as $[n(^{10}B,^{7}Li)\alpha]$, leading to the generation of α particles and ^{7}Li radiation. A prominent boron compound utilized in BNCT is Boronophenylalanine (BPA),

which has progressed to practical clinical application [2]. BPA-BNCT, employing BPA, received approval from the Ministry of Health, Labor and Welfare in Japan in 2020 for the treatment of "inoperable locally advanced or locally recurrent head and neck cancer," making it eligible for insurance coverage [3].

The expansion of BNCT applications involves not only BPA but also attempts to develop novel boron compounds using Sodium Borocaptate (BSH). BSH, represented as $(B_{12}H_{11}SH)Na_2$, is a small molecule, and through chemical modification of BSH, research is underway to develop novel boron compounds using Drug Delivery Systems (DDS) to impart tumor specificity and cell membrane permeability. Various BSH-based boron compound developments are progressing at the foundational research level [4,5].

In achieving selective treatment at the cellular level through BNCT, boron compounds play a crucial role, necessitating their selective accumulation in cancer cells. Desired properties for boron compounds, based on insights from past clinical studies, include a Tumor/Normal Ratio (T/N ratio) of 3 or more in terms of selectivity and an accumulation level of 20-40 ppm [6].

If a newly developed boron formulation fails to meet the target values and is deemed inadequate as a practical boron formulation, there may be instances where it does not reach practical use. In other words, there is a possibility that a newly proposed boron formulation, which might have had potential utility, is hindered by specific target values. In contrast to previously reported boron formulations, the cellular distribution of these novel formulations differs. Therefore, using conventional indices proposed for the evaluation of such boron formulations may compromise a proper assessment. Recognizing these issues, this study aims not only to assess the extent of boron content in cells and tissues, as conventionally done but also emphasizes the evaluation of the specific cellular regions where boron atoms are present by calculation using particle and heavy ion transport system (PHITS) [7,8]. This proposal is made with the intention of addressing the importance of such assessments, incorporating concrete numerical values.

2. Method

2.1. Construction of Cell Model

The method for constructing cellular structures referenced to a normal liver cell as a commonly used cellular model found in textbooks [9]. This model included various cellular organelles (Figure1).

2.2. Construction of Boron Accumulation Model

The boron concentration required for the anticipated cell-killing effect through BPA-BNCT is estimated to be approximately 15-40 ppm [6]. Therefore, in this study, we chose 30 ppm as a representative value, and set the boron concentration to be 30 ppm on a whole-cell basis.

Using this configuration, we developed models for boron accumulation in various cellular organelles and reported PolyR-BSH and A6K/BSH model. These is compared them with BPA accumulation models.

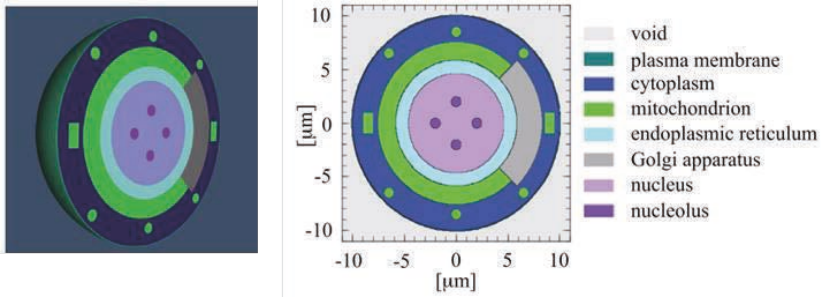

Figure 1 Created cell model for calculation using PHITS.
Shigehira T. et al., ***Adv. Theory Simul.*** ,(2023), 6(1), 2300163.

2.3. Cellular Nucleus Dose Analysis

A model simulating Boronophenylalanine (BPA) was created, serving as a reference to calculate the magnification of nuclear doses based on the intracellular localization of other boron compounds. Using this magnification, the equivalent BPA dose concentration (Boron Equivalent Dose Concentration, B-EDC) for each boron localization was calculated by dividing the reported effective tumor-inhibiting doses for BPA-BNCT (20-40 ppm, specifically using 30 ppm as a representative value) by the magnification.

2.4. IMR Analysis

In addition to nuclear dose analysis, Recognizing that localized doses concentrated within the nucleus are averaged in nuclear dose analysis, the study compared and evaluated the maximum value of locally concentrated doses within the nucleus, using the concept of Intra nuclear Minimal Region (IMR) with a defined diameter of 0.5 μm referred to concept of Microdosimetric Kinetic Model (MKM) [10], a cell survival rate evaluation model.

The comparison of IMR doses was conducted similarly to the comparison of nuclear doses, and the B-EDC in IMR was estimated.

2.5. MKM Analysis

Based on Hawkins' proposed model for cell survival rate evaluation [10], the study applied Sato and Horiguchi's proposed biological effect estimation in the current cell model [11,12]. The evaluation was conducted using the Relative Biological Effectiveness at 10% survival rate (RBE_{10}) for BPA as a reference based on boron localization within the cell.

3. Result

3.1. Cellular Nucleus Dose Analysis

A summary of the results when localized and accumulated in various cell organelles is presented (Figure2). The most significant dose change in the intracellular distribution of boron was indicated in the accumulation within the cell nucleus and nucleolus (Table1).

The respective magnifications of nuclear doses in comparison to the reference cytoplasmic distribution were 10.77 and 12.82. In cells resembling the cellular model of this study, it was found that the intracellular localization of boron resulted in a maximum difference of approximately 10 to 13 times in nuclear doses.

Furthermore, considering the equivalent concentration dose of boron from the perspective of BPA, it was revealed that by taking into account the intracellular localization of boron, it is possible to lower the required boron concentration to achieve a BPA-equivalent dose from 30 ppm to approximately 2-3 ppm.

Table 1 Nucleus dose , Magnification , and B-EDC in each subcellular localization of intracellular boron.

Accumulation pattern	Nucleus dose [Gy/source]	Magnification	Equivalent dose concentration [30 ppm/multiplication factor]
Cytoplasm and extranuclear organelle	6.92E-06	1.00	30.00
Intranuclear	7.45E-05	10.77	2.79
Nucleolus	8.87E-05	12.82	2.34
Boron agent	**Nucleus dose [Gy/source]**	**Magnification**	**Equivalent dose concentration [30 ppm/multiplication factor]**
BPA (boronophenylalanine)	6.92E-06	1.00	30.00
PolyR-BSH	1.54E-05	2.23	13.47
A6K/BSH	1.04E-05	1.51	19.87

Shigehira T. et al., ***Adv. Theory Simul***. ,(2023), 6(1), 2300163.

In PolyR-BSH and A6K/BSH, the respective nuclear doses increased by 2.23-fold and 1.51-fold. The equivalent concentration of BPA became 13.47 ppm and 19.87 ppm, respectively.

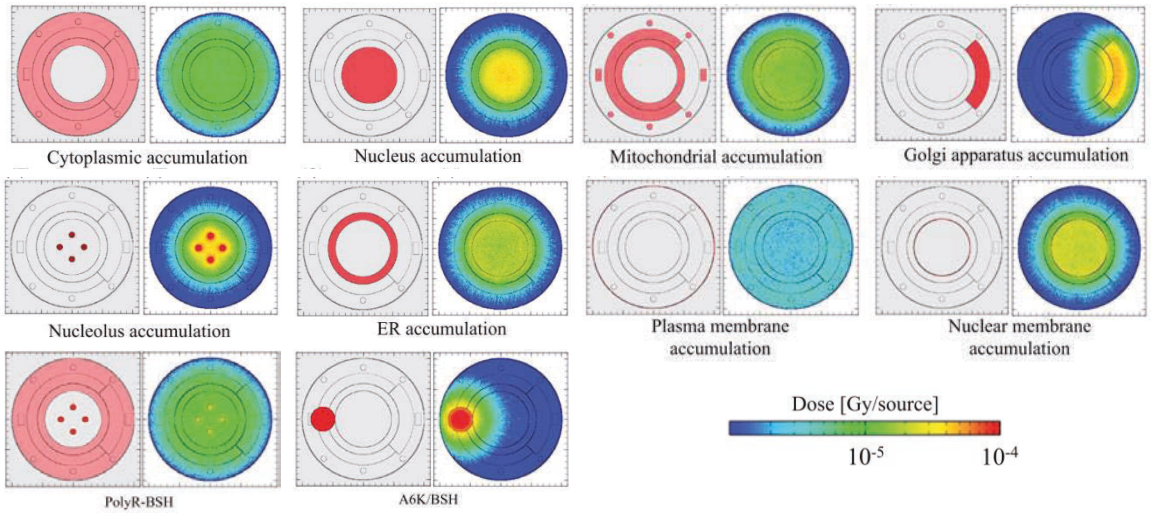

Figure 2 Dose distribution in each subcellular localization of intracellular boron.
Shigehira T. et al., ***Adv. Theory Simul.*** ,(2023), 6(1), 2300163.

3.2. IMR Analysis

We will indicate the results on the Figure3 and Table2. Focusing only on the most significant changes result, its case is boron distribution in the nucleolus, and the IMR dose multiplier is approximately 285 times higher compared to the Cytoplasmic accumulation (BPA distribution). In terms of the B-EDCin IMR, it was found to be 0.11 ppm.

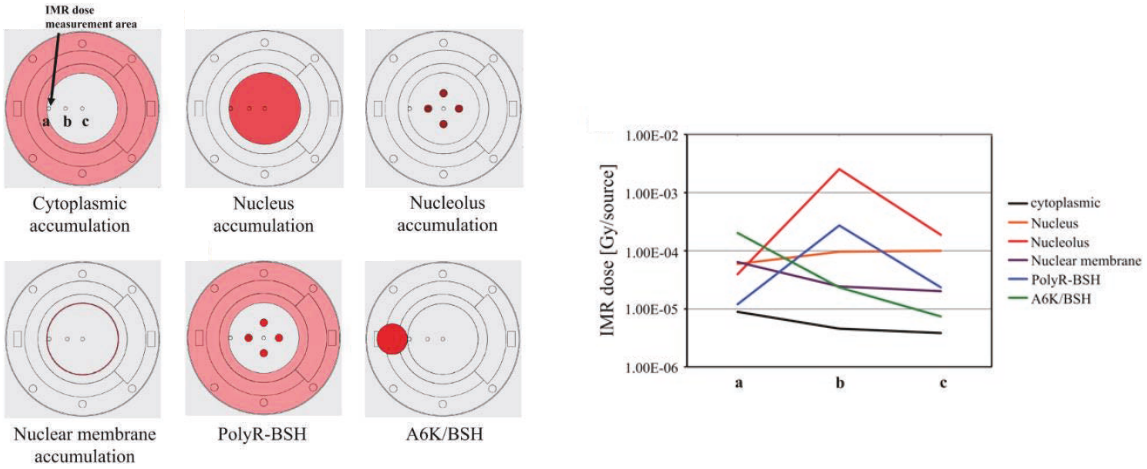

Figure 3 IMR dosimetry in each subcellular localization of intracellular boron.
Shigehira T. et al., ***Adv. Theory Simul.*** ,(2023), 6(1), 2300163.

Table 2 IMR dose , Magnification , and B-EDC$_{IMR}$ in each subcellular localization of intracellular boron

Accumulation pattern	IMR (intranuclear minimal region) dose [Gy/source]	Magnification	Equivalent dose concentration [30 ppm/multiplication factor]
Cytoplasmic uniform accumulation	8.83E-06	1.00	30.00
Uniform Nuclear Accumulation	1.01E-04	11.41	2.63
nucleolus accumulation	2.52E-03	285.52	0.11
Nuclear membrane accumulation	6.26E-05	7.09	4.23
PolyR-BSH	2.75E-04	31.09	0.97
A6K/BSH	2.04E-04	23.14	1.30

Shigehira T. et al., ***Adv. Theory Simul.*** ,(2023), 6(1), 2300163.

3.3. MKM Analysis

The cellular distribution of boron that exhibited the highest values was the accumulation in the nucleolus and the PolyR-BSH accumulation model. Both demonstrated localized accumulation within a subset of the nucleus, having features of the nucleolus (Figure4). In such cases, the relative biological effectiveness (RBE) for BPA was found to range from 1.75 to 1.82(Table3).

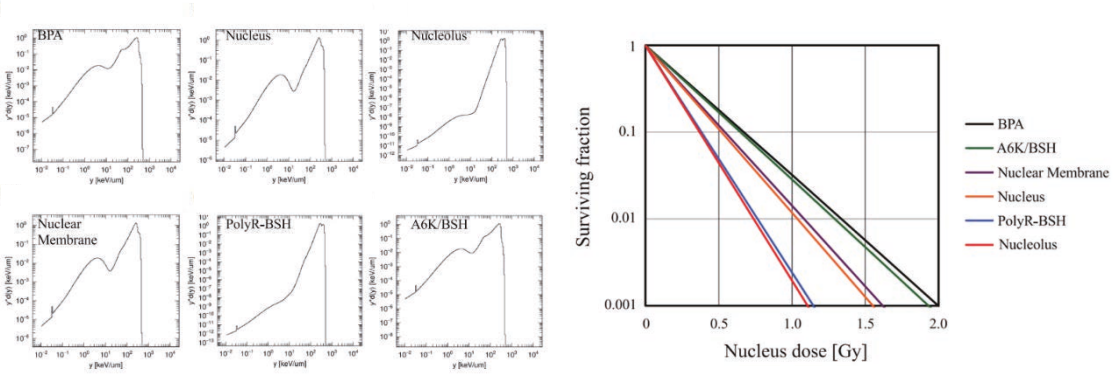

Figure 4 MKM Analysis in each subcellular localization of intracellular boron.
Shigehira T. et al., ***Adv. Theory Simul.*** ,(2023), 6(1), 2300163.

Table 3 IMR dose , Magnification , and B-EDC$_{IMR}$ in each subcellular localization of intracellular boron.

Accumulation pattern	RBE$_{10(BPA)}$
Cytoplasmic accumulation	1
Nuclear accumulation	1.29
Nucleolus accumulation	1.82
Nuclear membrane accumulation	1.24
PolyR-BSH	1.75
A6K/BSH	1.04

Shigehira T. et al., ***Adv. Theory Simul.*** ,(2023), 6(1), 2300163.

4. Conclusion

The above results indicate that if a boron compound targeting the nucleus or nucleolus is developed, the required boron delivery amount to achieve a comparable killing effect to current BPA-BNCT can be significantly reduced. In the development of novel boron compounds, it is suggested that achieving the conventional boron delivery target values (e.g., 15-40 ppm) may not necessarily be essential when sufficiently considering intracellular dynamics. This implies a strong endorsement for the societal derivation of innovative boron compounds that have not yet been practicalized.

References

[1] Gahbauer R., Gupta N., Blue T., Goodman J., Barth R., Grecula J., Soloway A.H., Sauerwein W., Wambersie A., Boron neutron capture therapy: principles and potential. Recent Results Cancer Res., vol.150, 1998, pp. 183-209. doi: 10.1007/978-3-642-78774-4_12. PMID: 9670292.
[2]Kondo N, Masutani M, Imamichi S, Matsumoto Y, Nakai K. Strategies for Preclinical Studies Evaluating the Biological Effects of an Accelerator-Based Boron Neutron Capture Therapy System. Cancer Biother

Radiopharm. 2023 Apr, Vol.38, no.3, pp.173-183. doi: 10.1089/cbr.2022.0057. Epub 2022 Sep 26. PMID: 36154293.
[3]Matsumura A, Asano T, Hirose K, Igaki H, Kawabata S, Kumada H. Initiatives Toward Clinical Boron Neutron Capture Therapy in Japan. Cancer Biother Radiopharm. 2023 Apr, Vol.38, no.3, pp.201-207. doi: 10.1089/cbr.2022.0056. Epub 2022 Nov 14. Erratum in: Cancer Biother Radiopharm. 2023 May;38(4):273. PMID: 36374236; PMCID: PMC10122211.
[4]Fujimura A, Yasui S, Igawa K, Ueda A, Watanabe K, Hanafusa T, Ichikawa Y, Yoshihashi S, Tsuchida K, Kamiya A, Furuya S. In Vitro Studies to Define the Cell-Surface and Intracellular Targets of Polyarginine-Conjugated Sodium Borocaptate as a Potential Delivery Agent for Boron Neutron Capture Therapy. Cells. 2020 Sep 23, Vol.9, no.10, pp.2149. doi: 10.3390/cells9102149. PMID: 32977522; PMCID: PMC7598271.
[5] Michiue H, Kitamatsu M, Fukunaga A, Tsuboi N, Fujimura A, Matsushita H, Igawa K, Kasai T, Kondo N, Matsui H, Furuya S. Self-assembling A6K peptide nanotubes as a mercaptoundecahydrododecaborate (BSH) delivery system for boron neutron capture therapy (BNCT). J Control Release. 2021 Feb 10, Vol.330, pp.788-796. doi: 10.1016/j.jconrel.2020.11.001. Epub 2020 Nov 11. PMID: 33188824.
[6] Japanese Society of Neutron Capture Therapy, http://www.jsnct.jp/about_nct/haikei.html [cited 2024 Janu 15 in Japanese].
[7] Shigehira T, Hanafusa T, Igawa K, Kasai K, Furuya S, Nishimori H, Maeda Y, Michiue H, Fujimura A. Particle and Heavy Ion Transport Code System-Based Microdosimetry for the Development of Boron Agents for Boron Neutron Capture Therapy. Adv. Theory Simul. 2023 Jul, Vol.6, no.7, 2300163. doi: 10.1002/adts.202300163
[8] Sato Tatsuhiko, Iwamoto Yosuke, Hashimoto Shintaro, Ogawa Tatsuhiko, Furuta Takuya, Abe Shin-Ichiro, Kai Takeshi, Matsuya Yusuke, Matsuda Norihiro, Hirata Yuho, Sekikawa Takuya, Yao Lan, Pi-En Tsai, Hunter N. Ratliff, Iwase Hiroshi, Sakaki Yasuhito, Sugihara Kenta, Shigyo Nobuhiro, Sihver Lembit & Niita Koji (2024) Recent improvements of the particle and heavy ion transport code system – PHITS version 3.33, Journal of Nuclear Science and Technology, Vol.61, no.1, pp.127-135, DOI: 10.1080/00223131.2023.2275736
[9] Alberts B, Johnson A, Lewis J, Raff M, Roberts K, Walter P, Molecular Biology of the Cell, 4th ed., GS (Garland Science), New York 2001 p. 661.
[10] R. B. Hawkins, Med. Phys. 1998, Vol.25, pp.1157-1170.
[11] Horiguchi H, Sato T, Kumada H, Yamamoto T, Sakae T. Estimation of relative biological effectiveness for boron neutron capture therapy using the PHITS code coupled with a microdosimetric kinetic model. J Radiat Res. 2015 Mar, Vol.56, no.2, pp.382-90. doi: 10.1093/jrr/rru109. Epub 2014 Nov 26. PMID: 25428243; PMCID: PMC4380055.
[12] Sato T, Masunaga SI, Kumada H, Hamada N. Microdosimetric Modeling of Biological Effectiveness for Boron Neutron Capture Therapy Considering Intra- and Intercellular Heterogeneity in ^{10}B Distribution. Sci Rep. 2018 Jan 17, Vol.8, no.1, pp.988. doi: 10.1038/s41598-017-18871-0. PMID: 29343841; PMCID: PMC5772701.

Acknowledgements

The authors thank T. Sato, T. Ogawa, and T. Kai for training T.S. on the PHITS calculation. The authors are grateful to all members of our laboratory for their valuable comments.

This work was supported by a grant from the Japan Society for the Promotion of Science (JSPS) KAKENHI(Grants-in-Aid for Scientific Research from the Ministry of Education, Culture, Sports, Science, and Technology of Japan), number JP21K07730 (to H.N.).

13. Simulation Analysis of Cosmic Ray Muon Penetrating Subsurface of Huge Mountain

Shoichi Nakamura[1], Kaoru Ijima[1], Eiko Torikai[1,2], Kanetada Nagamine[1,2,3], Tatsuhiko Sato[4]

1. Graduate School of Engineering / Graduate Faculty of Interdisciplinary Research, University of Yamanashi, 4-3-11, Takeda, Kofu, Yamanashi, Japan 400-8511
2. Institute of Materials Structure Science, High Energy Accelerator Research Organization (KEK), 1-1 Oho, Tsukuba, Ibaraki 305-0801 Japan
3. Nishina Center for Accelerator-Based Science, RIKEN, 2-1 Hirosawa, Wako, Saitama, 351-0198, Japan
4. Nuclear Science and Engineering Center, Japan Atomic Energy Agency (JAEA), 2-4 Shirakata, Tokai, Ibaraki 319–1195

e-mail:nakamurashoichi61@gmail.com

Abstract

We conducted a simulation analysis of the behavior of cosmic-ray muons (CRM) passing through a huge mountain using the newly established cosmic-ray muon mode in PHITS. In this analysis, we investigated various aspects, including the altitude and angle dependence of incident and transmitted muons, and further attenuation of decelerated muons after transmission of massive mountain by atmosphere.

Intensity of the incident CRM at 3776 m altitude is 1.8 times larger than that at ground level in elevation angle from 15 to 20 deg., while it is almost equivalent at 1300 m altitude. After transmission through standard rock, it was found that the ratio decreases down toward unity up to 2.0×10^4 g/cm^2 in density length (~75m in rock thickness), then increases again, resulting in 1.2 to 1.3 times in 2.0×10^5 g/cm^2 to 5.0×10^5 g/cm^2. On the other hand, we confirmed that the further attenuation by atmosphere during the flight to the detector is 5 % or less.

1. Introduction

The phreatic eruption at Mt. Ontake in 2014, which is the worst volcanic disaster causing the largest postwar victims, had taken place abruptly without any precursor. If such eruption might be in Mt. Fuji where number of climbers per day exceeded 7000 at maximum, it could be bigger catastrophe. The goal of this study is to explore a new approach to catch a sign of anomaly preceding such eruption at Mt. Fuji by using cosmic-ray muons (CRM). The CRM radiography is a unique method to provide transmission image of internal structure inside of active volcano [1-3].

CRM have high energies of GeV~TeV, making them possible to penetrate small volcanoes up to about 2 km in diameter. Mt. Fuji, however, is too large even for high-energy CRMs to probe dynamics of magma whose main path is located below the summit. The observation of the seasonal variation in CRM intensity

after passing through Mt. Kurokura in West Iwate mountains gives us a hint to challenge the fundamental research associated with phreatic eruption by CRM radiography: there found correlation between CRM intensity and frequency of steam explosion [4]. They suggested subsidence of water level by about 100m in the summer season compared to winter when steam explosion is more active compared to the other seasons. In Mt. Fuji, on the other hand, hidden underground streams are presumed for supplying sufficient spring water of over 5×10^6 m^3/day around the foot of the mountain [5]. The CRM tomography is expected useful to investigate the distribution of the subsurface streams. Once the underground streams are located, we can monitor its variation as was in Mt. Kurokura, comparing with the other observations in Mt. Fuji.

The Gotemba Tarobo Base, halfway along the new fifth station of the Mt. Fuji Skyline, was chosen to set up the detectors for muon imaging of the extremely huge mountain to begin with. From there, it has a wide dynamic range with an elevation angle from 0 to 20 degrees, altitude from 1300 to 3776 m, and path length from 0 to several kilometer even the observation range is limited to subsurface layer and near the summit. In this work, we report on the simulation study on (1) elevation angle dependence of incident muon energy spectrum at high altitude where no experimental data is available so far, and (2) further attenuation of decelerated muons by atmosphere during long flight to the detector.

2. Elevation angle and altitude dependence of incident and penetrating muon flux

2-1. Inconsistencies in previous works on elevation angle dependence

It is well known that the energy spectrum of cosmic ray muon (CRM) depends strongly on elevation angle (θ) and altitude (h). Estimation of incident muon flux and its attenuation passing through object with density length (X) in the range of (h,θ,X) covering the experimental condition is therefore essentially important for the CRM radiography.

There are a variety of preceding works on elevation angle dependence of muon flux $I_\mu(\theta,X)$ passing through standard rocks (density: 2.65 g/cm^3) at the ground level by means of the Monte Carlo simulation, since Nagamine et al. have proposed a new imaging method of volcanos by using near-horizontal CRM [1]. They have a common characteristic aspect that θ-dependence of $I_\mu(\theta,X)$ reverses within 1.3×10^5 g/cm^2 (500m in rock thickness); above the reverse thickness, $I_\mu(\theta,X)$ remains larger at smaller θ near horizontally than that in the greater θ, contrarily to the incident muon flux.

On the other hand, these works often showed inconsistencies with each other. For example, even in the works reported by the same authors in the same year (2015) [6,7], attenuation of the penetrating muon flux against the rock thickness differed significantly up to 5 times in magnitude at $X>2\times10^5$ g/cm^2. Another work [8] done by the different author using the same algorithm, shows intermediate attenuation between them. Two reasons can be considered as the cause of such inconsistency; one is the differences in calculation methods, and the other is the differences in energy spectrum of incident CRM.

The penetrating muon flux in most cases including references herein [6-8] was calculated by integrating the incident energy differential muon flux $N_\mu(E,\theta)$ over the range between the minimum energy $E_c(X)$

necessary for a muon to penetrate a given density length X of rock and infinity.

$$I_\mu(\theta, X) = \int_{E_c(X)}^{\infty} N_\mu(E, \theta) dE. \quad (1)$$

The table of $E_c(X)$ for monochromatic energy muons calculated by Monte Carlo method is given by Groom et al. as the Continuous Slowing Down Approximation (CSDA) Range between 10MeV and 100 TeV [9]. In order to evaluate the accuracy of the approach by Eq. (1), we first reproduced Groom's table using PHITS code [9][10] and confirmed that the results agreed within statistical error.

Figure 1 shows the integrated muon flux $I_\mu(\theta, X)$ by Eq. (1) using $E_c(X)$ calculated in this study by PHITS at θ= 5 and 15 (yellow and green lines), comparing with thos$_{e\ c}$alculated by PHITS without such approximation (red and blue lines). In all calculations, $N_\mu(E, \theta)$ was determined from the cosmic-ray source function based on the PHITS-based Analytical Radiation Model in the Atmosphere (PARMA) [11] implemented in PHITS.

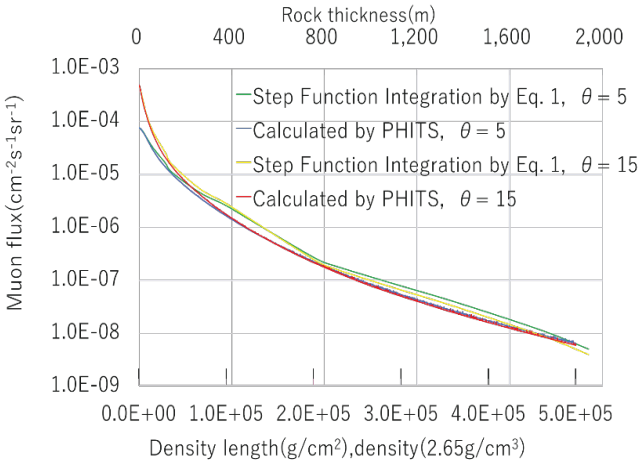

Fig. 1 Estimated $I_\mu(\theta, X)$ at θ=5 and 15 deg. Solid lines with red and blue are PHITS simulation. Those with yellow and green are calculated by using Eq. (1).

At the same incident angle, they are in close agreement down to 5×10^4 g/cm^2. But the difference between the integrated fluxes becomes larger above 5×10^4 g/cm^2. Curves of $I_\mu(\theta, X)$calculated by Eq. (1) crosses at around 2×10^5 g/cm^2, while those calculated by PHITS approaches equivalent. The results show that the integration approach by Eq. (1) is partially responsible to the crossing of curves of $I_\mu(5, X)$ and $I_\mu(15, X)$ that are commonly seen in preceding works.

Typical examples of penetrating muon flux for monochromatic energy muons are shown in Fig. 2. The CSDA Range in ref. [9] and $E_c(X)$ in this work were determined by the density length in which the penetrating muon flux becomes half of the incident flux. Integration approach by using Eq. (1) is a step function approximation in other words. It is clearly seen in the figure that the step function approximation underestimates the low-energy component and overestimates the high-energy component. Such a roughness of the integration approach in the vicinity of E_c causes the inconsistency shown in Fig. 1.

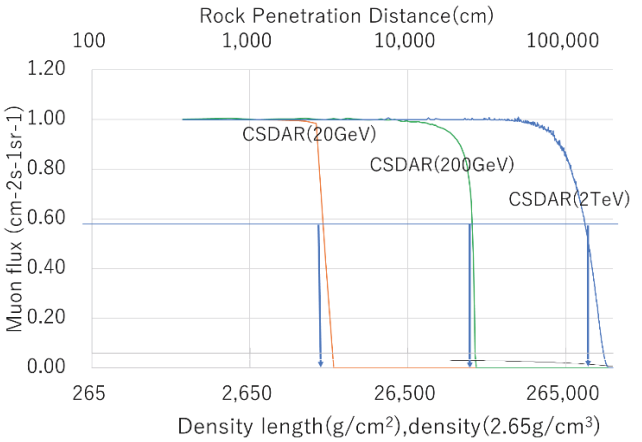

Fig. 2 Typical examples of penetrating muon flux for monochromatic energy muons

Another origin of discrepancies between preceding works are attributed to the energy spectra of incident muon flux adapted in the simulation. In general, measured muon fluxes were used for determining the energy spectrum, but the conditions such as h and θ of the available experimental data are limited. We therefore adopted the PARMA model for the determination, which can instantaneously calculate the cosmic-ray fluxes anytime and anywhere in the atmosphere by specifying date, latitude, longitude, altitude, and elevation angle of the users' interest. It is based on the results of the air shower simulation performed by PHITS, and its accuracy was well verified with various experimental data including ground level muon measurements [12-15].

Figure 3 shows muon energy spectra after various rock transmissions calculated by PHITS with incident CRM given by PARMA (upmost red line). It is clearly seen that the low energy muons below 100GeV attenuate rapidly, but high energy muons above TeV decrease gradually even passing through 1000 m in rock thickness.

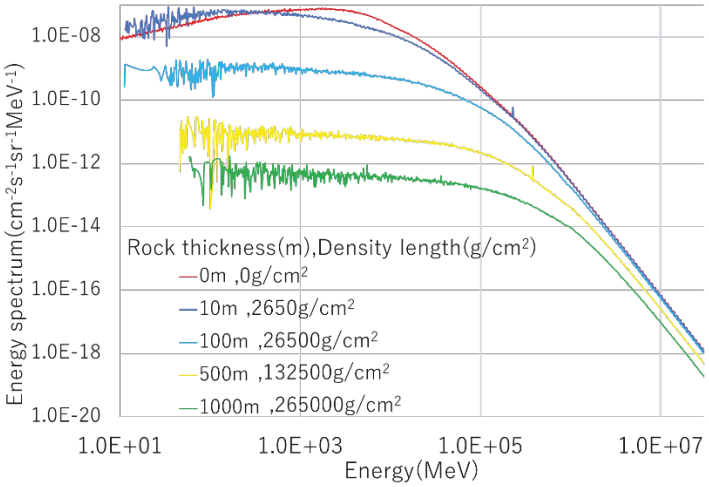

Fig. 3 Energy spectra of the incident and transmitted CRM at ground level.

2-2. Elevation angle dependence at high altitude

From the results discussed above, we strongly recognized the importance of the simulation method as well as estimation of the incident muon energy spectrum up to 100TeV to simulate the transmission experiment on Mt. Fuji. The incident CRM fluxes at altitudes of 0, 1300, and 3776 m and elevation angles from 5 to 20 deg, were provided by PAMRA.

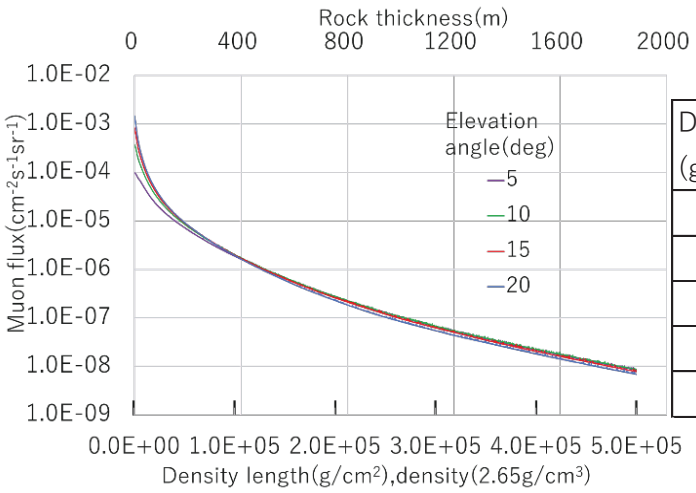

Table1: Summary of penetrating CRM flux: Ratio of 3776m altitude to 0m.

Density length (g/cm^2)	Elevation15	Elevation20
0	1.71	1.81
20000	1.08	1.08
50000	1.11	1.11
200000	1.21	1.21
500000	1.32	1.32

Fig. 4 Muon flux after rock penetration, elevation angle dependence at 3776m altitude.

The muon fluxes $I_\mu(h,\theta,X)$ after transmission through standard rocks at 3776 m is shown in Fig. 4. Elevation angle dependence of $I_\mu(h,\theta,X)$ reverses in rock thickness 5×10^4 g/cm^2 $< X <$ 1×10^5 g/cm^2 as was seen in the preceding works, but not so remarkable in this result.

Resultant muon fluxes are summarized in Table 1. At 3776 m altitude, the incident CRM flux is 1.8 times larger than at 0 m, while it was almost same level up to 1300 m altitude. Although the difference decreases up to a rock thickness of 2×10^4 g/cm^2, the difference opens up again after further penetration over a longer distance, resulting in a 1.3 times difference above 2×10^5 g/cm^2.

3. Influence of the atmosphere on decelerated muons after passing through huge mountain

We examined further attenuation of decelerated muons by atmosphere after passing through long distance in rocks. Total distance is fixed to 7000 m as is in the experimental condition at Gotemba Tarobo. Decelerated muons after transmitting 377 m in standard rocks (1.0×10^4 g/cm^2) decay to 96 % by lifetime during the flight of 6623m even in vacuum and down to 91% in air, hence the further attenuation by air is 5%. In case of longer penetration length, 1132 m in rocks decay (3.0×10^5 g/cm^2) by lifetime is 3% in flight of 5868 m in vacuum and is 4% in air, resulting contribution by air is 1%.

4. Summary

Elevation angle dependence at high altitude up to 3776m of the incident CRM and its attenuation passing through standard rock up to 5.0×10^5 g/cm^2 (1887m in rock thickness) has been investigated for the first time by using the Monte Carlo simulation code PHITS and PARMA, supposing application of the CRM radiography for imaging subsurface structure of Mt. Fuji. It was revealed that the intensity of the incident CRM at 3776 m in altitude is 1.8 times larger than that at 0 m in elevation angle from 15 to 20 deg. After transmission through standard rock, it was found that the ratio once decreases but increases again up to 1.3 times after transmission through 5.0×10^5 g/cm^2.

For the purpose to clarify the inconsistencies among the preceding works, the approach to integrate incident muon flux over energy from $E_c(X)$ to infinite was also investigated in detail. We concluded that the roughness of the step-function approach in the vicinity of E_c is partially responsible to such inconsistency besides the difference of energy spectra of incident CRM.

There remain further issues special in muon imaging of Mt. Fuji on (1) influence of asymmetric multiple scattering between muons travelling longer distance inside of the mountain and those from surface side, and (2) deflection by the earth field of decelerated muons travelling long distance up to 7 km to the detector. Simulation study associated with these issues is in progress.

Acknowledgements

One of the authors, SN, would like to thank the members of the Research Group for Radiation Transport Analysis of JAEA for their enlightening guidance and instruction for application of PHITS during the summer training course.

References

[1] K. Nagamine, M. Iwasaki, K. Shimomura, and K. Ishida, Method of probing inner-structure of geophysical substance with the horizontal cosmic-ray muons and possible application to volcanic eruption prediction, Nucl. Instr. Meth. Phys. Res., A356, 585-595, 1995.

[2] K. Nagamine, Introductory Muon Science, Cambridge University Press, 36-38, 170-184, 2003.

[3] H.K.M. Tanaka and K. Nagamine, Probing the Internal structure of a Volcano with Cosmic-ray Muons, Volcanoes, 48, 345-366, 2003 (in Japanese with English abstract).

[4] H.K.M. Tanaka et al., Radiographic measurements of the internal structure of Mt. West Iwate with near-horizontal cosmic-ray muons and future developments, Nucl. Instr. Method. Phys. 555, 164-172, 2005.

[5] R. Tsuchi, Groundwater and Springs of Fuji Volcano, Japan, in Volcano edited by S. Aramaki, T. Fujii, S. Nakata, N. Miyaji, Yamanashi Institute of Environmental Sciences and Volcanology Society of Japan, 375-387, 2007(in Japanese with English abstract).

[6] T. Kusagaya, H.K.M. Tanaka, Muographic imaging with a multi-layered telescope and its application to the study of the subsurface structure of a volcano, Geosci. Instrum. Method. Data Syst. Discuss., 501-510, 2015 and Proceedings of the Japan Academy 91, 501-510, 2015.

[7] T. Kusagaya and H.K.M. Tanaka, Development of the very long-range cosmic-ray muon radiographic imaging technique to explore the internal structure of an erupting volcano, Shinmoe-dake, Japan, Geosic. Instrum. Method. Data Syst., 4, 215-226, 2015.

[8] N. Lesparre, et al., Density muon radiography of La Soufrière of Guadeloupe volcano: comparison with geological, electrical resistivity and gravity data, Geophys. J. Int. 190, 1008–1019, 2012.

[9] D. E. Groom, Muon stopping power and range tables 10 MeV–100 TeV, Atomic Data and Nuclear Data Tables 78, 183–356, 2001.

[10] T. Sato, et al., Recent improvements of the Particle and Heavy Ion Transport Code System – PHITS version 3.33, J. Nucl. Sci. Technol., 61(1), 2024, pp.127-135.

[11] T. Sato, Analytical Model for Estimating the Zenith Angle Dependence of Terrestrial Cosmic Ray Fluxes, PloS ONE 11(8), e0160390, 2016, and Sato T, Analytical Model for Estimating Terrestrial Cosmic Ray Fluxes Nearly Anytime and Anywhere in the World, Extension of PARMA/EXPACS, PloS ONE 10(12), e0144679, 2015.

[12] H. Jokisch, et al., Cosmic-Ray Muon Spectrum up to 1-TeV at 75-Degrees Zenith Angle, Phys. Rev. D 19, 1368–1372, 1979.

[13] OC. Allkofer, et al., Cosmic-Ray Muon Spectra at Sea-Level up to 10 TeV, Nucl. Phys. B 259, 1–18, 1985.

[14] BC. Rastin, An Accurate Measurement of the Sea-Level Muon Spectrum within the Range 4 to 3000 GeV/c, J. Phys. G Nucl. Partic. 10, 1609–1628, 1984.

[15] M. Aglietta, et al., Muon “depth-intensity” relation measured by the LVD underground experiment and cosmic-ray muon spectrum at sea level, Phys. Rev. D 58, 092005, 1998.

14. Nuclear Heating and Damage Data in JENDL-5 Neutron ACE Library

Chikara KONNO*
Nuclear Science and Engineering Center, Japan Atomic Energy Agency
2-4 Shirakata, Tokai-mura, Naka-gun, Ibaraki-ken 319-1195, Japan
*Email: konno.chikara@jaea.go.jp

The JENDL-5 neutron ACE library was mainly produced with the FRENDY code, while the data on nuclear heating and damage (heating number, damage production energy) were done with the NJOY2016.65 code modified for JENDL-5. This paper reviews the data on nuclear heating and damage in the JENDL-5 neutron ACE library, which improves issues on nuclear heating and damage data found in those of the JENDL-4.0 and JENDL-4.0/HE neutron ACE libraries, for PHITS users.

1. Introduction

The official ACE libraries of JENDL-5 [1] were released in December, 2022. The neutron ACE library of JENDL-5 was produced mainly with the FRENDY2 [2] code except for data on nuclear heating and damage, which were produced with the NJOY2016.65 [3] code modified for JENDL-5 [4], and it was released as one of ACE libraries in ACE-J50 [4] in 2022. It has nuclear heating and damage data which are often important in PHITS [5] calculations. Here the nuclear heating and damage data in it are introduced in detail for PHITS users.

2. Nuclear Heating and Damage Data in ACE File

Neutron ACE files have heating numbers and damage production energy cross sections, which are related to KERMA (Kinetic Energy Released in MAterials) factors and DPA (Displacement Per Atom) cross section as below, as the nuclear heating and damage data [6].

$$Heating\ number = (KERMA\ factor) / \sigma_{tot}\ , \quad (1)$$

σ_{tot} : total cross section.

$$DPA\ cross\ section = \frac{0.8 \times T_d}{2 \times E_d}\ , \quad (2)$$

T_d : damage production energy cross section,

E_d : atomic displacement energy.

The KERMA factor and damage production energy cross section are produced with the HEATR module of NJOY. The KERMA factor is calculated with the following two methods [3].

1) Energy balance method

- This method calculates KERMA factors from differences of energies before and after reactions.

- If energies before and after reactions are not conserved, the calculated KERMA factor can be negative or too large.
- Note that the original NJOY stores only heating numbers from KERMA factors with this method to ACE files. Thus even official ENDF/B-VIII.0 and JEFF-3.3 neutron ACE libraries from LANL [7] and OECD/NEA [8], respectively, often include negative or too large heating numbers as shown in Figs. 1 and 2. In these figures the heating number of the ENDF/B-VIII.0 neutron ACE library is too large because it includes secondary gamma energy, and most of the data in that of the JEFF-3.3 neutron ACE library are negative because all secondary gamma data are stored in MT=3 of the ENDF-6 format [9], not in each MT, which breaks energy balance in NJOY. On the contrary the heating number of the JENDL-5 neutron ACE library calculated with the below kinematics method is not negative or too large.

2) Kinematics method

- This method calculates upper limit KERMA factors from energies provided to residual nuclei, which is estimated with the kinematics, and the calculated KERMA factor is not negative or too large.
- The upper limit KERMA factor is almost the same as the KERMA factor with the energy balance method where energies before and after reactions are conserved.

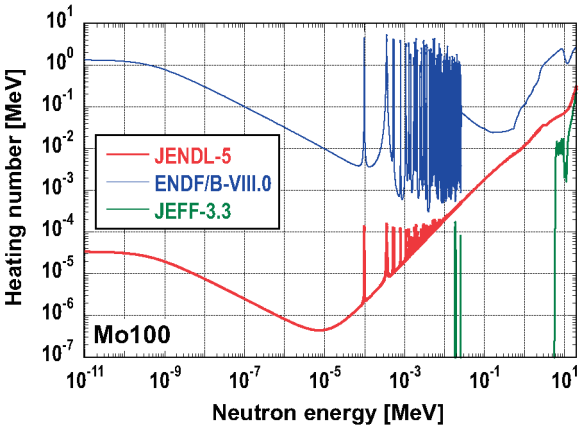

Fig. 1 Heating number of ^{100}Mo (log scale).

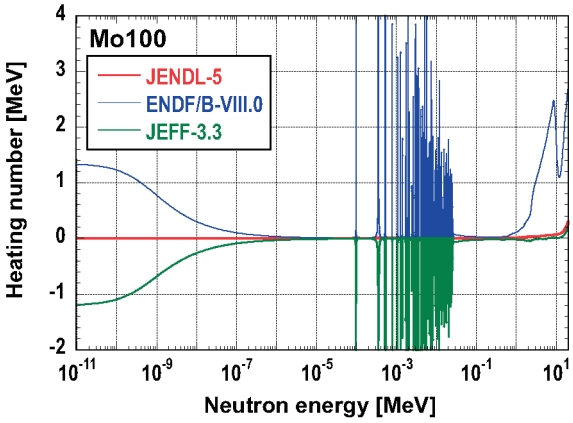

Fig. 2 Heating number of ^{100}Mo (linear scale).

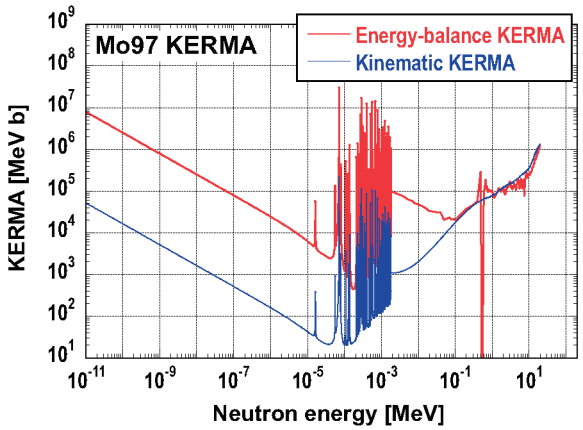

Fig. 3 KERMA factor of ^{97}Mo in JENDL-4.0.

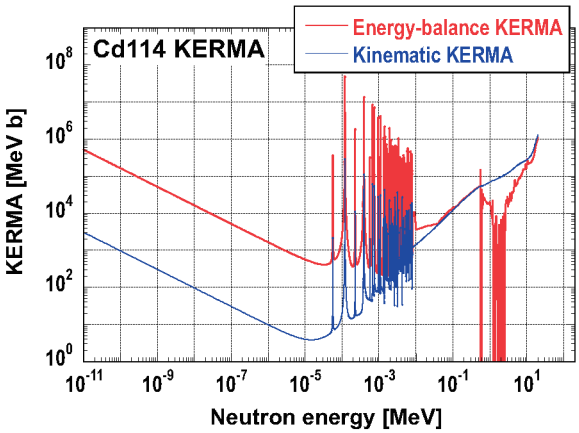

Fig. 4 KERMA factor of ^{114}Cd in JENDL-4.0.

3. Review of JENDL-4.0 Neutron ACE Library

The energies before and after reactions are not conserved in a lot of neutron files of JENDL-4.0. As a result, the KERMA factors with the energy-balance method were often negative or too large as shown in Figs. 3 and 4. Thus heating numbers from KERMA factors with the kinematics method were stored to the final JENDL-4.0 neutron ACE library [5] by using NJOY99 [10] modified for JENDL-4.0.

A lot of nuclei in JENDL-4.0 have unresolved resonance data as shown in Fig. 5. The probability table (p-table) is produced with NJOY for self-shielding correction in the unresolved resonance region. Figure 6 shows the p-table of total cross section at 100 keV in ^{93}Nb of JENDL-4.0.

The p-table is also produced for heating number in NJOY. It was found in 2013 that a lot of the ACE files in the JENDL-4.0 neutron ACE library had negative or too large p-tables of heating number as shown in Fig. 7 and the negative p-tables of heating number produced "NaN" (Not a number) for heating values in PHITS heating calculations. Then not only p-tables of heating number but also those of total, elastic and capture cross sections were removed from the ACE files with negative p-tables of heating number in the JENDL-4.0 neutron ACE library in 2014 [11], which is not good from the view of self-shielding correction. In 2019 we pointed out that the inadequate modification of NJOY99 for JENDL-4.0

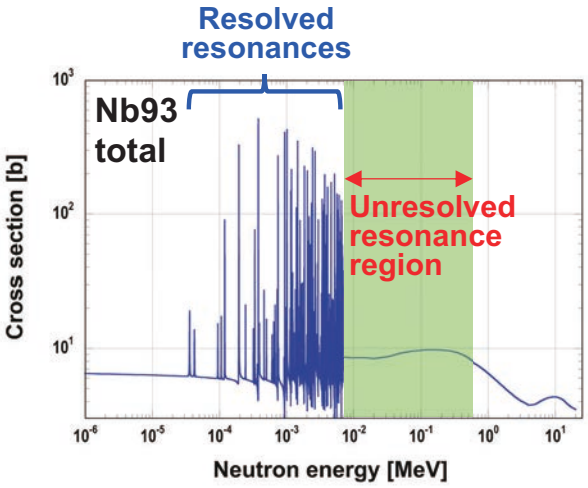

Fig. 5 Total cross section in ^{93}Nb of JENDL-4.0.

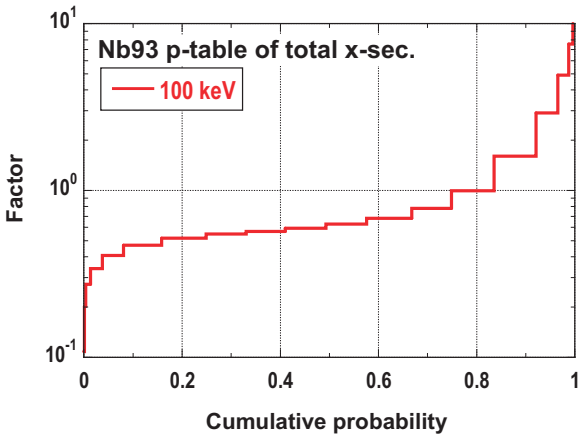

Fig. 6 P-table of total cross section at 100 keV in ^{93}Nb of JENDL-4.0.

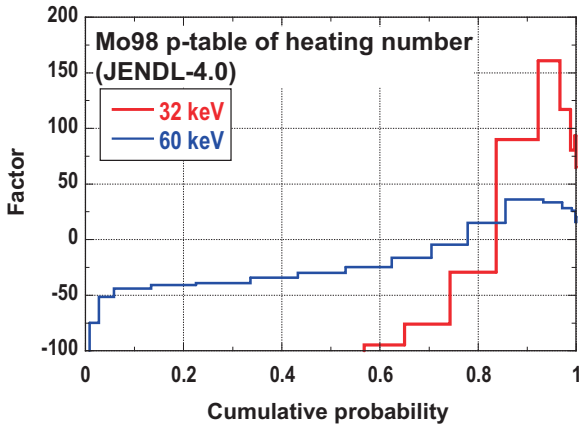

Fig. 7 P-table of heating number at 32 and 60 keV in ^{98}Mo of JENDL-4.0.

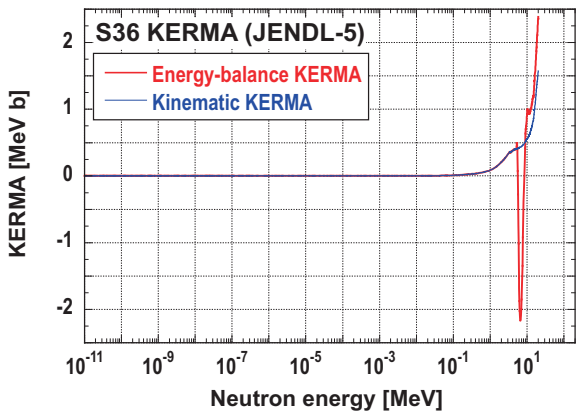

Fig. 8 KERMA factor of ^{36}S in JENDL-5.

caused the negative p-table of heating number [12, 13], but the JENDL-4.0 neutron ACE library has not been revised.

4. Status of JENDL-5 Neutron ACE Library

The energies before and after reactions are also not conserved in a lot of neutron files of JENDL-5. As a result, the KERMA factors with the energy-balance method are often negative or too large as shown in Figs. 8 and 9. Thus heating numbers from KERMA factors with the kinematic method were stored to all the ACE files of the JENDL-5 neutron ACE library by using adequately modified NJOY2016.65 for JENDL-5 [4], which produced no negative p-tables of heating number as shown in Fig. 10.

It was pointed out that damage production energy cross sections in neutron ACE files of FENDL-3.1d [14] from JENDL-4.0/HE [15] dropped down above 20 MeV as shown in Fig. 11 [16, 17] because of no energy distribution data of several residual nuclei above 20 MeV in JENDL-4.0/HE. JENDL-5, which inherits most of the data above 20 MeV in JENDL-4.0/HE, newly adds energy distribution data of all residual nuclei above 20 MeV in order to solve this issue [1] (see Fig. 11).

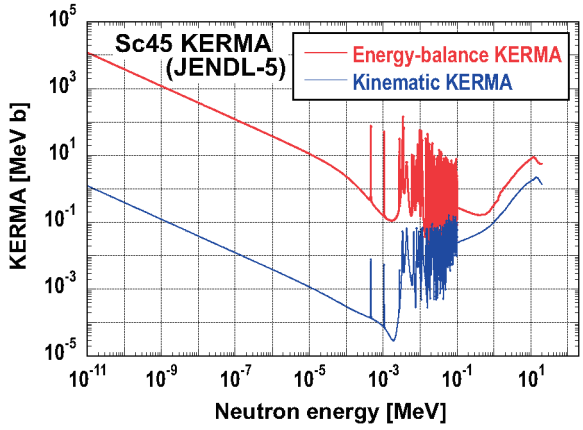

Fig. 9 KERMA factor of ^{45}Sc in JENDL-5.

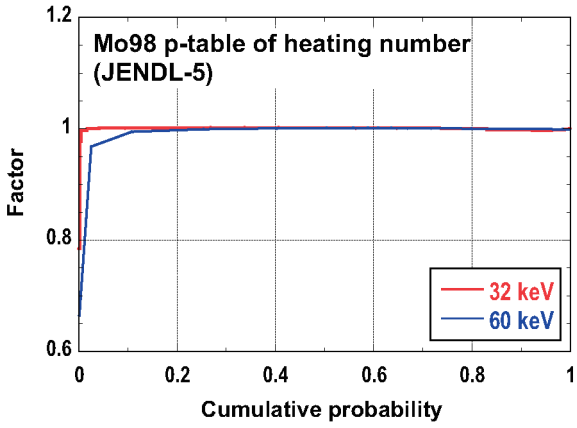

Fig. 10 P-table of heating number at 32 and 60 keV in ^{98}Mo of JENDL-5.

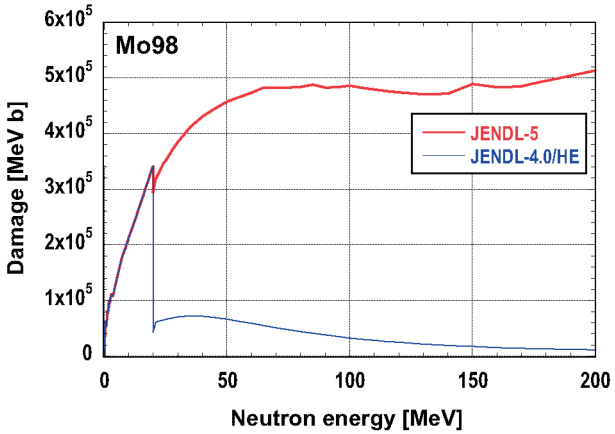

Fig. 11 Damage production energy cross section of ^{98}Mo.

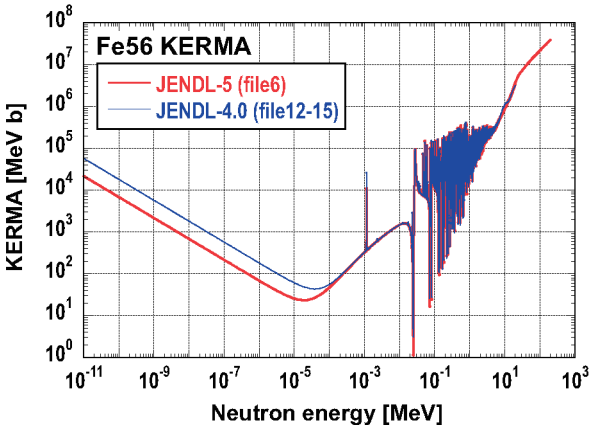

Fig. 12 KERMA factor of ^{56}Fe.

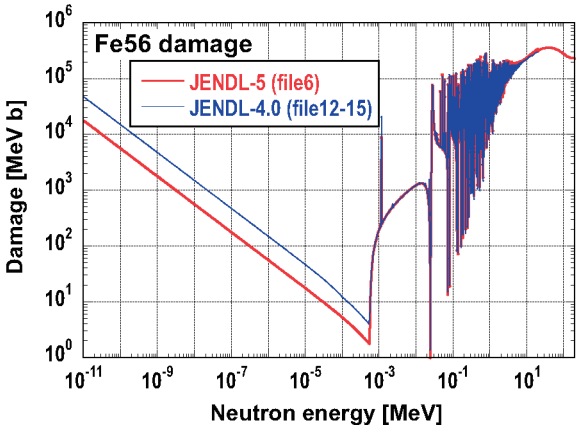

Fig. 13 Damage production energy cross section of ^{56}Fe.

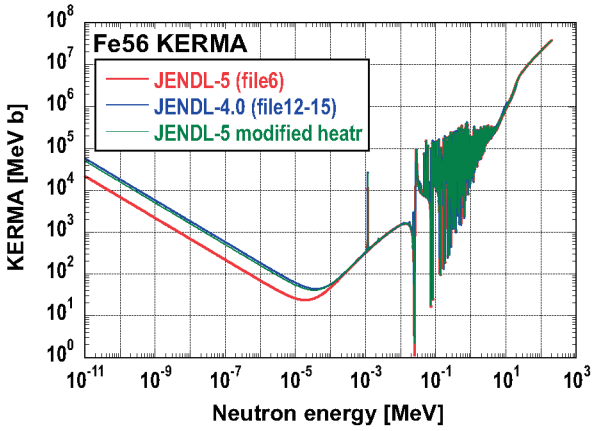

Fig. 14 KERMA factor of ^{56}Fe.

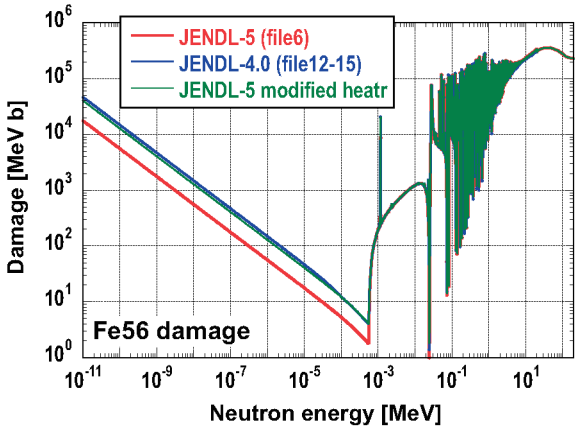

Fig. 15 Damage production energy cross section of ^{56}Fe.

5. NJOY bug

We found in 2016 that KERMA factors and damage production energy cross sections of a lot of nuclei with gamma data of the capture reaction in Files 12-15 [9] were different from those with gamma data of the capture reaction in File 6 [9] as shown in Figs. 12 and 13 [18]. Wu et al. reported in 2021 that the HEATR module of NJOY had a fatal bug that KERMA factors and damage production energy cross sections are calculated without multiplying secondary gamma yield if secondary gamma data were stored in File 6 [19]. The bug in HEATR module of NJOY was fixed for JENDL-5, which produced adequate KERMA factors and damage production energy cross sections of a lot of nuclei with gamma data of the capture reaction in File 6 as shown in Figs. 14 and 15.

6. Conclusion

Neutron ACE files have heating numbers and damage production energy cross sections, not KERMA factors nor DPA cross sections. The nuclear heating and damage data in the JENDL-5 neutron ACE library were explained in this paper. Heating numbers from KERMA factors with the kinematics method were stored to all the neutron ACE files of the JENDL-5 neutron ACE library, which was produced with the bug fixed NJOY2016 for JENDL-5 and had no negative p-tables of heating number in the JENDL-

4.0 neutron ACE library. I hope that the JENDL-5 neutron ACE library is used worldwide.

References

1) Iwamoto, O., Iwamoto, N., Kunieda, S., et al., Japanese Evaluated Nuclear Data Library version 5 : JENDL-5, J. Nucl. Sci. Technol. vol.60, 2023, pp.1-60.
2) Tada, K., Yamamoto, A., Kunieda, S., et al., Development of nuclear data processing code FRENDY version 2, J. Nucl. Sci. Technol., vol.61, 2024, pp.830-839. https://doi.org/10.1080/00223131.2023.2278600
3) MacFarlane, R.E., Muir, D.W., Boicourt, R.M., Kahler, A.C., Conlin, J.L., The NJOY Nuclear Data Processing System, Version 2016, LA-UR-17-20093, 2016.
4) https://rpg.jaea.go.jp/main/en/ACE-J50/ (accessed 2024-1-13).
5) Sato, T., et al., Recent improvements of the Particle and Heavy Ion Transport code System - PHITS version 3.33, J. Nucl. Sci. Technol., vol.61, 2024, pp.127-135. https://doi.org/10.1080/00223131.2023.2275736
6) Conlin, J.R (Ed.), A Compact ENDF (ACE) Format Specification, LA-UR-19-29015, 2019, 55p.
7) https://nucleardata.lanl.gov/ace/lib80x/ (accessed 2024-1-13).
8) https://www.oecd-nea.org/dbdata/jeff/jeff33/index.html (accessed 2024-1-13).
9) Trkov A., Brown D.A. (Ed.), ENDF-6 Formats Manual, BNL-203218-2018-INRE Rev.215, 2018, 400p.
10) https://t2.lanl.gov/nis/codes/njoy99/ (accessed 2024-1-13).
11) https://phits.jaea.go.jp/oldNews.html (accessed 2024-1-13).
12) Konno, C., Kwon, S., P-table problem of heating number in FENDL-3.1d ACE file, Atomic Energy Society Japan 2018 Annual Meeting, 3E04 (in Japanese).
13) Konno, C., Kwon, S., P-table problem of heating number in FENDL-3.1d ACE file (2), Atomic Energy Society Japan 2018 Fall Meeting, 2M04 (in Japanese).
14) https://www-nds.iaea.org/fendl31d/ (accessed 2024-1-13).
15) Kunieda, S., Iwamoto, O., Iwamoto, N., et al., Overview of JENDL-4.0/HE and benchmark calculation, JAEA-Conf 2016-004, 2016, pp.41–46.
16) Kwon, S., Konno, C., Ohta. M., Kasugai, A., Problems of DPA cross-sections above 20 MeV in FENDL-3.1d found in A-FNS neutronics analysis, J. Nucl. Sci. Technol. vol.57, 2020, pp.344-351.
17) Konno, C., New JENDL-4.0/HE neutron and proton ACE files, J. Nucl. Sci. Technol., vol.61, 2024, pp.121-126. https://doi.org/10.1080/00223131.2023.2237970
18) Konno, C., Sato, S., Ohta, M., Kwon, S., Ochiai, K., New remarks on KERMA factors and DPA cross section data in ACE files, Fusion Eng. Design vol.109-111, 2016, pp.1649-1652.
19) Wen, Y., Zu, T., Cao, L., Wu, H., Remarks and improvements on neutron KERMA factors and radiation damage cross sections calculated by NECP-Atlas and NJOY21 using different evaluated nuclear data libraries, Annals of Nuclear Energy vol.164, 2021, p.108624.

15.Simulation of aluminum activation experiment at CERN/CHARM

Tsuyoshi KAJIMOTO[†1], Noriaki NAKAO[2], Toshiya SANAMI[3], Kenichi TANAKA[4], Satoru ENDO[1], and Robert FROESCHL[5]

[1]Hiroshima University, 1-4-1 Kagamiyama, Higashi-Hiroshima, 739-8527, Japan
[2]Shimizu Corporation, 3-4-17 Etchujima, Koto-ku, Tokyo, 135-8530, Japan
[3]High Energy Accelerator Research Organization, Oho, Tsukuba, 305-0801, Japan
[4]Kyoto Pharmaceutical University, 5 Nakauchi-cho, Misasagi, Yamashina-ku, Kyoto, 607-8414, Japan
[5]The European Organization for Nuclear Research, 1211 Geneva 23, Switzerland
[†]Email: kajimoto@hiroshima-u.ac.jp

Abstract

The experiment at CERN/CHARM was simulated for the benchmark of particle transport codes used in the radiation shielding design of high-energy accelerators. The neutron streaming was observed by ^{24}Na production rate in aluminum samples defined at various positions from upstream to downstream of the corridor. These neutrons originated from 24 GeV/c proton beam hitting a copper target. Calculated values by two particle transport codes were compared with each other. Furthermore, the measurement of the other nuclides was investigated, and the production rate induced by proton and $\pi^{\pm}$ was checked.

1 Introduction

Neutrons induced by the reaction between beam particle and a target in high-energy accelerators have higher energies above MeV. Since these neutrons have strong penetration ability and biological effect stronger than that of photons, the neutron leakage from the facility is suppressed by installing shields and constructing the corridor with many corners. To suppress the installation of excess shields, the design is needed to be based on experimental data. However, the data on attenuation in the shield and streaming in the corridor has been significantly less reported for accelerators with beam energy above 10 GeV.

Experiments at CHARM (CERN High energy AcceleRator Mixed field facility) [1] were started to measure data on radiation shielding design of high-energy accelerators. CHARM has supplied mixed radiation fields formed by 24 GeV/c proton bombarded with a target. Nakao et al. measured the neutron attenuation in shields [2, 3] and the neutron streaming in the corridor [4] by setting activation samples at various positions. In 2022, ^{24}Na produced in aluminum samples set in the target room and the corridor was only measured to observe neutron streaming. These values will be compared to the calculation by particle transport codes.

The experiment in 2022 was simulated for the benchmark of neutron streaming. In this paper, calculated ^{24}Na production rate in aluminum samples was compared between two codes, PHITS [5] and GEANT4 [6]. The contribution to production rates by proton and $\pi^{\pm}$ was additionally checked due to setting aluminum samples near the target of CHARM. The measurement of ^{7}Be,

^{22}Na, and ^{27}Mg production rates was also investigated by the simulation. The measurement of additional nuclides may inform the shape change of neutron energy distribution in neutron streaming from the shape difference of production cross sections to the incident particle energy.

2 Simulation

The experiment at CHARM in 2022 was introduced for the simulation. Twelve aluminum samples were located in the target room and corridor of CHARM, and exposed to a radiation field formed by 24 GeV/c proton beam bombarding to a 50 cm length copper target. The aluminum sample had two cylindrical shapes with different sizes. Smaller sample was 0.4 cm length and 4.0 cm diameter and located at positions of inside and near entrance of the target room. Larger one was 1.0 cm length and 8.0 cm diameter and set in the corridor. After the irradiation, photons emitted from the sample were measured using a high-purity germanium (HPGe) detector.

The experiment was simulated by two calculations. The geometry of the experimental facility was constructed by each of PHITS and GEANT4. Score regions instead of the aluminum samples were defined in the geometry. The data when a particle enters the region was scored event by event. The production rates of ^{7}Be, ^{22}Na, ^{24}Na, and ^{27}Mg were derived by connective calculation as sources a particle from the event by event data.

2.1 Calculation using code

Two particle transport codes, PHITS3.30 and GEANT4.11.1 were used for the calculation. The physics model in PHITS calculation was set to default, for example of neutron inelastic processes, JAM [7] coupled with GEM [8] above 3 GeV, INCL4.6 [9] and GEM between 20 MeV and 3 GeV, and JENDL-4 [10] less than 20 MeV were used. Two calculations were performed by changing the physics list [11] for GEANT4 calculation. The physics lists were FTFP_BERT_HP and QGSP_BIC_HP in which used models have been described in Ref. [12]. The neutron cut off energy was set to be 0.1 MeV.

Figure 1 (a) shows the cross sectional view of constructed geometry. The geometry has wide region of 21 m $\times$ 31 m $\times$ 16 m. Instead of aluminum samples, spherical score regions with diameter of 10 cm were located at the experiment positions and additional positions. The 50 cm length copper target was bombarded with 24 GeV/c protons. When a particle entered the score region, the values of particle type, position, direction, energy, and weight were scored event by event.

2.2 Connective calculation

Production rates of ^{7}Be, ^{22}Na, ^{24}Na, and ^{27}Mg were derived by the connective calculation with a geometry consisting of a sphere filled in air and cylindrical aluminum sample as shown in Fig. 1 (b). The particle was generated on the sphere surface following scored data. The attenuation of particle was simulated. The production probability was calculated in the attenuation of the cylindrical aluminum.

The same values of production cross sections (XSs) for aluminum were used in the connective calculations. The used XSs are shown in Fig. 2. The methods to acquire production XSs are summarized in Table 1. Production XSs were also calculated using PHITS and GEANT4 to check the validity and the use of calculation values.

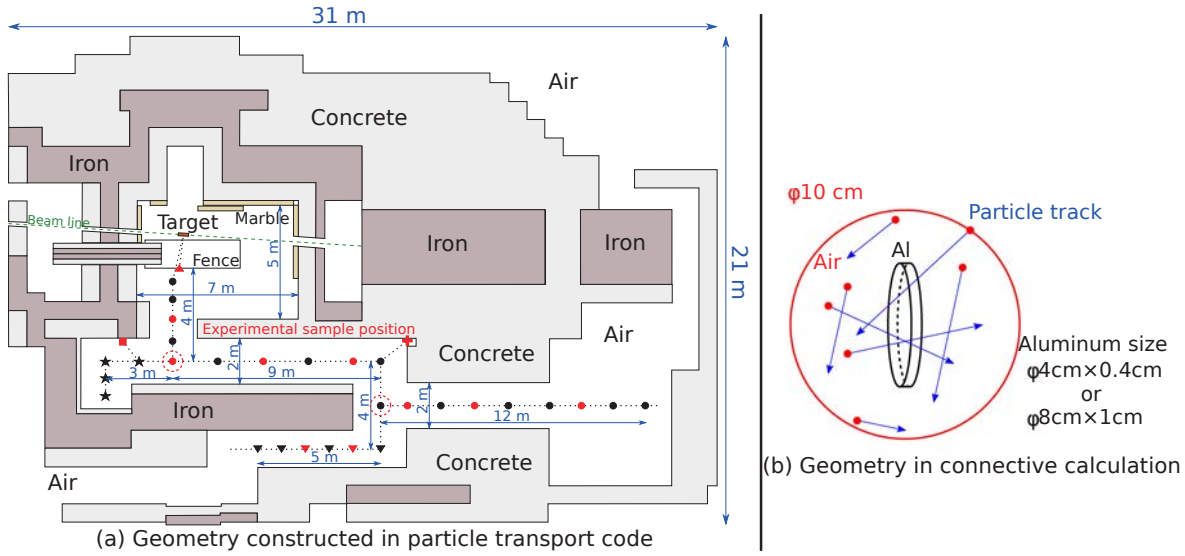

Figure 1: (a) Geometry constructed in particle transport codes. Markers show positions of the score region. (b) Geometry in the connective calculation.

Table 1: Acquisition of production XSs for aluminum. XSs were obtained by smoothing in case of many experimental values, and by eye guide in case of several measured values. In case of no reports, eye guide or calculated values was used by comparing calculations by particle transport codes.

	^{7}Be	^{22}Na	^{24}Na	^{27}Mg
Neutron	Eye guide	Smooth	Ref. [14]	Smooth
Proton	Smooth	Ref. [15]	Ref. [15]	Eye guide
π^+	QGSP_INCLXX_HP	QGSP_INCLXX_HP	Ref. [16]	QGSP_INCLXX_HP
π^-	Eye guide	Eye guide	Ref. [16]	QGSP_INCLXX_HP

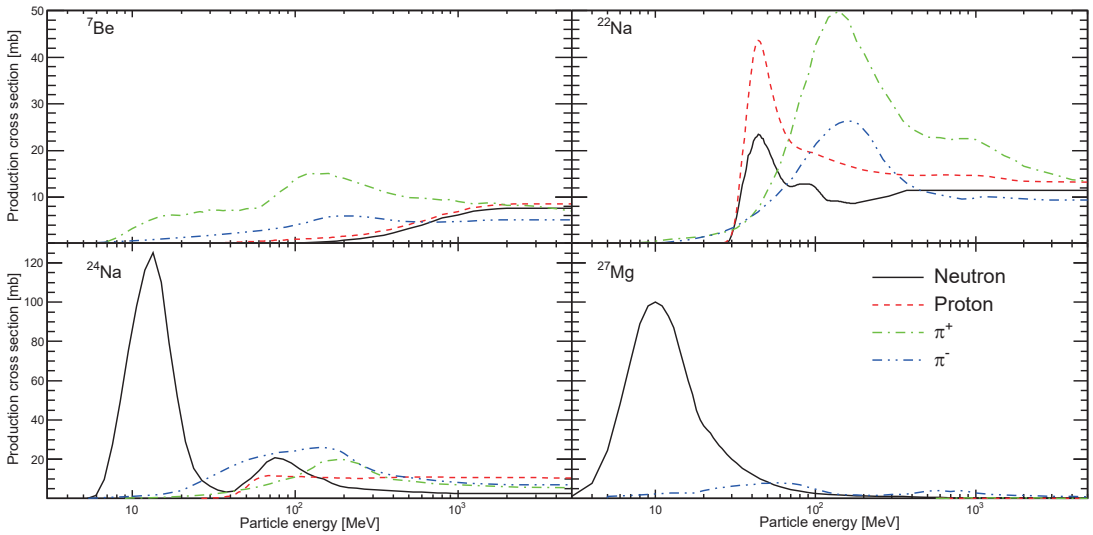

Figure 2: Production cross sections for aluminum. These values were used in connective calculations.

Table 2: Parameters used to estimate valid production rates.

	^{7}Be	^{22}Na	^{24}Na	^{27}Mg
Half-life	53.2 day	2.60 year	15.0 hour	9.46 minute
Energy of γ-ray	0.478 MeV	1.275 MeV	1.369 MeV	0.844 MeV
Emission probability: I_γ	0.1044	0.9994	0.9999	0.718
Cooling time: t_{cool}	5 day	5 day	1 hour	0.75 hour
Measurement time: t_{meas}	1 day	1 day	6 hour	0.25 hour

3 Estimation of valid production rates

Valid ^{7}Be, ^{22}Na, ^{24}Na, and ^{27}Mg production rates for the measurement were derived from a requirement: acquisition of 1000 counts of peak of interest in γ-ray measurement using a HPGe detector. As the experiment, the flow was beam irradiation, cooling, and the measurement using a HPGe detector. The condition in the flow, such as the time, was not optimized, however, the derived rates would give reasonable values.

The production rate R [1/atom/primary] was derived as following

$$R = \frac{C_p}{N_A\, N_B\, \{\sum_i \exp[-\lambda\,(t_i\, +\, t_{cool})\,]\}\, [1\, -\, \exp(-\lambda\, t_{meas})]\, I_\gamma\, \varepsilon_\gamma}, \tag{1}$$

where C_p is the count of full-energy peak by γ-ray of interest in a HPGe detector measurement and set to be 1000, N_A is the number of atoms in aluminum sample, N_B is the proton beam intensity, subscription i is beam pulse number, λ is the decay constant of production nuclide, t_i is the time between the pulse irradiation and proton beam stop, t_{cool} is the cooling time, t_{meas} is the measurement time using the HPGe detector, I_γ is the emission probability of the γ-ray, ε_γ is the full-energy peak efficiency of the γ-ray.

Beam intensity and irradiation time referred to those of earlier experiments [2, 3, 4]. The half-life, γ-ray of interest, emission probability of the γ-ray, cooling time, measurement time are summarized in Table 2. The full-energy peak efficiency was set to be 2-6% for small sample and 1-3% for large one.

4 Results and discussion

Figure 3 shows calculated production rates of ^{7}Be, ^{22}Na, ^{24}Na, and ^{27}Mg by neutron, proton, and $\pi^{\pm}$. Statistical uncertainty by the Monte Carlo calculation is only shown as error bar. Production rates have a tendency to decrease with the increase of cumulative distance. Large rate of ^{22}Na, ^{24}Na and ^{27}Mg excluding ^{7}Be is given by FTFP_BERT_HP than PHITS and QGSP_BIC_HP. The black dash-dot lines indicate valid production rates for the measurement. A validity from ^{24}Na production rate is obtained by being roughly equal to that at farthest position of the experiment. ^{27}Mg production rate could be measured in the target room and at positions of the corridor near the target room. The measurement of ^{7}Be and ^{22}Na production rates is limited to positions near the target.

Figure 4 shows ratio of production rates by neutron to neutron, proton, and $\pi^{\pm}$. ^{27}Mg and ^{24}Na are excellent and good activated nuclides to observe the streaming of only neutron, respectively. For ^{7}Be and ^{22}Na, there are quite a few activations by proton and $\pi^{\pm}$ at positions until 7 m of cumulative distance where particles emitted from the target were directly hit. The contribution by direct π remains at positions between red dotted lines because high-energy $\pi^{\pm}$ penetrated 80 cm thick concrete wall being from the target to the sample position.

It is suggested that the ratio of ^{27}Mg to ^{24}Na production rate is useful to observe neutrons with around 10 MeV and above 40 MeV. The XSs of ^{27}Al(n, x)^{24}Na and ^{27}Al(n, x)^{27}Mg have a resonance peak at neutron energies of 13 and 10 MeV, respectively. On the other hand, the production of ^{24}Na against ^{27}Mg is sensitive to neutrons above 40 MeV. Thus, the change of ratio roughly gives the shape change of neutron energy distributions.

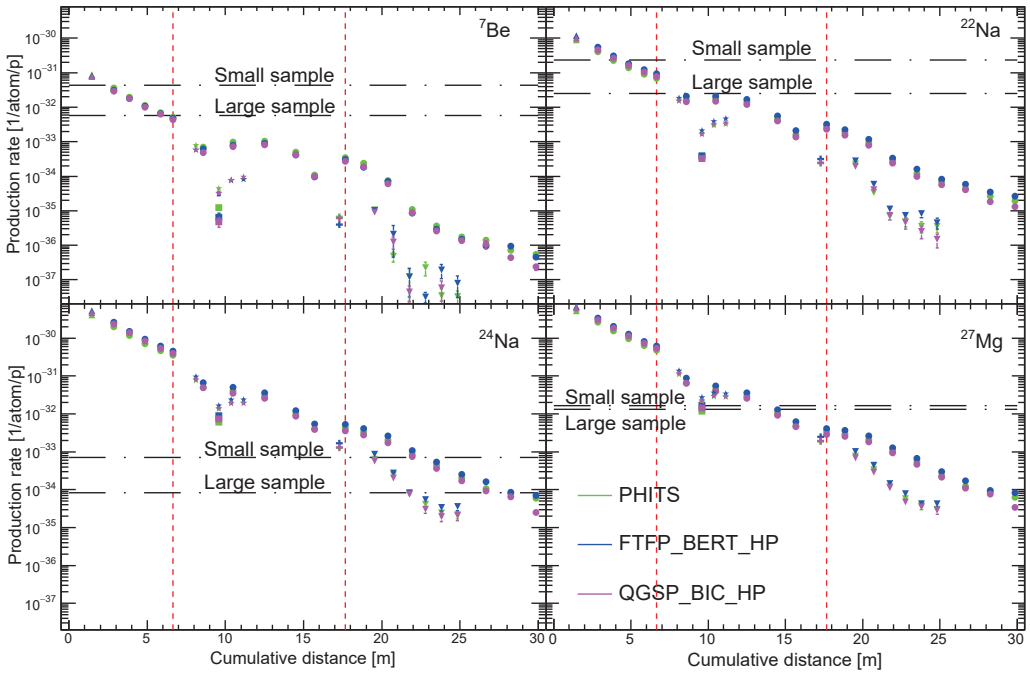

Figure 3: Calculated ^{7}Be, ^{22}Na, ^{24}Na, and ^{27}Mg production rates by neutron, proton, and $\pi^{\pm}$. The horizontal axis shows distance along the black dotted line indicated in Fig. 1. The symbols are changed at the branch in the corridor, and the dashed red lines show the positions surrounded by circular line in Fig. 1. The dash-dot lines indicate measurable rates.

5 Summary

The aluminum activation experiment at CHARM was simulated using PHITS and GEANT4. Aluminum samples were set in the target room and corridor. Production rates of ^{7}Be, ^{22}Na, ^{24}Na, and ^{27}Mg in the aluminum sample by neutron, proton, and $\pi^{\pm}$ were calculated using the same production cross sections between codes.

The production rates were compared between codes. Large rate of ^{22}Na, ^{24}Na, and ^{27}Mg was given by GEANT4 with FTFP_BERT_HP than PHITS and GEANT4 with QGSP_BIC_HP. The proton and $\pi^{\pm}$ contributions were also checked from ratio of the production by neutron to that by neutron, proton and $\pi^{\pm}$. The ^{7}Be and ^{22}Na produced by proton and $\pi^{\pm}$ were quite a few at positions where particles emitted from the target were directly hit.

It is possible to measure ^{27}Mg production rate by shortening cooling and measurement times after the irradiation. The ratio of ^{27}Mg to ^{24}Na production rate is useful to observe neutrons with about 10 MeV and above 40 MeV from the energy dependency of production cross sections by neutron. The change of ratio would roughly indicate the shape change of neutron energy distributions.

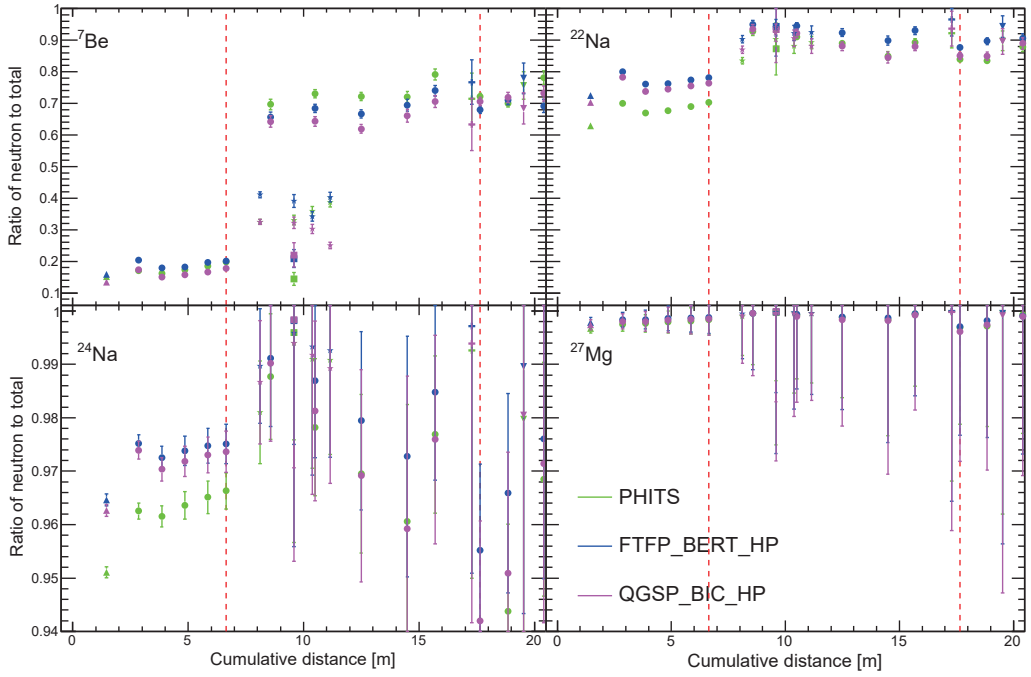

Figure 4: Ratio of production by neutron to that by neutron, proton, and $\pi^{\pm}$. The horizontal axis and the symbols are the same as Fig. 3. The distance is shown until 20 m due to giving large errors over 20 m.

References

[1] Froeschl R., Brugger M., Roesler S., Proceedings of SATIF-12, NEA/NSC/R(2015)3, 14–25.

[2] Nakao N., Sanami T., Kajimoto T., et al., J. Nucl. Sci. Technol., 57(9), 2020, 1022–1034.

[3] Nakao N., Sanami T., Kajimoto T., et al., J. Nucl. Sci. Technol., 61(4), 2024, 429–447.

[4] Nakao N., Kajimoto T., Sanami T., et al., J. Nucl. Sci. Technol., 58(8), 2021, 899–907.

[5] Sato T., Iwamoto Y., Hashimoto S., et al., J. Nucl. Sci. Technol., 55(5-6), 2018, 684–690.

[6] Allison J., Amako K., Agostinelli A., et al., Nucl. Instrum. Meth. A, 835, 2016, 186–225.

[7] Nara Y., Otuka H., Ohnishi A., et al., Phys. Rev. C, 61, 2000, 024901.

[8] Furihata S., Nucl. Instrum. Meth. B, 171(3), 2000, 251–258.

[9] Boudard A., Cugnon J., David J.C., et al., Phys. Rev. C, 87(1), 2013, 014606.

[10] Shibata K., Iwamoto O., Nakagawa T., et al., J. Nucl. Sci. Technol., 48, 2011, 1–30.

[11] Allison J., Amako K., Apostolakis J., et al., IEEE Transactions on Nuclear Science, 53(1), 2006, 270–278.

[12] Geant4 collaboration, Physics Reference Manual, `https://geant4-userdoc.web.cern.ch/UsersGuides/PhysicsReferenceManual/fo/PhysicsReferenceManual.pdf` (Accessed 16 Oct. 2023).

[13] Otuka N., Dupont E., Semkova V., et al., Nucl. Data Sheets, 120, 2014, 272–276.

[14] Maekawa F., Von Möllendorff U., Wilson P.P.H., et al., Production of a dosimetry cross section set up to 50 MeV, Proceedings of 10th International Symposium on Reactor Dosimetry, 2001, 417.

[15] Hermanne A., Ignatyuk A.V., Capote R., et al., Nucl. Data Sheets, 148, 2018, 338–382.

[16] Dropesky B.J., Butler G.W., Giesler G.C., et al., Rhys. Rev. C, 32(4), 1985, 1305–1311.

16. Test of ^{107}Pd transmutation with macroscopic quantities

Yasuto MIYAKE[1*] and Hiroki OKUNO[1]
[1]Nishina Center for Accelerator-Based Science, RIKEN
2-1 Hirosawa, Wako, Saitama 351-0198, Japan
[*]Email: yasuto.miyake@riken.jp

Palladium is one of the nuclides targeted for recycling from spent nuclear fuel. Reasonable nuclear reaction paths for ^{107}Pd and the cross-sections for proton- and deuteron-induced spallation in inverse kinematics have been investigated. However, a transmutation experiment using long-lived fission products as the target would be required for an actual system. To experimentally demonstrate the feasibility of ^{107}Pd transmutation by deuteron irradiation under continuous irradiation with the existing azimuthally varying field (AVF) ring cyclotron at RIKEN RIBF, we conducted a test with macroscopic quantities to transmute ^{107}Pd by deuteron beams produced by the accelerator. To effectively detect the reaction products of the ^{107}Pd + d reaction, we prepared a material with a ^{107}Pd-concentration of almost 100% by ion implantation. The implanted samples were irradiated for several days with deuterons produced by the AVF ring Cyclotron at RIKEN RIBF. After cooling, gamma-ray measurements of the irradiated sample were conducted. ^{105}Pd and ^{106}Pd produced from transmutation of ^{107}Pd were estimated using DCHAIN. The ^{107}Pd in the irradiated samples was measured by ICP-MS. The isotopic ratios of ^{105}Pd/^{107}Pd and ^{106}Pd/^{107}Pd obtained from the experimental results were compared with those obtained by calculation using PHITS. In this paper, an outline of the test of ^{107}Pd transmutation with macroscopic quantities is presented and certain experimental results are reported.

1. Introduction

High-level radioactive waste (HLW) generated from the reprocessing of spent nuclear fuel contains long-lived fission products (LLFPs). It is essential to isolate these from the human environment for a significantly long period until their long half-life nuclides decay. For this purpose, a method of vitrification and disposal in a deep underground layer has been proposed. Technical developments are underway. However, if it becomes feasible to separate radionuclides or stable nuclides contained in HLW and use these for appropriate applications or to promote the decay of LLFPs, this would be a new means for HLW management and the effective utilization of uranium resources.

In recent years, the development of the science and technology of accelerators has enabled an efficient acquisition of nuclear data using innovative nuclear-physics methods. Furthermore, the development of nuclear transmutation systems using accelerators is being realized through the development of nuclear-reaction simulation software such as the particle and heavy ion transport code system (PHITS) [1], and the construction of evaluated nuclear-reaction databases. Against this background, ‘Reduction and Resource Recycling of High-level Radioactive Wastes through Nuclear

Transmutation' was established as one of the R&D programs of Impulsive Paradigm Change through Disruptive Technologies Program (ImPACT) [2]. This program aimed to establish a rational transmutation method by investigating LLFP transmutation pathways, convert LLFP into stable or shot-lived nuclides, and utilize resources such as rare metals contained in recovered products.

Nuclear data of LLFPs were obtained in the project. In particular, palladium is a valuable material for industrial use and is one of the nuclides targeted for recycling via nuclear transmutation [3]. To investigate reasonable nuclear transmutation paths for ^{107}Pd, an experiment to obtain the cross-sections for proton- and deuteron-induced spallation in inverse kinematics was conducted at the RIKEN Radioactive Isotope Beam Factory (RIBF) [4]. The experimental results indicated that ^{107}Pd can be converted into ^{106}Pd by a proton or deuteron. However, considering the actual system, LLFPs should be irradiated with proton or deuteron beams.

To experimentally demonstrate the feasibility of ^{107}Pd transmutation by deuteron irradiation under continuous irradiation with the existing azimuthally varying field (AVF) ring cyclotron at RIKEN RIBF, we conducted a test with macroscopic quantities to transmute ^{107}Pd by deuteron beams produced by the accelerator. The transmutation reaction was detected by measuring the amount of stable Pd generated from ^{107}Pd. For this purpose, a target with a ^{107}Pd concentration of 100% was required because the reaction rate was moderate. To prepare the ^{107}Pd target, we procured a material with a ^{107}Pd concentration of 15%. Next, an ion implantation beamline to concentrate ^{107}Pd was constructed, and a target with ^{107}Pd concentration of almost 100% was prepared. This target was irradiated with deuterons at 24 MeV (12 MeV/nucleon). Furthermore, gamma-ray measurements and ICP-MS analysis were performed after irradiation. The ^{107}Pd implantation and deuteron irradiation experiments were conducted two times.

In this paper, an outline of the test of ^{107}Pd transmutation with macroscopic quantities is presented. Detailed experimental methods and data have already been reported in the following paper [5].

2. Methods

2.1. ^{107}Pd-concentrated sample

The ^{107}Pd-concentrated material was purchased from the Nuclear Research and Consultancy Group (NRG), Arnhem, Netherlands [6]. The total amount of sample was 1 g, which corresponds to an activity of 2.9 MBq. The isotopic abundances of ^{107}Pd-concentrated material were 0% (^{102}Pd), 1.7% (^{104}Pd), 48.5% (^{105}Pd), 22.95% (^{106}Pd), 15.3% (^{107}Pd), 8.75% (^{108}Pd), and 2.8% (^{110}Pd).

To efficiently produce a sufficient beam current of Pd ions, a Pd sample was combusted at 600 ℃ in an electric furnace and converted into PdO. The PdO powder was then pressed into an aluminum cathode holder and inserted into the ion source in the implantation beamline.

2.2. Implantation of ^{107}Pd

The implantation beamline consists of an ion source, an 80 cm-radius double focusing 90° bending magnet, a target chamber, quadrupole magnets (Q0, 1, 2), magnetic ion beam steerers (St1, 2), ant other components (Figure 1). Negative ^{107}PdO ion beams were produced from the ion source, extracted with an acceleration voltage of 20-30 kV, and mass-analyzed. A single slit with a diameter of 3 mm and electrically suppressed Faraday cup were placed in the target chamber and thus, the beam size of the target was approximately 3 mm.

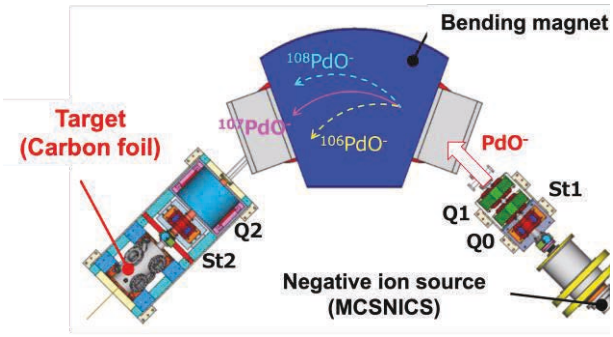

Figure 1 ^{107}Pd implantation beamline

The target material was carbon foil with a thickness of approximately 360 μg/cm^2. It was a multilayer graphene sheet developed by KANEKA [7], which is suitable for high-intensity ion beam irradiation because of its remarkable durability and the marginal amount of impurities required for Pd ion implantation. Two samples were fabricated for this experiment (samples 1 and 2). After implantation, the samples were covered with graphite to a thickness of 50 μg/cm^2 to prevent sputtering by deuteron irradiation.

2.3. Deuteron irradiation

The ^{107}Pd-implanted sample was irradiated by deuterons at 12 MeV/nucleon produced by the AVF ring cyclotron at RIKEN RIBF [8]. The irradiation chamber consists of an aluminum beam stopper, suppressor, and two Ta slits with a diameter of 3 mm. The sample was placed on a beam stopper and fixed to a suppressor.

The cumulative irradiation charge was monitored during the experiment using a digital current integrator. Deuteron irradiation was conducted with a beam current of 1-2 pμA for a week for sample 1 and 25 days for sample 2. Finally, the cumulative irradiation charge attained 1.09 C and 3.19 C, respectively, corresponding to the irradiation with a beam current of 1 pμA for 12.6 d and 37 d.

2.4. Gamma-ray and ICP-MS measurements

After the moderate cooling period, gamma-ray measurements were performed using a high-purity Ge detector. The measurement data were collected using a multichannel analyzer. The cooling periods for samples 1 and 2 were 17 d and 23 d, respectively.

The irradiated carbon foil was then removed from the sample holder and dissolved in inverse aqua regia (a mixture of concentrated HNO_3 and concentrated HCl at a volume ratio of 1:3) mixed with perchloric acid. The solution was dried and concentrated HNO_3 was added up to a total weight of 0.66 g. Then, 0.1 g of the sample was picked out and diluted up to 50-66 times for measurement with inductively coupled plasma mass spectrometry (ICP-MS).

Because there is no standard material for ^{107}Pd in ICP-MS, the counts of each Pd isotope in the natural Pd standard material were measured and added. The concentration of the standard Pd material was 10 ppb. Its total concentration corresponded to the total counts of all the Pd isotopes except ^{102}Pd because the natural abundance ratio of ^{102}Pd is 1.02%, and it did not significantly affect the measurement [9].

2.5. Calculation by PHITS

The production yield of nuclides per deuteron was calculated using PHITS to estimate the total amount of ^{106}Pd and ^{105}Pd generated in the experiment [1]. For the calculation, ^{107}Pd with a diameter of 3 mm was deposited on a thin carbon film with a radius of 10 mm and thickness of 0.01 mm. The thickness of ^{107}Pd was set to 1.29×10^{-5} cm, and its weight was 10 μg. ^{107}Pd was irradiated with deuterons at 12

MeV/nucleon with a beam current of 1 μA. The deuteron beam diameter was 3 mm, and the irradiation time was 30 days.

3. Results and discussion

3.1. Results of ICP-MS and gamma-ray measurements

The concentration of ^{107}Pd in the sample solution was 8.19 ± 0.21 ppb for sample 1 and 2.16 ± 0.12 ppb for sample 2, respectively. The dilution factors for sample 1 and 2 were 50 and 66. The total weight of the sample solution was 0.66 g. Thus, the amount of ^{107}Pd implanted in a carbon foil was calculated to be 270.03 ± 6.97 ng and 112.91 ± 4.99 ng, respectively.

The activities of ^{106m}Ag and ^{105}Ag, which were generated by the transmutation of ^{107}Pd implanted in a carbon foil, were calculated from the gamma-ray spectra at 450 keV and 344 keV [11]. The activity was determined using the total net count under the selected gamma-ray peak. The gamma-ray measurement revealed that for sample 1, the amounts of ^{106m}Ag and ^{105}Ag produced after cooling for 17 days from the end of irradiation were 2.19 ± 0.02 pg and 0.57 ± 0.02 pg, respectively. For sample 2, the amounts of ^{106m}Ag and ^{105}Ag produced after cooling for 23 days from the end of irradiation was 1.91 ± 0.02 pg and 1.51 ± 0.04 pg, respectively.

3.2. Estimation of isotopic ratio of Pd/^{107}Pd and comparison with simulation

When ^{107}Pd reacts with a 24 MeV deuteron, the reaction pathway by which ^{106}Pd is produced is considered. In this energy region, isotopes of Rh, Pd, and Ag are likely to be generated by a spallation reaction, and certain stable isotopes are produced directly. In addition, other radioactive isotopes are converted into stable Pd via beta decay. Only ^{106m}Ag can be detected because most of these radionuclides have a short half-life and decay during gamma-ray measurements. However, suppose the production ratio of ^{106m}Ag to ^{106}Pd of the total amount of nuclides is known. In this case, it is feasible to estimate the amount of ^{106}Pd produced by the ^{107}Pd + d reaction from the amount of ^{106m}Ag observed by gamma-ray measurement. This also applied to ^{105}Pd.

However, ^{106m}Ag and ^{105}Ag decay during irradiation after their generation. Therefore, the generation ratio of ^{106m}Ag and ^{105}Ag at the time of gamma-ray measurement was decay-corrected and determined using the generation and decay analysis code DCHAIN for radioactive and stable nuclides [12].

Assuming that the entire ^{106m}Ag and ^{105}Ag detected by gamma-ray measurement was converted into ^{106}Pd and ^{105}Pd at the time just after irradiation, ^{106m}Ag and ^{105}Ag accounted for 22.7% and 85.7% of the ^{106}Pd and ^{105}Pd, respectively, produced by deuteron irradiation for sample 1. When gamma-ray measurements were performed after 17 days of cooling, both ^{106m}Ag and ^{105}Ag decayed, and the ratio shifted to 5.5% and 64.4%, respectively. For sample 2, the ratios of ^{106m}Ag and ^{105}Ag in the ^{106}Pd and ^{105}Pd generated were 1.9% and 51.0%, respectively. Therefore, the production amounts of ^{106}Pd and ^{105}Pd were calculated to be 39.98 ± 0.36 pg and 0.88 ± 0.04, respectively, for sample 1, and 98.3 ± 0.96 pg and 2.96 ± 0.07 pg, respectively, for sample 2.

Considering that the amount of ^{107}Pd implanted was estimated to be 270 ng and 113 ng, the isotopic ratios of ^{105}Pd/^{107}Pd and ^{106}Pd/^{107}Pd were calculated to be $(3.29 \pm 0.16) \times 10^{-6}$ and $(1.49 \pm 0.04) \times 10^{-4}$, respectively, for sample 1, and $(2.60 \pm 0.13) \times 10^{-5}$ and $(8.79 \pm 0.40) \times 10^{-4}$, respectively, for sample 2.

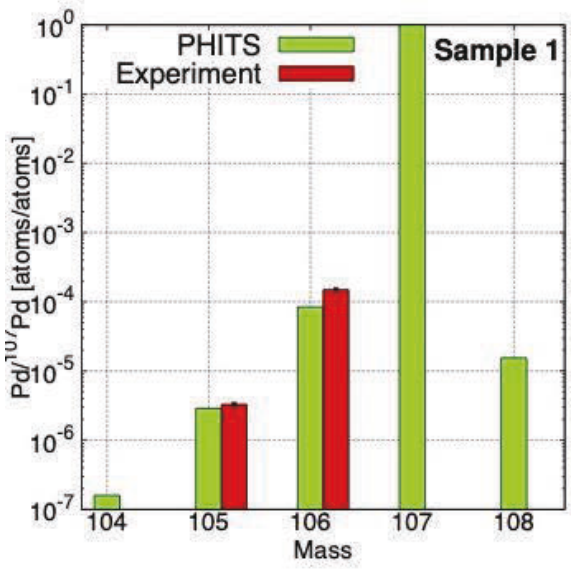

Figure 2 Comparison of Pd/^{107}Pd isotopic ratio of experiment data with calculation by PHITS for sample 1.

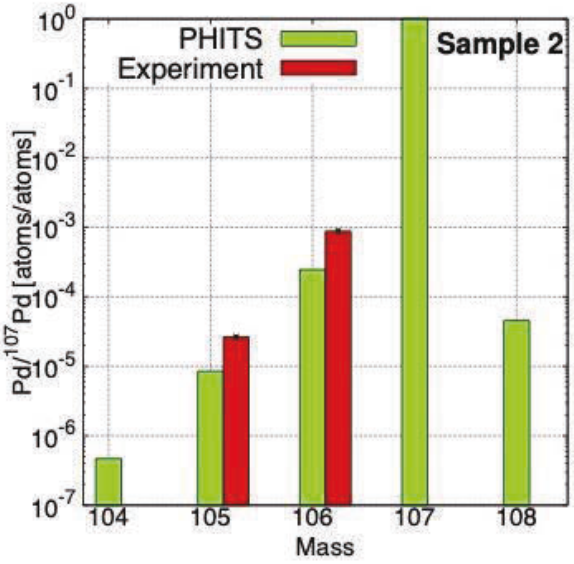

Figure 3 Comparison of Pd/^{107}Pd isotopic ratio of experiment data with calculation by PHITS for sample 2.

The isotopic ratios of ^{105}Pd/^{107}Pd and ^{106}Pd/^{107}Pd after deuteron irradiation were also evaluated using PHITS. Considering the production yield of each nuclide, the isotopic ratios of ^{105}Pd/^{107}Pd and ^{106}Pd/^{107}Pd were estimated to be 2.90×10^{-6} and 8.43×10^{-5}, respectively, for deuteron irradiation performed with a beam current of 1 pμA over 12.6 d for sample 1. For sample 2, the cumulative irradiation charge was 3.19 C, which corresponds to irradiation with a beam current of 1 pμA for 37 d. Thus, the isotopic ratios of ^{105}Pd/^{107}Pd and ^{106}Pd/^{107}Pd were estimated to be 8.48×10^{-6} and 2.46×10^{-5}, respectively. A comparison of the experimental results with the calculations by PHITS is shown in Figures 2 and 3. In these figures, the green bars denote the isotopic ratio calculated by PHITS, and the red bars denote the isotopic ratios obtained in this study. The cross-section of the ^{107}Pd + d reaction with an energy of 24 MeV was not obtained experimentally. Thus, the calculation results may include the uncertainties in this cross-section. However, the estimations of the isotopic ratios of ^{105}Pd/^{107}Pd and ^{106}Pd/^{107}Pd agree with the experimental results. In addition, the ^{107}Pd transmutation using deuterons was verified preliminarily.

4. Conclusion

In this study, ^{107}Pd transmutation with macroscopic quantities was tested. To effectively detect the ^{107}Pd + d reaction, we prepared a material with a ^{107}Pd concentration of almost 100% via ion implantation. The implanted sample was irradiated for several days with deuterons produced by the AVF ring cyclotron at RIKEN RIBF. After cooling, gamma-ray measurements of the irradiated samples were performed. ^{105}Ag and ^{106m}Ag (originating from the ^{107}Pd + d reaction) were detected. The amounts of ^{105}Pd and ^{106}Pd produced by nuclear transmutation were evaluated considering the conversion ratios (^{105}Ag to ^{105}Pd and ^{106m}Ag to ^{106}Pd) and the decay of ^{105}Ag and ^{106m}Ag during deuteron irradiation in the simulation conducted by PHITS and DCHAIN. The amount of ^{107}Pd in the irradiated samples was measured by ICP-MS. Thereby, the isotopic ratios of ^{105}Pd/^{107}Pd and ^{106}Pd/^{107}Pd were obtained. These were consistent with those obtained by calculation using PHITS. Thus, the ^{107}Pd transmutation using deuteron was verified preliminarily.

References

1) T. Sato, et al., Recent improvements of the Particle and Heavy Ion transport code System - PHITS version 3.33, J. Nucl. Sci. Technol., 2023.
2) Impulsing Paradigm Change through Disruptive Technologies Program ImPACT, https://www.jst.go.jp/impact/en/program/08.html (accessed 2024-01-12).
3) Y. Seo, and S. Morimoto, Analyzing platinum and palladium consumption and demand forecast in Japan, Resources, 6(4), 2017, 61.
4) H. Wang, et al., Spallation reaction study for the long-lived fission product ^{107}Pd, Prog. Theor. Exp. Phys., Vol. 2017, Issue 2, 2017, 021D01.
5) Y. Miyake, et al., Test of ^{107}Pd transmutation with macroscopic quantities, J. Nucl. Sci. Technol., Vol. 59, Issue 12, 2022, pp. 1536-1545.
6) Nuclear Research and Consultancy Group, https://www.nrg.eu (accessed 2024-01-12).
7) A. Tatami, et al., Preparation of multilayer graphene sheets and their applications for particle accelerators. AIP Conference Proceedings; Stellenbosch, South Africa. 2018;1962:03005.
8) S. Kohara, et al., Flattop acceleration system in the RIKEN AVF cyclotron, Nucl. Instr. Meth. Phy. Res. A526, 2004, pp.230–238.
9) R. Aono, et al., Development of ^{93}Zr, ^{93}Mo, ^{107}Pd and ^{126}Sn analytical methods for radioactive waste from Fukushima Daiichi Nuclear Power Station. JAEA-Technology 2017-025, 2017, 32p. [in Japanese].
10) WWW Chart of the Nuclide 2014, https://wwwndc.jaea.go.jp/CN14/index.html (accessed 2014-01-12).
11) R. L. Heath, Gamma-ray spectrum catalog: Ge(Li) and Si(Li) spectrometry. Fourth ed. Idaho Falls (Idaho): Aerojet Nuclear Co, 1974.
12) T. Kai, et al., DCHAIN-SP 2001: high energy particle induced radioactivity calculation code. JAERI-Data/Code 2001-016, Japan, 2001 [in Japanese].

Acknowledgements

We wish to thank the accelerator staff of the RIKEN Nishina Center for providing deuteron beams. We express our gratitude to Dr. Hiroyuki Matsuzaki (University of Tokyo) for helping with the start-up of the ion source. This study was funded by the ImPACT Program of the Council for Science, Technology, and Innovation (Cabinet Office, Government of Japan).

17. Design of radiation shield for RI production beam line by PHITS

Atsuko AKASHIO[1*], Kanenobu TANAKA[1], Nobuhiro SHIGYO[2], Kenta SUGIHARA[2, 3] and Hiromitsu HABA[1]

[1]RIKEN Nishina Center for Accelerator-Based Science
2-1 Hirosawa, Wako, Saitama 351-0198, Japan
[2]Department of Applied Quantum Physics and Nuclear Engineering, Kyushu University
744 Motooka, Nishi-Ku, Fukuoka 819-0395, Japan
[3]High Energy Accelerator Research Organization (KEK)
1-1 Oho, Tsukuba, Ibaraki 305-0801, Japan
[*]Email: horigome@riken.jp

The accelerator production of a medical radioisotope, astatine-211 (^{211}At), in the ^{209}Bi (^{4}He,2n) ^{211}At reaction requires a high-intensity helium-4 (^{4}He) beam irradiation, which generates a high radiation from the bismuth-209 (^{209}Bi) target. A ^{4}He beam with an energy of approximately 28 MeV and an intensity of 100 particle μA is planned to be irradiation on the ^{209}Bi target at the new beam line of the Superconducting RIKEN Liner Accelerator. An effective shield for the ^{209}Bi target is necessary to maintain the radiation dose rate below the legal limit at the border of the radiation-controller area. In this work, the compact shield with multiple shielding materials was designed to achieve the radiation dose rate below the limit at the border using the Particle and Heavy Ion Transport code System (PHITS).

1. Introduction

Astatine-211 (^{211}At), an alpha-particle emitting radionuclide with a half-life of 7.2 h, is produced for medical research at the RI Beam Factory (RIBF) of RIKEN [1]. Because the alpha-particle have a short range and high energy transfer to materials, ^{211}At is a leading candidate for use in targeted alpha-particle therapy.

Astatine-211 is produced through the ^{209}Bi(^{4}He,2n) ^{211}At reaction by irradiating a 28-MeV helium-4 (^{4}He) beam to a bismuth-209 (^{209}Bi) target. At the RIBF of RIKEN, ^{211}At has been produced with a 25-particle-μA (pμA) ^{4}He beam on the beam line of the AVF cyclotron. A new beam line for the larger-scale ^{211}At production with the higher beam intensities such as 100 pμA is under construction on the beam line of the Superconducting RIKEN Liner Accelerator (SRILAC) [2].

The larger-scale production of ^{211}At with the high-intensity beam, which generates high radiations from the target. In addition to the 50-cm-thick shield of the Linac building, a local shield at the target is necessary to maintain the radiation dose rate below the legal limit at the border of the radiation-controlled area. In this study, the local shield with multiple shielding materials was conceptually designed to achieve

a radiation dose rate of less than 10 μSv/h on the outside of the local shield using the Particle and Heavy Ion Transport code System (PHITS) [3]. A three-dimensional shielding structure was also studied, considering the building and distance to the border of the radiation-controlled area.

2. Structure of shield

Figure 1 shows a schematic of the concept of a local shield. The radiation dose rate around the ^{209}Bi target at a 100-pμA ^{4}He beam was estimated to be 3 × 10^{8} μSv/h using PHITS calculations. Thus, shielding is required to reduce the radiation dose rate by seven orders of magnitude.

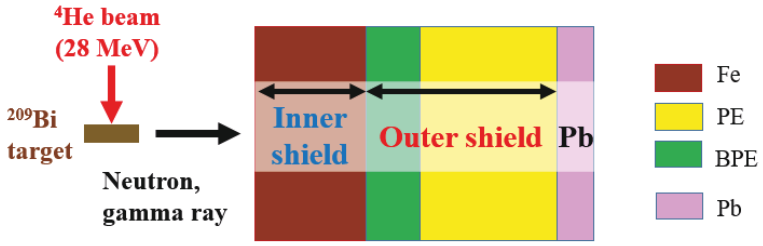

Side cross-sectional view

Figure 1: Schematic of a concept of the local shield. Iron (Fe), polyethylene (PE), boron-containing polyethylene (BPE), and lead (Pb) are applied.

The floor load-bearing capacity and the space for the local shield are limited. Thus, the local shield is necessary to be less than 10 t and less than 2 m × 2 m. If the local shield is made of the concrete, its weight and width are more than 50 t and 4 m × 4 m, respectively.

Neutrons with energies of up to 15 MeV were generated by the reaction [4]. In general, neutrons with energies less than a few MeV are shielded effectively by hydrogen-rich materials, such as polyethylene (PE) or water, and the radiation dose rate is reduced by elastic scattering of neutron by proton, i.e., hydrogen-1. Inelastic scattering with high-density material such as iron is first applied to shield high-energy neutrons to reduce the neutron energy. Second, PE and boron-containing polyethylene (BPE) are placed outside the high-density material to shield the low-energy neutrons effectively. Gamma-rays are shielded with iron and lead.

Generally speaking, the nuclear reaction models implemented in PHITS cannot be applied for the nuclear reactions at small incident energies, such as 28-MeV ^{4}He incidence on ^{209}Bi. However, we already measured the neutron production from the reaction of interest [4]. The Intra-Nuclear Cascade of Liège (INCL) [5] in PHITS version 3.20 was utilized to calculate the nuclear reactions of ^{4}He incidence on ^{209}Bi and the attenuation of a radiation dose rate in the shielding materials.

3. Attenuation of neutron dose rate

The conceptual design was studied using a simple structural model with only a target and a shield. First, neutron shielding was investigated. Figure 2 shows the neutron dose rate distribution for a simple model as shown in Fig. 1 calculated by PHITS at 100-pμA beam intensity. The dose conversion coefficients [6] were used to convert from the neutron flux to the radiation dose rate. The yellow-dotted line shows the result in which all the shields consist of PE only. The radiation dose rate is decreased at an exponentially constant rate. By contrast, the pink, black, and blue lines show the calculations in which

iron and PE were used as an inner and outer shield, respectively. In the iron region, the neutron energy is decreased by inelastic scattering, though the radiation dose rate is less decreased than that in the case of the PE inner shield. It is, however, noted that in the outer shield region of the PE, the radiation dose rate is decreased more effectively than when using the PE only.

If only PE is used, the distance between the target and the outside of the shield is 10-cm longer than the case of iron inner shield to achieve the goal of 10 μSv/h, as shown in Fig. 2. In the case of both iron and PE, the sizes of the shielding to reduce the radiation dose rate to 10 μSv/h were the same whether the iron was 20 or 30-cm thick. Thus, we concluded that the iron thickness of 30 cm is enough to attenuate the neutron dose rate in the conceptual design.

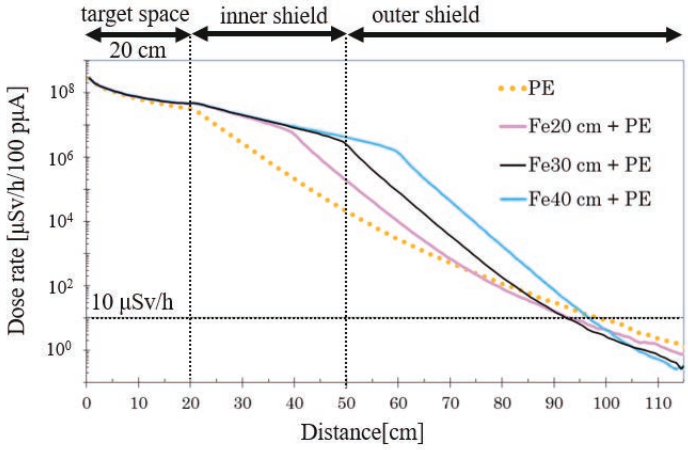

Figure 2: Distribution of the neutron dose rate in the shield for the shielding setup of Fig. 1. Lead part for gamma-rays attenuation as shown in Fig. 1 is not included in this calculation.

4. Attenuation of gamma-ray dose rate

As the shielding structure for neutrons was determined above, a shielding structure for both neutrons and gamma-rays was optimized hereafter. Figure 3 shows the dose rate distributions of neutrons and gamma-rays when iron and PE were used for the shield. As with the neutron dose rate, the dose conversion coefficients [6] were used to convert from the gamma-rays flux to the radiation dose rate. The thickness of the iron is 30 cm, based on the neutron shielding evaluation above. Primary gamma-rays from the target were shielded by the inner iron shield. It is clearly observed that the gamma-ray dose rate is increased at the iron and PE connection region. In the PE region, approximately 100 keV or less low-energy neutrons produce 2.2-MeV gamma-rays through nuclear reactions with proton. Therefore, a 10-cm-thick BPE was inserted just outside the iron. As low-energy neutrons were absorbed by the boron, lower-energy (478 keV) gamma-rays are produced instead of 2.2-MeV gamma-rays. The red-dotted line in Fig. 3 shows the radiation dose rate distribution when a 10-cm thick BPE was inserted. The gamma-ray dose rate was reduced to one-eighth of that without BPE. Additionally, the lead shield was installed to reduce the gamma-ray dose rate less than 10 μSv/h on the outside of the local shield.

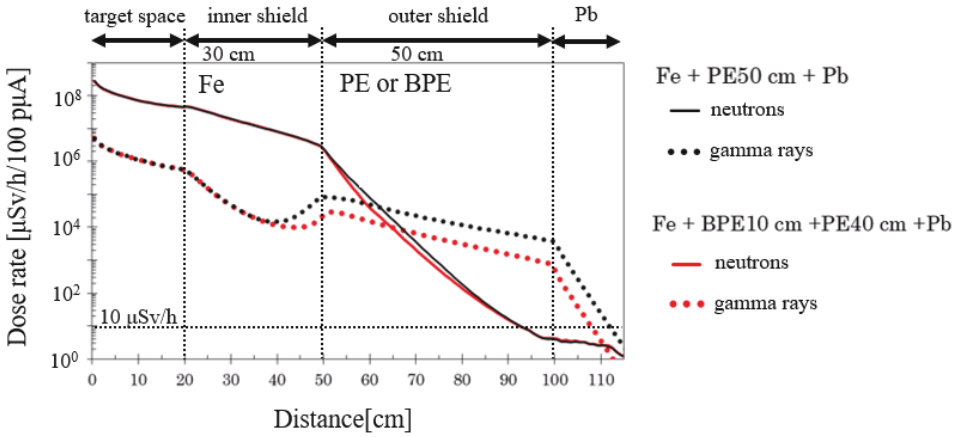

Figure 3: Dose rate distributions of neutrons and gamma-rays.

Thus, the optimized conceptual shielding consists of 30-cm-thick iron, 10-cm BPE containing 10% B_2O_3, and 40-cm PE. The density of PE and BPE were given as 0.935 g/cm^3 in this study. In addition, 10-cm-thick lead was used to shield the secondary gamma-rays.

5. Three-dimensional design

Based on the conceptual design, the local shield to be installed on the beam line of SRILAC was designed in three dimensions. Figure 4 shows a cross-sectional view of the local shield. An iron bending magnet and its stage are also involved in the local shield. The width and length of the local shield were 2 m × 2 m and the weight was 9.8 t. As the lead plates as shown in pink in Fig. 4 were heavy, they were placed minimally in the direction of the nearest border of the radiation-controlled area.

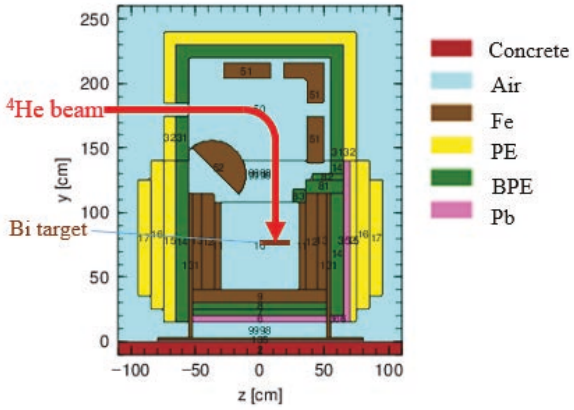

Figure 4: Side cross-sectional view of the local shield.

Figure 5 shows the radiation dose rate around the local shield as calculated by PHITS. The dose rate distributions are shown in the color maps, the neutron dose rate ranges up to 10^8 μSv/h and gamma-ray dose rate 10^6 μSv/h. For the side direction of the target, neutrons were successfully shielded by the local shield, but some of them came out of the local shield through beam ducts and other paths. The primary gamma-rays around the target were shielded by iron. The radiation dose rate on the outside of the local shield exceeded the conceptual-design goal of 10 μSv/h. This was because the local shield was designed

slightly thinner and lighter than in the conceptual design, considering the effect of the additional concrete shield of the building walls and distance to the border of the radiation-controlled area.

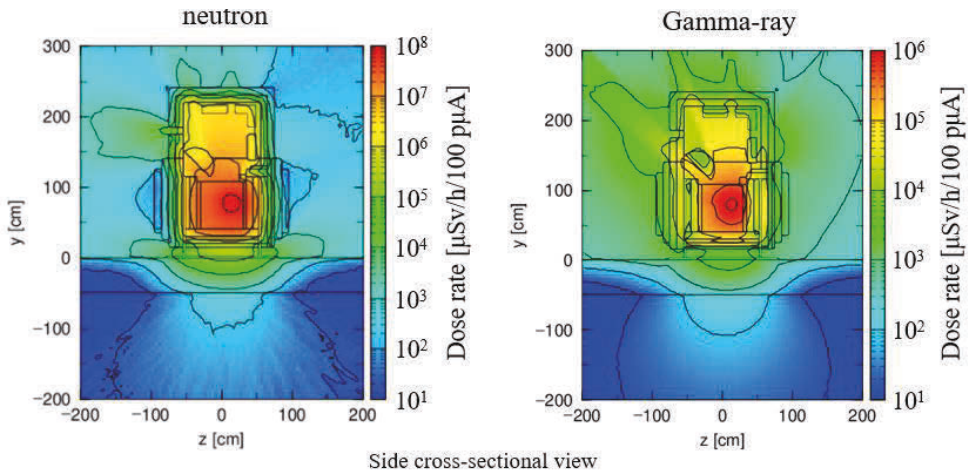

Figure 5: Dose rate distribution around local shield.

6. Dose rate at the border of the radiation-controlled area

The radiation dose rate at the border of the radiation-controlled area was evaluated. Figure 6 shows a top cross-sectional view of the radiation dose rate distribution around the irradiation room calculated using PHITS. The distance between the target and the nearest border of the radiation-controlled area is approximately 10 m. The concrete wall in the irradiation room of the Linac building is 50-cm thick. The neutrons and gamma-rays emitted from the local shield are further reduced by the concrete shield of the building wall. At the nearest border of the radiation-controlled area, the neutron dose rate was 0.2 μSv/h and the gamma-ray dose rate was 0.7 μSv/h. Therefore, the total dose rate was 0.9 μSv/h, which was lower than the legal limit of 2.6 μSv/h. Although the radiation dose rate of the secondary gamma-rays produced in the shield was high, it was maintained below the legal limit by the lead shield, which was placed only in the direction to the nearest border of the radiation-controlled area, as shown in Fig. 4. The other directions are far enough to the border of the radiation-controlled area.

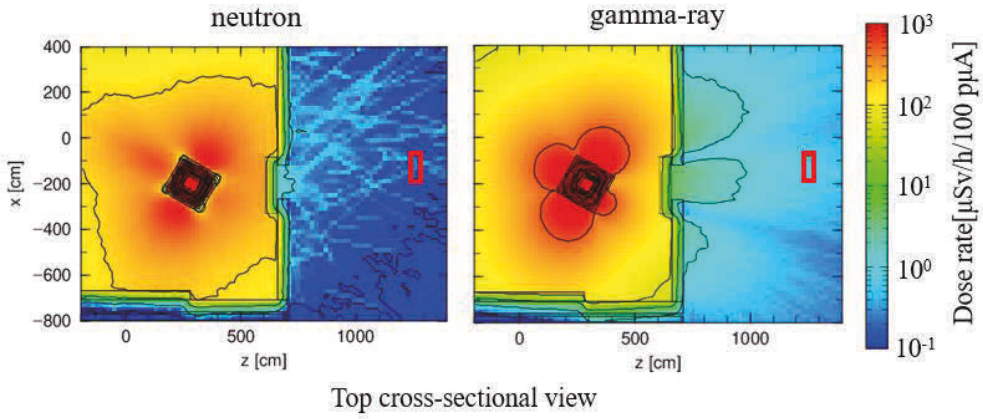

Figure 6: Dose rate distribution around the irradiation room of the Linac building. The red square shows the nearest border of the radiation-controlled area.

7. Conclusions

A compact and lightweight local shield for the new beam line for the ^{211}At production at SRILAC was designed using PHITS. It was confirmed that the radiation dose rate at the border of the radiation-controlled area could be maintained below the legal limit of 2.6 μSv/h. Based on this design, local shielding will be installed on the new beam line to produce ^{211}At in the future.

References

[1] Yin, X. et al., Progress of ^{211}At production at the RIKEN AVF cyclotron, RIKEN Accel. Prog. Rep. vol. 56, 2023, 151-152.

[2] Yamada, K. et al., Successful Beam Commissioning of Heavy- Ion Superconducting Linac at RIKEN, Proceedings of 20th Int. Conf. on RF Superconductivity (SRF2021), East Lansing, 2021, 167-174, https://doi.org/10.18429/JACoW-SRF2021-MOOFAV01.

[3] Sato, T. et al., Recent improvements of the Particle and Heavy Ion Transport code System - PHITS version 3.33, J. Nucl. Sci. Technol. 61, 2024, 127-135.

[4] Sugihara, K. et al., Nucl. Inst. and Meth. B 470, 2020, 15-20.

[5] Boudard, A. et al., New potentialities of the Liège intranuclear cascade model for reactions induced by nucleons and light charged particles, Phys. Rev. C87, 2013, 014606.

[6] Sakamoto, Y et al., “Dose conversion coefficients for high-energy photons, electrons, neutrons and protons”, 2003, JAERI 1345, 103p.

18. Calculation of the Skyshine Radiation Measurement Experiment in Kansas by PHITS

Yusuke YASUNO[1], Hironari SHIRAKAWA[1], and Shigeaki AOKI[1]
[1] Mitsubishi Nuclear Fuel Co., Ltd
622-1 Funaishikawa, Tokai-mura, Naka-gun, Ibaraki-ken 319-1197, Japan
*Email: yusuke.yasuno.qm@nu.mhi.com

Kansas State University measured exposure dose from skyshine radiation using ^{60}Co sources at Kansas in 1977 [1]. Mitsubishi Nuclear Fuel (MNF) performed calculation of this experiment using a three-dimensional Monte Carlo code PHITS v3.24 (Particle and Heavy Ion Transport code System), which is developed by JAEA [2].

For nuclear facilities, it is necessary to calculate the exposure dose objective to public which is calculated direct and skyshine radiation. Direct radiation is gamma rays emitted from the ^{60}Co source that penetrate the shielding wall (i.e. concrete) and reach the detector location directly. Skyshine radiation is gamma rays emitted from the ^{60}Co source that penetrate the relatively thin ceiling, are reflected in the sky, and reach the detector location.

The analysis method for the skyshine radiation is adopted the one-time scattering calculation method which is adopted by G33 code. For the skyshine calculation of the MNF facilities, G33 code or Pre-GAM/S code, which has equivalent performance, is used.

However, the one-time scattering calculation method has the disadvantage that it cannot correctly calculate the effect of attenuation of gamma rays for a concrete ceiling condition. In addition, due to the characteristics of the calculation method, it cannot accurately simulate the geometry of the analysis system. Furthermore, gamma rays that are scattered multiple times in the sky cannot calculated.

A solution of this situation is to use a Monte Carlo code in three dimensions that can handle a wide variety of geometries, and PHITS code can treat accurate model geometries. The radiation behavior can be correctly analyzed by applying a relatively accurate geometry model.

However, PHITS code makes the analysis more complicated. In particular, the shielding analysis, in which the number of particles decreases due to transmission through concrete and other materials, has a large uncertainty. And large number of histories is necessary to obtain sufficiently reliable analysis results. Recent advances in computers have made it possible to achieve this.

In this study, MNF performed a calculation of the skyshine measurement experiment and found that PHITS code has a good accuracy on prediction within 10% error between experiment and calculation.

In contrast, the conventional code, G33 has tendency to overestimate the results of the experiment by about five times. These results confirm that PHITS code can simulate the skyshine measurement experiment more accurately than G33 code.

In the future, MNF expects to improve the accuracy of shielding calculation using the analysis code to PHITS. As a result, more rational shielding design will be expected.

1. Introduction

Nuclear facilities, etc. are required to reduce the exposure dose at the site boundary sufficiently. Therefore, it is necessary to evaluate the exposure dose at the boundary of the site using a confirmed analysis code and to design appropriate shielding.

A summary of the dose assessment is shown in Fig.1. It is assumed a source surrounded by a shielding wall and a ceiling in Fig.1. The calculation considers a direct line where radiation from the source directly reaches the measurement point. In addition, it considers the skyshine line that emitted from source, scattered in the air, and reaches the measurement point, through a relatively thin ceiling. The exposure dose of the skyshine line is equal to or larger than that of the direct line. This is because the ceiling cannot be as thick as the wall from the viewpoint of earthquake resistance.

In this paper, we discuss the skyshine line, which has a large effect on dose at the site boundary and is complicated to calculate.

For the skyshine line, a measurement experiment using a ^{60}Co source was conducted in Kansas in 1977. In the test, the source was placed in the concrete and radiation detectors were placed several hundred meters away, and the skyshine line was measured. The strength of the ^{60}Co source was varied by the thickness of the shielding concrete: 10.3Ci, 229Ci, and 3800 Ci. In this paper, we calculated the experiments and show the results.

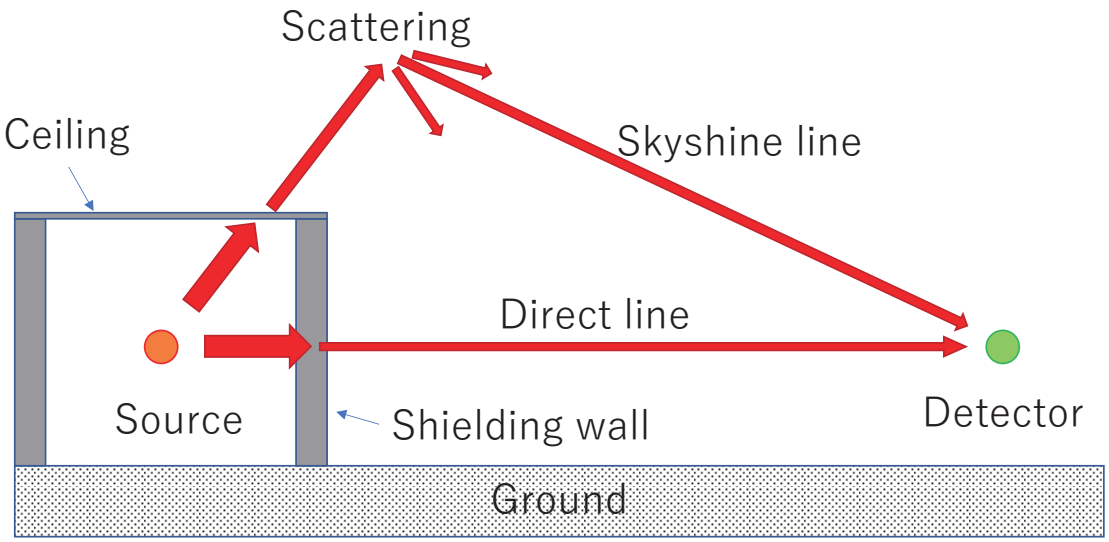

Fig.1 Overview of Site Boundary Dose Calculations

2. Calculation Model

The calculation of the skyshine line is calculated with the one-time scattering method.

The calculation is composed by three phenomena. (1) gamma ray attenuation and buildup in the air, (2) scattering, and (3) attenuation and buildup.

The buildup factor is adopted by the G-P method. The scattering cross section is obtained based on the database which is calculated with Klein-Nishina's formula.

The one-time scattering method has the advantage that it is a deterministic evaluation and relatively reasonable to calculate. On the other hand, it has several problems. This slide shows the disadvantages of the one-time scattering method together with the advantages of PHITS. The first problem is, the exact shape cannot be simulated. The second is, they need other code for attenuation in concrete calculations.

Finally, it is unable to calculate buildup accurately and becomes conservative. These problems can be solved by introducing PHITS.

By introducing PHITS, it will be able to simulate the model shape accurately. And we can simulate inelastic scattering in the air, and in the shielding concrete. And we can simulate not only one-time scattering, but also multiple scattering. Finally, we will be able to eliminate buildup maintainability.

However, PHITS has the disadvantage of being computationally time-consuming due to its use of Monte Carlo methods. However, considering recent progress of computers, we will introduce three dimensional Montel Carlo code, PHITS.

Fig.2 shows the calculation model in PHITS. The ^{60}Co source is installed in the concrete. The gamma rays emitted from the ^{60}Co source are collimated to conical 150.5 degrees angle. The concrete is placed on the ground. The space to be analyzed is a sphere with a radius of 2000 m, filled with air. This allows analysis of skyshine lines scattered up to 2000 m high. By using the Monte Carlo method for the analysis, it is possible to calculate more than two-time scattering in the sky and reflection on the ground, which cannot be handled by conventional methods.

The calculation conditions are as follows.

- ✓ PHITS 3.24 (using JENDL-4 library)
- ✓ The number of histories is about 5 billion.
- ✓ This was set target error rate of 1%, which is similar to the accuracy of 1% in the skyshine measurement experiment.
- ✓ Calculations were performed for three cases of ceiling thickness: 0 cm, 21 cm, and 42.8 cm.
- ✓ The analysis uses a cylindrical coordinate system around the z-axis.
- ✓ Tully spaces are of torus type whose cross section is a square with a side of 2m.

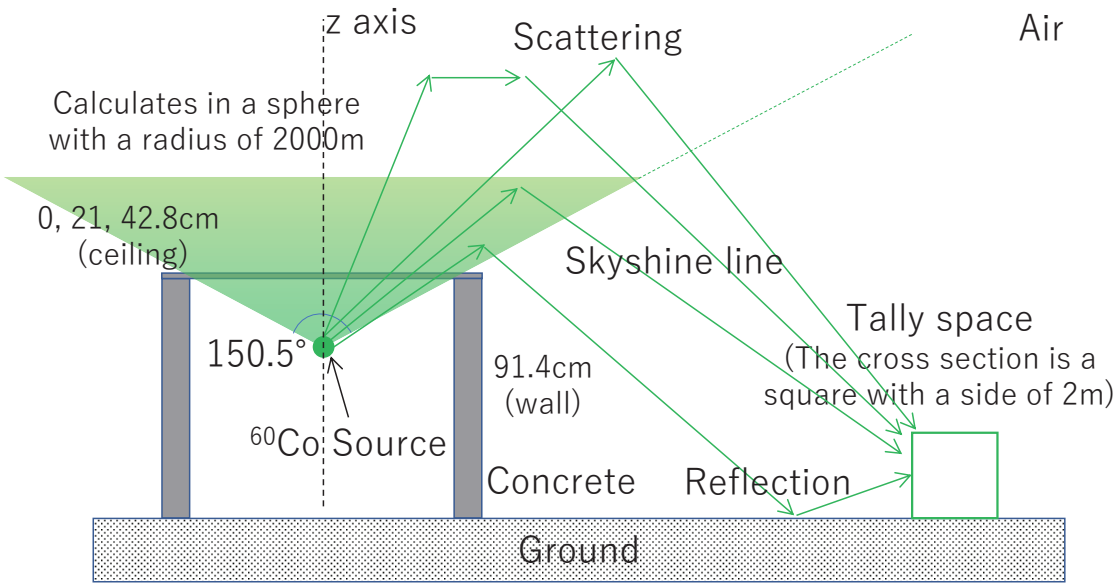

Fig.2 Calculation Model

3. Calculation Results

The results of the calculations are shown in Fig.3. The calculation results show three cases with varying ceiling thickness. The thicknesses are 0 cm, 21 cm, and 42.8 cm, respectively. Fig.3 shows the experimental results of measurement at the University of Kansas in 1977, calculation results by PHITS and calculation results by the conventional code G33.

Comparing the PHITS and experimental results, we can see that they are in much better consistency than the conventional code results: the difference between the PHITS and experimental results is within ±10% error. On the other hand, the difference between the conventional code and experimental results is about 5 times larger. These relationships are similar in all three cases with varying ceiling thickness. This may be caused due to the following reasons.

- ✓ The energy attenuation and direction change of particles due to inelastic scattering during concrete penetration is not analyzed correctly.
- ✓ Buildup effect is considered conservatively for simplifying calculations.

As you can see, the conventional code shows a large deviation from the measurement results, while PHITS shows highly accuracy results.

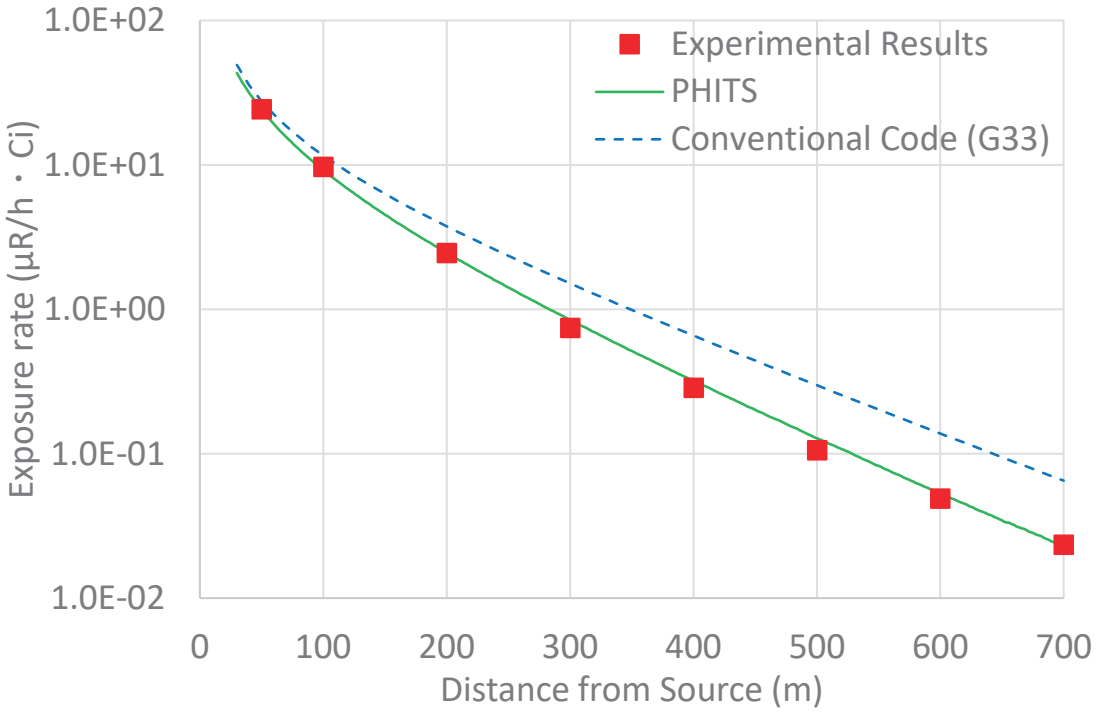

Fig.3(1/3) Calculation Results (No Ceiling)

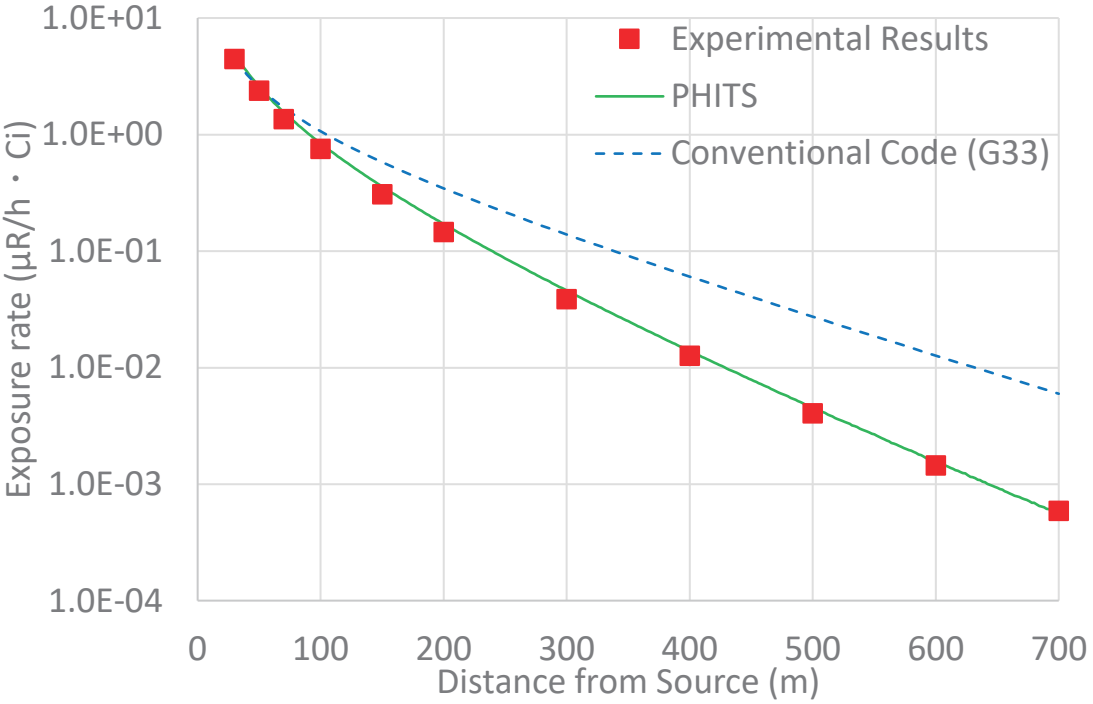

Fig.3(2/3) Calculation result (Ceiling 21 cm)

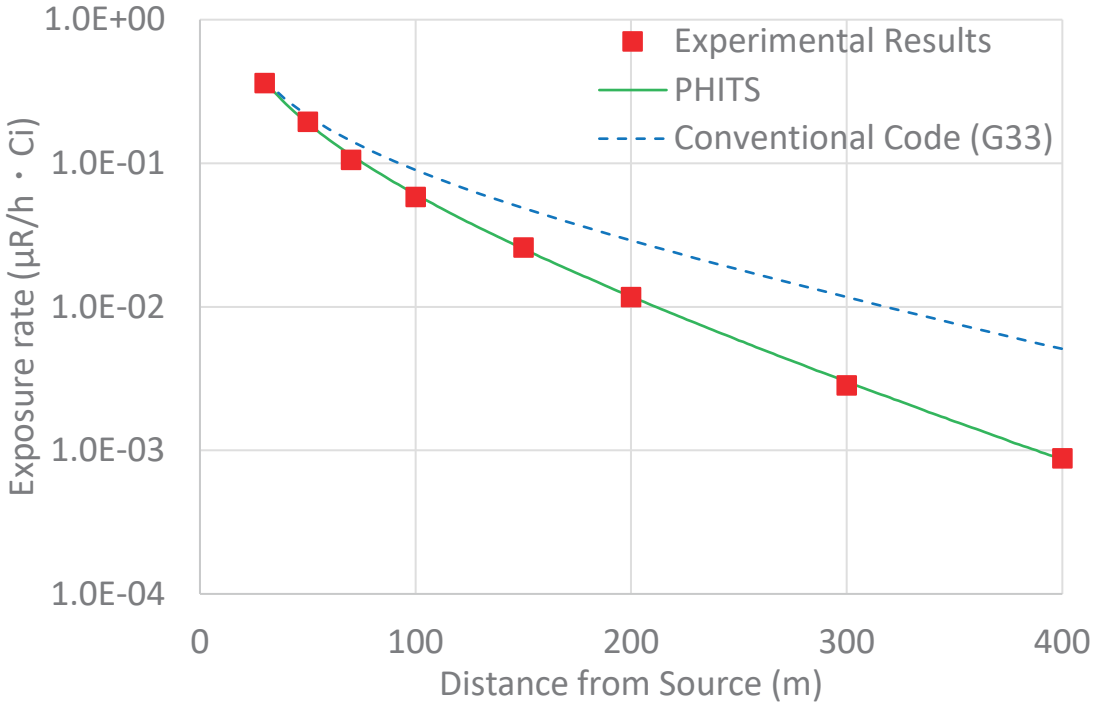

Fig.3(3/3) Calculation result (Ceiling 42.8 cm)

4. Conclusion

It is necessary to calculate the exposure dose around nuclear facilities. In the calculation, direct line and skyshine line are considered. The three dimensional Monte Carlo code PHITS enables more precise calculations. Through the calculation of the skyshine line measurement experiment carried out in Kansas, it was obtained that the calculation result which simulated the measurement result well. This confirms the accuracy of PHITS in calculating the skyshine line. In the future, it is expected to be applied to dose calculation of fabrication plant of Mitsubishi Nuclear Fuel.

References

1) R. R. Nason, J. K. Shultis, R. E. Faw and C. E. Clifford; A benchmark gamma-ray skyshine experiment, Nucl. Sci. Eng., 79, 404-416 (1981).
2) T. Sato, Y. Iwamoto, S. Hashimoto, et al.; “Features of Particle and Heavy Ion Transport code System (PHITS) version 3.02”, J. Nucl. Sci. Technol. 55(5-6), (2018), pp. 684-690.

19. Study of INC model for alpha-induced reactions at 230 MeV/u

Toshimasa Furuta[1]*, Yusuke Uozumi[1], and Yuji Yamaguchi[2]
1.Department of Applied Quantum Physics and Nuclear Engineering, Kyushu University
744 Motooka, Nishi-ku, Fukuoka-shi, Fukuoka-ken, Japan
2.Japan Atomic Energy Agency
*Email: furuta.toshimasa.451@s.kyushu-u.ac.jp

The Intranuclear Cascade model have been improved for calculation of alpha-induced reactions. Fragmentation reaction is one of the main reactions in alpha-induced reactions where composite particles are produced. It is occurs when an alpha particle is induced on target nucleus and the alpha particle is broken up to some fragments. The production probabilities of fragments reflect cluster states of the alpha particle and incident position of alpha particle. In addition, the collisions between induced particles and clusters in the target nucleus are adopted to explain composite particle productions in low energy region. The calculation results were compared with experimental data of double differential cross sections of charged particles produced from the reaction of alpha particles at incident energy of 230 MeV/u on ^{27}Al.

1. INTRODUCTION

There are some simulation models for nuclear reactions caused by various particles, for example, JQMD model, INCL model and so on, which are assembled into PHITS (Particle and Heavy Ion Transport code System)[1]. However, there is no calculation models that are capable of simulating alpha-induced reaction at few hundred MeV.

INC (Intra-Nuclear Cascade) model is one of simulation models for nuclear reactions. Generally, this model has good compatibility for calculations for proton-induced reactions above 200 MeV. However, experimental result for double differential cross sections (DDXs) for alpha-induced reactions for all lighter charged particles than $Z < 4$ was only measured by J. R. Wu[2] at 35 MeV/u and that is out of energy range for INC model. Therefore, there was a problem to develop INC model for alpha-induced reactions that experimental results are lack.

Under this circumstances, experimental result for DDXs for alpha-induced reaction for emission charged particles at 230 MeV/u was measured by our group[3]. In them, triton-to-^{3}He ratio of α-breakup yield is 1:2, which is similar to lower incident energy experiment. In addition, our analysis reveals that proton, deuteron and triton tend to be generated when alpha incidents near the center of target nucleus. In contrast, ^{3}He and alpha are released when peripheral and central incident.

In this study, the INC model is improved to explain alpha-induced reactions at incident energy of a few MeV/u by using findings from the analysis and the results of the INC model are compared with

experimental results of DDXs measured by our group. In particular, to reflect the analysis of the experimental results, the treatment of fragmentation reaction is modified, which is one of the major reactions that composite particles are generated for alpha-induced reactions. In addition, collisions between induced particles and clusters in the target nucleus are adopted, which have been successfully used in proton-induced reactions[4].

2. INC MODEL

The main processes contained in the INC model for alpha-induced reactions are fragmentation reaction and cascade process. Schematic diagram about INC model for the case where induced alpha is broken up into two deuterons by fragmentation reaction is shown in Figure 1. The fragmentation reaction occurs at the phase when alpha is incident on the target. The deuterons enter cascade process and are emitted through collisions with nucleons or clusters in the target nucleus.

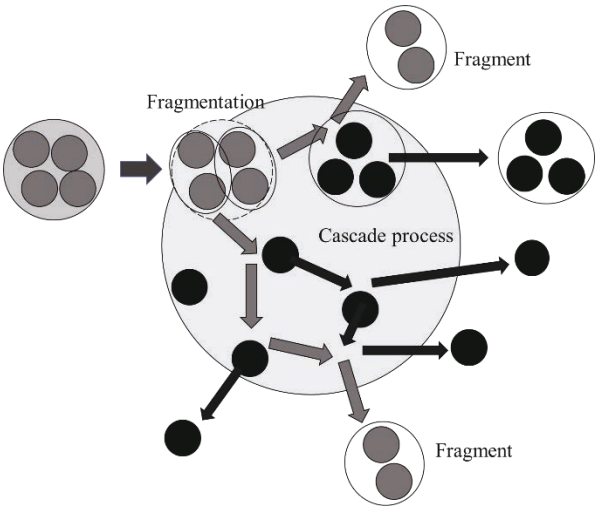

Fig.1 Schematic diagram for INC model

2.1. Fragmentation reaction

Alpha particles are composed of overlaps of some cluster states according to wave function of an alpha particle which is showed as

$$\left|\alpha\right\rangle \rightarrow C_{\alpha}|\alpha\rangle + C_{\mathrm{pt}}|\mathrm{p},\mathrm{t}\rangle + C_{\mathrm{dd}}|\mathrm{d},\mathrm{d}\rangle + C_{^{3}\mathrm{Hen}}\left|\,^{3}\mathrm{He},\mathrm{n}\right\rangle + C_{\mathrm{ppnn}}|\mathrm{p},\mathrm{p},\mathrm{n},\mathrm{n}\rangle \quad (1)$$

When an alpha particle is induced into a target nucleus, it can lose the bond as the alpha particle caused by temporarily forming a composite nucleus with the target nucleus. As a result, only one cluster state in alpha particles remains and that is equivalent to the splitting of the alpha particle. Viewed in this light, fragmentation reactions are regarded as reactions that incident alpha particles are broken up some fragments with a probability according to wave function of them by interaction with target nucleus.

On the other hands, the production probability of fragments generated from fragmentation reaction has the relationship to b-parameter according to experimental result; the production probabilities of proton,

deuteron and triton are large when b-parameter is small (conversely, the probabilities of ^{3}He and alpha are also large when b-parameter is large). Therefore that probability is described using Woods-Saxon function (which is used for density distribution of target nucleus) having b-parameter dependence,

$$f_i = \frac{C_i}{1 + \exp\left(\frac{b - r_i}{s_i}\right)} \tag{2}$$

where i is each cluster state, f_i is production probability of generated fragments, r_i is the radial parameter and s_i is diffuseness parameter. The values of each parameter are shown in Table 1 and the shape of the production probability is shown in Figure 2.

Table 1 Parameters of production probability of each fragments

	2p+2n	d+d	t+p	^{3}He+n
C_i [-]	0.009	0.018	0.018	0.054
r_i [fm]	3	3	4	5
s_i [fm]	0.5	0.5	1.0	1.0

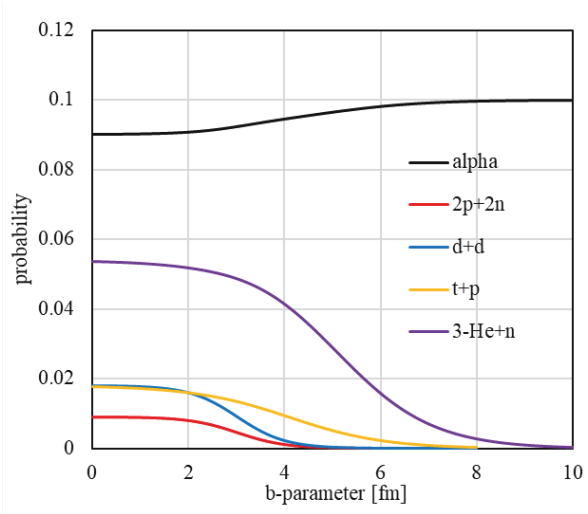

Fig.2 The shape of production probability of each fragment. The production probability of alpha is equal to the probability that fragmentation reaction does not occur and shown multiplied by 10^{-1}.

2.2. Cluster-nucleon collision

Composite particles generated by fragmentation reactions travel in target nucleus and collide with nucleon. These cluster-nucleon collisions can be replaced by collision between nucleon in composite particles and nucleon in the target nucleus. As well as nucleon-nucleon collision, whether there is a cluster-nucleon collision or not is determined by

$$r_{ij} = \sqrt{\sigma/\pi} \tag{3}$$

where r_{ij} is distance between nucleons inside and outside of the cluster, and σ is collision cross section of nucleon-nucleon collision. For σ, Cugnon's formula is adopted in this study[5]. After, momentum transfer of the nucleon in the cluster experimenting elastic collision is treated as one of the whole composite particle.

On the other hands, collisions such as below is prohibited; between nucleons in the same cluster, nucleons in separate particles generated fragmentation reaction, a nucleon in a cluster and a nucleon that have already collided another nucleon in that cluster once, and nucleons that have energies after the collision is under the Fermi energy.

3. RESULT AND DISCUSSION

The calculated DDX spectra for all charged particles (proton, deuteron, triton, ^{3}He and alpha) on aluminum at 230 MeV/u at laboratory angle of 15˚ and 40˚ by INC model are shown in Figures 3 and 4 with and experimental data, respectively. Factors indicated in figures were multiplied to data to avoid overlaps of the each DDX spectrum between different particles. The GEM (Generalized Evaporation Model) [6] is introduced to reproduce lower energy spectra than about 50 MeV/u and exciting energy calculated from the rest condition in the INC model is used to calculate for it.

There are good agreements between calculated and experimental DDX spectra for proton, deuteron, triton and ^{3}He at 15˚. The proton DDX spectrum and the composite particles DDX spectra at lower energy at 40˚ are in close agreement with experimental result. This indicated that the momentum transfer of particles kicked out by incident alpha particles or fragment is disciplined. Therefore, cluster-nucleon collisions are working well.

These particles are generated from both the incident alpha particle and the target nucleus by fragmentation reactions and cascade process, respectively. The DDX spectra of proton, triton and ^{3}He generated from incident alpha particles or target nucleus are shown in Figure 5. The triton and ^{3}He DDX spectra at lower energy than about 100 MeV/u are reproduced by the yield of each particle from target nucleus. Conversely, these DDXs at the higher energy than about 100 MeV/u are reproduced by that from incident alpha particles, in other words, there are reproduced by contributions of fragmentation reactions.

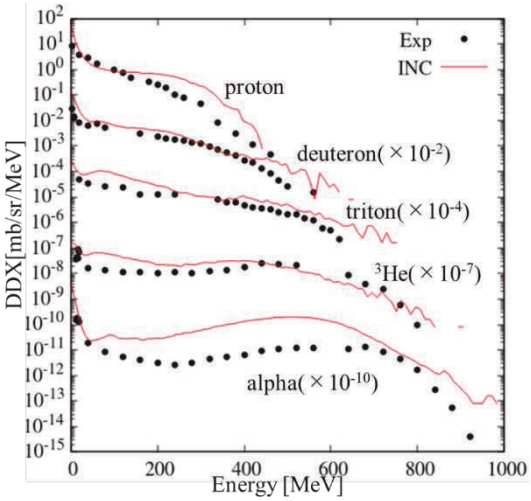

Fig.3 Calculated (solid line) and experimental (dots) DDXs for the Al(α,x) reaction at 230MeV/u at 15˚. Kinetic energy spectra for d, t, ^{3}He and α are shown multiplied by 10^{-2}, 10^{-4}, 10^{-7} and 10^{-10}, respectively.

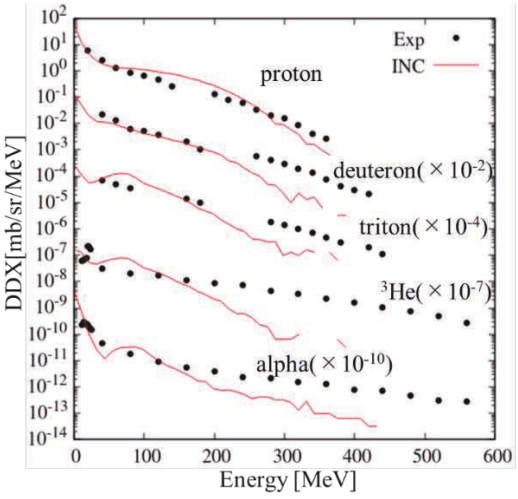

Fig.4 Calculated (solid line) and experimental (dots) DDXs for the Co(α,x) reaction at 230MeV/u at 40˚. Kinetic energy spectra for d, t, ^{3}He and α are shown multiplied by 10^{-2}, 10^{-4}, 10^{-7} and 10^{-10}, respectively.

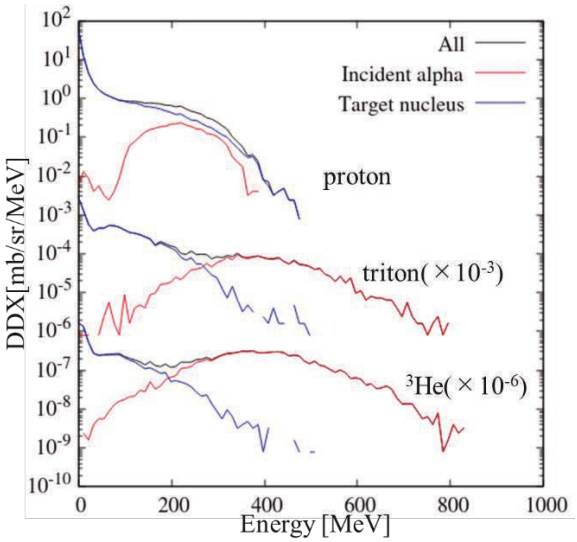

Fig.5 DDX spectra of p, t and ^{3}He generated from incident alpha (red) or target nucleus (blue) on ^{27}Al at 230 MeV/u at 15°. Kinetic energy spectra for t and ^{3}He are shown multiplied by 10^{-3} and 10^{-6}, respectively.

The proton and alpha DDX spectra at 15° calculated by improved INC model are compared with the results calculated by INCL model[7] and JQMD model[1], and that is shown in Figure 6. The results for proton by improved INC model reproduces the experimental results better than them by INCL model and JQMD model. The yield of protons kicked out by incident alpha particles or fragments is large in improved INC model. In contrast, large peaks around 200 MeV in INCL model and JQMD model may indicate that protons are mainly generated from incident alpha particles. Significant characteristics in alpha-induced reactions are large peaks in ^{3}He and alpha spectra. Only the result by the improved INC model shows the peak in the alpha DDX spectra.

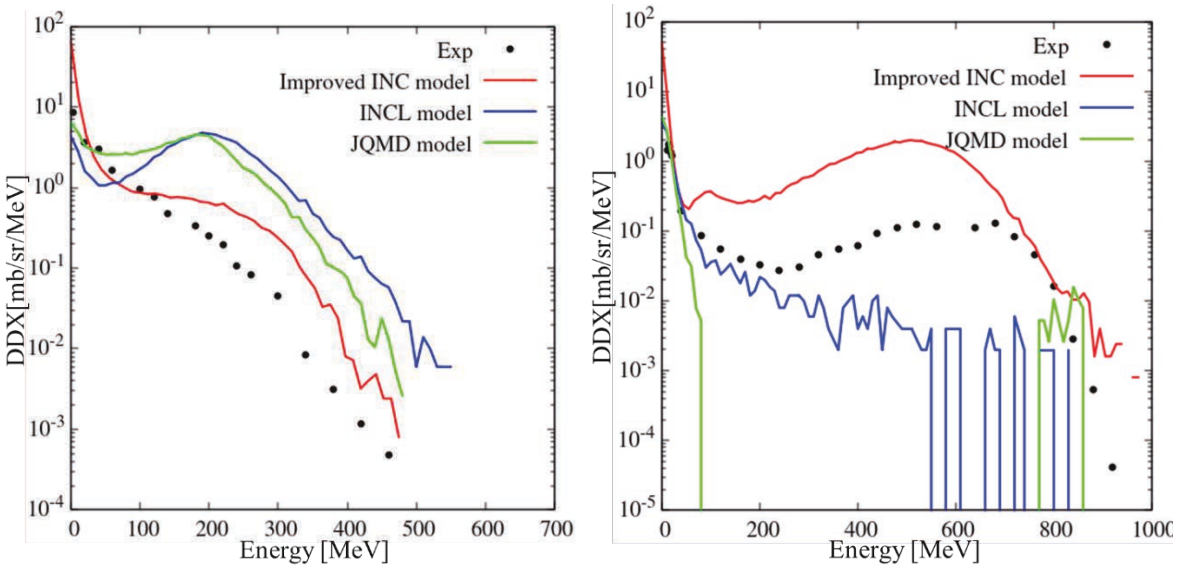

Fig.6 DDX spectra of proton and alpha calculated by improved INC model (red line), INCL model (blue line) and JQMD model (green line) on ^{27}Al at 230 MeV/u at 15° with the experimental result (dots).

4. CONCLUSION

In this study, the INC model was improved for alpha-induced reactions with incident energy of a few hundred MeV/u, using the experimental results at incident energy of 230 MeV/u on aluminum measured by our group. In fragmentation reaction, the production probability in the form of Woods-Saxon function was introduced to reflect the wave-function of alpha particles and the b-parameter dependence as indicated from the experimental results. As a result, for deuteron, the triton and ^{3}He DDX spectra at the emission angle of 15˚ and for the proton DDX spectrum at 40˚, calculated results by the INC model were almost consistent with the experimental results. In the INC model, protons are mainly generated from target nucleus, and as a result, the proton DDX spectrum at 15˚ is reproduced the experimental result well than the results calculated by INCL model and JQMD model.

ACKNOWLEDGEMENTS

This work was conducted under the Research Project with Heavy Ions at QST-HIMAC.

This study was partially supported by JSPS KAKENHI Grant Numbers 22K04989 and 17H03522.

This work was supported by Neutron Source Section of J-PARC center, Japan Atomic Energy Agency under Contract R05K168.

REFERENCES

[1] T. Sato, Y. Iwamoto, S. Hashimoto, T. Ogawa, T. Furuta, S. Abe, T. Kai, P.-E. Tsai, N. Matsuda, H. Iwase, H. Shigyo, L. Sihver, and K. Niita, “Features of Particle and Heavy Ion Transport code System (PHITS) version3.02”, J. Nucl. Sci. Technol. 55, 2018, 684-690.

[2] J. R. Wu, C. C. Chang, and H. D. Holmgran, “Charged particle spectra: 140 MeV α particle bombardment of ^{27}Al, ^{58}Ni, ^{90}Zr, ^{209}Bi, and ^{232}Th”, Phys. Rev. C 19, 1979, 659-673.

[3] T. Furuta, Y. Uozumi, Y. Yamaguchi and et al.. “Double-differential cross sections for charged particle emissions from α particle impinging on Al at 230 MeV/u”, J. Nucl. Sci. Technol., https://doi.org/10.1080/00223131.2023. 2294192

[4] Y. Uozumi Y. Fukuda, Y. Yamaguchi and et al., “Direct pickup and knockout processes in inclusive (p,αx) reactions from 42 to 300 MeV”, Phys. Rev. C 97, 2018, 34630.

[5] J. R. Cugnon, and et al., “Simple parametrization of cross-sections for nuclear transport studies up to the GeV range”, Nucl. Instruments Methods Phys. Res. Sect. B Beam Interact. with Mater. Atoms 111, 1996, 21.

[6] S. Furihata, “Statistical analysis of light fragment production from medium energy proton-induced reactions”, Nucl. Inst. Meth. in Phys. Res. B 171, 2000, 251.

[7] A. Boudard, J. Cugnon, J. C. David, S. Leray, and D. Mancusi, “New potentialities of the Liège intranuclear cascade model for reactions induced by nucleons and light charged particles”, Phys. Rev C87, 2013, 014606.

20. Calculation of Fission Fragment Yields for Thermal Neutron Reaction of ^{239}Pu

Futoshi Minato

Department of Physics, Kyushu University, Fukuoka 819-0395, Japan
RIKEN Nishina Center for Accelerator-Based Science, Wako, Saitama 351-0198, Japan
Nuclear Data Center, Japan Atomic Energy Agency, Tokai, Ibaraki 319-1195, Japan
Email: minato.futoshi@phys.kyushu-u.ac.jp

Abstract

Fission fragment yield evaluation in the past has been done mainly by considering independent and cumulative fission yields. In addition to them, the fission fragment yields are related to various observables such as total kinetic energy, prompt fission neutron, decay heats, etc. Various improvements were carried out in the fission fragment yield evaluation of JENDL-5 [1], however it did not consider correlations between such fission observables and fragment yields. A new evaluation including fission observables is thus required for the next generation of evaluated data. We recently developed a new calculation system using CCONE code to calculate fission fragment yields. This calculation system enables us to compare various fission observables with the experimental data simultaneously. In this work, we calculated thermal-induced fission of ^{239}Pu. We present the result of prompt fission neutrons, decay heats, and delayed neutrons.

1 Introduction

Fission is a phenomenon that generates various by-products in addition to fission fragments such as prompt neutrons (PN), decay heats (DH), and delayed neutrons (DN). The number of PN is also concerned with excitation energies of fragments, which are dependent on total kinetic energies (TKE) of fragments. It is desirable to prepare evaluated data that have correlations between those fission observables and fragment yields. In JENDL-5 [1] fission fragment yield data are newly evaluated, where several improvements in spin-parity states, isomers, and shell corrections have been done successfully. However, correlations between the fission observables and fragment yields were not considered when JENDL-5 was made.

We recently developed a new calculation system [3] for fission fragment yields using CCONE [2]. Within the framework in CCONE, one can estimate fission fragment yields and fission observables and compare them with the experimental data simultaneously. The evaluation of thermal neutron-induced fission on ^{235}U was carried out in Ref. [3]. We recently carried out the calculation of fission fragment yields of thermal neutron-induced fission on ^{239}Pu. We will present our results in this paper.

2 Formalism

The calculation method for fission fragment yield of ^{239}Pu is almost the same as that of ^{235}U [3]. There are some characteristic points that are different from ^{235}U and we will illustrate them mainly in this paper.

Table 1: Experimental data used for the parameter search.

PFY	[5], [6], [7], [8], [9], [10], [11] [12], [13], [14]	**PG**	[22]
TKE	[6], [7], [8], [11], [15]	**DN**	[23]
IFY	[16], [17], [18], [19], [20], [21]	**PN**	[11], [24], [25], [26], [27]
CFY	[19]	**DH**	[28], [29], [30] [31]

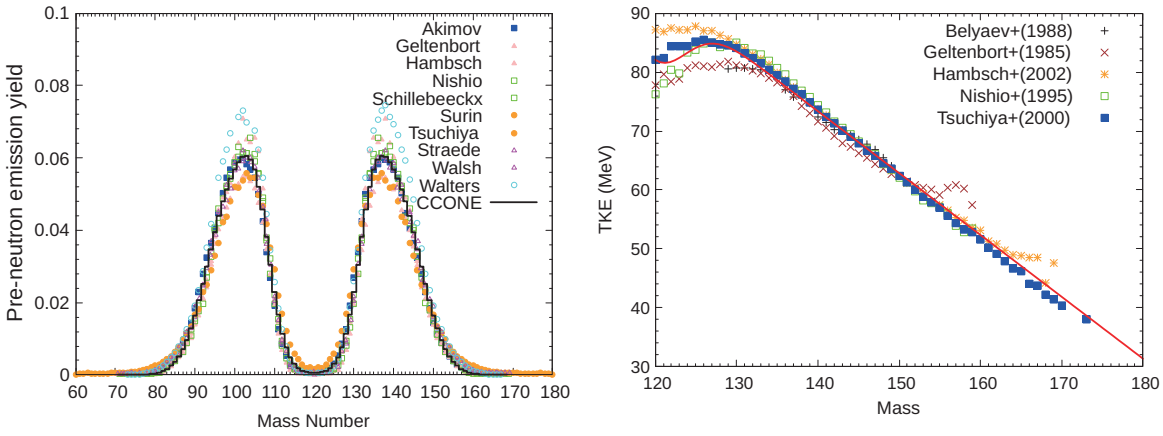

Figure 1: (left) The PFY calculated from a sum of four Gaussians and experimental data. (right) The TKE curves fitted by Eq. (4) (red solid line) and experimental data.

The main difference is the pre-neutron emission mass yields (PFY). They are approximated by a sum of four Gaussians

$$Y(A) = N_1 Y_1(A) + N_2 Y_2(A) \tag{1}$$

with

$$Y_i(A) = \frac{1}{\sqrt{2\pi}\sigma_i}\left\{\exp\left(-\frac{(A-\mu_i/2)^2}{2\sigma_i^2}\right) + \exp\left(-\frac{(A-(A_c-\mu_i/2))^2}{2\sigma_i^2}\right)\right\} \tag{2}$$

for $i = 1, 2$. A_h and A_c are the mass of a heavy fragment and a compound nucleus, respectively. The normalization constants N_i in Eq. (1) μ_i, σ_i in Eq. (2) are determined from experimental data (Table 1) via the least square fitting. We obtained $N_1 = 0.21, \mu_1 = 14.44, \sigma_1 = 3.593, N_2 = 0.79, \mu_2 = 20.60$, and $\sigma_2 = 6.299$. The result is shown in the left panel of Fig. 1 together with experimental data.

Charge distributions are approximated by the Z_p-model [4] with modifications of the most probable atomic number $Z_p(A)$ and the standard deviation $\sigma_p(A)$ in the range of $64 \leq A \leq 176$:

$$C(A, Z) = \int_{Z-0.5}^{Z+0.5} \frac{1}{\sqrt{2\pi}\sigma_p(A)} \exp\left(-\frac{(Z' - Z_p(A))^2}{2\sigma_p(A)^2}\right). \tag{3}$$

The parameters of $Z_p(A)$ and $\sigma_p(A)$ are determined from the least square fitting using the experimental data listed in Table 1. We used independent fission yields (IFY), cumulative fission yields (CFY), the total number of prompt γ-rays per fission (PG), PN, DH, and DN for the parameter search.

A total kinetic energy (TKE) is also approximated by using the following function, which is originally proposed by [32]:

$$\mathrm{TKE}(A_h) = (p_0 - p_1 A_h)\left(1 - p_2 \exp\left(-\left(A_h - \frac{A_c}{2}\right)^2 p_3\right)\right) + \epsilon_{\mathrm{TKE}}. \tag{4}$$

The parameters p_i $(i = 0, 1, 2, 3)$ are determined so as to reproduce experimental data listed in Table 1. The results are $p_0 = 220.4, p_1 = 1.050, p_2 = 0.1303$, and $p_3 = 29.77$. In Eq. (4), $\epsilon_{\rm TKE}$ is introduced to satisfy the average TKE value of experimental data $\overline{\rm TKE} = 178$ MeV [10, 33, 34]. The result of TKE using this parameter set is shown in the right panel of Fig. 1. A fluctuation of TKE from Eq. (4) is considered by introducing a width parameter $\sigma_{\rm TKE}(A_l) = \sigma_{\rm TKE}(A_h) = s_0 - s_1 \exp\left[-s_2\left(A_h - \frac{A_c}{2}\right)^2\right]$, where s_i $(i = 0, 1, 2)$ are the parameters. They are also determined from uncertainties of the experimental data, and we obtain $s_0 = 5.520, s_1 = 5.750, s_3 = 5512$.

Excitation distributions of fission fragment yields are estimated as follows. First, total excitation energy (TXE) is calculated by ${\rm TXE} = E_n + S_n + M_f - (M_l + M_h) - {\rm TKE}$, where E_n is the incident neutron energy, S_n is neutron threshold of fissioning nucleus, and M_f, M_l, and M_h are the mass of fissioning nucleus, light fragment, and heavy fragment, respectively. To sort TXE into two fission fragments, we use an anisothermal model [35]

$$R_T = \frac{T_l}{T_h} = \sqrt{\frac{a_h(U_h)U_l}{a_l(U_l)U_h}}, \tag{5}$$

where $U_{l,h} = E_{l,h} - \Delta$ with Δ being a correction energy attributed from pairing correlations [36]. The function $a_{l,h}(U_{l,h})$ is given by $a_{l,h}(U_{l,h}) = a^*\left(1 + E_{sh}\frac{1-e^{1-\gamma U_{l,h}}}{U_{l,h}}\right)$, where a^*, E_{sh}, γ are the asymptotic level density parameter, the shell correction, and the shell damping factor, respectively, and taken from Ref. [36]. The mean excitation energies $E_{l,h}$ are estimated numerically from Eq. (5) with a condition of $E_l + E_h = {\rm TXE}$. The excitation energy distributions are then estimated by [37]

$$G_{l,h}(E) = \frac{1}{\sqrt{2\pi}\sigma_{l,h}} \exp\left(-\frac{(E - E_{l,h})^2}{2\sigma_{l,h}^2}\right), \tag{6}$$

where $\sigma_{l,h} = \frac{E_{l,h}}{\sqrt{E_l^2 + E_h^2}}\sigma_{\rm TKE}$. Odd-even effects of fission fragment yields are considered via f_z and f_n [38]. Fission fragment yields including spin-parity distributions are then given by

$$Y(A, Z, J^\pi, {\rm TKE}) = \frac{1}{2}\frac{J + 1/2}{2f_s^2\sigma^2} \exp\left(\frac{(J + 1/2)^2}{2f_s^2\sigma^2(U)}\right) Y(A)C(A, Z)G_{l,h}(E) \tag{7}$$

The parameters for $f_s = 2.756$ in Eq. (7), odd-even effect parameters $f_z = 1.120$, $f_n = 1.020$ and the scaling factor of asymptotic level density parameter $f_a = 0.6$ are adjusted by hand so that the calculated delayed neutrons and prompt neutrons come closer to the experimental data.

3 Result

The result of neutron multiplicities as a function of fragment mass is shown in the left panel of Fig. 2. The experimental data used for the parameter search within the least square fitting are also shown. Our calculations roughly reproduce the seesaw structure as found in the experimental data. In this framework, the result of CCONE shows some deviations from the experimental data for light fragments $(60 \leq A \leq 120)$, while it is relatively in a good agreement with the experiments for heavy fragment sides $(135 < A \leq 150)$. The right panel of Fig 3 shows the delayed neutron yields as a function of time after fission burst launched by instant neutron irradiation. The present CCONE calculation is comparable to the evaluated data of JENDL-5, which nicely reproduces the Keepin's experimental data [23].

Figure 3 shows decay heats of β-rays and γ-rays. The present framework of CCONE reasonably reproduces the experimental data both for β and γ-rays. In particular, this work improved the result of γ decay heat as compared to the evaluation of JENDL-5 which overestimated around time after fission burst $t = 80$ (s).

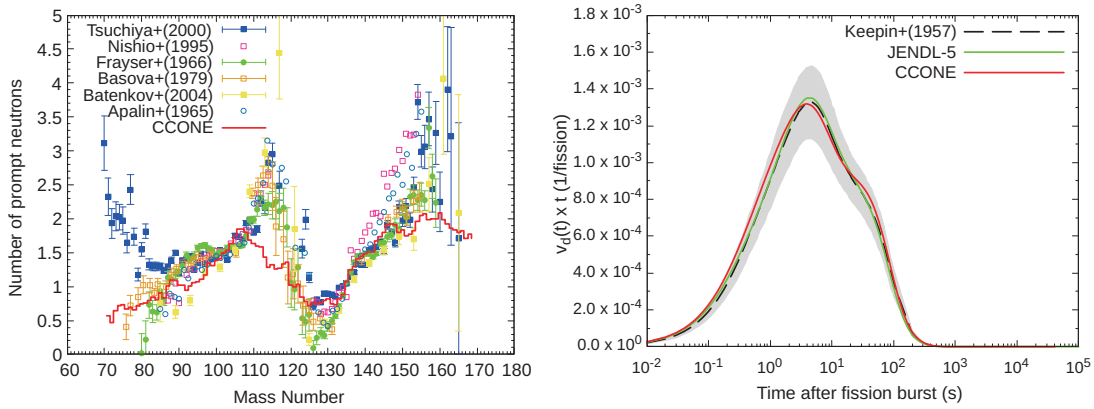

Figure 2: (Left) Calculated and experimental neutron multiplicities as a function of fragment mass. (Right) Delayed neutron yields as a function of time after fission burst. The result is shown together with the JENDL-5 evaluations.

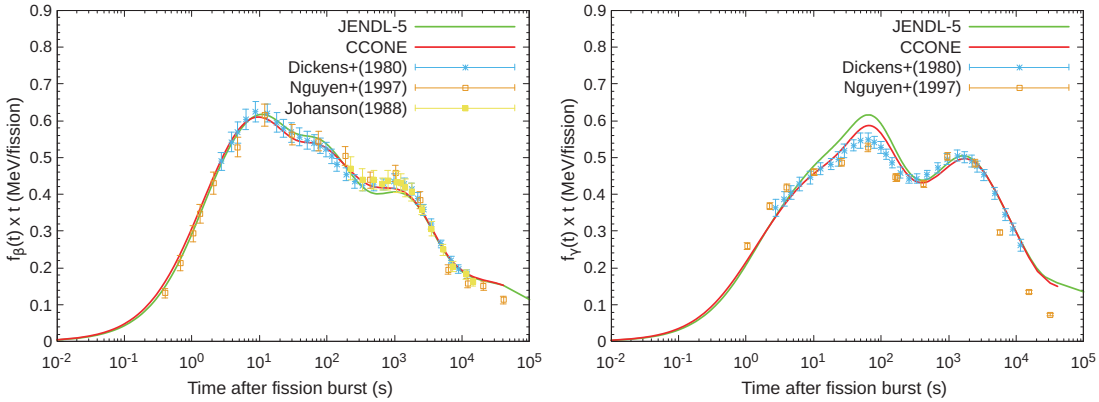

Figure 3: β-ray (Left) and γ-ray (Right) decay heats as a function of fission burst.

4 Summary

We calculated fission fragment yields of thermal neutron induced fission on ^{239}Pu with a newly developed CCONE code system. The calculated result is compared with experimental data and the evaluation of JENDL-5. We could obtain a reasonable agreement with experimental data and found that the result is comparable to JENDL-5 although some discrepancies from the experimental data are found in neutron multiplicities. We will calculate fission fragment yields of different systems using this CCONE code system.

References

[1] Iwamoto O., Iwamoto N., Kunieda S., et al., Japanese evaluated nuclear data library version 5: JENDL-5. Journal of Nuclear Science and Technology, 2003;60;1–60.

[2] Iwamoto O., Iwamoto N., Kunieda S., et al., The CCONE Code System and its Application to Nuclear Data Evaluation for Fission and Other Reactions. Nuclear Data Sheets 2016;131;259–288.

[3] Minato F. and Iwamoto O., Fission Fragment Yields Of ^{236}U(n, f) Evaluated By The CCONE Code System, doi:10.48550/arXiv.2404.17728.

[4] Wahl A.C., Systematics of Fission-Product Yields, LANL, LA-13928, 2002.

[5] Akimov N.I., Vorobeva V.G., Kabenin V.N., et al., Effect of Excitation Energy on Yields and Kinetic Energies of Fragments in Fission of ^{239}Pu by Neutrons, Soviet J. Nucl. Phys. 1971;13;272.

[6] Geltenbort P., Connewein F. and Oed A., Precision measurements of mean kinetic energy release in thermal-neutron-induced fission of ^{233}U, ^{235}U and ^{239}Pu, Conf. Nucl. Data f. Basic a. Appl.Sci., Santa Fe, Vol. 1, 1985, 393p.

[7] Franz-Josef Hambsch, Luca Demattè, Bax H., et al., Fission of ^{239}Pu with resonance neutrons, J. Nucl. Sci. Technol. 2002;39;307-310.

[8] Nishio K., Nakagome Y., Kanno I., et al., Measurement of Fragment Mass Dependent Kinetic Energy and Neutron Multiplicity for Thermal Neutron Induced Fission of Plutonium-239, J. Nuc. Sci. Technol. 1995;32;404.

[9] Schillebeeckx P., Wagemans C., Deruytter A.J., et al., Comparative Study of the Fragments Mass and Energy Characteristics in the Spontaneous Fission of ^{238}Pu, ^{240}Pu and ^{242}Pu and in the Thermal-Neutron-Induced Fission of ^{239}Pu, Nucl. Phys. A 1992;545;623.

[10] Surin V.M., Sergachev A.I., Rezchikov N.I., et al., Yields and Kinetic Energies of Fragments in the Fission of U233 and Pu239 by 5.5- and 15-MeV Neutrons, Sov. J. Nucl. Phys. 1972;14;523.

[11] Tsuchiya C., Nakagome Y., Yamana H., et al., Simultaneous Measurement of Prompt Neutrons and Fission Fragments for ^{239}Pu(n_{th}, f), J Nucl. Sci. Technol. 2000;37;941.

[12] Wagemans C., Allaert E., Deruytter A., et al., Comparison of the energy and mass characteristics of the ^{239}Pu(n_{th}, f) and the ^{240}Pu(sf) fragments, Phys. Rev. C 1984;30;218.

[13] Walsh R.L., Boldeman J.W. and Elcombe M.E., Viscosity effects at low excitation in the neutron fission of ^{239}Pu, IAEA Symp. Phys. Chem. of Fission, Juelich, Vol.2, 1979, 129p.

[14] Walter F.J., Schmitt H.W. and Neiler J.H., Fragment Mass Distributions for Thermal-Neutron-Induced Fission of Pu^{239} and Pu^{241}, Phys. Rev. 1964;133;B1500.

[15] Belyaev A.D., Bikbova Z.S., Kogan V.I., et al., Usmandiyarov A.M., Structure of the mass distributions of the products of thermal-neutron fission of ^{235}U and ^{239}Pu for a fixed energy of the fission products, J. Sci. Nucl. Phys. 1984;40;720.

[16] Guenther H., Siegert G., Ferguson R.L., et al. Fission-fragment charge distributions in thermal-neutron induced fission of ^{239}Pu and ^{235}U, Nucl. Phys. A 1972;196;401.

[17] Dubey S., Echler A., Egelhof P., et al., Precise ^{92}Rb and ^{96}Y yields for thermal-neutron-induced fission of ^{235}U and ^{239,241}Pu determined using calorimetric low-temperature detectors, Phys. Rev. C 2020;102;044602; Dubey S., Echler A., Egelhof P., et al., Isotopic distributions of thermal-neutron-induced fission fragments of near-symmetric fission of ^{239,241}Pu determined using calorimetric low-temperature detectors, Phys. Rev. C 2021;104;034621.

[18] Srivastava A., Goswami A., Srivastava B.K., et al.,Fragment shell effect in low energy fission: Independent yields of technetium isotopes in the thermal-neutron-induced fission of ^{239}Pu, Phys. Rev. C 1986;33;969.

[19] Naik H., Dange S.P., Singh R.J., et al., Post neutron mass yield distribution in the thermal neutron induced fission of ^{239}Pu, Nucl. Sci. Eng. 2022;196;824.

[20] Bogdzel A.A., Gundorin N.A., Gohs U., et al., Peculiarities of Pu-239 fission by resonance neutrons, Conf.on Nucl. Data for Sci.and Technol., Juelich, 1991, 150p.

[21] Fritze K., Mullen C.C.MC, Thode H.G., Absolute yields of the isotopes of xeon and krypton in the neutron fission of plutonium-239, Second Internat. At.En. Conf., Geneva 1958;15;436.

[22] Pleasonton F., Ferguson R.L., Schmitt H.W., Prompt Gamma Rays Emitted in the Thermal-Neutron-Induced Fission of ^{233}U, ^{235}U and ^{239}Pu and the Spontaneous Fission of ^{252}Cf, ORNL-4844, 1972, 109p.

[23] Keepin G.R., Wimett T.F., Zeigler R.K., Delayed neutrons from fissionable isotopes of uranium, plutonium and thorium, J. Nucl. Energy 1957;6;2-21.

[24] Basova B.G., Ryazanov D.K., Rabinovich A.D., et al., Neutrons emitted by fragments of the spontaneous fission of ^{252}Cf and the fission of ^{239}Pu by thermal neutrons, Soviet Atomic Energy 1979;46;282.

[25] Fraser J.S., Milton J.C.D., Nuclear Fission, Ann. Rev. Nucl. 1966;16;379.

[26] Batenkov O.A., Boykov G.A., Hambsch F.-J., et al., Prompt neutron emission in neutron-induced fission of ^{239}Pu and ^{235}U, AIP Conf. Proc. 769, 2005, pp.1003-1006.

[27] Apalin V.F., Gritsyuk Yu.N., Kutikov I.E., et al., Neutron emission from U233, U235 and Pu239 fission fragments, Nucl.Phys. 1965;71;553.

[28] Akiyama M., An S., Measurement of fission product decay heat for fast reactor, Proc. of Int. Conf. on Nucl. Data for Science and Technol., Antwarp, Bergium, 1982, 237p.

[29] Nguyen, H.V., et al., Decay Heat Measurements Following Neutron Fission of ^{235}U and ^{239}Pu, Proc. Int. Conf. on Nucl. Data for Science and Technol., Trieste, Italy, 1997, 835p.

[30] Dickens J.K., Love T.A., McConnell J.W., et al., Fission Product Energy Release for Time following Thermal Neutron Fission of ^{235}U between 2 and 14,000 seconds, Nucl. Sci. Eng. 1980;74;106-129.

[31] Johanson P.-I, Integral DEtermination of the Beta and Gamma Heat in Thermal-Neutron-Induced Fission of ^{235}U and ^{239}Pu, and of the Gamma Heat in Fast Fission of ^{238}U, Proc. of Int. Conf. on Nucl. Data for Science and Technol., Mito, Japan, 1988, 257p..

[32] Okumura S., Kawano T., Jaffke P., et al., ^{235}U(n,f)Independent fission product yield and isomeric ratio calculated with the statistical Hauser-Feshbach theory, J. Nucl. Sci. Technol. 2018;55;1009-1023.

[33] Vorobèva V.G., D'yachenko N.D., Kolosov N.P., et al., Effect of nucleonic composition of fissioning nuclei on the mean kinetic energy of the fragments, Sov. J. Nucl. Phys. 1974;19;489.

[34] Kolosov N.P., Kuzm̀inov B.D., Sergachev A.I., et al., Value of nu-bar from energy balance in U-233 and Pu-239 fission, Soviet Atomic Energy 1972;32;92.

[35] Kawano T., Talou P., Stetcu I., et al., Statistical and evaporation models for the neutron emission energy spectrum in the center-of-mass system from fission fragments, Nucl. Phys. A 2013;913;51-70.

[36] Mengoni A. and Nakajima Y., Fermi-Gas Model Parametrization of Nuclear Level Density, J. Nucl. Sci. Technol. 1994;31;151-162.

[37] Okumura S., Kawano T., Lovell A.E., et al., Energy dependent calculations of fission product, prompt, and delayed neutron yields for neutron induced fission on ^{235}U, ^{238}U, and ^{239}Pu, J. of Nucl. Sci. Technol. 2021;59;96-109.

[38] Minato F., Neutron energy dependence of delayed neutron yields and its assessments, J. Nucl. Sci. Technol. 2018;55;1054-1064.

Acknowledgments

This work is supported by JSPS KAKENHI Grant Number 21H01856 and MEXT Innovative Nuclear Research and Development Program ”Fission product yields predicted by machine learning technique at unmeasured energies and its influence on reactor physics assessment” entrusted to the Tokyo Institute of Technology.

21. Development of an EXFORTABLES-Inspired Structured Database through EXFOR Parser

Shin Okumura[†] [*1], Georg Schnabel[1], and Arjan Koning[1]

[†]Email: s.okumura@iaea.org
[1]Nuclear Data Section, International Atomic Energy Agency, Vienna A-1400, Austria

Abstract

The utilization of experimental nuclear reaction data from EXFOR necessitates preprocessing of the data format, which remains challenging for users aiming to apply contemporary computational methods in their modern data analysis and nuclear data evaluation efforts. To address this issue, a directory-structured projectile/nuclide/reaction database inspired by EXFORTABLES has been created using the EXFOR Parser. This parser converts EXFOR format into JSON format and extracts physical quantities as datasets in a tabulated format (x, y, dx, dy), as well as in an SQL database, making retrieval and utilization much more straightforward for users.

1 Introduction

There is an emerging trend to use Machine Learning (ML) models in scientific research, particularly in the analysis of experimental data, by using algorithms that learn from data to make predictions or to find hidden patterns. However, this process involves data preparation, also referred to as data preprocessing, where raw data undergoes transformations to enable data scientists and analysts to apply ML algorithms effectively. In the fields of nuclear physics and nuclear data, a significant challenge arises from the format of the Experimental Nuclear Reaction Database (EXFOR) [1].

EXFOR follows a document-oriented database style, which is a semi-structured and key-value store data format. It was originally designed decades ago for the transmission of nuclear reaction data in ASCII text with fixed width column constraints, EXFOR format served its purpose in an era with limited computing capabilities. Even now, accessing EXFOR data programmatically requires users to undergo a data preparation process before use. However, the current landscape demands a more flexible approach and accessing EXFOR data programmatically is essential. The Nuclear Data Section (NDS) at the International Atomic Energy Agency (IAEA) is entrusted with developing access to EXFOR data, such as the EXFOR web retrieval system [2]. Besides the dissemination from NDS, already long before, such inconvenience was recognized and the X4toC4 code [3] has been developed to make numerical data more accessible in the common computational format, i.e., the C4 format.

A Subgroup (SG30) on the topic of "Quality Improvement of the EXFOR database" [4] was initiated in the early 2000s within the Working Party on International Evaluation Cooperation (WPEC) under the Nuclear Energy Agency (NEA). The subgroup's objective was to

[*]Present address: Nuclear Data Section, International Atomic Energy Agency, Vienna A-1400, Austria

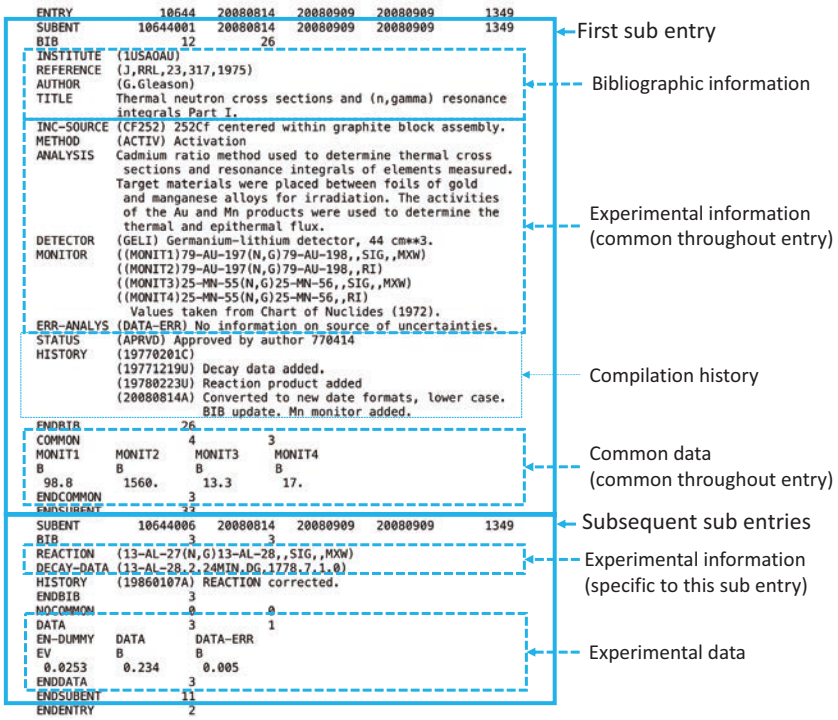

Figure 1: Structure of an EXFOR entry: The bibliographic information and common experimental conditions in `BIB` and common data block in `COMMON` appear in the first `SUBENT`. The subsequent `SUBENT`s have numerical data table in `DATA` section.

establish EXFOR as an easily accessible and accurate database. A directory-structured projectile/nuclide/reaction database, Newbase, was developed as the outcome of the SG30, allowing easy access to the experimental data by restructuring C4 data file. Later, Newbase was superseded by EXFORTABLES [5, 6] and is still actively used for the TENDL library [7] evaluation. A similar approach has been taken for the NucML system [8], which was the first example of an open-source, python-based supervised ML pipeline. NucML uses the C4 data file parser to prepare data that sorts the EXFOR datasets by projectile, target, MF, MT numbers defined in ENDF-6 format [9], and incident energy in separate files for each target [10] in directories for each projectile. These examples have proven that the original EXFOR format is not sufficient for these large-scale data analyses and applications. Another example for the visualization purpose is the Matlab extension [11] to plot nuclear reaction cross-section data as a function of the incident particle energy found in the C4 data file.

The strong motivations underlying the example above to use C4 data file are tabulated in (x, y, dx, dy) format, the unit conversion and unification, as well as the separation of an EXFOR entry into the nuclear physics-relevant dataset, in other words, the assignment of relevant MT-MF number defined in ENDF-6 format. The original EXFOR contains the numerical data with units as reported in the publication (i.e., barn as `B` or millibarn as `MB` in the `DATA` section). Hence, one needs to convert units accordingly. However, these reformat and data preparation tasks require a considerable amount of knowledge about the EXFOR format [12] and compilation rules, resulting that it is not a work size suitable for users to undertake.

To our best knowledge, the first use case outside the NRDC community involving the handling of the EXFOR master file to convert datasets without relying on X4toC4 was x4i [13]. It parses EXFOR sections such as `BIB, COMMON, DATA` and fields such as `REACTION, MONITOR`, and creating a database and interface to access datasets. Expanding on the similar concept as

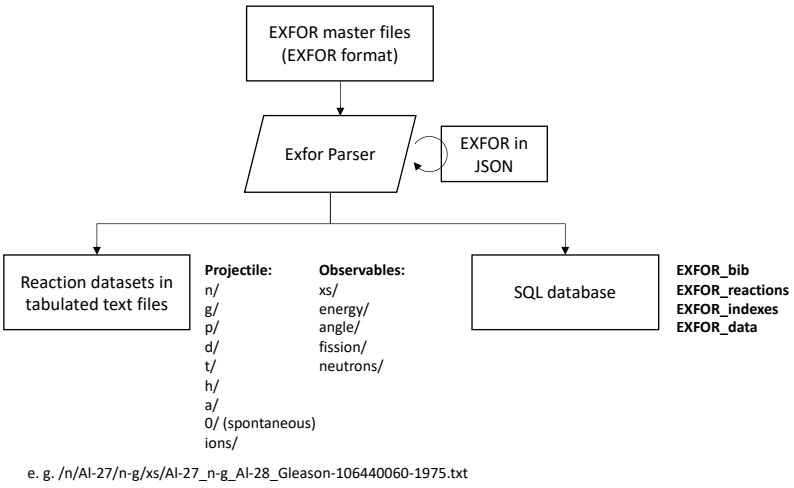

Figure 2: Schematic view of dataset creation from EXFOR master files.

x4i, NDS also enhanced our capabilities by developing two EXFOR parsers [14]. These parsers offer comprehensive control over the EXFOR fields and sections, enabling us to extract meaningful dataset based on the nuclear physics perspective in a tabulated format, akin to creating EXFORTABLES alike structured database. This approach ensures that we can navigate the complexities of the EXFOR more effectively.

2 Utilization of EXFOR master file format

The `ENTRY` in EXFOR corresponds to one piece of experimental work, typically representing one publication. Each work may consist of some separate experiments or physical quantities and hence datasets. The first sub-entry, `SUBENT`, contains bibliographic information and experimental conditions in `BIB` section, along with common data in the `COMMON` section. Subsequent sub-entries can also contain the same particulars for the sub-entry, accompanied by the actual experimental data in the `DATA` section, as illustrated in Fig. 1. The `REACTION` field is the key field that describes what nuclear reaction and quantity were measured. For instance,

```
REACTION   (13-AL-27(N,G)13-AL-28,,SIG,,MXW)
```

where ^{27}Al is the target nuclide, and ^{28}Al is the reaction product of Maxwellian-averaged `MXW` neutron capture `(N,G)` cross section `SIG` (a physical observable). The reaction product is obvious in this case, while in the following case;

```
REACTION   (92-U-238(N,F)ELEM/MASS,CUM,FY)
```

where the several cumulative fission products from neutron induced fission `(N,F)` of ^{238}U are measured and defined by mass and charge (`ELEM/MASS`). Thus, the complete reaction products cannot be uncovered until one examines the `ELEM` and `MASS` columns in the `DATA` section.

To handle and organize such information, including bibliographic and experimental details along with the numerical data, proper parsing is essential. The goal is to make these details searchable from a nuclear-physics perspective and accompanied data being easily accessible and to facilitate efficient retrieval and analysis. The parser is designed to construct the reaction index as a database that accommodates target nuclide, reaction path, reaction product, excited state, incident particle energy and measured physical quantities, and enabling the dataset to be searchable.

2.1 Generation of EXFORTABLES-Inspired Structured Database

Figure 2 illustrates the database creation process from EXFOR. Initially, the EXFOR parser reads the original EXFOR format and converts it into JSON. Subsequently, the parser processes the JSON to reconstruct the dataset based on bibliographic and `REACTION` information.

Similar to EXFORTABLES, the EXFOR parser generates files organized in directories such as projectile/nuclide/reaction/observable. For instance, directories for various projectiles like n/ g/ p/ d/ t/ h/ a/ and ion/ (heavy ions) are created. Additionally, observables such as xs/ angle/ energy/ fission/ are nested under the projectile/nuclide/reaction/ directory. As an example, the complete file name follows the format

`/n/Al-27/n-g/xs/Al-27_n-g_Al-28_Gibbons-11329-006-0-1961.txt.`

The file format is quite similar to that of EXFORTABLES as shown in Fig. 3. These generated text files are accessible online [15], and data tables are also stored in an SQL database. Consequently, a total of 596,067 reactions have been indexed, resulting in the creation of 564,833 files for cross sections (`SIG`), angular distributions (`DA`), energy distributions (`DE`), fission products (`FY`), and neutron observables (`NU`) from 25,919 entries. Our future plans include extending this indexing to cover additional observables.

```
# entry-subent-pointer  : 11329-006-0
# EXFOR reaction        : ['13-AL-27', ['N,G'], '13-AL-28,,SIG']
# incident energy       : 3.0000e-02 MeV
# target                : Al-27
# product               : Al-28
# level energy          : -
# MF-MT number          : 3 - 102
# first author          : J.H.Gibbons
# institute             : (1USAORL): Oak Ridge National Laboratory, Oak Ridge, TN
# reference             : (J,PR,122,182,1961)
# year                  : 1961
# facility              : (VDG): Van de Graaff
# git                   : https://github.com/IAEA-NDS/exfor_master/blob/main/exforall/113/11329.x4
# nds                   : https://nds.iaea.org/EXFOR/11329
#
#       E_in(MeV)       dE_in(MeV)            XS(B)           dXS(B)
      3.00000E-02      7.00000E-03      2.80000E-03      7.00000E-04
```

Figure 3: An example of ASCII text file in the structured database.

3 Conclusion

In spite of EXFOR data compilation effort, the retrieval of experimental data from EXFOR and the necessary data preparation before use have remained to pose significant challenges, causing delays in applying contemporary computational methods on modern users' work and nuclear data evaluation efforts. To address these challenges, we have developed the EXFORTABLES-inspired structured database using the EXFOR parser. While the idea to create EXFORTABLES originated in the early 2000s through the efforts of SG30 utilizing C4 data files, we have chosen to follow a similar path. Our approach involves leveraging EXFOR master files and ensuring the proper parsing of all relevant information. It is anticipated that the developed database with files containing EXFOR data in tabular (x, y, dx, dy) format will facilitate the retrieval of pertinent experimental data for data analysis and ML applications.

References

[1] Otuka, N. et al. "Towards a More Complete and Accurate Experimental Nuclear Reaction Data Library (EXFOR): International Collaboration Between Nuclear Reaction Data Centres (NRDC)". *Nuclear Data Sheets* 120 (2014), pp. 272–276.

[2] Zerkin, V. and Pritychenko, B. "The Experimental Nuclear Reaction Data (EXFOR): Extended Computer Database and Web Retrieval System". *Nuclear Instruments and Methods in Physics Research Section A: Accelerators, Spectrometers, Detectors and Associated Equipment* 888 (2018), pp. 31–43.

[3] Cullen, D. and Trkov, A. "Program X4TOC4". IAEA-NDS-80 (2001).

[4] Koning, A. "Quality Improvement of the EXFOR Database". NEA/NSC/WPEC/DOC(2010)428 (2011).

[5] Koning, A. "EXFORTABLES-1.0: An experimental nuclear reaction database based on EXFOR". IAEA-NDS-0235 (2020).

[6] Koning, A. *EXFORTABLES-2.0: Experimental nuclear reaction database based on EXFOR.* 2023. URL: https://nds.iaea.org/talys/.

[7] Koning, A. et al. "TENDL: Complete Nuclear Data Library for Innovative Nuclear Science and Technology". *Nuclear Data Sheets* 155 (2019). Special Issue on Nuclear Reaction Data, pp. 1–55. ISSN: 0090-3752. DOI: https://doi.org/10.1016/j.nds.2019.01.002. URL: https://www.sciencedirect.com/science/article/pii/S009037521930002X.

[8] Vicente-Valdez, P. J. *NucML*. 2022. URL: https://github.com/pedrojrv/nucml.

[9] Trkov, A., Herman, M., and Brown, D. A. *ENDF-6 Formats Manual: Data Formats and Procedures for the Evaluated Nuclear Data Files ENDF/B-VI, ENDF/B-VII and ENDF/B-VIII*. Tech. rep. CSEWG Document ENDF-102, BNL-203218-2018-INRE. Brookhaven National Laboratory, 2018.

[10] Vicente-Valdez, P. J. *ML_Nuclear_Data*. 2021. URL: https://github.com/pedrojrv/ML_Nuclear_Data.

[11] Selman, A. A. *ENEL (EXFOR Nuclear Extraction Library)*. 2024. URL: https://www.mathworks.com/matlabcentral/fileexchange/110930-enel-exfor-nuclear-extraction-library.

[12] Schwerer, O. *EXFOR Formats Manual*. Tech. rep. IAEA-NDS-207. Vienna: International Atomic Energy Agency, 2015.

[13] Brown, D. "x4i - The EXFOR Interface". Report LLNL-CODE-484151 (2011).

[14] Okumura, S., Schnabel, G., and Koning, A. "Developing a New Web Service for Experimental Nuclear Reaction Database (EXFOR) Using RESTful API and JSON". *Proceedings of the 16th International Conference on Nuclear Reaction Mechanisms (Varenna, Italy, June 11 - 16, 2023)*. EPJ Web of Conferences, 2024, (in press).

[15] Okumura, S. *EXFORTABLES_py: EXFORTABLES created by a Python based exfor_parser*. 2023. URL: https://github.com/IAEA-NDS/exfortables_py.

22. Neutron total and capture cross section measurements of ^{nat}Er at ANNRI

Gerard ROVIRA[†1], Atsushi KIMURA[1], Shoji NAKAMURA[1], Shunsuke ENDO[1], Osamu IWAMOTO[1], Nobuyuki IWAMOTO[1], and Tatsuya KATABUCHI[2]

[1]Nuclear Science and Engineering Center, Japan Atomic Energy Agency, Ibaraki, Japan
[2]Laboratory for Zero-Carbon Energy, Tokyo Institute of Technology, Tokyo, Japan
[†]Email: gerard.rovira@jaea.go.jp

Abstract

Neutron total and capture cross section of ^{nat}Er experiments have been conducted at the Accurate Neutron-Nucleus Reaction measurement Instrument (ANNRI) of the Materials and Life science Facility (MLF) in the Japan Proton Accelerator Research Complex (J-PARC). Neutron transmission experiments were performed to determine the neutron total cross section using Li-glass detectors with three samples with different thicknesses of 1 mm, 0.175 mm and 0.05 mm. For the neutron capture cross section, neutron time-of-flight experiments were conducted by using two 0.025 mm thick samples with two different detector setups, a NaI(Tl) spectrometer and a Ge spectrometer. Preliminary cross section results obtained with the different samples and detector setups are compared and discussed.

1 Introduction

In order to improve the economic viability of nuclear reactors, the extension of the nuclear fuel life has long been seen as an effective approach. Notwithstanding, due to criticality concerns, this was always thwarted by the 5 wt% limitation on ^{235}U, as an increase above the 5 wt% threshold would mean a major reformulation of both reactor criticality and safety assessments for the present nuclear reactors. An innovative fuel configuration involving the use of Erbium, the Erbia-credit super high burnup (Er-SHB) fuel, has been proposed which allows for the fuel life to be extended while providing several physical improvements. The negative reactivity introduced by Erbium offers a means to increase the enrichment of ^{235}U above 5 wt% while treating the fuel as if the enrichment of ^{235}U were to be lower than 5 wt%, similar to present LWR reactions. This means that, the present fuel configuration could be used in present LWR reactors without any major reformulation [1, 2]. However, for this to be achievable, an improvement of the nuclear data accuracy for the neutron capture cross section of Erbium is required [3]. One of the main reasons for this is the lack of experimental data for the neutron capture cross section of ^{nat}Er. To solve this, in the present work, the neutron capture cross section of ^{nat}Er was measured using two different detectors setups, a NaI(Tl) spectrometer and a Ge spectrometer, to increase the reliability of the present results. Moreover, since the capture cross section is very large and close to the neutron total cross section, neutron transmission measurements were also performed using three samples with different thicknesses and Li-glass detectors. In the present paper, preliminary results obtained with the different samples and detector setups are presented and compared.

2 Experimental Setup

The experiments were conducted at the Accurate Neutron-Nucleus Reaction measurement Instrument (ANNRI) of the Materials and Life science Facility (MLF) in the Japan Proton Accelerator Research Complex (J-PARC) using the pulsed neutron beam generated by 3 GeV protons impinging to the Japanese Spallation Neutron Source (JSNS). Neutrons were generated at a repetition rate of 25 Hz with a beam power of about 800 kW, in double-bunch mode.

For the neutron total cross section experiments, neutrons were detected using two Li-glass detectors, a GS20 (95% and higher ^{6}Li-enriched) and a GS30 (99% and higher ^{7}Li-enriched) detectors, which were used in conjunction at a flight length position of about 28.7 m from the moderator surface. The GS20 detector was employed to detects neutrons by means of the ^{6}Li(n,α)^{3}H reaction. Nonetheless, since the detector also contains ^{7}Li, it is also susceptible to detect γ-rays. Hence, the GS30 detector, with a high concentration of ^{7}Li, was utilized to determine the background level mainly caused by γ-rays.

In the neutron capture experiments, two different detector setup were employed to detect prompt capture γ-rays in separate measurements. The first one consisted on a NaI(Tl) spectrometer situated at a flight path of 27.9 m and at a 90° angle with respect to the neutron beam axis. The second setup comprised two germanium cluster-type detectors at a flight path of 21.5 m. In both capture experiments, the neutron time of flight (TOF) was determined as the time difference between the spallation event that generated neutrons and the successive detected prompt γ-rays by the two detector setups. Further information about the three different experimental setups can be found elsewhere [4, 5, 6].

2.1 Measured Samples

In the present experiments, several foils of ^{nat}Er were employed to derive both the neutron total and the neutron capture cross sections.

For the neutron transmission experiments, three samples were measured with different thicknesses of 1 mm, 0.175 mm and 0.05 mm. These samples consisted of metallic foils with area densities of 3.4×10^{-3}, 5.7×10^{-4} and 1.5×10^{-4} at/b and were placed before the intermediate collimator of the ANNRI beamline, so that scattered neutrons at the sample would not induce into background events.

For the neutron capture experiments, metallic foils of 0.025 mm thickness were employed. In the case of the experiments with the NaI(Tl) spectrometer, a sample with a diameter of 20 mm and an area density of 7.9×10^{-5} at/b was employed. For the Ge spectrometer experiments however, the sample diameter was 5 mm and a similar area density of 7.4×10^{-5} at/b to reduce the dead time, as the sample position of the Ge spectrometer is much closer to the detector than that of the NaI(Tl) spectrometer. Moreover, carbon samples were employed to determine the sample-dependent background, gold samples were used to normalize the neutron capture cross section results and finally, boron samples were also measured to obtain the energy dependence of the incident neutron flux, for each detector setup.

3 Data Analysis

The measured data for both the neutron transmission and capture experiments were analyzed in offline analysis. The data was recorded in two-dimensional list data files with time-of-flight and pulse-height data information.

3.1 Neutron Total Cross Section

For the neutron transmission experiments, the transmitted neutrons through the sample were measured with the GS20 detector. Background events from γ-rays emitted by surrounding materials capturing neutrons in the experimental room were also detected. To remove the influence of the background events, the GS30 detector was employed since it displays an extremely low sensitivity to neutrons and can accurately determine the γ-rays background level in the experimental room. The background level obtained was normalized using measurements with thick black filters of Ag, Mn, Co, Cd and In. These elements present large scattering resonances in which all incoming neutrons interact, creating time windows where no neutrons reach the experimental area. In these time windows the event rate becomes very low since it only includes the γ-rays background level and allowing for the GS30 detector measured events to be normalized to the event rate of the GS20 detector in these regions.

The neutron transmission ratio for each measured sample was then determined by dividing the detected net neutron events, after subtracting the influence of background γ-rays, of each sample by that measured in a blank measurement without any sample.

3.2 Neutron Capture Cross Section

The neutron capture yields, for both the NaI(Tl) and Ge experiments, were determined from the measured prompt γ-rays emitted in the capture events by means of the pulse height weighting technique. To accurately accomplish that, several layers of background events had to be removed. These background layers include sample-independent background events, estimated using a blank resonance without any sample and also using the long 160 ms TOF window, when protons are sent to different facilities and, hence, no neutrons are generated at the JSNS; and sample-dependent background events, which were determined using carbon sample measurements.

The relative neutron capture cross section was then obtained by dividing the neutron capture yields by the incident neutron flux, for the experiments with both the NaI(Tl) and Ge detectors. The shape of the incident neutron flux was derived by gating the 478 keV γ-rays emitted from the ^{10}B(n,α)^{7}Li reaction measured with the boron samples, after removing the energy-dependent component of the ^{10}B(n,α)^{7}Li reaction rate using the Monte-Carlo code PHITS [7].

4 Cross Section Calculation

The preliminary neutron total cross section for ^{nat}Er was determined from the transmission ratios using the following equation:

$$\sigma_{tot_{Er}}(E_n) = \frac{logT(E_n)}{S_{Er}}, \tag{1}$$

where $\sigma_{tot_{Er}}$ and T are the neutron total cross section of ^{nat}Er and the transmission ratio for each sample, respectively, as a function of neutron energy E_n; and S_{Er} is the area density for each sample.

For the case of the neutron capture cross section, the relative neutron capture cross section was normalized using the Au sample measurements. In the experiment with the NaI(Tl) detector, the saturated resonance method was applied using the first resonance of Au. The principle of this method is that, since the first resonance of Au is completely saturated, all incoming neutrons interact with the sample and, hence, the neutron capture yield equals 98% the incident neutron flux, assuming 2% of the incident neutrons are backscattered. For the experiments with the Ge detector, this method could not be applied since the event rate at the first resonance

was too high. In this case, the cross section at the thermal energy point was employed to normalize the present results since it has been widely measured, making the cross section at for the thermal point of Au highly reliable. The process to determine the preliminary neutron capture cross section can be expressed as:

$$\sigma_{capt_{Er}}(E_n) = \frac{Y(E_n)}{\phi(E_n) S_{Er}} N_{det}, \tag{2}$$

where $\sigma_{capt_{Er}}$, $Y(E_n)$ and $\phi(E_n)$ are the neutron capture cross section, neutron capture yield and the incident neutron flux measured by each detector; and S_{Er} and N_{det} mean the sample area density in at/b and the normalization factor for each detector setup.

5 Preliminary Results and Discussion

Preliminary results for the neutron total and neutron capture cross sections of ^{nat}Er were determined using the formulations explained in section 4. The neutron total cross section obtained with the three samples are shown in Fig 1.

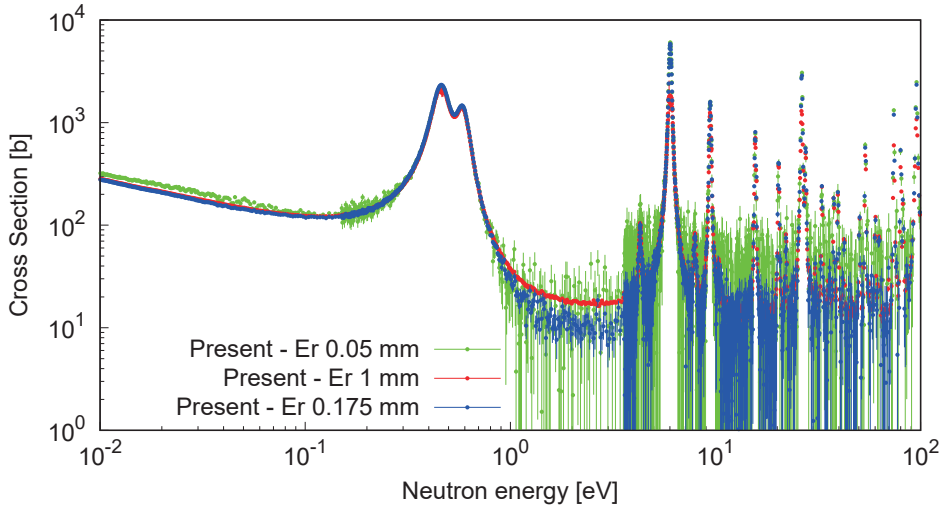

Figure 1: Preliminary results for the ^{nat}Er neutron total cross section from 0.01 to 100 eV obtained from the three measured samples.

The present results only include the contribution from the statistical uncertainty but it seems that good agreement was obtained from 0.01 eV up to the third resonance between the 1 mm and the 0.175 mm thick samples. Below 0.1 eV the thinner 0.05 mm thick sample displays a larger cross section value. Further analysis is required to determine the cause of this discrepancies, together with a quantification of the present systematic uncertainties.

For the neutron capture cross section results, the results measured with both detector setups are compared in Fig. 2. These preliminary results do not include corrections from self-shielding and multiple scattering effects and, since the self-shielding effect has a large impact on the cross section, the present results cannot be compared to nuclear data libraries. Nonetheless, since the samples have similar area densities, the agreement between the cross sections measured with

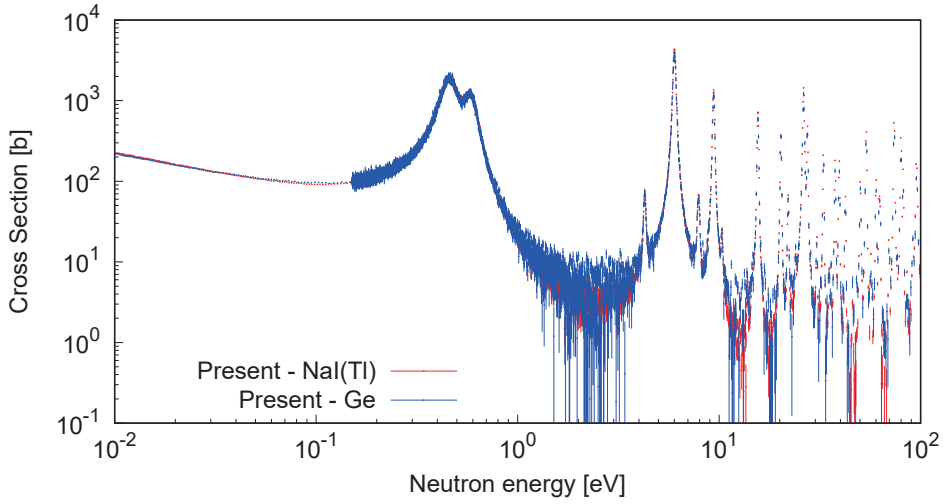

Figure 2: Preliminary results for the ^{nat}Er neutron capture cross section from 0.01 to 100 eV measured with the two different detector setups. The data below 0.2 eV was evaluated with a different bin width of 100 μs, making the statistical uncertainty very small.

both detector setups can still be evaluated. Above 10 eV, the agreement cannot be evaluated visually since the detectors are situated at a different flight length and, hence, the effects of the pulse width together with the double-bunch mode makes the resonance shapes much different. In order to accurately evaluate this, a resonance analysis is required taking into account the resolution function of the ANNRI beamline.

6 Summary

The neutron total and capture cross section of ^{nat}Er were measured at the ANNRI beamline of MLF/J-PARC.

For the transmission experiments, three natural Er erbium foils with different thicknesses of 1 mm, 0.175 mm and 0.05 mm were used and neutrons transmitted through the foils were measured using Li-glass detectors. Preliminary results obtained with the 1 mm and the 0.175 mm samples agree from 0.01 to about 10 eV. In contrast, the results of the thinner 0.05 mm sample provide higher results below 0.1 eV.

For the neutron capture cross section, preliminary results with both detector setups were shown. These results do not include corrections for self-shielding, which are expected to be important. Notwithstanding, since the samples have very similar area densities, these results can be still used to evaluate the performance of both detector setups. Good agreement was obtained from 0.01 to 10 eV between both detectors. Above 10 eV, a more accurate analysis using a resonance analysis code accounting for the ANNRI resolution function is required.

References

[1] Yamasaki M, et al. Development of erbia-credit super high burnup fuel: Experiments and numerical analyses. Nucl Technol. 2012;177:63–72.

[2] Pergreffi R, et al. Neutronics characterization of an erbia fully poisoned PWR assembly by means of the APOLLO2 code. EPJ Nucl Sci Technol. 2017;3:8.

[3] Guglielmelli A. NEA Nuclear Data High Priority Request List [Internet]. Available from: https://www.oecdnea.org/dbdata/hprl/hprlview.pl?ID=539.

[4] Kimura A, et al. Neutron total and capture cross-section measurements of ^{155}Gd and ^{157}Gd in the thermal energy region with the Li-glass detectors and NaI(Tl) spectrometer installed in J-PARC MLF ANNRI. J. Nucl. Sci. Technol. 2023; 60:678-696.

[5] Rovira G, et al. Neutron capture cross-section measurement and resolved resonance analysis of ^{237}Np. J. Nucl. Sci. Technol. 2020;57:24-39.

[6] Endo S, et al. Neutron capture and total cross-section measurements and resonance parameter analysis of niobium-93 below 400 eV. J. Nucl. Sci. Technol. 2022; 59:318-333.

[7] Sato T et al., Features of Particle and Heavy Ion Transport Code System PHITS Version 3.02, J. Nucl. Sci. Technol. 2018; 55:684-690.

23. Measurement of the very-forward-angle neutron elastic scattering and PHITS simulation for neutron shielding

Tomoya NAKADA[†1], Tatsuya WADA[2], Saya IWAI[1], Teppei IWAMOTO[1], Airu MAKITA[3], Mariko TACHIBANA[1], Toi TACHIBANA[1], Juzo ZENIHIRO[1], Harutaka SAKAGUCHI[4], Masanori DOZONO[1], Shintaro OKAMOTO[1], and Takayuki YANO[1]

[1]Department of Physics, Kyoto University
[2]Yukawa Institute for Theoretical Physics (YITP), Kyoto University
[3]International Center for Elementary Particle Physics (ICEPP), University of Tokyo
[4]Research Center of Nuclear Physics (RCNP), Osaka University
[†]Email: nakada.tomoya.83m@st.kyoto-u.ac.jp

Abstract

We have proposed a neutron elastic scattering at very forward angles for precise determination of neutron root-mean-square radius, which is important to understand the symmetry energy of the nuclear matter equation of state. Neutron elastic scattering cross sections at 63.4 MeV have been measured at laboratory angles of 4° and 7°. The obtained data is consistent with a theoretical calculation and the previous data, but had large statistical errors because there were too many backgrounds. To investigate origins of the backgrounds, Monte-Carlo simulations with the code PHITS have been performed. A new setup that can reduce statistical errors has been studied with the PHITS simulations.

1 Nuclear matter EoS

In equation of state (EoS) of nuclear matter, energy per nucleon, E, is described as a function of density, ρ, and isospin asymmetry degree, δ, in the following.

$$E(\rho, \delta) = E(\rho, 0) + S(\rho)\delta^2 + \mathcal{O}(\delta^4) \tag{1}$$

$S(\rho)$ is the symmetry energy as

$$S(\rho) = S_0 + \frac{L}{3\rho_0}(\rho - \rho_0) + \mathcal{O}((\rho - \rho_0)^2), \tag{2}$$

where $\rho_0 \sim 0.16\,\mathrm{fm}^{-3}$ is the saturation density and L is called the slope parameter. Constraints on the symmetry energy is important for understanding of the nuclear many-body system which is related to high-density objects, such as neutron stars. The symmetry energy is essential in neutron matter ($\delta = 1$), but it is still less certain than the symmetric nuclear matter EoS, $E(\rho, 0)$.

It is well known, especially in ^{208}Pb, that there is a strong linear correlation between the slope parameter and neutron skin thickness from various mean-field calculations [1]. The neutron skin thickness is defined as

$$\begin{aligned} \delta R_{np} &= R_n - R_p \\ &= \sqrt{< r_n^2 >} - \sqrt{< r_p^2 >}, \end{aligned} \tag{3}$$

where R_n, R_p are neutron and proton root-mean-square (RMS) radius. The uncertainty of the neutron RMS radius in ^{208}Pb is still large, while its proton RMS radius is precisely determined by electron scattering.

2 Neutron elastic scattering

Proton elastic scattering (PES) and the parity radius experiment (PREX) which is based on parity violation are well-known methods to determine the neutron RMS radius. PES has a large cross section, but there is theoretical uncertainty at backward angles. It also has the disadvantage that the Coulomb force is dominant in low momentum transfer, $q^2 \to 0$, where cross section data is more sensitive to the nuclear size. Neutron elastic scattering (NES) at very forward angles was employed as a probe to precisely determine the neutron RMS radius. Therefore, we have proposed the the very-forward-angle NES, whose cross section is as large as that of the PES and that is without the Coulomb force.

To study the neutron RMS radius from the NES angular distribution, we have developed a new reaction program. A relativistic impulse approximation (RIA) model originaly developed by Horowitz, Hillhouse *et al*. successfully has explained the experimental results of PES from 60 MeV to 200 MeV [2–4]. Based on the RIA model for PES, we have developed a new RIA model (Neutron-RIA) describing NES by assuming charge symmetry of nucleon-nucleon interaction. In order to determine the neutron RMS radius from the differential cross section, the model that considers medium effects in the nucleus has been developed. According to the present Neutron-RIA, if the cross section can be determined within approximately 5%, the neutron RMS radius can be determined within 1% errors. NES at very forward angle had not been performed yet. Therefore, We have proposed a new experiment to measure NES cross section with 5% precision.

3 Experiment

3.1 Experimental method

The experiment was performed in N0 course (ToF tunnel) at Research Center of Nuclear Physics (RCNP) in Osaka University. 65 MeV proton beams were employed to produce secondary neutron beams by the reaction of ^{7}Li(p, n)^{7}Be (G.S. + 1$^{\text{st}}$ E.S.). The neutron beams were irradiated to ^{208}Pb and ^{40}Ca targets. Elastic scattering was measured at laboratory angles of 4.01°, 4.49°, 7.18°, and 7.67°. Figure 1 shows a top view of the experimental setup. Since the secondary neutron beams spatially spread, it was collimated by iron collimator. In addition to the collimator in front of the targets, shielding blocks were placed next to the targets, and a downstream shield with another collimator of iron was placed downstream. Scattered neutrons were measured with liquid scintillators (BC-501A) by the pulse shape discrimination method. The energy of the neutrons was also measured by the Time-of-Flight (ToF) method.

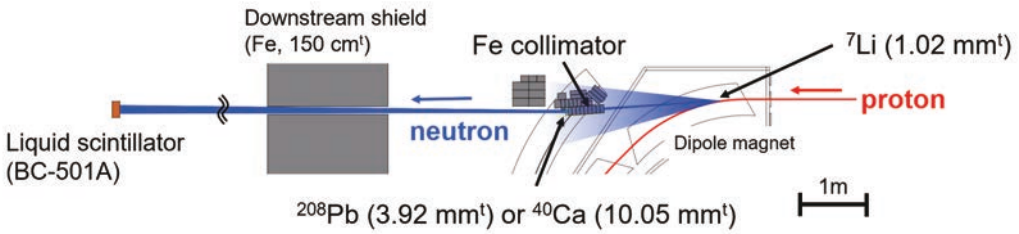

Figure 1: Top view of the experimental setup. The ^{7}Li target was irradiated with proton beams from AVF cyclotron. It produced the secondary neutron beams by the reaction of ^{7}Li(p, n)^{7}Be. Scattered neutrons for ^{208}Pb(n, n) and ^{40}Ca(n, n) were measured by using the liquid scintillators

3.2 Results

Figure 2 shows the measured angular distribution for ^{208}Pb(n, n) and ^{40}Ca(n, n). The measurements has been conducted at $\theta_{\mathrm{lab.}} = 4.01°$, 4.49°, 7.18°, and 7.67° and the results for ^{208}Pb(n, n) (red circles) and ^{40}Ca(n, n) (blue circles) are plotted. Theoretical calculations by Neutron-RIA and the previous data by E. L. Hjort *et al.* [5] are also included in Fig. 2. The results for $\theta = 7°$ are consistent with the previous data. We also obtained the NES differential cross sections at $\theta = 4°$ for the first time.

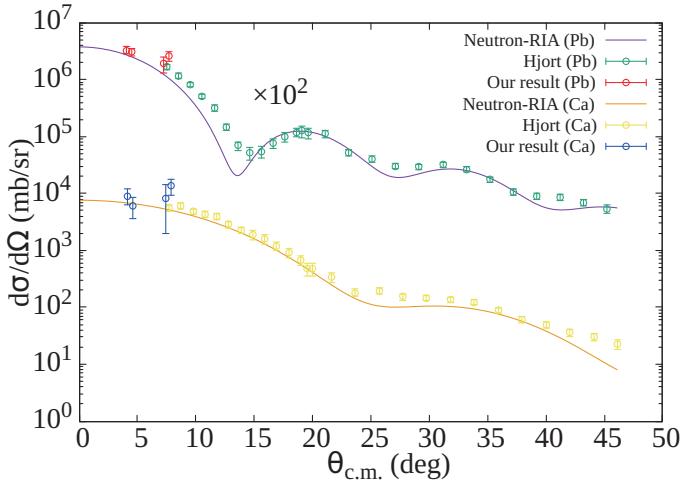

Figure 2: Comparison of ^{208}Pb(n, n) and ^{40}Ca(n, n) differential cross sections at 63.4 MeV from this experiment (red and blue circles) with the previous data at 65 MeV by E. L. Hjort *et al.* [5]. The Neutron-RIA calculations are also shown.

However, the statistical errors of the results ranged from 15.0% to 32.5%, which was more than three times worse than the requirement. Estimation of signal-to-noise ratio, S/N, which was based on scattering cross sections from nuclear data, before the experiment was $S/N \sim 10$, but the real value was $S/N \sim 10^{-1}$, that the background events were about 100 times more than estimated.

To keep the statistical errors within 5%, at least a ten-fold increase in S/N, namely $S/N \sim 1$, is required. The number of background neutrons must be reduced to less than one-tenth of the present number for next measurements. We have analyzed the present setup, especially the background shielding, by Monte-Carlo simulations with the code PHITS [6], and we will report the results of the simulations.

4 PHITS simulation for high-energy neutron shielding

To investigate the backgrounds, PHITS simulations have been performed. We have reproduced the same setup on PHITS and performed particle transport calculations. In the setup at $\theta = 4°$, the background rate was higher than in the setup at $\theta = 7°$. We reproduced the setup including collimator, shielding blocks, dipole magnet and downstream shield at $\theta = 4°$. Neutron beams were generated by using real data of energy spectrum of the reaction of ^{7}Li(p, n)^{7}Be, which was measured in the same setup. Figure 3 shows the energy structure of background neutrons, with a peak around 63 MeV, which is consistent with the experimentally measured ToF spectrum. Table 1 shows the number of background neutrons coming to the detector at $\theta_{\text{lab.}} = 4.01°$. The simulation results have a large standard error due to limited simulation time. However, the simulaiton results agree with the experimental results. Therefore, considering the PHITS simulations in the present experimental condition to be valid, further simulations were performed under the same settings.

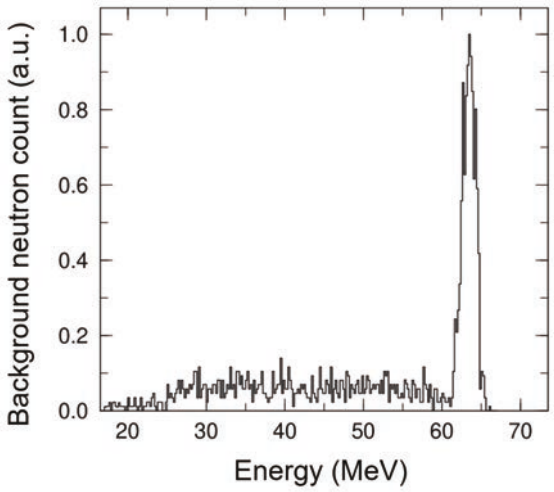

Figure 3: Energy structure of neutrons that came to detector in PHITS simulation.

Table 1: Comparison of number of background neutrons at 62 MeV $< E <$ 64.6 MeV in the PHITS simulations and our experimental result. Both are background counts at $\theta_{\text{lab.}} = 4.01°$. The counts below are converted to the counts in the actual measurement time.

Angle (deg) (lab.)	Simulation result	Our experimental result
4.01	3198 ± 406	3629 ± 60

We have simulated where the background neutrons were scattered and come to the detector. Figure 4 shows the setup near the target. The shielding in the setup was classified into four regions: collimator, shielding blocks, downstream shield, and others. We have investigated where the background neutrons were scattered in the four regions. Table 2 is the result of the origin of the background neutrons. It shows that the percentage of scattered neutrons only in the collimator is 80.6%, and in both the collimator and the shielding blocks is 6.5%. Therefore, the neutrons scattered in the collimator account for 87.1% of the total. Most of the backgrounds are come from the collimator.

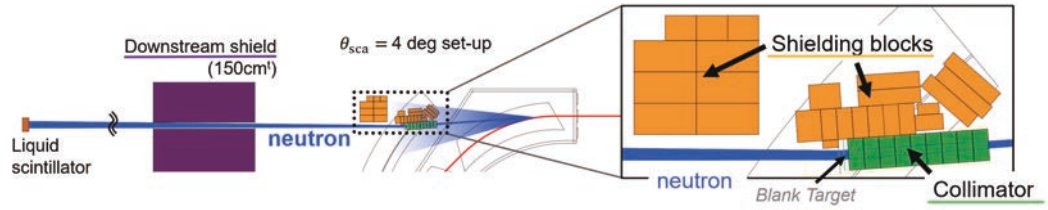

Figure 4: Top view of experimental setup and definition of collimator (green), shielding blocks (orange) and downstream shield (purple) in the geometry of the PHITS simulations.

Table 2: Origin of background neutrons.

Origin of background neutrons	Background neutrons count	Percentage
All background neutrons	3198 ± 406	100%
Scattered only in collimator	2579 ± 365	80.6%
Scattered in both collimator and shielding blocks	206 ± 103	6.5%
Scattered only in shielding blocks	103 ± 73	3.2%
Other (Downstream shield, supporting frame, etc.)	309 ± 74	9.7%

We also performed simulations by changing collimator thickness. Figure 5 shows the results of background neutron count for different collimator thicknesses. The red circles are the simulation results for the Fe collimator. It was found that the background count decreases exponentially with increasing the collimator thickness.

Simulations were also performed when the material was changed from iron to a tungsten alloy (W-alloy) with higher density. The blue circles in Fig. 5 show the background count with the W-alloy collimator. It was found out that the W-alloy collimator has a higher shielding ability than the Fe collimator.

As mentioned in Chapter 3, S/N needs to be reduced to approximately one-tenth of the present value to achieve statistical errors of less than 5%. In Fig. 5, the red line is the value where $S/N \sim 1$ can be achieved. If the thickness is increased up to 75 cm, S/N can be reduced to $S/N \sim 1$.

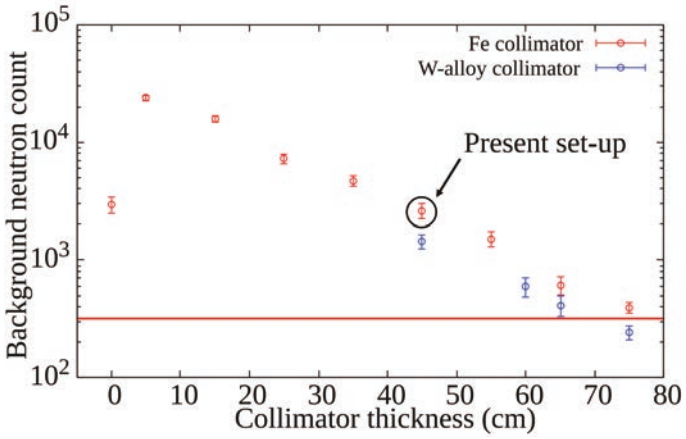

Figure 5: Simulations of neutron count for different collimator thickness. Comparison of the results with Fe collimator (red circle) and W-alloy collimator (blue circle) is shown. An approximate count that makes $S/N \sim 1$ possible (red line) is also shown.

5 Summary

We have measured ^{208}Pb(n, n) and ^{40}Ca(n, n) at very forward angles ($\theta = 4°$ and $7°$) at RCNP. The measured angular distributions were consistent with the previous data and the RIA model, which we have developed. However, since the background was still large, the statistical errors of the cross section data were over 15.0%. To evaluate the backgrounds, Monte Carlo simulations with the code PHITS were performed, and the PHITS results were confirmed that they were consistent with the experimental results. PHITS calculations have revealed that scattering in the collimator for the secondary neutron beams was major cause of the backgrounds. The shielding ability with respect to the collimator thickness was also evaluated. Based on these simulations, to reduce the backgrounds, we found out that we need to make the collimator thicker. Measurements with a 75 cm thick collimator will be performed.

References

[1] Roca-Maza, X. et al., Neutron Skin of ^{208}Pb, Nuclear Symmetry Energy, and the Parity Radius Experiment, Phys. Rev. Lett., vol. 106, 2011, 252501.

[2] Horowitz, C.J. et al., The Relativistic Impulse Approximation, In: Langanke, K. et al. (eds) Computational Nuclear Physics 1. Springer, Berlin, Heidelberg, 1991, pp.129-151.

[3] Li, Z.P. et al., Energy-dependent Lorentz covariant parameterization of the NN interaction between 50 and 200 MeV, Phys. Rev. C, vol. 77, 2008, 014001.

[4] Li, Z.P. et al., Validity of the relativistic impulse approximation for elastic proton-nucleus scattering at energies lower than 200 MeV, Phys. Rev. C, vol. 78, 2008, 014603.

[5] Hjort, E.L. et al., Measurements and analysis of neutron elastic scattering at 65 MeV, Phys. Rev. C, vol. 50, 1994, pp.275-281.

[6] Sato, T. et al., Recent improvements of the particle and heavy ion transport code system – PHITS version 3.33, J. Nucl. Sci. Technol., vol. 61, 2024, pp.127-135.

24. Evaluation of Photonuclear Reaction Cross-section Data for ^{209}Bi at 13 and 17 MeV Photon Energies

Thuong Thi Hong NGUYEN[1], Nobuyuki IWAMOTO[2], Toshiya SANAMI[1,3]
[1]SOKENDAI, Shonan Village, Hayama, Kanagawa 240-0193, Japan
[2]Nuclear Data Center, Japan Atomic Energy Agency
2-4 Shirakata, Tokai-mura, Naka-gun, Ibaraki-ken 319-1195, Japan
[3]KEK, 1-1 Oho, Tsukuba-shi, Ibaraki-ken 305-0801, Japan
[*]Email: ngthuong@post.kek.jp

Newly obtained experimental data on photoneutron energy spectra for ^{209}Bi at 13 and 17 MeV photon energies were involved in the photonuclear data evaluation that was done using the CCONE code system and the reaction cross-section data from the EXFOR database. The evaluation by the CCONE fits the spectrum at 13 MeV by reproducing the total photoneutron cross-section reasonably but doesn't do that at 17 MeV. In addition, good agreements in the partial photoneutron production cross-sections between the reproduction by the evaluation and the experiments have been achieved.

1. Introduction

Photonuclear data containing information on interactions between photons and nuclei play an important role in a wide range of applications such as radiation shielding, radiation transport analyses, nuclear waste transmutation, and calculation of absorbed dose in the human body during radiotherapy [1]. As a result, many measurements of photonuclear reaction cross-section, so far, have been carried out all over the world and reviewed in references [2-5]. Despite such experimental works, systematic differences still exist among the data measured with different experimental facilities and methodologies. This fact makes it difficult to prepare a photonuclear data library for all nuclei covering a wide range of photon energies only based on the measured cross-sections.

The photonuclear data evaluation, in general, consists of three steps: compilation of experimental cross-section data, reproduction of the cross-section using suitable theoretical nuclear reaction models, and assessment of the reproduction based on the experimental data. Following the evaluation, production cross-section, and energy and angular distribution of emitted particles at a desired incident photon energy can be obtained, which is applicable in practice. However, the evaluation use of the energy and angular distributions of emitted particles has been limited because of scarce experimental data on those types of information.

Recently, double differential cross-sections (DDXs) of photoneutron production for several medium-heavy elements at 13, 17, and 20 MeV photon energies have been measured by our group [6-9]. To take into account these data in the photonuclear data library for applications as well as assess these kinds of data produced by theoretical nuclear reaction models, we would like to propose a new methodology to

evaluate the photonuclear data based on the DDXs of photoneutron production using the CCONE code system [10] which was developed for nuclear data evaluation for the particle-induced reactions below 200 MeV and applied for photonuclear data evaluation on 2014 [11]. As a first effort, the evaluation has been done for a monoisotopic target material, bismuth, which has the available data of photoneutron DDXs at 13 and 17 MeV photon energies given in [8-9].

2. Methodology

The proposed methodology starts with the compilation of experimental photonuclear reaction cross-section data from the EXFOR database [12]. Our concerns are the total photoneutron cross-sections (γ, sn), photoneutron production cross-sections $(\gamma, \mathrm{x}n)$, and partial reaction cross-sections. The cross-section measurements, so far, have been performed mainly at Lawrence Livermore National Laboratory (LLNL, USA), CEA Paris-Saclay (France), and recently at the NewSUBARU facility at the University of Hyogo (Japan). The results obtained at the three laboratories for the same nuclei show discrepancies in magnitude for (γ, sn) as well as the partial cross-section [1].

The CCONE code system used in this study is based on the Hauser-Fechbach statistical model and preequilibrium two-component exciton model. CCONE gives not only reaction cross-sections but also partial reaction cross-sections and DDX. Firstly, the total photoneutron cross-sections were reproduced by adjusting the level density and gamma strength function of nuclei. After that, the calculated DDXs of photoneutron production were compared to the measured data. The emission of photoneutrons is described by two processes, preequilibrium and compound, in CCONE. To apply CCONE to a photonuclear reaction, a 1p-0h initial state for cascade-exciton calculation was selected [1]. The fraction of the photoneutron production during the two processes was controlled via a multiplying factor denoted as *n-factor* by the state density of the neutron shell in the exciton model. In this study, the factor was determined to reproduce the experimental DDX as much as possible, especially for the photoneutron energy region with the available DDX data, for instance, above 4 MeV. Finally, to assess this methodology, the partial and $(\gamma, \mathrm{x}n)$ reaction cross-sections were extracted and compared with experimental data.

3. Results and discussions

3.1. Reaction cross-sections

For comparison with the (γ, sn) and partial reaction cross-sections, we chose the experimental data by Gheorghe et al. [13], which have been obtained with high-intensity monoenergetic photon beams at the NewSUBARU facility.

Figure 1 shows the results of (γ, sn), (γ, n), and $(\gamma, 2n)$ cross-sections together with the experimental ones. The reproduction for the (γ, sn) cross-section is acceptable as shown in the upper left piece of the figure. As aforementioned, we used the experimental partial reaction cross-sections to assess our evaluation. On the pieces of (γ, n) and $(\gamma, 2n)$ cross-sections, the black and blue lines correspond to the cross-sections with two distinct values of *n-factor*, default one (1.0) and adjusted one of 0.55. The value of 0.55 was determined by the possibility of reaching the experimental data at 17 MeV photon energy, especially for photoneutron energy above 4 MeV, as shown in the next section. The reason for consideration of 17 MeV photon energy is the underestimation of the experimental (γ, n) cross-section and overestimation of $(\gamma, 2n)$ one for photon energies above 15 MeV, as shown in Figure 1. A good reproduction for the (γ, n) cross-section has been achieved with *n-factor* of 0.55. We missed the

leading edge for the $(\gamma, 2n)$ cross-section but virtually reproduced the curve for photon energies higher than approximately 17 MeV. As shown in these figures, the *n-factor* has an impact on the magnitude of the (γ, n) and $(\gamma, 2n)$ cross-sections around the high energy tail of giant-dipole resonance. Here, the (γ, sn) cross-section was not affected by the adjustment of the *n-factor* since this parameter's role is to change the photoneutron production ratio between preequilibrium and compound processes.

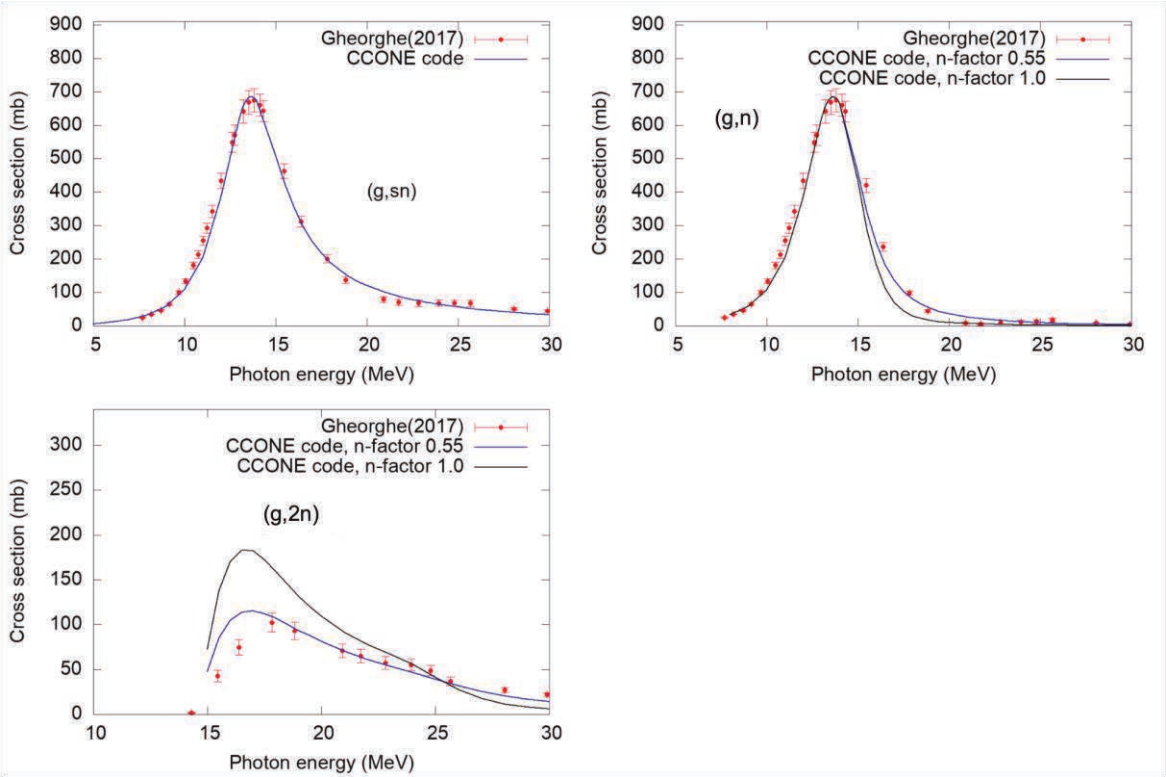

Figure 1: The reproduced reaction cross-sections by CCONE code together with the set of experimental data by I. Gheorghe [13] for ^{209}Bi.

3.2. DDX

Figure 2 shows reproduced DDX with two *n-factor* values, 1.0 and 0.55, in comparison with measured data of photoneutron production at 13 and 17 MeV photon energies at the emission angle of 90°.

For 13 MeV photon energy, we obtained an acceptable reproduction for the DDXs indicated by the blue line. For 17 MeV photon energy, although we virtually reached the experimental data, the evaluation procedure still needs to be improved to reproduce the data below 4 MeV. It should be noted that the impact of the double-neutron production $(\gamma, 2n)$ reaction can be observed around the low energy peak for 17 MeV photon energy. As a result, the photoneutron production at 17 MeV photon energy is much more complex than that of 13 MeV. In addition, the effects of the complex neutron production can be reproduced by adjusting the *n-factor* according to DDXs of photoneutron production as well as partial reaction cross-sections. As shown in Figure 2, the impact of the *n-factor* adjustment is more easily observed in the case of 17 MeV photon energy since the contribution of the preequilibrium process on the photoneutron production at 17 MeV photon energy is more substantial than that of 13 MeV.

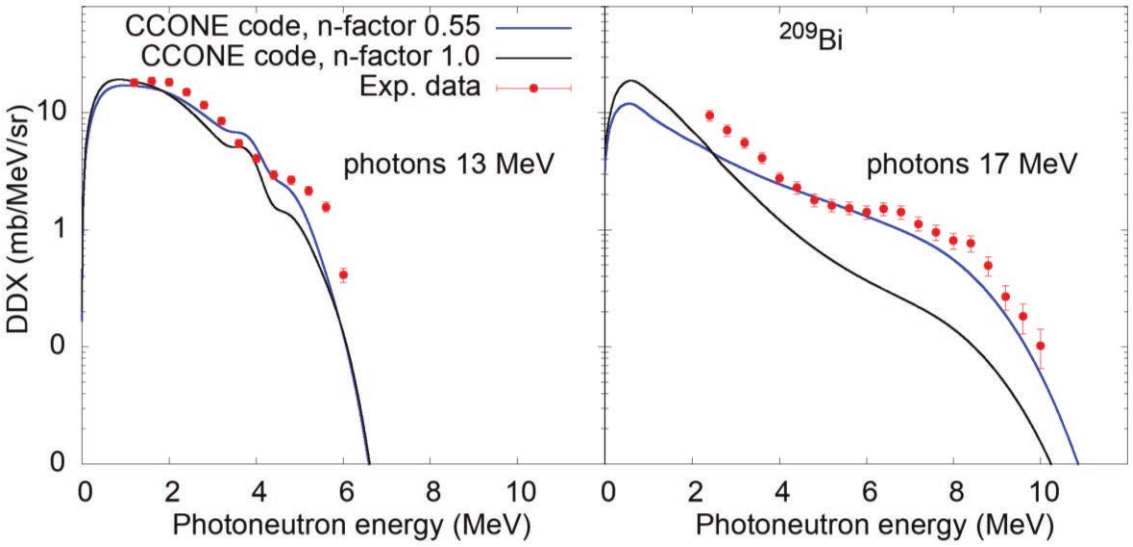

Figure 2: DDXs of photoneutron production for ^{209}Bi by the CCONE code and measurements at 13 and 17 MeV photon energies at 90° emission angle.

4. Conclusions

We have introduced a new methodology for photonuclear data evaluation based on the experimental DDX data of photoneutron production. As a first effort, the evaluation for ^{209}Bi has been done. Good agreements with the (γ, sn) and partial reaction cross-sections have been achieved and compared between the evaluation methodology only based on the reaction cross-sections and ours. However, more improvements in the evaluation procedure are required to describe the photoneutron production, especially when the $(\gamma, 2n)$ reaction occurs. This proposed methodology will be applied to other target materials, the experimental DDX data of which are available. We expect this methodology to be another option for the photonuclear data evaluation in the absence of the photoneutron production cross-section (γ, xn) or partial reaction cross-sections.

References

1) Kawano, T. et al., IAEA photonuclear data library 2019. Nucl. Data Sheets, vol.163, 2020, pp.109-162.
2) Dietrich, S.S. and Berman, B.L., Atlas of photoneutron cross sections obtained with monoenergetic photons, At. Data Nucl. Data Tables, vol.38, 1988, pp.199-338.
3) "Handbook on nuclear activation data," Tech. Rep. Technical Report Series No.273, International Atomic Energy Agency, 1987.
4) Blokhon, A.I. and Nasyrova, S.M., Plots of the experimental and evaluated photonuclear cross-sections, Tech. Rep. INDC(CCP)-337, International Atomic Energy Agency, 1991.
5) Varlamov, A.V. et al., "Atlas of giant dipole resonances, parameters and graphs of photonuclear reaction cross sections," Tech. Rep. INDC(NDS)-394, International Atomic Energy Agency, 1999.
6) Kirihara, Y. et al., Neutron emission spectrum from gold excited with 16.6 MeV linearly polarized monoenergetic photons, J. Nucl. Sci. and Technol., vol.57, no.4, 2020, pp.444-456.

7) Tuyet, T.K. et al., Energy and angular distribution of photo-neutrons for 16.6 MeV polarized photon on medium–heavy targets, Nucl. Instr. Meth. in Phys. A, vol.989, 2021, pp.164965.
8) Nguyen, T.H.T. et al., Experimental study of photoneutron spectra from tantalum, tungsten, and bismuth targets for 16.6 MeV polarized photons, J. Nucl. Sci. and Technol., 2023, pp.1-8.
9) Nguyen, T. et al., "Target mass dependence of photoneutron spectra from the photonuclear reaction for 13 MeV photons", AESJ Fall Meeting, 3N03, 2023.
10) Iwamoto, O. et al., The CCONE code system and its application to nuclear data evaluation for fission and other reactions, Nucl. Data Sheets, vol.131, 2016, pp.259.
11) Iwamoto, N. and Terada, K. Theoretical Analysis of Gamma-ray Strength Function for Pd Isotopes, Nucl. Data Sheets, vol.118, 2014, pp.246-249.
12) Otsuka, N. et al., Towards a More Complete and Accurate Experimental Nuclear Reaction Data Library (EXFOR): International Collaboration Between Nuclear Reaction Data Centres (NRDC), Nucl. Data Sheets, vol.120, 2014, 272-276.
13) Gheorghe, I. et al., Photoneutron cross-section measurements in the ^{209}Bi(γ,xn) reaction with a new method of direct neutron-multiplicity sorting, Phys. Rev. C, vol.96, no.4, 2017, pp.044604.

25. Measurement of double differential cross sections of charged particles produced by 100 MeV/u ^{12}C beam nuclear reactions

Ryota IKOMA[1*], Toshimasa FURUTA[1], Yusuke UOZUMI[1], Yuji YAMAGUCHI[2], Yosuke IWAMOTO[3] and Yusuke KOBA[4]
[1]Kyushu University
744 Motooka, Nishi-ku, Fukuoka-ken 819-0395, Japan
[2]Neutron Source Section, Materials & Life Science Division, J-PARC Center, Japan Atomic Energy Agency
2-4 Shirakata, Tokai-mura, Naka-gun, Ibaraki-ken 319-1195, Japan
[3]Nuclear Science and Engineering Center, Japan Atomic Energy Agency
765-1 Tokai-mura, Naka-gun, Ibaraki-ken, 319-1184, Japan
[4]Quantum Medical Science Directorate, National Institutes for Quantum Science and Technology
4-9-1 Anagawa, Inage-ku, Chiba-ken, 263-8555, Japan
[*]Email: ikoma@nucl.kyushu-u.ac.jp

Experimental data on double differential cross sections are widely needed for radiation damage in space and dose evaluation in heavy particle therapy. Charged particle spectra from carbon induced reactions were investigated at the incident energy of 100 MeV/u. The obtained double differential cross sections for proton and deuteron productions were discussed through comparison with previous experiments and the moving source model calculation. The proton spectra are found to be in reasonable agreement over the entire region, while the deuteron spectra show discrepancy on the high energy side.

1. Introduction

The space program in recent years has aimed for human exploration of planets such as the Moon and Mars. Exposure to ionizing radiation encountered during space travel can increase the risk of inducing cancer, and therefore radiation hazard is one of the most important issues to be resolved for long-duration missions. Accumulating and organizing the nuclear fragmentation data, especially double differential cross section (DDX) data is required to obtain accurate dose evaluation. Detailed knowledge of nuclear fragment production is an important issue in also heavy ion radiotherapy because secondary ions induce undesired dose in the patient's body.

Although fragmentation reactions have been studied for many years, DDX data are lacking. Auble et al. conducted extensive studies in the 1980s, mainly using ^{16}O beams [1-4], and revealed general trends of fragmentation reactions: for example, the shape of proton spectrum is target-independent, but only the magnitude depends on target mass number, and the scaling law holds for the incident energy. However, only a small amount of DDX data currently exists. At that time, experiments using ^{12}C beams were also carried out [5,6], but similarly very little data remain. A recent report [7] from the National Aeronautics

and Space Administration (NASA) highlights the absence of DDX data for ^{12}C-induced reactions producing charged particles at incident energies between 100 and 500 MeV/u. In the energy region below 100 MeV/u, experimental studies were conducted around 2010; namely charged particle DDXs were measured at 62 MeV/u [8] and 95 MeV/u [9] in the context of heavy ion radiotherapy. In both of measurements, detected particles ranged from hydrogen to heavy ions, but targets were limited to light elements that make up the human body. Much of the data is available in the data library EXFOR [10]. According to the energy-scaling law, there appears to be a contradiction among them.

In this study, we measure ^{12}C-induced reaction data at 100 MeV/u. One of the motivations lies in the discrepancy between the 62 MeV/u and 95 MeV/u data. The measured data are discussed through comparison with those data, neutron DDX data [11] and the results of moving source model [3,12] calculations.

2. Method

2.1. Experiment

Experiments were conducted at the PH2 beamline of the Heavy Ion Medical Accelerator in Chiba (HIMAC), National Institutes for Quantum Science and Technology, Japan. The ^{12}C ions of 100 MeV/u provided by HIMAC were focused within 5-mm diameter on the target, which located in the vacuum chamber of 50-cm diameter. The target used was ^{nat}C, which is natural metals. its thicknesses is 0.1 mm.

The emitted particles were detected by two different counter telescopes. For detection of light particles (p, d, t, ^{3}He and α), they were two ΔE-E telescopes comprising two silicon-surface-barrier detectors (SSDs), a GSO(Ce) crystal and four PWO crystals, shown in Fig.1. The detectors for particles heavier than α were telescopes consisting of two SSDs and CsI(Tl) crystals, the sketch of which is depicted in Fig. 2. An overview of the detector system, including the vacuum chamber and beamline, is shown in Fig. 3.

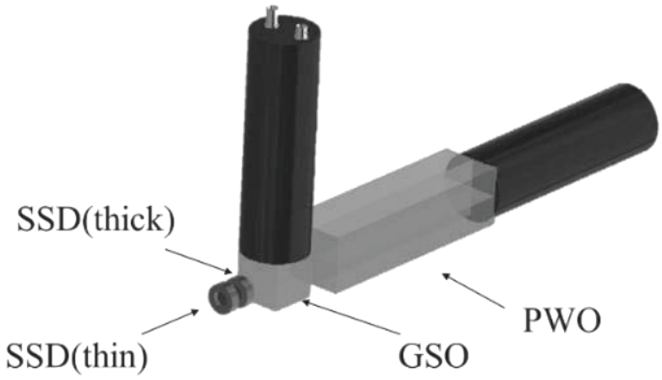

Fig. 1 Telescope for p, d, t, ^{3}He, and α

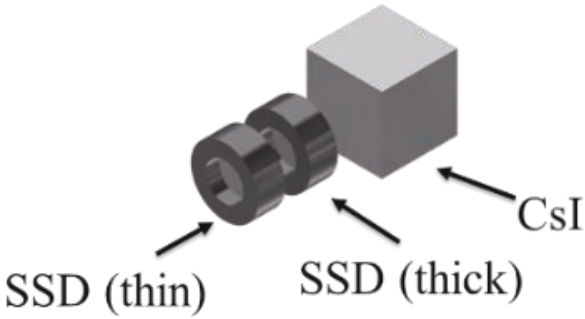

Fig. 2 Telescope for particles heavier than α

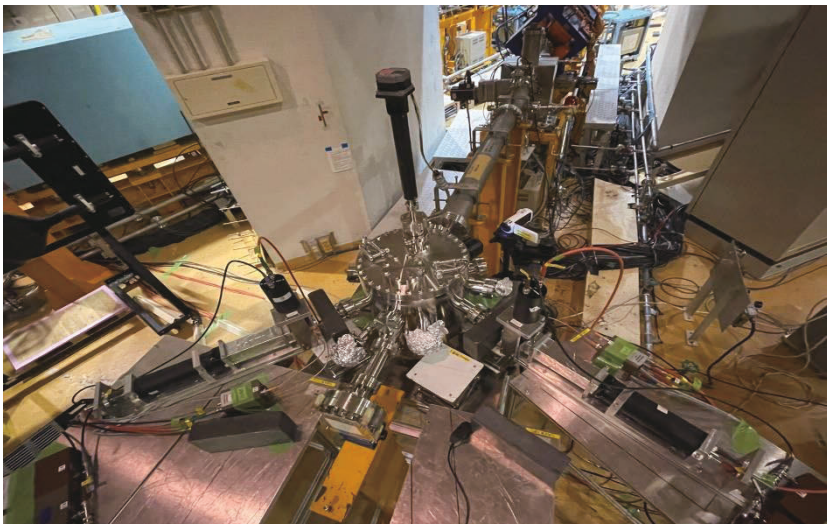

Fig. 3 overview of the detector system at PH2 course.

2.2. Moving source calculation

The moving source model has reproducing power for the energy spectra of nuclear reactions at intermediate energies. The model assumes that energy distribution of observed particles can be attributed to particle emission from a hot traveling source, produced by collisions of atomic nuclei. The source is characterized by its travel velocity and temperature. The entire energy range of spectrum is described by three hot sources [3] representing the projectile fragmentation [3], the preequilibrium [12] and the evaporation [3].

3. Results and Discussion

The spectra of DDXs for 100-MeV/u $^{nat}C(^{12}C,px)$ and $^{nat}C(^{12}C,dx)$ reactions at 15, 20 and 40 degrees compared with the moving source model are shown in Fig.4 and Fig.5, respectively. The reason why DDXs are missed in the medium energy region is mainly due to the influence of the air and reflective material between the detectors that make up the counter telescope. The resulting spectra decrease exponentially on the high-energy side, which were well reproduced using the moving source model. We also compared the spectra with those at 62 MeV/u, 95 MeV/u and neutron DDX data at 15 and 20 degrees under the energy scaling law in Fig.6 and Fig.7. The proton spectra are found to be in reasonable agreement over the entire region in Fig.6. The proton spectrum at 100 MeV/u show similar behavior to

the neutron spectrum data in the high energy region. While deuteron spectra show discrepancy on the high energy side at 15 degrees, they well agree with those of 62 MeV/u at 20 degrees.

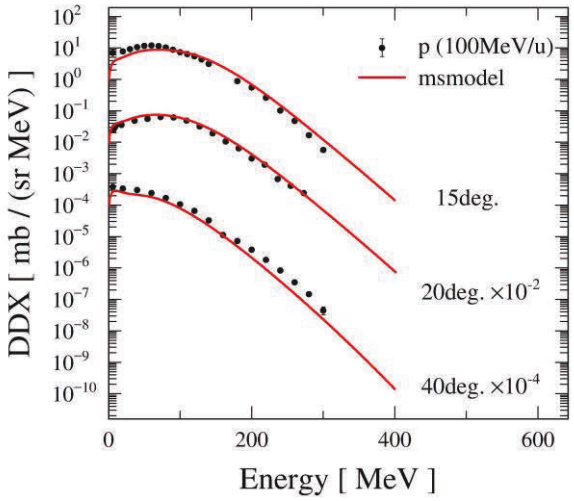

Fig.4 DDXs of $^{nat}C(^{12}C,px)$ reaction and the moving source model

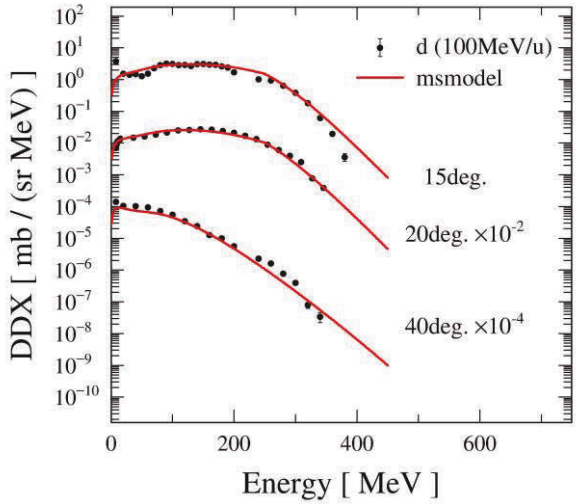

Fig.5 DDXs of $^{nat}C(^{12}C,dx)$ reaction and the moving source model

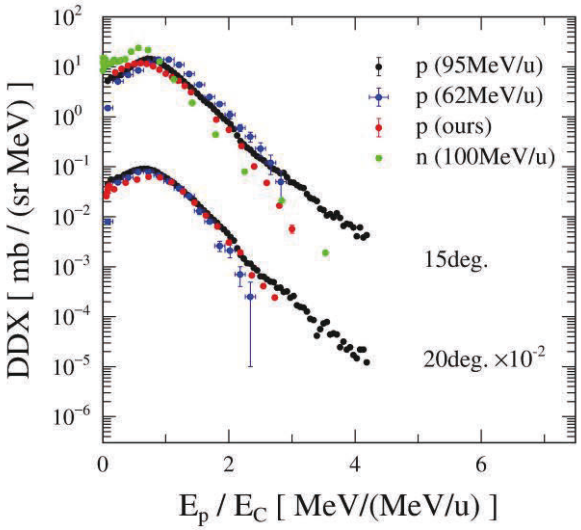

Fig.6 Comparison of proton DDXs

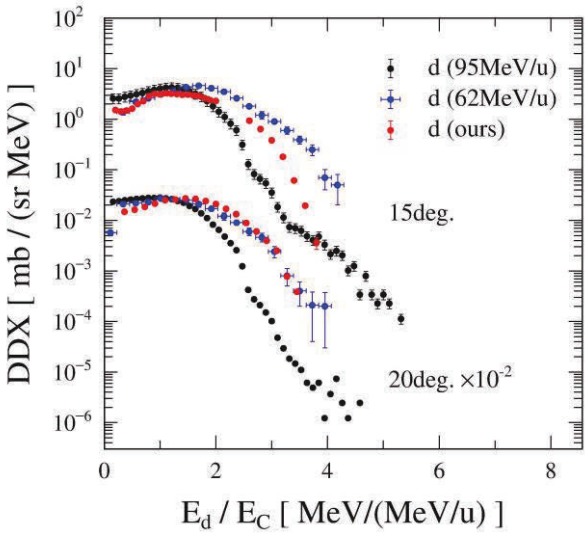

Fig.7 Comparison of deuteron DDXs

4. Conclusion

The double differential cross sections of charged particles from ^{12}C-induced reactions were measured at 100 MeV/u. The resulting spectra decrease exponentially on the high-energy side, which were well reproduced using the moving source model. We compared the spectra with previous experiments under the energy scaling law. The proton spectra are found to be in reasonable agreement over the entire region, while the deuteron spectra show discrepancy on the high energy side.

Acknowledgements

This study was partially supported by JSPS KAKENHI Grant Numbers 22K04989 and 17H03522.

This work was supported by Neutron Source Section of J-PARC center, Japan Atomic Energy Agency under Contract R05K168.

References

1) R. L. Auble, et al., Target-A Dependence of Light-Ion Emission from Reactions Induced by 100-MeV/u ^{16}O. Phys. Rev. Lett. 49, 441, 1982
2) R. L. Auble, et al., Light-ion emission in heavy-ion collisions: Beam energy dependence. Phys. Rev. C 25, 2504, 1982
3) R. L. Auble, et al., Light ion emission from reactions induced by 0.8-2.4 GeV ^{16}O projectiles. Phys. Rev. C 28, 1552, 1983
4) R. L. Auble, et al., Target/projectile mass dependence of light ion yields from heavy ion collisions. Phys. Rev. C 37, 390, 1988
5) B. Jakobsson, et al., Proton emission in 58A and 86A MeV ^{12}C-induced heavy-ion reactions. Physics Letters B Volume 102, Issues 2–3, 1981, pp.121-126.
6) J. Mougey, et al., Projectile fragments from 86 MeV/nucleon ^{12}C induced reactions. Physics Letters B Volume 105, Issue 1, 24, 1981, pp.25-29.
7) J. W. Norbury, et al., Nuclear data for space radiation. Radiat. Meas., 47:315–63, 2012.
8) M. De Napoli, et al., Carbon fragmentation measurements and validation of the GEANT 4 nuclear reaction models for hadrontherapy. Phys. Med. Biol. 57, 7651–7671, 2012.
9) J. Dudouet, et al., Double differential fragmentation cross sections measurements of 95 MeV/u ^{12}C on thin targets for hadrontherapy. Phys. Rev. C 88, 024606, 2013.
10) IAEA, Experimental Nuclear Reaction Data (EXFOR), https://www-nds.iaea.org/exfor/ (accessed 2023-12-01)
11) N. Shigyo, et al., Measurement of 100- and 290-MeV/A Carbon Incident Neutron Production Cross Sections for Carbon, Nitrogen and Oxygen. Nuclear Data Sheets, Volume 119, 2014, pp. 303-306.
12) I. G. Bogatskaya, et al., Fireball model for baryonic inclusive spectra in particle-nucleus and nuclei-nucleus collisions at high energy. Phys. Rev. C 22, 209, 1980.

26. Production of Np isotopes from ^{238}U beam at BigRIPS

Chihaya FUKUSHIMA[†1,2], Riku MATSUMURA[2,3], Daiki NISHIMURA[1], Hideaki OTSU[2], He Wang[4], Hidetada BABA[2], Naoki FUKUDA[2], Tadaaki ISOBE[2], Kei KOKUBUN[5], Mizuki KURATA-NISHIMURA[2], Shinichiro MEIGO[6], Takahiro NISHI[2], Hiroyoshi SAKURAI[2], Masaki SASANO[2], Hiromi SATO[2], Yohei SHIMIZU[2], Toshiyuki SUMIKAMA[2], Hiroshi SUZUKI[2], Hiroyuki TAKAHASHI[1], Hiroyuki TAKEDA[2], Junki TANAKA[2], Yasuhiro TOGANO[2], Koichi YOSHIDA[2], and Masahiro YOSHIMOTO[2]

[1]Tokyo City University 1-28-1 Tamazutumi, Setagaya, Tokyo 158-8557, Japan
[2]RIKEN Nishina Center 2-1 Hirosawa, Wako, Saitama 351-0198, Japan
[3]Saitama University 255 Shimookubo, Sakura, Saitama, Saitama 338-8570, Japan
[4]RIKEN HENP Laboratory 2-1 Hirosawa, Wako, Saitama 351-0198, Japan
[5]The University of Tokyo 7-3-1 Hongo, Bunkyo, Tokyo 113-0033, Japan
[6]JAEA 765-1 Funaishikawa, Tokai, Naka, Ibaraki 319-1184, Japan
[†]Email: g2381908@tcu.ac.jp

Abstract

We conducted an experiment to determine the production cross section of ^{237}Np. To validate the production of the $^{237}Np^{91+}$ a two dimensional (2D) Gaussian fitting approach was conducted in accordance with the distribution patterns of neighboring ions of $^{234}U^{90+}$,$^{235}U^{90+}$, and $^{232}Pa^{89+}$. It is found that Np isotope can be counted up with contaminated U/Pa isotopes using the 2D Gaussian fitting technique. The production cross sections of ^{234}U, ^{235}U, ^{236}U, ^{232}Pa, and ^{233}Pa as well as Np isotopes were derived.

1 Introduction

A variety of unstable nuclear beams with atomic numbers Z up to 92 can be produced by the projectile fragmentation and in-flight fission from high intensity ^{238}U beams at RIKEN's Radioactive Isotope Beam Factory (RIBF) [1]. Recent developments of production and identification technique in BigRIPS enable access to the unstable nuclei in the high-Z region [2][3]. When the fragmentation of ^{238}U includes proton pick-up or charge-exchange reactions, it is possible to produce the Neptunium (Np) isotopes with $Z = 93$. Although Np isotopes do not exist in nature, they are artificially produced through nuclear reactions in nuclear reactors. Consequently, Np is contained in radioactive waste, especially ^{237}Np with a half-life of 2.14 million years. The nuclear data of the Np isotopes is important for not only revealing the nuclear structure and nuclear reaction mechanism but also transmutating minor actinides. In a previous study at GSI, production cross sections of $^{234-238}$Np isotopes with ^{238}U beam with an energy of 1 GeV per nucleon impinging on deuteron target were investigated [4]. To establish the supply of the Np beam at RIBF, the production cross sections of Np isotopes from ^{238}U on ^{9}Be target were measured. The nuclides for which production cross sections were obtained in this study are shown in blue in the table of nuclides in Figure 1.

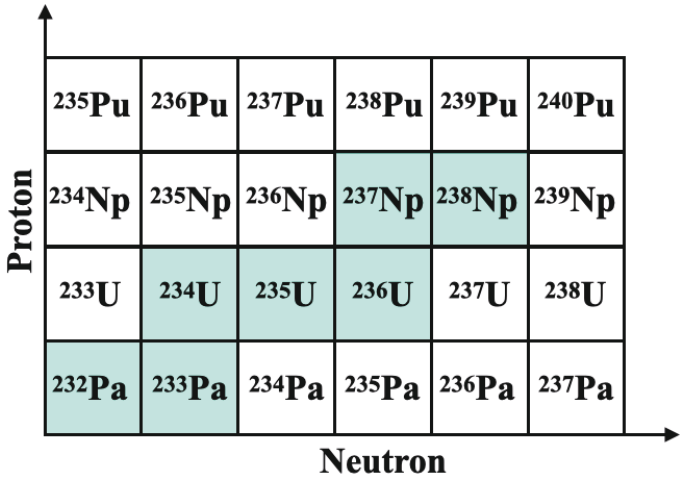

Figure 1: Table of nuclides. In this study, production of cross section for ^{232}Pa, ^{233}Pa, ^{234}U, ^{235}U, ^{236}U, ^{237}Np, and ^{238}Np were determined, painted in blue. Np was produced by the reaction including proton pick up reaction directly from ^{238}U beam.

2 Experiment

The experiment of production cross section measurement for Np isotopes were performed using BigRIPS [5] at the RIBF facility in RIKEN. The experimental setup of the BigRIPS is shown in Figure 2. A primary beam of ^{238}U with an energy of 345 MeV/nucleon and with an intensity of 0.0013 pnA were accelerated by the super conducting ring cyclotron (SRC).

The ^{238}U primary beam impinged on a 1-mm-thick ^{9}Be target, resulting in the production of a secondary beam containing Np. Secondary particles were initially separated in the first stage of the BigRIPS. As no materials were installed at F1, charge states of ions were not changed between F0 and F3. The magnetic rigidities at D1, D2, D3-D4 and D5-D6 were set to be optimized for fully-strip, fully-strip, H-like and He-like of ^{232}Pa which has the same A/Q value of the ^{237}Np. Plastic scintillators at F3 and F7 for the TOF , and parallel-plate avalanche counters (PPACs) at F3, F5, and F7 for the $B\rho$ were installed, respectively. Further, newly developed ionization chamber (IC) with xenon-based gas was utilized at F7 for better separation of Z at high-Z region [6]. The choice of Xe-based gas IC is motivated by its ability to minimize charge fluctuation of the gas, enabling a reliable count of electrons associating Z. The charge state in the Xe-based gas has a large enough average number of charge state changes [7].

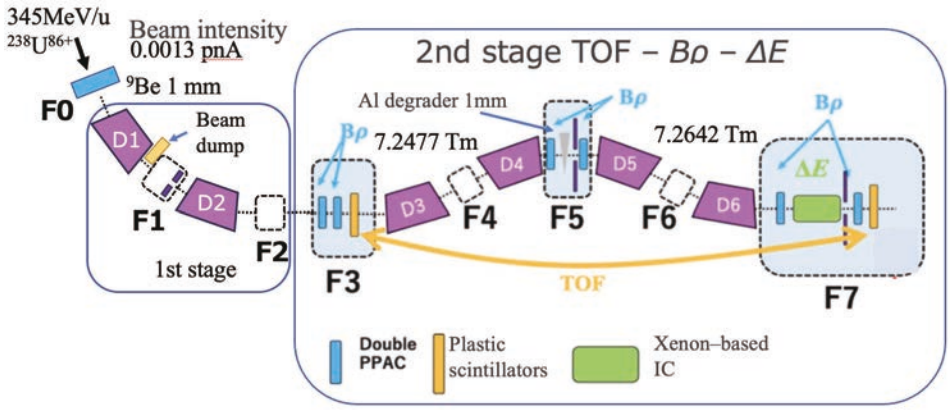

Figure 2: Schematic view of this experimental set up at BigRIPS in RIKEN. Illustration of quadrupole magnets were omitted.

3 Results

Figure 3 shows the particle identification plot for secondary beam. The mass to charge ratio (A/Q) was defined as the value between F5 to F7. The relative Z resolution was 0.42 % with Xe-based gas IC and the relative A/Q resolution was 0.057 % at this high-Z region, respectively. As illustrated in Figure 3, the events of Np isotopes overlapped with the Pa and U isotopes. Consequently, a three-dimensional histogram was generated and fitted with a two-dimensional (2D) Gaussian function as shown in Figrue 4.

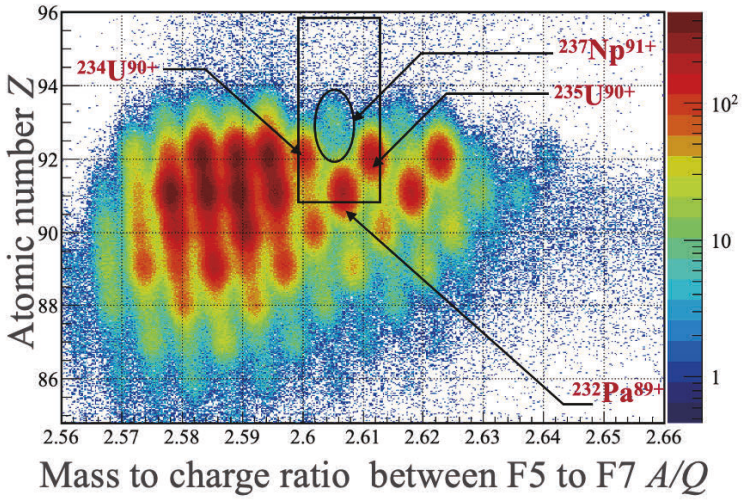

Figure 3: Particle identification plot Z vs A/Q between F5 to F7 for fragments production in the 345 MeV/nucleon ^{238}U. The box region around ^{237}Np^{91+} was used for the two dimensional fitting approach

The 2D Gaussian fitting approach was conducted in accordance with the distribution patterns of neighboring ions of ^{234}U^{90+}, ^{235}U^{90+}, and ^{232}Pa^{89+}. Figure 4(a) shows experimental data and

the fitted distribution by the 2D Gaussian function in color lego and red mesh. By subtracting the fitted distribution from the experimental data, the residuals were deduced as shonw in Figure 4 (b). As evident the blob of ^{237}Np^{91+} at Z of 93 and A/Q of 2.604. It is found that ^{237}Np^{91+} can be counted up with contaminated U and Pa isotopes using the 2D Gaussian fitting technique. By further fitting a 2D Gaussian to this residual, the yield of Np was derived. The same approach as for ^{237}Np was used to obtain yields for ^{238}Np surrounded by ^{235}U^{90+}, ^{236}U^{90+} and ^{233}Pa^{89+}. The production cross sections were obtained as follows

$$\sigma = \frac{Ne}{Ft}\frac{A}{\rho x N_A}\frac{1}{T}, \tag{1}$$

where N is the Np yield, e is the elementary charge, F is the beam intensity of 0.0013 pnA, t is the live time, and N_A is the Avogaddro number, respectively. The values of A, ρ, and x are the atomic weight, the density and thickness of ^{9}Be in the target, respectively. The transmission T was approximately around 0.8 %, which was calculated by LISE++ [8]. The production cross sections of Pa, U, and Np, were deduced from these calculations as shown in Figure 5. The cross sections for Np isotopes with proton pick-up process were approximately 10 times smaller than those for U and Pa isotopes without the pick-up process.

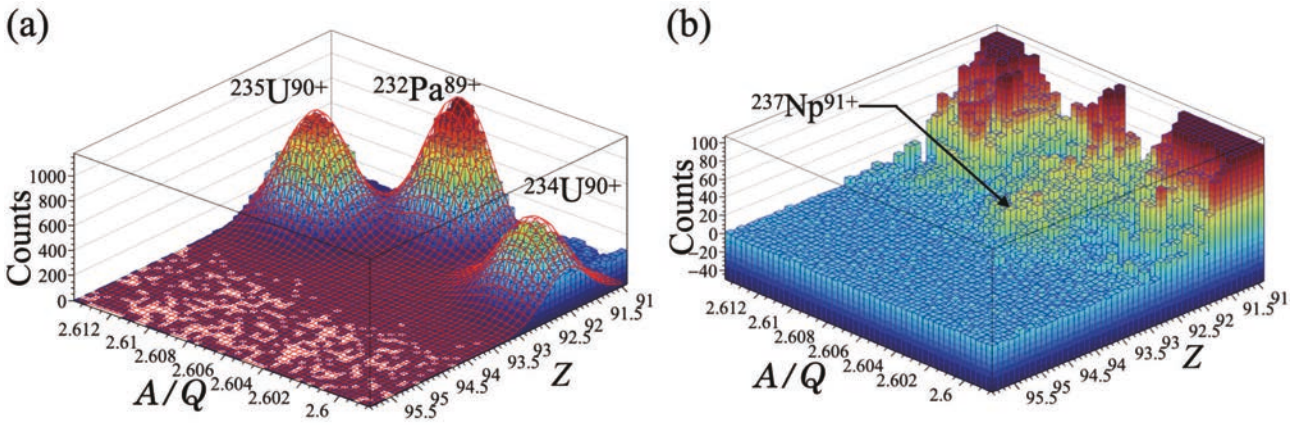

Figure 4: (a) 3D-lego plots of PID around ^{237}Np^{91+} in the box region of figure 2. (b) Residual by subtracting the fitted distribution from the experimental data.

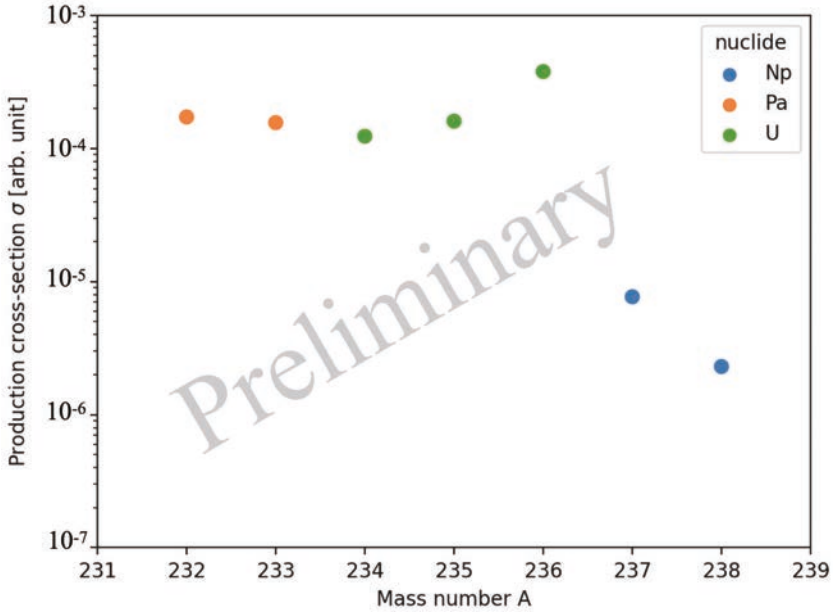

Figure 5: Production cross section for ^{238}U + ^{9}Be reaction at 335 MeV/nucleon in the center of ^{9}Be target, where transmission was calculated by LISE++. Transmission is approximately around 0.8 %.

4 Summary and future prospected

The production cross sections for the vicinity of the ^{237}Np isotopes from ^{238}U + ^{9}Be reaction at 335 MeV/nucleon were derived thanks to recent development of Xe-based gas IC. Since the production cross section measurement at the beam energy of 250 MeV/nucleon was also performed, we will determine the energy dependence of the the cross-sections.

References

[1] Y. Yano, The RIKEN RI Beam Factory Project: A status report, Nucl. Instr. Meth. B **261** (2007) 1009-1013.

[2] N. Fukuda *et al.*, Development of ^{216}Th and ^{220}Th beams at the BigRIPS separator, RIKEN Accel. Prog. **54**, 81 (2020).

[3] T. Sumikama *et al.*, First success of RI-beam separations and particle identification for nuclei with atomic number $Z > 82$ at RIKEN RI beam factory, Nucl. Instrum. Meth. B **463**, 237 (2020).

[4] E. Casarejos *et al.*, Isotopic production cross sections of spallation-evaporation residues from reactions of ^{238}U(1A GeV) with deuterium, Phys. Rev. C **74**, 044612 (2006).

[5] T. Kubo, *et al.*, BigRIPS separator and ZeroDegree spectrometer at RIKEN RI Beam Factory, Prog. Theor. Exp. Phys. 2012 (2012) 03C003.

[6] N. Fukuda *et al.*, Identification and separation of radioactive isotope beams by the BigRIPS separator at the RIKEN RI Beam Factory, Nucl. Instrum. Meth. B **317**, 323 (2013).

[7] M. Yoshimoto *et al.*, Xenon-gas ionization chamber to improve particle identification of heavy ion beams with $Z > 70$, arXiv:2401.08679.

[8] O.B. Tarasov and D. Bazin, LISE++: Radioactive beam production with in-flight separators, Nucl. Instrum. Methods Phys. Res. B, 266 (2008) 4657 - 4664, https://lise.nscl.msu.edu

27. Isotopic production of high-radiotoxic nuclide ^{90}Sr via proton- and deuteron-induced reactions and new analytical model for its longitudinal momentum distribution

Riku Matsumura[†1, 2], Hideaki Otsu[1], He Wang[3], and Xiaohui Sun[4]

[1]RIKEN Nishina Center for Accelerator-Based Science, Saitama 351-0198, Japan
[2]Department of Physics, Saitama University, Saitama 338-8570, Japan
[3]RIKEN Cluster for Pioneering Research, Saitama 351-0198, Japan
[4]School of Science, Huzhou University, Zhejiang 313000, China
[†]Email: riku@ribf.riken.jp

Abstract

We have been systematically measuring the isotopic production cross sections via proton- and deuteron-induced spallation reactions of ^{90}Sr and other radionuclides using the inverse kinematics method. Utilizing this technique, we can also measure the longitudinal momentum distribution of each residual product. The distribution has asymmetry with a tail on the low momentum side, and it is known to become more pronounced at lower incident energies. Until now, the asymmetry has been mainly evaluated by using a Gaussian function with different widths on the higher and lower sides of the distribution. Although this approach reproduces experimental results, it is significantly artificial, and such obtained asymmetry is difficult to correlate directly with physical phenomena. Therefore, we attempted to devise a new analytical model. In contrast to the conventional method, the proposed equation reproduces the distribution with higher accuracy and is found to be universally applicable with a specific asymmetric parameter α' for a wide range of produced isotopes. Furthermore, the relation between the skewness expressed in terms of third-order moments and the introduced α' is made explicit. The results indicate that the longitudinal momentum distribution may be explained physically by introducing an asymmetric parameter of about $0 < \alpha' < 0.15$.

1 Introduction

It is essential to understand the reaction mechanism comprehensively to improve the predictive accuracy of the production cross sections in model calculations, including Particle and Heavy Ion Transport code System (PHITS) [1], which requires the systematic behavior of the production cross sections. At relativistic energies, the shape of the longitudinal momentum distribution for residual prodcuts can be expressed a Gaussian function [2], and its width σ is well described by the statistical model [3]

$$\sigma = \sigma_0 \sqrt{\frac{K(A-K)}{A-1}}, \tag{1}$$

proposed by Goldhaber. Here, A is the mass number of the projectile, K is the mass number of the residual product, and σ_0 is known to be about 90 MeV/c. In contrast, when produced at intermediate or low energies, it has an asymmetric shape with a tail on the low momentum side as shown in Fig. 1.

Reference [4] considered theoretically that the tail on the low momentum side is due to the momentum shift of the outgoing two nucleons inside an attractive potential caused by the residual nucleus. The cutoff on the high momentum side is due to the phase volume effect reflecting the energy and momentum conservation. This discrepancy in the momentum distribution leads to a large ambiguity in deriving the

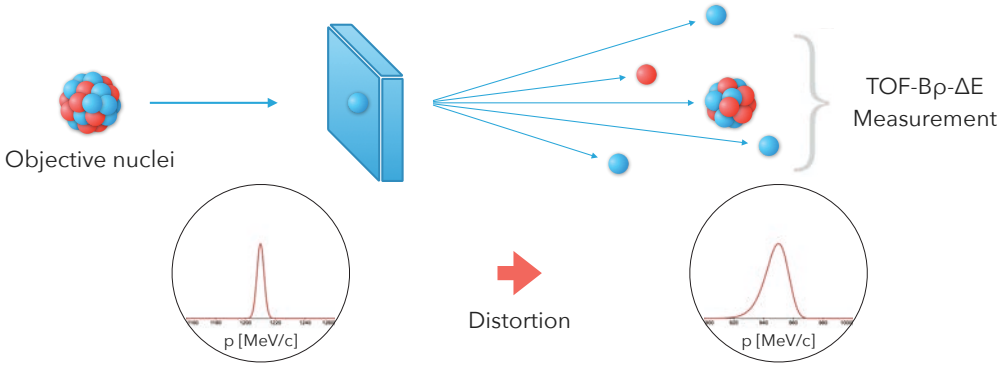

Figure 1: Schematic illustration of the spallation reaction and the associated distorted momentum distribution using the inverse kinematics method.

production cross section from the measured yields of the residual products. To evaluate this asymmetry, Ref. [5] introduced an asymmetry coefficient α, defined in Eq. (2) as

$$\alpha = \frac{\sigma_{\mathrm{Low}}}{\sigma} - 1 = 1 - \frac{\sigma_{\mathrm{High}}}{\sigma}. \tag{2}$$

Accordingly, for each σ_{High} and σ_{Low} is solved to obtain different widths on the higher and lower sides of the momentum distribution,

$$\begin{cases} \sigma_{\mathrm{Low}} & = \sigma\,(1+\alpha)\,, \\ \sigma_{\mathrm{High}} & = \sigma\,(1-\alpha)\,. \end{cases} \tag{3}$$

Note that this value has been experimentally verified to be acceptable up to 30 % according to Ref. [6]. However, it is difficult to understand why the division into cases is required to reproduce a single physical quantity. Thus, we attempted to devise a new analytical model.

2 Experiment

The series of experiments [7–10] were performed at the RIBF by using the BigRIPS separator [11] and the ZeroDegree spectrometer [11]. An experimental setup is shown in Fig. 2. The details of the experiment are given in Ref. [8]. The secondary beam, including ^{90}Sr, was produced by in-flight fission of ^{238}U at 345 MeV/nucleon on a 3-mm thick ^{9}Be production target at the BigRIPS first stage. In the following second stage, the beam particles were selected and identified event-by-event using the TOF-$B\rho$-ΔE method [12].

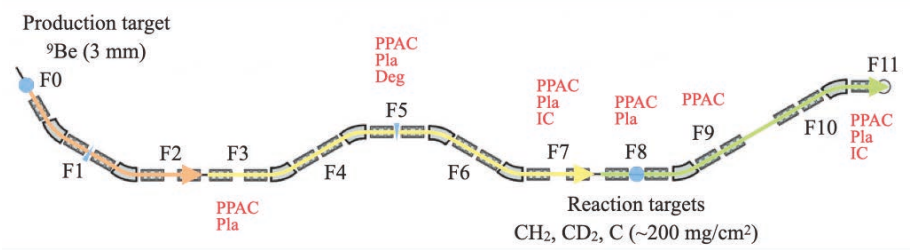

Figure 2: Schematic view of the BigRIPS separator and the ZeroDegree spectrometer.

The beam particles bombarded at 104 MeV/nucleon to CH_2 (179.2 mg/cm^2), CD_2 (218.2 mg/cm^2), and C (226.0 mg/cm^2) reaction targets, which placed at the entrance of the ZeroDegree spectrometer. The residual nuclei produced in reactions were identified in the ZeroDegree spectrometer with the same method as the BigRIPS. Because the momentum acceptance of the ZeroDegree spectrometer is limited to ±3 %, the experiment was carried out by using five different momentum settings ($\Delta(B\rho)/B\rho = -9$, -6, -3, 0, and $+3$ %) for each target to accept the wide range of mass-to-charge ratio A/Q. Figure 3 shows an example of particle identifications after selecting ^{90}Sr ($Z = 38$, $A/Q = 2.37$) for the projectile and the $\Delta(B\rho)/B\rho = -6$ % setting at the ZeroDegree spectrometer. The production cross sections for each isotopes were deduced from the number of each residual nuclei normalized by the number of incident secondary ^{90}Sr particles using the thickness of the targets. The backgrounds of carbon from CH_2 and CD_2 targets and beam-line materials were subtracted by using the empty and carbon target runs. The right panel of Fig. 3 shows that momentum distributions (solid curves) using Eqs. (1) and (2) with parameters optimized for ^{86}Sr. This expression, however, cannot reproduce the data for other residual nuclei. Thus, we need to create a new expression to describe momentum distribution with a simple formula.

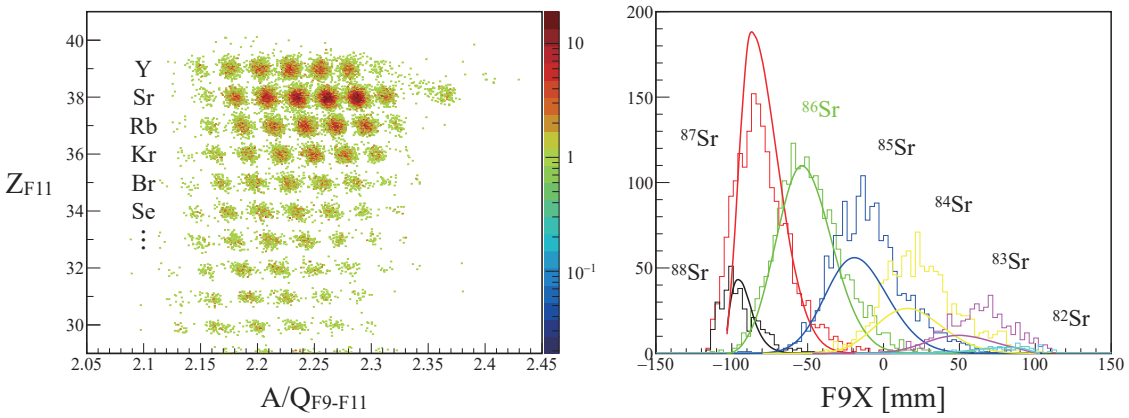

Figure 3: Left) Residual particle identifications at the ZeroDegree spectrometer. Right) Measured momentum distributions are compared with calculated ones when optimized for the ^{86}Sr spectrum.

3 New analytical model

To reproduce the momentum distribution of 104 MeV/nucleon incident energy data, the newly devised model function is given by as

$$\sigma(p) = \sigma_0' + \alpha'(p - \mu), \tag{4}$$

where σ_0' is core width, α' is a newly introduced asymmetric parameter, p is the momentum itself, and μ is the mean value of the momentum. This function will be intuitive and easy to understand, as it is completely separated into the core width σ_0' and the asymmetric parameter α'. Figure 4 shows momentum distributions of residual products after the reaction with the CH_2 target and the blue dashed lines are the fitting results using Eq. (4). It seems to reproduce the asymmetry well for all nuclides by gradually changing the width σ.

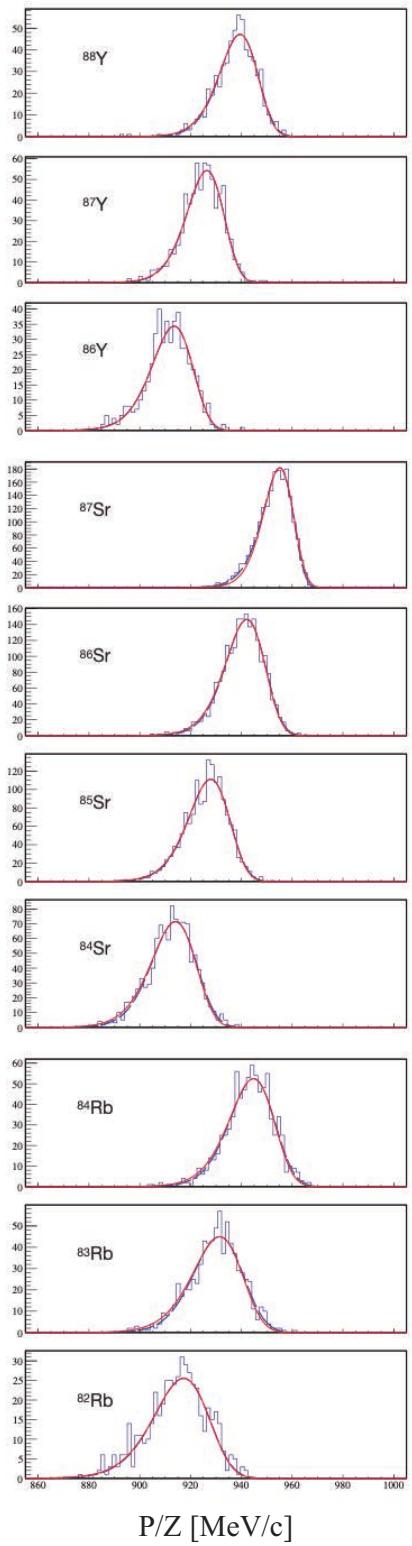

Figure 4: Momentum distributions measured in the ZeroDegree spectrometer. Those simply fit for parameter search (blue dashed line) and fit with a weighted average of the asymmetric parameter α' obtained for them (red solid line).

3.1 Behavior of the model

Figures 5 and 6 show the asymmetric parameter α' and the core width σ'_0, respectively, obtained by fitting each residual momentum distribution with Eq. (4) for all $B\rho$ settings measured. The core width of the distribution can be explained based on the Goldhaber model [1], and the asymmetry was confirmed to be constant over the wide isotope range measured, although there may be a reaction energy dependence and target dependence. In contrast to the conventional method, the proposed equation reproduces the distribution with higher accuracy and is found to be universally applicable with a specific asymmetric parameter α' for a wide range of produced isotopes.

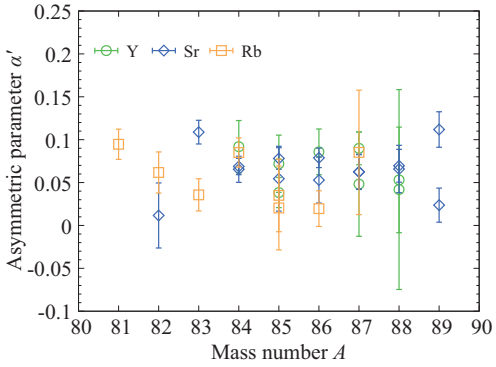

Figure 5: Asymmetric parameter α' obtained from the fitting shown in Fig. 4 plotted against the mass number A.

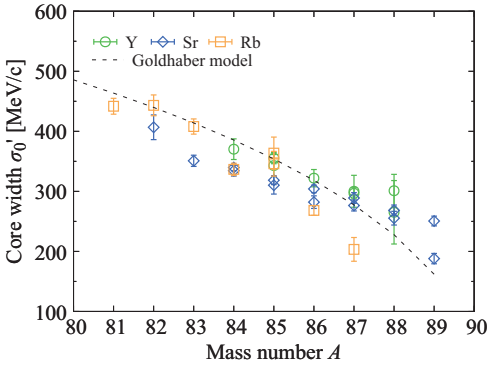

Figure 6: Core width σ'_0 obtained from the fitting shown in Fig. 4 plotted against the mass number A.

3.2 Mathematical consideration

Figure 7 expands Eq. (4) to third-order moments and confirms the relation with the introduced asymmetric parameter α'. Skewness is a statistical measure that indicates how much a distribution deviates from a normal distribution, serving as an indicator of symmetry in the distribution. In the range $0 < \alpha' < 0.15$, the mathematical requirement that the distribution function be uncorrelated for each moment is fully satisfied. Obtained from the experimental data, all asymmetric parameters α' are within this range independent of the target type. Hence, it can be inferred that this phenomenologically and mathematically correct function has some physical significance.

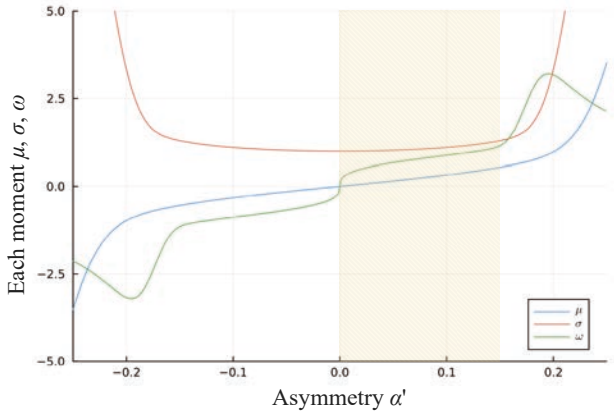

Figure 7: Relation between asymmetric parameter α' and each moment up to the third order.

3.3 Yield restoration

Based on the above, even for events that are partially cutoff by the momentum acceptance of the spectrometer shown in the left panel of Fig. 8, the central and sigma value of momentum can be inferred from other nuclides with full acceptance because of its linearity, and the yield can be reproduced to a certain extent. If only the rise on one side could be determined, the original momentum distribution might be reproduced. This is measured with five patterns of magnetic field settings as described in Sec. 2, which leads to a reduction of statistical errors for particles in overlapping regions. We have counted its yield in the $\Delta(B\rho)/B\rho = -3\,\%$ setting, where ^{87}Sr is definitely within the momentum acceptance, but by using this method, the yield in the $\Delta(B\rho)/B\rho = -6\,\%$ setting is found to agree within the error.

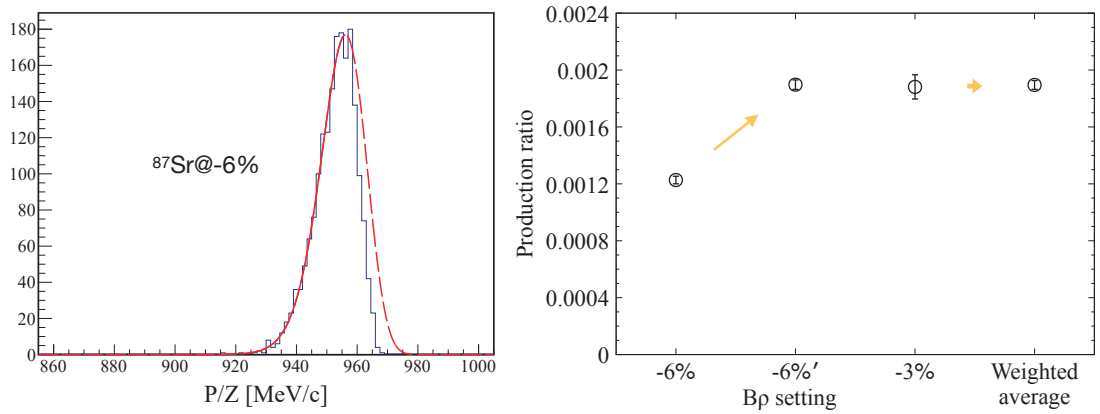

Figure 8: Left) As can be seen from Fig. 3 right, ^{87}Sr deviates slightly from the momentum acceptance, but the model function introduced this time can reproduce the original statistics. Right) The vertical axis is the production ratio, normalized by the number of incident ^{90}Sr beam.

4 Conclusion

We devised a new analytical model to reproduce the longitudinal momentum distribution. In spite of the simplicity of the function, in contrast to the conventional method, the proposed expression can well reproduce the distribution with higher accuracy. The value of the asymmetric parameter α' is almost constant within the error, and the introduction of specific value is sufficient to reproduce the momentum distribution of the isotope in this incident energy region. Note that this value may only be dominant for C within CH_2; thus, we are considering a method to extract the momentum component of only H by some method such as subtraction. We plan to analyze the energy dependence of α' at other energies, as it may be an important physical quantity involved in the reaction mechanism.

5 Acknowledgments

We are grateful to the accelerator staff of the RIKEN Nishina Center for providing a high-quality ^{238}U beam. This work was supported by RIKEN Junior Research Associate Program.

References

[1] T. Sato *et al.*, "Recent improvements of the particle and heavy ion transport code system – PHITS version 3.33", J. Nucl. Sci. Technol. **61**, 127 (2024).

[2] H.H. Heckman *et al.*, "Fragmentation of ^{14}N Nuclei at 29 GeV: Inclusive Isotope Spectra at 0°", Phys. Rev. Lett. **28**, 926 (1972).

[3] A.S. Goldhaber, "Statistical models of fragmentation processes", Phys. Lett. B **53**, 306 (1974).

[4] K. Ogata *et al.*, "Asymmetry of the parallel momentum distribution of (p, pN) reaction residues", Phys. Rev. C **92**, 034616 (2015).

[5] M. Notani *et al.*, "Projectile fragmentation reactions and production of nuclei near the neutron drip-line", Phys. Rev. C **76**, 044605 (2007).

[6] S. Momota *et al.*, "Momentum peak shift and width of longitudinal momentum distribution of projectilelike fragments produced at $E = 290$ MeV/nucleon", Phys. Rev. C **97**, 044604 (2018).

[7] H. Wang *et al.*, "Spallation reaction study for fission products in nuclear waste: Cross section measurements for ^{137}Cs and ^{90}Sr on proton and deuteron", Phys. Lett. B **754**, 104 (2016).

[8] S. Kawase *et al.*, "Study of proton and deuteron induced spallation reactions on the long-lived fission product ^{93}Zr at 105 MeV/nucleon in inverse kinematics", Prog. Theor. Exp. Phys. **2017**, 093D03 (2017).

[9] K. Nakano *et al.*, "Isotope production in proton-, deuteron-, and carbon-induced reactions on ^{93}Nb at 113 MeV/nucleon", Phys. Rev. C **100**, 044605 (2019).

[10] X.H. Sun *et al.*, "Spallation and fragmentation cross sections for 168 MeV/nucleon ^{136}Xe ions on proton, deuteron, and carbon targets", Phys. Rev. C **101**, 064623 (2020).

[11] T. Kubo *et al.*, "BigRIPS separator and ZeroDegree spectrometer at RIKEN RI Beam Factory", Prog. Theor. Exp. Phys. **2012**, 03C003 (2012).

[12] N. Fukuda *et al.*, "Identification and separation of radioactive isotope beams by the BigRIPS separator at the RIKEN RI Beam Factory", Nucl. Instrum. Meth. B **317**, 323 (2013).

28. Measurement of the spallation neutron spectrum by unfolding at 180° from 3-GeV protons and ^{nat}Hg with the ^{209}Bi(n,xn) reactions

Kenta SUGIHARA[†1,2], Shin-ichiro MEIGO[3], Hiroki IWAMOTO[4], and Fujio MAEKAWA[3]

[1]High Energy Accelerator Research Organization (KEK), Oho, Tsukuba, Ibaraki 305-0801, Japan
[2]The Graduate University for Advanced Studies (SOKENDAI), Hayama, Kanagawa 240-0193, Japan
[3]J-PARC Center, Japan Atomic Energy Agency, 2-4 Shirakata, Tokai-mura, Naka-gun, Ibaraki 319-1195, Japan
[4]Nuclear Science and Engineering Center, Japan Atomic Energy Agency, 2-4 Shirakata, Tokai-mura, Naka-gun, Ibaraki 319-1195, Japan
[†]Email: kenta.sugihara@kek.jp

Abstract

A neutron energy spectrum is important for shielding design at an Accelerator-Driven System facility (1.5-GeV p + Lead Bismuth Eutectic). A similar spectrum can be obtained at J-PARC (3-GeV proton + ^{nat}Hg). To check the validity of the unfolding, the unfolding with the ^{209}Bi(n,xn) reactions and the response functions (JENDL/HE-2007 and TALYS) was applied. In our poster, we present the derivation of the spectrum and comparison with the spectrum with a Time-of-Flight technique.

1 Introduction

Combinations of an unfolding and the ^{209}Bi(n,xn) reactions are often applied to measure the neutron source term [1–3], which is required for shielding design of accelerator facilities. At an Accelerator-Driven System (ADS) [4–7] facility proposed by JAEA, the unfolding method is helpful to estimate the neutron source term for the reaction of 1.5-GeV proton beam and a Lead-Bismuth Eutectic (LBE) alloy target because continuous wave (CW) operation will be applied there. Under the CW operation, it is crucial to obtain the neutron spectrum based on a reliable unfolding regardless a Time-of-Flight (TOF) of neutrons.

At J-PARC [8, 9], the reaction between 3-GeV protons and ^{nat}Hg can be used. Neutron energy spectra generated by the ^{nat}Hg(p,X) reaction are similar to those by the reaction of protons and nuclei in LBE. The neutron energy spectrum (Thick Target Yield: TTY) via the ^{nat}Hg(p,X) reaction was already measured with the TOF technique [10]. Then, we decided to confirm the availability of the unfolding prior to applying to the future ADS facility.

This paper presents an activation measurement of TTY with the ^{209}Bi(n,xn) reactions at J-PARC. With the reaction rates and response functions of JENDL/HE-2007 [11] and TALYS [12], the derivation of the neutron energy spectrum by the unfolding is also presented. Additionally,

the unfolding spectrum is compared with the spectrum obtained by TOF and the calculated one to confirm the validity of the unfolding.

2 Experiment

Our experiment was carried out at the J-PARC beam transport line. Experimental procedures, such as sample setting, proton beam irradiation, and γ-ray measurements, were performed by the same way in previous studies [10]. Thus, only a brief explanation is provided hereafter.

The neutrons were generated by the reaction between 3-GeV protons and ^{nat}Hg. The neutron irradiation lasted from June 16th, 2023 to June 22nd, 2023. The proton intensity was 1.76×10^{15} protons per second, which was equivalent to 869.4 kW. The target setup for ^{209}Bi was identical to Ref. [10]. The size and mass were 26 mm $\times$ 26 mm $\times$ 2 mm and 13.7 g, respectively.

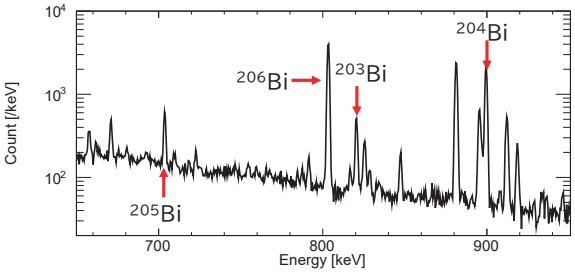

Figure 1: A γ-ray spectrum by the HPGe detector. The horizontal and vertical axes are γ-ray energy [keV] and pulse height [/keV], respectively.

The γ-ray measurements were conducted with a High-Purity Ge (HPGe) detector. The γ-ray detection efficiency was determined by standard γ-ray sources of ^{60}Co, ^{152}Eu, and ^{241}Am. The activated targets were placed on a 50-mm acrylic holder for the γ-ray measurements. The γ-ray spectrum obtained using the HPGe detector is shown in Fig. 1. In this measurement, the peaks of four nuclides, ^{203}Bi, ^{204}Bi, ^{205}Bi, and ^{205}Bi, were successfully acquired. The half-lives ($T_{1/2}$), γ-ray energies (E_γ) used in our analysis, and threshold energies ($E_{\rm th}$) of the ^{209}Bi(n,xn) reactions (x=4-7) are tabulated in Table 1.

Table 1: Properties of the ^{209}Bi(n,xn) reactions (x=4-7).

	$T_{1/2}$	E_γ [keV]	$E_{\rm th}$ [MeV]
^{209}Bi(n,4n)^{206}Bi	6.24 d	803.1	22.5
^{209}Bi(n,5n)^{205}Bi	14.91 d	703.45	29.6
^{209}Bi(n,6n)^{204}Bi	11.22 h	899.15	38.1
^{209}Bi(n,7n)^{203}Bi	11.76 h	820.2	45.4

3 Cross sections of the ^{209}Bi(n,xn) reactions

The cross sections of the ^{209}Bi(n,xn) reactions of JENDL/HE-2007, TALYS, and preceding results [13–18] are shown in Fig. 2. Red and blue lines represent JENDL/HE-2007 and TALYS, respectively. Markers stand for the previous results.

At approximately 10-MeV interval, the steep peak are observed for ^{209}Bi(n,xn) reactions. Basically, the peak energies of JENDL/HE-2007 are greater than those of TALYS. Focusing on the peak region of the cross sections, it is explicit that TALYS is larger than JENDL/HE-2007.

As an overall trend, TALYS shows better agreement with the measured data than JENDL/HE-2007. Especially, this tendency is remarkable for the ^{209}Bi(n,4n) and ^{209}Bi(n,5n) reactions. On the other hand, JENDL/HE-2007 reproduces the measured data better in a certain energy range, e.g., from 60 MeV to 150 MeV of the ^{209}Bi(n,4n) reaction.

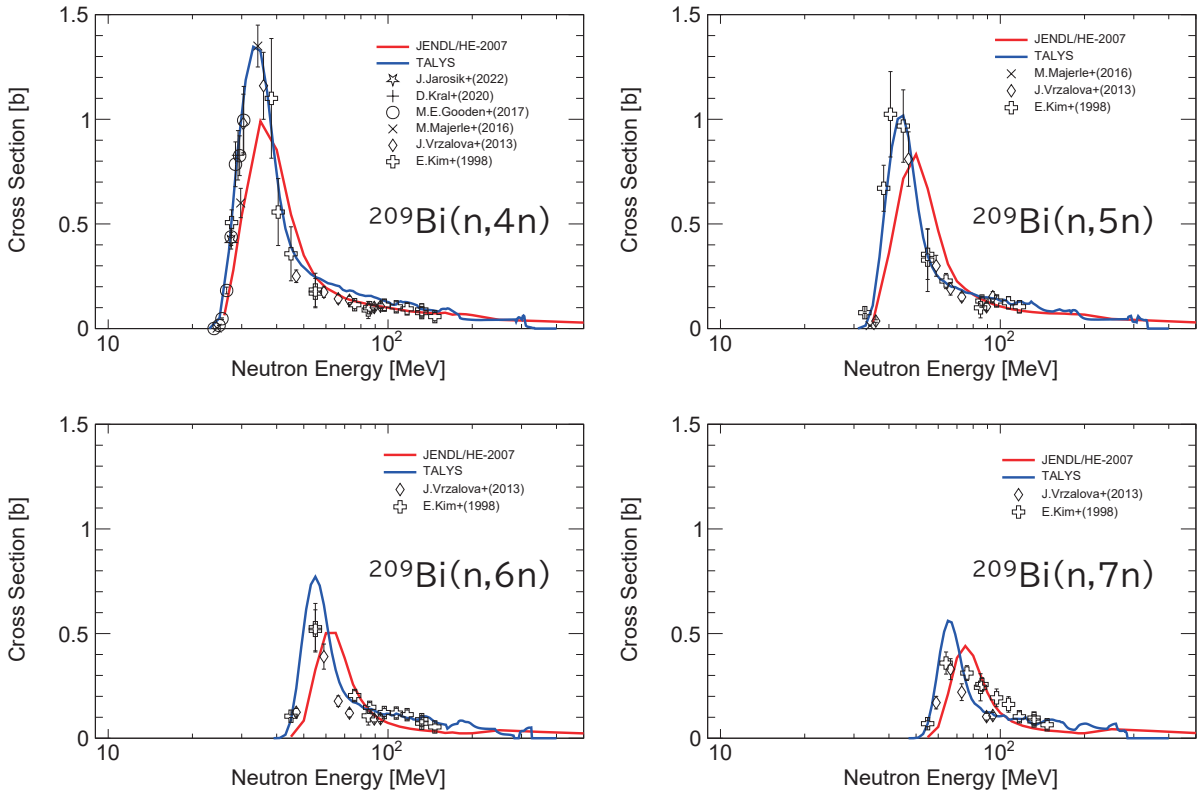

Figure 2: Excitation functions of the ^{209}Bi(n,xn) reactions used in this study.

4 Results and discussion

Due to the limited space, we omit how to analyze. The way of analysis is given in Ref. [10].

4.1 Reaction rates

According to the peak counts of γ-ray spectrum measured by the HPGe detector, the reaction rates (R_{exp}) were obtained. Additionally, the integration of the multiplication of the neutron energy spectrum measured by TOF [10] and response functions gave the reaction rates. The reaction rates by JENDL/HE-2007 and TALYS are denoted as R_{jendl} and R_{talys}, respectively. The reaction rates are tabulated in Table 2. In Table 2, ratios of R_{jendl} and R_{talys} to R_{exp} are also given.

As x of the ^{209}Bi(n,xn) reactions increases, the reaction rates decrease. This is because the cross sections as shown in Fig. 2 become smaller.

Except for the ^{209}Bi(n,5n) reaction, R_{jendl} / R_{exp} is smaller than 1.0. This is consistent with the excitation function which underestimates the measured data. For the ^{209}Bi(n,5n) reaction, R_{jendl} / R_{exp} equals to be 1.0 within uncertainty. According to Fig. 2, underestimation and overestimation are seen below and above the peak energy of JENDL/HE-2007, respectively. These tendencies cancel each other.

R_{talys} agrees with our measured data within 10%. Overestimation is obtained for the ^{209}Bi(n,4n) and ^{209}Bi(n,5n) reactions. Underestimation is observed for the ^{209}Bi(n,6n) and ^{209}Bi(n,7n) reactions. The tendency is consistent with the reproducibility of the peak regions as shown in Fig. 2.

Table 2: Measured and calculated reaction rates [/nucleus/proton] of the ^{209}Bi(n,xn) reactions (x=4,5,6,7). Ratios of R_{jendl} and R_{talys} to R_{exp} are also given.

	R_{exp}	R_{jendl}	R_{talys}
		R_{jendl} / R_{exp}	R_{talys} / R_{exp}
^{209}Bi(n,4n)^{206}Bi	$(1.64 \pm 0.05) \times 10^{-34}$	$(1.44 \pm 0.03) \times 10^{-34}$	$(1.80 \pm 0.04) \times 10^{-34}$
		0.880 ± 0.036	1.10 ± 0.04
^{209}Bi(n,5n)^{206}Bi	$(1.07 \pm 0.03) \times 10^{-34}$	$(1.10 \pm 0.03) \times 10^{-34}$	$(1.18 \pm 0.03) \times 10^{-34}$
		1.03 ± 0.04	1.11 ± 0.04
^{209}Bi(n,6n)^{206}Bi	$(7.46 \pm 0.93) \times 10^{-35}$	$(5.03 \pm 0.15) \times 10^{-35}$	$(7.40 \pm 0.20) \times 10^{-35}$
		0.674 ± 0.087	0.992 ± 0.127
^{209}Bi(n,7n)^{206}Bi	$(4.67 \pm 0.25) \times 10^{-35}$	$(3.96 \pm 0.14) \times 10^{-35}$	$(4.55 \pm 0.14) \times 10^{-35}$
		0.849 ± 0.054	0.975 ± 0.061

4.2 Unfolding

In this paper, Unfolding with MAXED and GRAVEL (UMG) code [19] was used. Neutron energy spectrum can be derived by the Response Function (RF), Initial Guess (IG), and aforementioned reaction rates. In this work, JENDL/HE-2007 and TALYS were used as RF. The TOF spectrum and calculation results of Liège Intra-Nuclear Cascade (INCL) [20] in PHITS [21] were applied to IG. The comparison among the unfolding results, TOF spectrum, and INCL is shown in Fig. 3. In the left and right figures, JENDL/HE-2007 and TALYS were applied to RF, respectively. The red star, green triangle, and black circle represent the results of UMG(IG: TOF), UMG(IG: INCL), and TOF spectra, respectively. The blue line stands for the INCL calculation.

According to the ratio to TOF, UMG(IG: TOF) are 1.0 within uncertainty. The result of UMG(IG: TOF) with RF of TALYS is smaller than with RF of JENDL/HE-2007. This is caused by the fact that the cross sections registered in JENDL/HE-2007 are smaller than those in TALYS.

On the other hand, the situation of UMG(IG: INCL) looks different. When TALYS was applied to RF, ratios to TOF of UMG(IG: INCL) are approximately 1.0 from 30 MeV to 60 MeV. The smaller ratios are observed from 70 MeV to 150 MeV. This could be interpreted that the TALYS results are basically larger than the previous data as shown in Fig. 2 for the ^{209}Bi(n,xn) reactions (x=4,5).

For the case of applying JENDL/HE-2007 to RF, ratios to TOF of UMG(IG: INCL) fluctuate around 1.0. This could be explained by the changes of underestimation and overestimation of JENDL/HE-2007 regarding to the energy of interest, as shown in Fig. 2.

As an overall trend, the unfolding with UMG reproduces the TOF spectrum within approximately 40%.

5 Conclusion

We confirmed the prediction accuracy of the unfolding with UMG by the activation method of the ^{209}Bi(n,xn) reactions at J-PARC beam transport line. As the initial guess, the measured spectrum by TOF and the INCL calculation were applied. As the response function, JENDL/HE-2007 and TALYS were utilized.

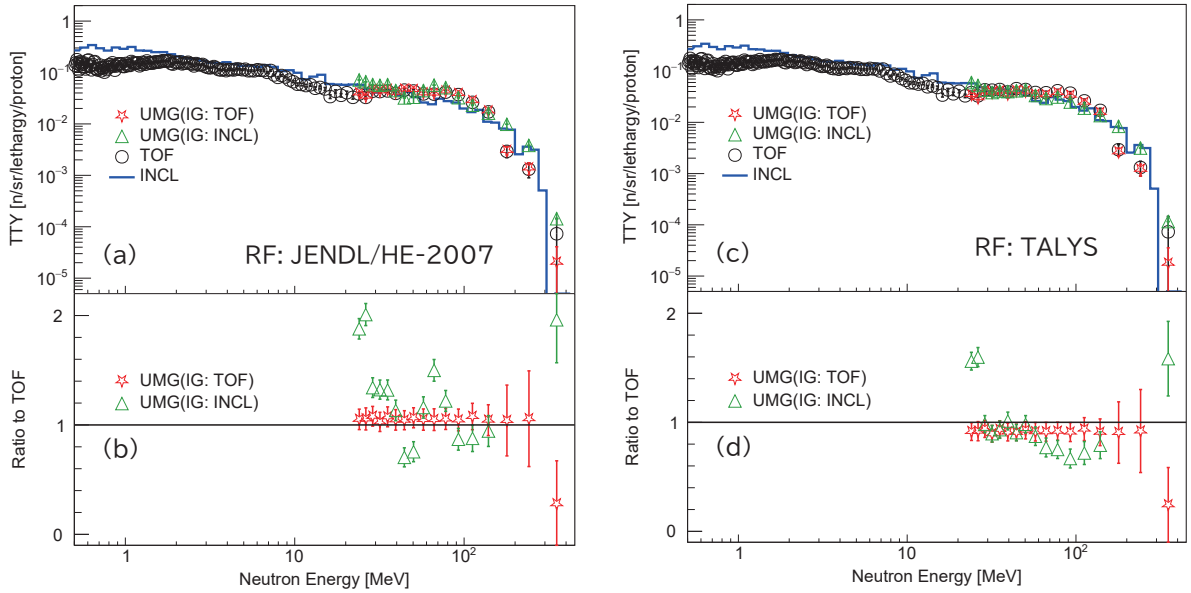

Figure 3: Comparison among unfolding results, TOF spectrum, and INCL. The horizontal and vertical axes in a graph above ((a) and (c)) represent the neutron energy [MeV] and TTY [n/sr/lethargy/proton], respectively. The horizontal and vertical axes in a graph below ((b) and (d)) stand for the neutron energy [MeV] and ratios to TOF, respectively.

In this work, we successfully acquired the reaction rates of the ^{209}Bi(n,xn) reactions (x=4-7). The reaction rates with JENDL/HE-2007 basically underestimated the measured reaction rates. In contrast, the reaction rates with TALYS generally reproduces the measured data within 10%.

Additionally, the neutron energy spectrum was successfully obtained by the unfolding with UMG. For the case of the initial guess of TOF spectrum, UMG spectrum agreed with the TOF spectrum within uncertainty. For the initial guess of INCL calculation, UMG spectrum showed agreement with the the data of TOF within approximately 40%. It should be noted that the cross sections of evaluated data used for response function do not show complete agreement with the experiment. The neutron spectrum obtained with unfolding may be improved with the evaluation of ^{209}Bi(n,xn) reaction cross section using machine learning, such as Gaussian Process Regression.

Acknowledgments

This paper includes results obtained with the Subsidy for Research and Development on Nuclear Transmutation Technology.

References

[1] Chiesa D., *et al.*, Measurement of the neutron flux at spallation sources using multi-foil activation: Nucl. Instr. Methods A, 902, (2018), pp. 14-24.

[2] Lhersonneau G., *et al.*, Neutron yield from carbon, light- and heavy-water thick targets irradiated by 40 MeV deuterons: Nucl. Instr. Methods A, 603, (2009), pp. 228-235.

[3] Trinh N.D., *et al.*, Double differential neutron spectra generated by the interaction of a 12 MeV/nucleon ^{36}S beam on a thick ^{nat}Cu target: Nucl. Instr. Methods A, 896, (2018), pp. 152-164.

[4] Sugawara T., *et al.*, Conceptual design study of beam window for accelerator-driven system with subcriticality adjustment rod: Nucl. Eng. Des., 331 (2018), pp. 11-23.

[5] Tsujimoto K., *et al.*, Neutronics Design for Lead-Bismuth Cooled Accelerator-Driven System for Transmutation of Minor Actinide: J. Nucl. Sci. Technol. 41 (2004), pp. 21-36.

[6] Cui W., *et al.*, Temperature control for spallation target in accelerator driven system: Nucl. Instr. Methods B 448, (2019) pp. 5-10.

[7] Abderrahim H.A., *et al.*, The Accelerator Driven Systems, a 21st Century Option for Closing Nuclear Fuel Cycles and Transmuting Minor Actinides: Sustain., 13, (2021), 12643.

[8] Hotchi H., *et al.*, Beam commissioning of the 3-GeV rapid cycling synchrotron of the Japan proton accelerator research complex: Phys. Rev. ST Accel. Beams, 12 (2009), 040402.

[9] Hotchi H., *et al.*, Achievement of a low-loss 1-MW beam operation in the 3-GeV rapid cycling synchrotron of the Japan proton accelerator research complex: Phys. Rev. Accel. Beams, 20 (2017), 060402.

[10] Matsuda H., *et al.*, Measurement of thick target neutron yield at 180° for a mercury target induced by 3-GeV protons: Nucl. Instr. Methods B, 483, (2020), pp. 33-40.

[11] Watanabe Y., *et al.*, Status of JENDL high energy file: J. Korean Phys. Soc., 59 (2011), pp. 1040-1045.

[12] Koning A.J., *et al.*, TALYS-1.0: Proc. of International Conference on Nuclear Data for Science and Technology 2007, pp. 211-214.

[13] Jarošík J., *et al.*, Activation cross-section measurement of fast neutron-induced reactions in Al, Au, Bi, Co, F, Na, and Y: Nucl. Instr. Methods B, 511, (2022), pp. 64-74.

[14] Kral D., *et al*, Cross section determination for TAD materials in quasi mono-energetic neutron spectrum from p(Li) reaction: Proc. 2019 International Conference on Nuclear Data for Science and Technology (ND2019), EPJ Web of Conf. 239 (2020), 20004.

[15] Gooden M.E., *et al.*, Measurement of the ^{209}Bi$(n, 4n)^{206}$Bi and ^{169}Tm$(n, 3n)^{167}$Tm cross sections between 23.5 and 30.5 MeV relevant to reaction-in-flight neutron studies at the National Ignition Facility: Phys. Rev. C, 96, (2017), 024622.

[16] Majerle M., *et al.*, Au, Bi, Co and Nb cross-section measured by quasimonoenergetic neutrons from p + ^{7}Li reaction in the energy range of 18-36 MeV: Nucl. Phys. A, 953, (2016), pp. 139-157.

[17] Vrzalová J., *et al.*, Studies of (n,xn) cross-sections in Al, Au, Bi, Cu, Fe, I, In, Mg, Ni, Ta, Y, and Zn by the activation method: Nucl. Instr. Methods A, 726, (2013), pp. 84-90.

[18] Kim E., *et al.*, Measurements of Neutron Spallation Cross Sections of ^{12}C and ^{209}Bi in the 20- to 150-MeV Energy Range: Nucl. Sci. Eng., 129, (1998), pp. 209-223.

[19] Reginatto M., The "multi-channel" unfolding programs in the UMG package: MXD_MC33 GRV_MC33 and IQU_MC33, UMG package version 3.3: Physikalisch Technische Bundesanstalt (PTB), (2003).

[20] Boudard A., *et al.*, New potentialities of the Liège intranuclear cascade model for reactions induced by nucleons and light charged particles: Phys. Rev. C 87, (2013), 014606.

[21] Sato T., *et al.*, Recent improvements of the particle and heavy ion transport code system - PHITS version 3.33: J. Nucl. Sci. Technol., 61(1), (2024), pp. 127-135.

29. C/Be neutron converter design for increasing production amount of medical radioisotopes in accelerator neutron method

Takahiro KIHARA[1], Tadahiro KIN[1*], Mary Alfonse Gorge MIKHAIL[1], Taisei ETO[1], Masato ASAI[2] and Kazuaki TSUKADA[2]
[1]Interdisciplinary Graduate School of Engineering Sciences, Kyushu University
6-1 Kasugakouen, Kasugasi, Fukuoka-ken 816-8580, Japan
[2] Advanced Science Research Center, Japan Atomic Energy Agency
2-4 Shirane, Shirakata, Tokai-mura, Naka-gun, Ibaraki-ken 319-1195, Japan
[*]Email: tadahirokin@kyudai.jp

For medical RIs production with the accelerator-neutron method, we have developed a C/Be neutron converter that can keep neutron yield with achieving long timespan required to exchange the converter caused by degradation. The converter is made of carbon and beryllium parts. The beryllium part is placed on the deuteron incident side to produce intense neutrons. Subsequently, almost all of deuterons are absorbed inside the carbon part with generating feint neutrons. This design aims to slow down the degradation of the converter caused by blistering, which is caused by the accumulation of deuteron inside the converter. We have conducted an experiment to investigate the performance of the converter at the JAEA Tandem accelerator. Deuterons having 19.9 MeV of kinetic energy were irradiated on the converter to produce accelerator neutrons. The neutrons were measured by the multiple foil activation method. We derived the double-differential thick target neutron yield by the unfolding process using GRAVEL code using cross sections stored in JENDL-5 as its response functions. These results indicate that the present converter can provide sufficient neutron yields comparable to a single-element Be converter with 90 times slow deuteron accumulation in beryllium part.

1. Introduction

Accelerator neutrons generated by deuterons have been studied to produce radioisotope (RI) for this decade. As shown in Figure 1 a), a thick neutron converter made of a single-element light nuclide such as C or Be is irradiated with deuterons to produce neutrons by the (*d*,*n*) reaction. The produced neutrons are injected into a raw material. The raw material is turned into medical RI by direct reactions. The proposed RIs are ^{64}Cu, ^{67}Cu, ^{90}Y, and ^{99m}Tc[1][2]. When producing these RIs, we must consider the byproducts and their yield. The byproducts must be kept low because they can be causes of the difficulty of the chemical separation process. In addition, higher yield can simply increase the number of possible tests and treatments with the RIs. These issues can be improved by the optimal neutron production irradiation systems adjusting deuteron incident energy and selecting appropriate neutron

converters.

In this system, the neutron converter especially has a significant effect on neutron flux. As a feature of an element used in neutron converters, are listed below:

i) Carbon: Exhibiting long life and generating fairly high neutrons, but the energy distribution is slightly shifted to lower energy side because the C(d,n) reaction is the endothermic reaction.

ii) Beryllium: As the Be(d,n) reaction is the exothermic reaction, it can generate higher energy neutrons with stronger intensity. However, the beryllium starts expanding during deuteron irradiation and finally breaks as illustrated in Figure 1, b). This expanding matter is known as “blistering” and should be suppressed for a long-lived converter.

Then, we designed a C/Be combined converter that can produce many neutrons while suppressing blistering. We conducted a neutron generation experiment to investigate the performance of the converter at the JAEA Tandem accelerator.

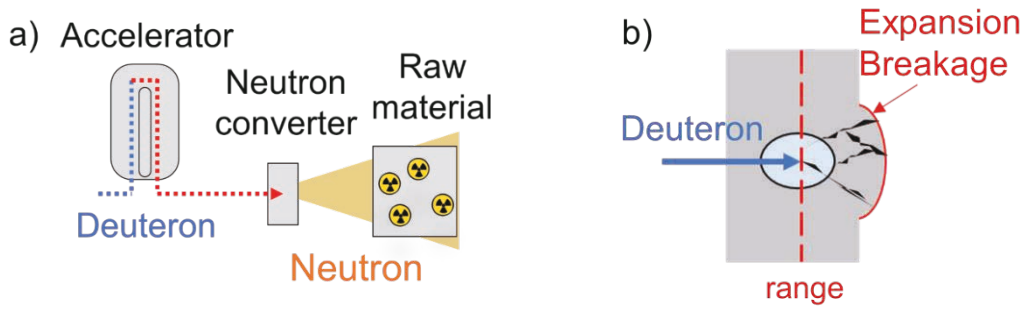

Fig. 1 a) Deuteron accelerator neutron source diagram, b) Schematic diagram of blistering generation mechanism.

2. Method

2.1. Design of the Carbon/Beryllium converter

On the deuteron incident side, the beryllium part is placed to generate intense neutrons. The thickness of beryllium is slightly thinner than the incident deuteron range to dispose the deuterons, i.e., it is dependent on the kinetic energy of the projectile deuterons. The penetrated deuterons are absorbed inside the thick carbon part generating feint neutrons. The beryllium thickness is determined to dispose 99.87% of deuterons. Using the mean range μ and its deviation σ_{Be} calculated by the SRIM [3] code, the beryllium target having $\mu - 3\sigma_{Be}$ mm thickness can achieve the disposing condition as shown in Figure 2. The thickness of carbon is determined enough to absorb all deuterons.

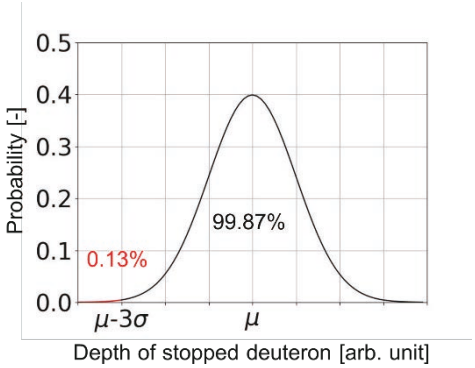

Fig. 2 Probability density function of stopped-deuteron depth in Be.

2.2. Combined neutron converter performance test at JAEA Tandem accelerator

To evaluate the neutron yield of the converter, a double-differential thick target neutron yield (DDTTNY) measurement using the multiple foil activation method was performed at Tandem accelerator in Japan Atomic Energy Agency (JAEA). Deuterons were accelerated to 19.9 MeV by the tandem accelerator and irradiated on the present converter (Be: 1.5 mm^t, C: 10 mm^t). Figure 3 shows the converter design diagram. Figure 4 shows the multiple foil irradiation system. The foils were made of Al (15 mm × 15 mm × 0.05 mm^t), Au (10 mm × 10 mm × 0.05 mm^t), Co (15 mm × 15 mm × 0.1 mm^t), Cu (15 mm × 15 mm × 0.1 mm^t), Ni (15 mm × 15 mm × 0.1 mm^t), Zn (15 mm × 15 mm × 0.2 mm^t), Zr (15 mm × 15 mm × 0.05 mm^t), and Mo (15 mm × 15 mm × 0.2 mm^t). The foils were placed at 122.5 mm downstream from the converter and at 0, 15, 30 and 45 degrees to the direction of the deuteron beam. The average deuteron beam current was about 0.8 μA. After 17-hours irradiation, gamma rays emitted from the activated multiple foils were measured with a HPGe detector.

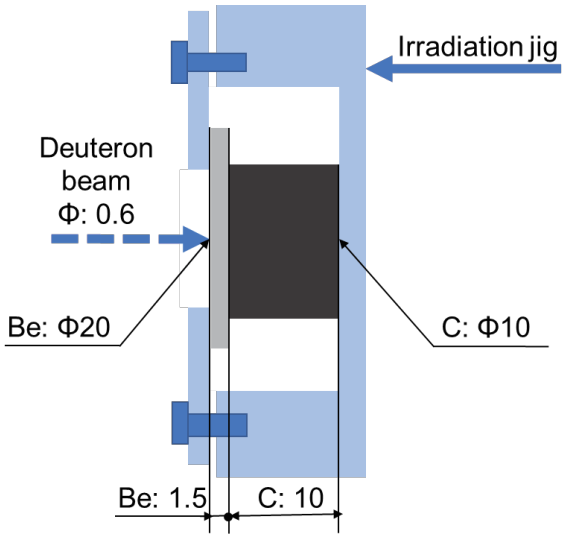

Fig. 3 C/Be converter design drawing.

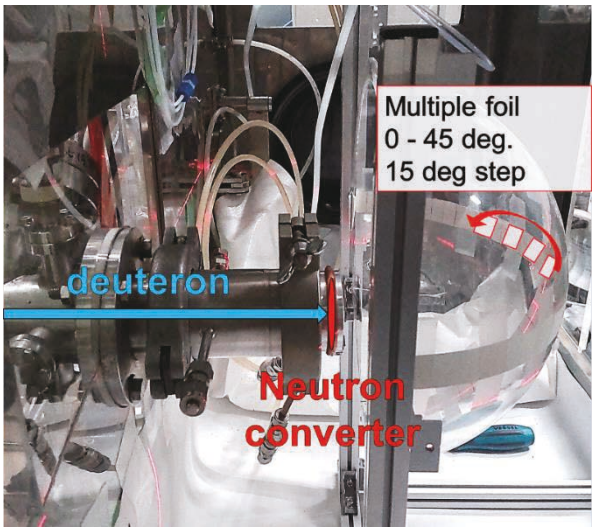

Fig. 4 Picture of irradiation system.

2.3. Unfolding

The unfolding code GRAVL [4] derived the neutron yields ϕ by solving an inverse problem expressed by the following equation:

$$\begin{pmatrix} N_1 \\ N_2 \\ \vdots \\ N_i \\ \vdots \\ N_n \end{pmatrix} = \begin{pmatrix} R_{x,E_1} & R_{x,E_2} & \cdots & R_{x,E_j} & \cdots & R_{x,E_m} \\ R_{y,E_1} & R_{y,E_2} & \cdots & R_{y,E_j} & \cdots & R_{y,E_m} \\ \vdots & \vdots & \ddots & \vdots & \square & \vdots \\ R_{i,E_1} & R_{i,E_2} & \cdots & R_{i,E_j} & \cdots & R_{i,E_m} \\ \vdots & \vdots & \square & \vdots & \ddots & \vdots \\ R_{n,E_1} & R_{n,E_2} & \cdots & R_{n,E_j} & \cdots & R_{n,E_m} \end{pmatrix} \begin{pmatrix} \phi_{E_1} \\ \phi_{E_2} \\ \vdots \\ \phi_{E_j} \\ \vdots \\ \phi_{E_m} \end{pmatrix} \quad (1)$$

where N_i, $R(i, E_j)$ and ϕ_{E_j} represent the number of produced atoms via the reaction i, the production rate of reaction i with a neutron energy group j, and average flux of j-th energy group respectively. The response functions were determined analytically from the cross sections stored in JENDL-5 [5]. The initial guess spectrum was derived by the Monte Carlo simulation code PHITS [6] using the nuclear data of JENDL/DEU-2020[7].

3. Result and Discussion

3.1. Converter lifetime

Assuming that the deuteron dispersion in a single element Be converter can be expressed with the following Gaussian distribution:

$$f(x) = \frac{1}{\sqrt{2\pi\sigma^2}} \exp\left(-\frac{(x-\mu)^2}{2\sigma^2}\right) \quad (2)$$

where μ is the mean range of the incident deuterons in the beryllium, and σ is the standard deviation caused by energy straggling and other physical processes. Given that blistering is caused by volume changes resulting from deuteron accumulation, the timespan required to exchange the converter caused by degradation of the converter must be inversely proportional to the maximum local accumulation of deuteron inside Be part. Under this assumption, let us denote the maximum local accumulation of deuteron for a single-element Be and C/Be converters as $\rho_{max,Be}$ and $\rho_{max,C/Be}$. They can be expressed by using the Gaussian distribution given in eq. (2) as follows:

$$\rho_{max,Be} = f(\mu) \quad (3)$$

$$\rho_{max,C/Be} = f(\mu - 3\sigma). \quad (4)$$

The relative timespan compared with the single-element converter can be obtained to calculate the ratio of eq. (4) to eq. (3). As a result, we found the combined converter has about 90.0 times longer timespan than that of the single element converter.

3.2. Double-differential thick target neutron yield (DDTTNY)

Table 1 shows the produced number of interested atoms derived by the photo peaks analysis in the measured gamma-ray spectra. These data were used as input for the unfolding process using GRAVEL code. In the unfolding process, we used a response function derived by multiplications of cross sections stored in JENDL-5, the solid angle of each foil [sr], the total charge of the deuteron beam [μC] and the surface density of atoms [cm^{-2}]. The response functions are shown in Figure 5. Initial guess DDTTNYs of the combined converter for unfolding analysis was determined by a simulation result obtained by PHITS code using JENDL/DEU-2020.

The derived DDTTNY, the initial guess spectrum and the other experimental results measured by Weaver[5] are shown in Figure 6. Note that Weaver's DDTTNYs are slightly different from the present conditions, i.e., 20-MeV deuteron DDTTNY bombarded on a single-element Be converter. Our DDTTNYs has similar trend with those of PHITS, but the absolute values were 2-3 times smaller. Weaver's DDTTNY has different trend in 8-13 MeV range, but the absolute values are in good agreement at the lower energy range, 3-8 MeV.

Our results indicate that the absolute values of our results and Weaver's are correct (because of experimental value) and that the converter can provide a neutron yield comparable to that of the Be, although the neutron yield may be lower in the 8-13 MeV range.

Table 1 Interested activation reaction,
the number of produced atoms measured in the gamma-ray experiment.

Reaction	Number of produced atoms			
	0 deg	15 deg	30 deg	45 deg
^{90}Zr(n,$2n$)^{89}Zr	3.76E+08	3.00E+08	1.16E+08	4.08E+07
^{68}Zn(n,a)^{65}Ni	5.40E+06	2.63E+06	-	-
^{64}Zn(n,p)^{64}Cu	2.46E+09	1.34E+09	5.86E+08	3.37E+08
^{58}Ni(n,$2n$) ^{57}Ni	1.05E+08	9.24E+07	3.74E+07	1.08E+07
^{65}Cu(n,p)^{65}Ni	1.68E+07	9.09E+06	-	-
^{59}Co(n,a) ^{56}Mn	7.35E+07	3.96E+07	1.49E+07	-
^{59}Co(n,$2n$)^{58g} Co	3.05E+09	2.29E+09	9.58E+08	3.69E+08
^{197}Au(n,$2n$) ^{196g} Au	5.31E+09	2.80E+09	1.13E+09	5.05E+08

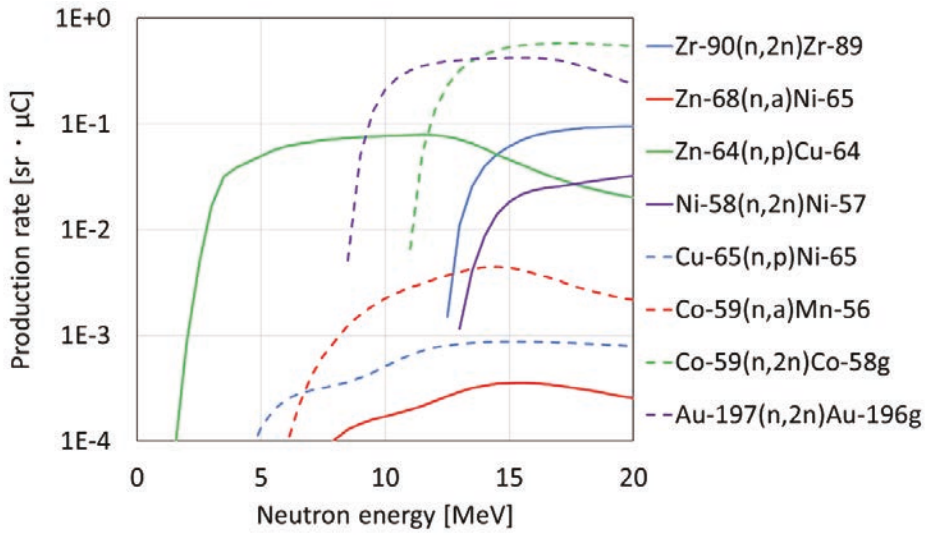

Fig. 5 Production rate plotted as a function of neutron energy for each activation reaction.

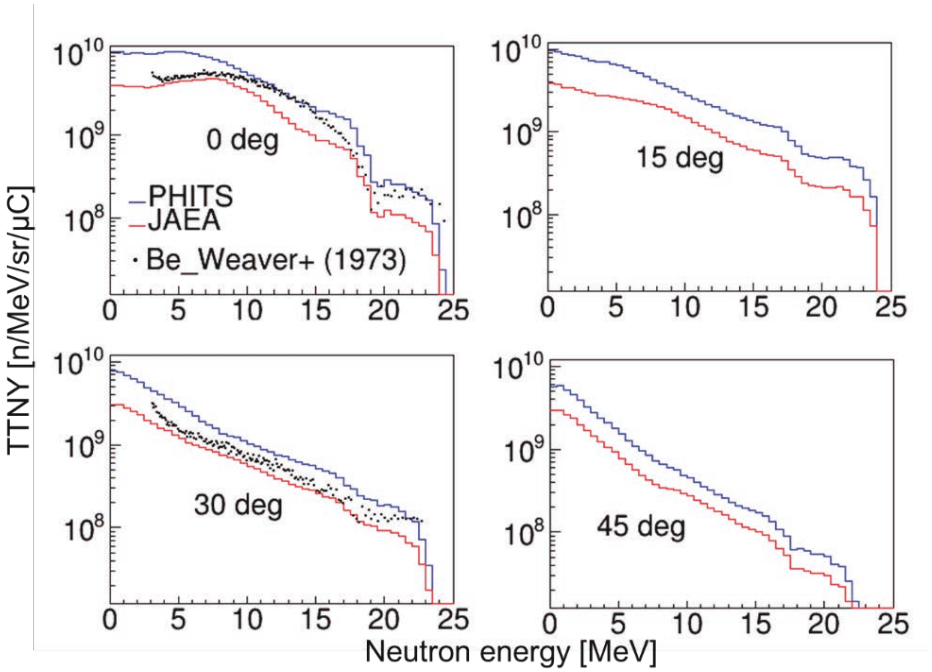

Fig. 6 DDTTNY of JAEA experiment and PHITS simulation.

4. Conclusion

To produce more medical RIs using long timespan required to exchange the converter caused by degradation neutron converter, we have developed the C/Be combined converter. It has the beryllium part on the deuteron incident side to generate intense neutrons and the other side equips the carbon part to absorb deuterons with generating feint neutrons. The proposed converter has more than 90 times longer timespan than a single-element Be converter by reducing accumulation inside the Be part to avoid from blistering. To investigate the performance, double-differential thick target neutron yields (DDTTNYs) were measured by using the combined converter at JAEA Tandem accelerator with multiple foil activation method. The DDTTNYs were derived by unfolding code, GRAVEL. These results indicate that the present converter can provide a neutron yield comparable to that of the single-element Be converter. In the future, we would like to obtain experimental data on the timespan of the converters.

References

[1] Y. Nagai, “Medical Isotope Production using High Intensity Accelerator Neutrons,” *Phys. Procedia*, vol. 66, pp. 370–375, 2015, doi: 10.1016/j.phpro.2015.05.046.

[2] T. Kin, T. Kawagoe, S. Araki, and Y. Watanabe, “Production of high-purity medical radio isotope 64Cu with accelerator-based neutrons generated with 9 and 12 MeV deuterons,” *J. Nucl. Sci. Technol.*, vol. 54, no. 10, pp. 1123–1130, 2017, doi: 10.1080/00223131.2017.1344585.

[3] J. F. Ziegler, M. D. Ziegler, and J. P. Biersack, “SRIM - The stopping and range of ions in matter (2010),” *Nucl. Instruments Methods Phys. Res. Sect. B Beam Interact. with Mater. Atoms*, vol. 268, no. 11–12, pp. 1818–1823, 2010, doi: 10.1016/j.nimb.2010.02.091.

[4] M. Matzke, “Unfolding of pulse height spectra: the HEPRO program system,” Braunschweig, 1994. [Online]. Available: https://cds.cern.ch/record/275528

[5] O. Iwamoto *et al.*, “Japanese evaluated nuclear data library version 5: JENDL-5,” *J. Nucl. Sci. Technol.*, vol. 60, no. 1, pp. 1–60, 2023, doi: 10.1080/00223131.2022.2141903.

[6] T. Sato *et al.*, “Recent improvements of the particle and heavy ion transport code system–PHITS version 3.33,” *J. Nucl. Sci. Technol.*, vol. 61, no. 1, pp. 127–135, 2023, doi: 10.1080/00223131.2023.2275736.

[7] S. Nakayama, O. Iwamoto, Y. Watanabe, and K. Ogata, “JENDL/DEU-2020: deuteron nuclear data library for design studies of accelerator-based neutron sources,” *J. Nucl. Sci. Technol.*, vol. 58, no. 7, pp. 805–821, 2021, doi: 10.1080/00223131.2020.1870010.

Acknowledgements

I would like to thank all those involved in this research.

30. Small-angle neutron scattering and neutron transmission of hardened cement paste

Kaoru Y. HARA[1*], Masato OHNUMA[1], Yuya YODA[2] and Kosuke HIROI[3]
[1]Hokkaido University, Kita 13 Nishi 8, Kita-ku, Sapporo 060-8628, Japan
[2]Shimizu Corporation, Etchujima 3-4-17, Koto-ku, Tokyo 135-8530, Japan
[3]Japan Atomic Energy Agency, Shirakata 2-4, Tokai-mura, Naka-gun, Ibaraki 319-1195, Japan
[*]Email: hara.kaoru @ eng.hokudai.ac.jp

Small-angle neutron scattering measurements of hardened cement paste samples were conducted to characterize the nano-scale structure using a contrast variation method in BL15 TAIKAN of MLF at J-PARC. Additionally, the neutron transmissions of the hardened cement paste samples were measured and calculated to evaluate the water contents including the samples. The current data analysis is reported.

1. Introduction

We have measured a small-angle neutron and X-ray scattering (SANS and SAXS) of cement paste to investigate a nanoscale structure of cement paste [1–3]. Through the in-situ SAXS measurements of cement paste, we have focused on a fine nanostructure that emerged with time as a shoulder on the SAXS profiles at the high-q region of around 3 nm^{-1}. Based on a microstructure model of cement paste [4] and a previous SANS work [5], it is expected that the fine nanostructure consists of calcium silicate hydrate (C-S-H) gel and pore water, where C, S, and H stand for respectively CaO, SiO_2, and H_2O in a conventional notation of cement chemistry. The C-S-H is a major hydrate among the cement hydrates and relates closely with the compressive strength of hardened cement paste (HCP).

Recently, to obtain information of the elemental composition of the fine nanostructure, SANS measurements of HCP samples were conducted using a contrast variation method at J-PARC [6]. In addition, the neutron transmissions of the HCP samples were also measured because water contents including these samples were evaluated for subtracting the background due to incoherent scattering of hydrogen from the SANS profiles. In the data analysis, for the evaluation of the water contents, the neutron transmissions which were calculated using the PHITS code [7] were compared with the measured neutron transmissions, where the JENDL-5 ACE library (ACE-j50; neutron induced nuclear data and thermal scattering law data for hydrogen and deuterium in water) [8, 9] was applied to the PHITS calculations. The current data analysis of the neutron transmissions is briefly reported together with a part of data of SANS measurements.

2. Experimental

2.1. Sample preparation of hardened cement paste

Ordinary Portland cement (OPC) and water were used to prepare a cement paste with water-to-

cement ratio (w/c) of 0.4, where the water was light water (H_2O). The cement paste was sealed into a plastic bottle and cured at 20℃ in a thermostatic chamber until the age of 28 d. The cylindrical HCP which was demolded from the plastic bottle was sliced to disk-shaped samples with the thickness of approximately 1 mm. The HCP samples were immersed with various H_2O/D_2O fluid mixtures for 1 day to control the scattering contrast of the nanostructure of HCP. The atomic ratio of deuterium to total hydrogen isotope (D/HD) which was contained in the fluid mixture was adapted as 0.0, 0.3, 0.55, 0.8, and 1.0. Lastly, each HCP sample was taken out from the fluid mixture and sealed into an 1-mm gap titanium cell with quartz windows (See Fig. 1). To collimate a neutron beam, a cadmium sheet having an 1-cm hole in diameter was assembled in the cell at the upstream side of the quartz window.

2.2. Measurements

The SANS and neutron transmissions were measured using the HCP samples in BL15 TAIKAN [10] of MLF at J-PARC. In addition, the SANS and neutron transmissions were measured for H_2O, D_2O, and cement samples which were sealed in the cells. These samples were mounted on the automatic sample changer at the curing temperature of 20℃. The scattered and transmitted neutrons were counted by using ^{3}He position sensitive detectors (PSD) and a nitrogen detector, respectively.

The measured SANS profiles for the HCP samples are shown at D/HD = 0.0, 0.8, and 1.0 by the triangle in Fig. 2, where q (= $4\pi \sin\theta/\lambda$) is a magnitude of scattering vector and 2θ is the scattering angle. The color of triangle stands for the variation of D/HD. In the high-q region of Fig. 2, the flat component level decreases with D/HD because the background neutron arise from the incoherent hydrogen elastic scattering is a dominant component. For comparison, the measured SANS profiles of the 1-mm-thickness H_2O and D_2O samples are also plotted by the gray and black lines, respectively, in Fig. 2. The neutron scattering intensity for H_2O is much larger than one for D_2O.

The neutron transmissions of the HCP samples are shown at D/HD = 0.0, 0.8, and 1.0 in Fig. 3(a). The values of D/HD are given in the legends. On the other hand, the neutron transmissions of the H_2O, D_2O, and cement samples are shown in Fig. 3(b).

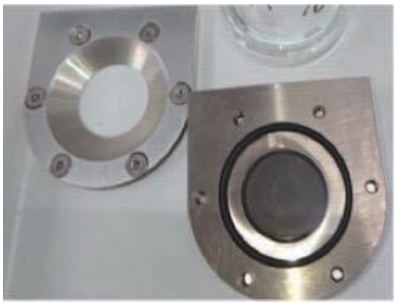

Figure 1: BL15 assembly-type cell and HCP sample. The HCP sample was sandwiched between two quartz windows.

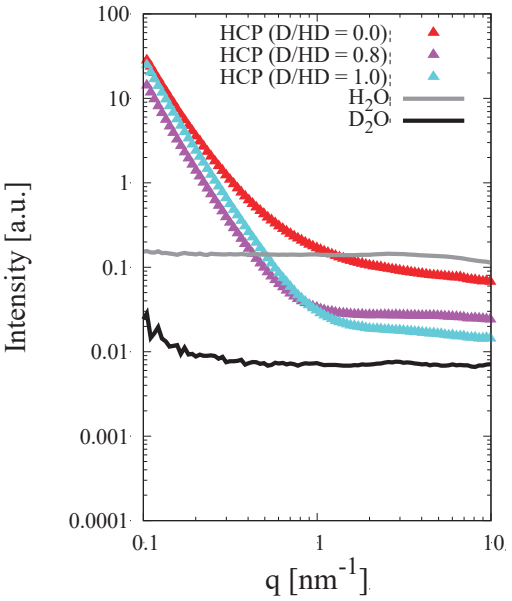

Figure 2: Measured SANS profiles

3. Data analysis using PHITS code

It is important to evaluate the water contents of sample (in particular, the amount of ^{1}H) in this data analysis for subtracting the background on the SANS profile. As the evaluation, the PHITS code was utilized to reproduce the measured neutron transmission. The PHITS version was 3.13. The input geometry was very simple; a source, a sample, and a tally were defined in a void space as shown in Fig. 4. White neutrons were generated at the source position in the energy range from 0.1 meV to 1 eV and emitted toward the sample as a pencil like beam with a diameter of 1 cm. The distance between the source and the sample (L_1) was 14.35 m. The geometry of sample was set 1 cm in diameter and 0.1 cm in thickness. The transmitted neutrons were counted by the tally, where the neutron flight path length (L_2) from the source to the tally was 20 m. The time of flight (TOF) was calculated for the PHITS output.

First, to confirm the results of calculation, the calculated neutron transmission for each ingredient of the HCP sample (H_2O, D_2O, and cement) was compared with the measured ones. The neutron wavelength on the horizontal axis was derived from the TOF value. As shown in Fig. 3(b), the calculation for H_2O (or D_2O) was in good agreement with the measurement. The calculation for cement was in reasonable agreement with the measurement. However, it somewhat overestimated above 0.6 nm. We have presumed that this difference between the measurement and calculation was induced from the gain of total neutron cross section due to the coherent scattering.

In the next step as an approximate correction, therefore, the measured transmission of the HCP sample was divided by the measured one of the cement sample; where the density of cement sample corresponded to the amount of cement that was involved in the HCP sample with the thickness of about 0.95 mm. Note that the thickness of the actual HCP samples was 0.91−0.96 mm. And then the corrected transmission of HCP sample was regarded as the transmission of D_2O/H_2O mixture fluid. After the correction, the transmission of D_2O/H_2O mixture fluid was simulated using the PHITS code to reproduce the corrected transmission of HCP sample. To simplify the simulation process, in the current data analysis, the fixed value was used for the number density of water molecule of mixture fluid (N_t) which was 55 percent relative to the number density of water molecule of light water. The N_t was determined from the simulation for reproducing of the measured transmission of HCP sample at D/HD = 0.0 as shown in Fig. 5(a). The gray line stands for the results of simulation. The tringle and cross stand for respectively the measured and corrected transmissions of the HCP sample in Fig. 5.

The neutron transmission of HCP samples at D/HD = 0.8 and 1.0 were simulated as shown by gray line in Fig. 5(b) and (c), respectively. The measured and corrected transmissions of the HCP sample are also plotted by tringle and cross, respectively. In the simulations, the value of D/HD (Cal) was adjusted to reproduce the corrected transmission while N_t was same at all simulations. As the result of the simulations, the plot of the obtained D/HD (Cal) vs. D/HD (Exp) is shown in Fig. 5(d), where the D/HD (Exp) corresponds to the D/HD of the D_2O/H_2O mixture fluid which used for immersing the HCP sample. In Fig. 5(d), the D/HD (Cal) has a offset and is not 100 at D/HD (Exp) = 100 because the replacement of D from H in the HCP sample dose not fully complete. The water content of the HCP sample was estimated from the D/HD (Cal) and the N_t.

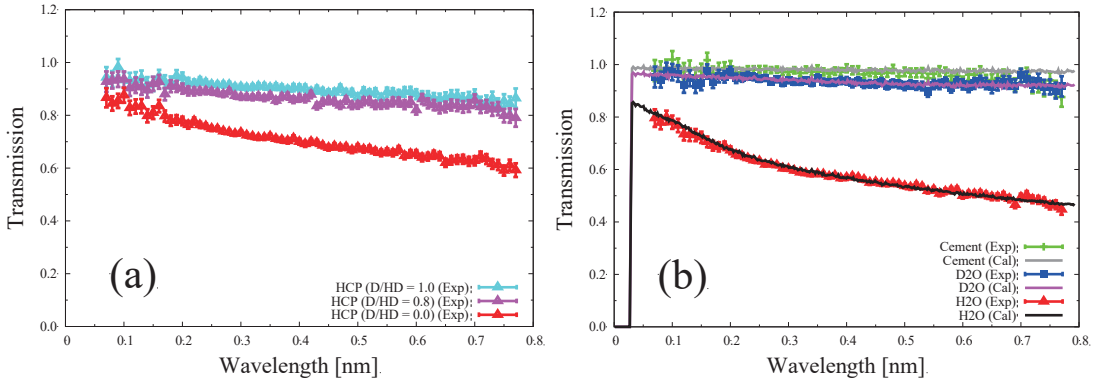

Figure 3: Measured neutron transmissions of the cement paste samples (a). The neutron transmissions of H_2O, D_2O, and cement samples (b).

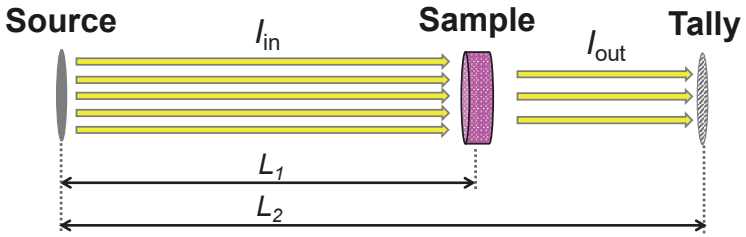

Figure 4: Schematic view of the input geometry in the PHITS calculation

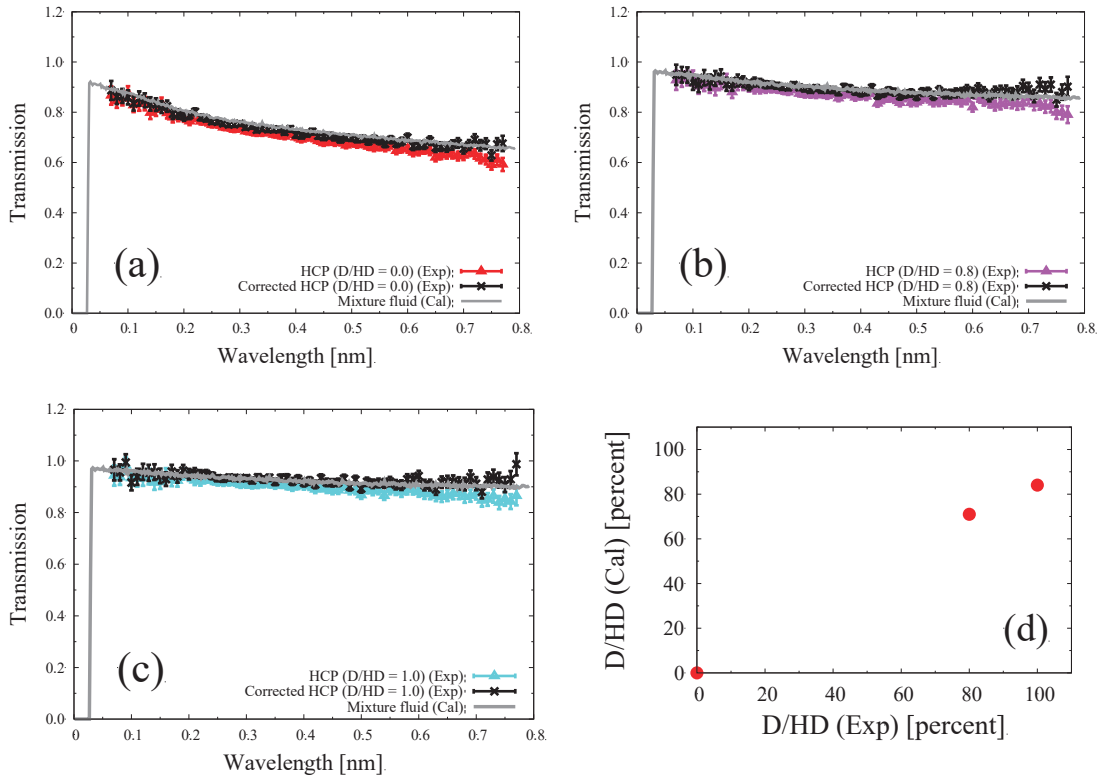

Figure 5: Neutron transmissions of the HCP samples (a)−(c). In each figure, the measured and corrected transmissions are shown by tringle and cross, respectively. The calculated transmission is shown by gray line. The obtained D/HD (Cal) vs. D/HD (Exp) is plotted in (d).

4. Results and discussion

Figure 6 shows the SANS profiles which were obtained by subtracting the background based on the information of water contents which was estimated from the PHITS simulation. In the high-q region around 3 nm^{-1}, the intensity closes to a minimum at D/HD = 0.8 among three SANS profiles. It is consistent the match point that was determined from the intensities at q of 1−2 nm^{-1} in the previous work [5]. On the other hand, our SANS data extends to the high-q region compared to the data of previous work [5]. A shoulder which corresponds to the fine nanostructure is observed around 3 nm^{-1} on the SANS profiles at D/HD = 0.0.

In the cases of D/HD = 0.8, the superposition of the SANS profiles of H_2O and D_2O samples were used to subtract the background as a replacement for the SANS profile of H_2O/D_2O mixture fluid. However, the SANS profile of H_2O/D_2O mixture fluid is generally a little different from the superposition profile in the high-q region because of the effect of hydrogen inelastic scattering. In Fig. 6, indeed, the residual components on the SANS profiles are observed at D/HD = 0.8 above 6 nm^{-1}. The residual component above 6 nm^{-1} should be invalid information because the uncertainty remains. The usage of the SANS profile of H_2O/D_2O mixture fluid would be better for more precise subtraction. Therefore, additional measurements were already performed with the H_2O/D_2O mixture fluid samples. The data analysis using the data of the H_2O/D_2O mixture fluid sample is ongoing now.

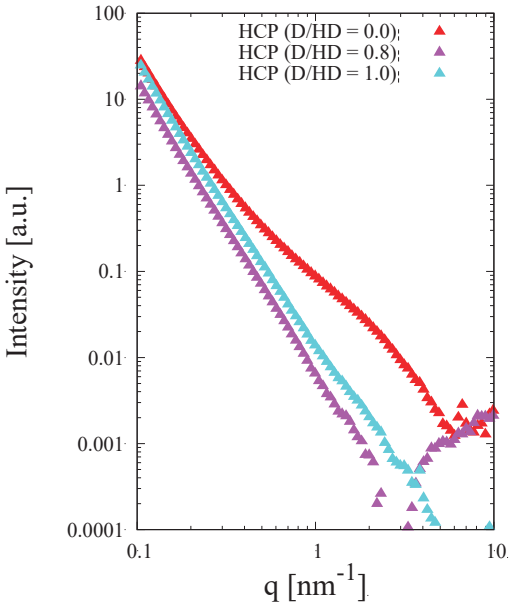

Figure 6: Obtained SANS profiles of the HCP samples after the background subtraction

5. Conclusion

The SANS and neutron transmissions of the HCP samples were measured at J-PARC. In the data analysis, the PHITS simulation was utilized to reproduce the measured neutron transmissions of the HCP samples and to estimate the water contents including the HCP samples. By combining the estimated water contents and the measured SANS profiles for the H_2O and D_2O samples, the background due to the incoherent neutron scattering on hydrogen was subtracted from the measured SANS profile and coherent scattering profiles of the HCP samples were obtained. After the subtraction, as shown in Fig. 6, the shoulder of the fine nanostructure was observed around 3 nm^{-1} on the SANS profiles at D/HD = 0.0 while

the detail analysis is in process. On the other hand, the intensities of SANS profiles were varied with the D/HD of D_2O/H_2O mixture fluid. Based on the present results of SANS measurements, the fine nanostructure which has been focused from our SAXS measurements would be identified by obtaining the SAXS/SANS ratio in the next step of data analysis.

References

1) Hara KY, Morinaga Y, Yoda Y, Ohnuma M. Small-angle scattering measurements for cement paste samples using X-rays and neutrons in Hokkaido University, Proc. 2021 Symp. Nuclear Data (2022) pp.109−114. (JAEA-Conf 2022-001).
2) Hara KY, Morinaga Y, Yoda Y, Ohnuma M. Measurements of small-angle X-ray scattering for cement paste samples with light water and heavy water, IEEE 2021 NSS-MIC, **N-28-064**; 2021 Oct. 16−23; Online Conference. Conf. Record (DOI: 10.1109/NSS/MIC44867.2021.9875809).
3) Hara KY, Morinaga Y, Yoda Y, Tsujino M, Nishida A, Ohnuma M. Effect of initial curing temperature on cement nanostructure, AESJ 2020 Fall Meeting, **3L11**; 2020 Sep 16−18; Online Meeting [in Japanese].
4) Pinson MB, Masoero E, Bonnaud PA, Manzano H, Qing J, et al. Hysteresis from multiscale porosity: modeling water sorption and shrinkage in cement paste, Phys. Rev. Applied 2015;3:064009(1−17).
5) Allen AJ, Thomas JJ, Jennings HM. Composition and density of nanoscale calcium-silicate-hydrate in cement, Nat. Mater. 2007;6:311−316.
6) Hara KY, Ohnuma M, Yoda Y, Hiroi K. Small-angle neutron scattering measurements of hardened cement paste with light and heavy water. AESJ 2023 Fall Meeting, **2I18**; 2023 Sep 6 −8: Nagoya [in Japanese].
7) Sato T, Iwamoto Y, Hashimoto S, Ogawa T, Furuta T, et al. Recent Improvements of the Particle and Heavy Ion Transport code System - PHITS version 3.33, J. Nucl. Sci. Technol., 2024;61:127 −135.
8) Web page of JAEA reactor physics team, https://rpg.jaea.go.jp/main/en/ACE-J50/ (accessed 2023 Jan 09-14).
9) Iwamoto O, Iwamoto N, Kunieda S, Minato F, Nakayama S. et al., Japanese evaluated nuclear data library version 5: JENDL-5. J. Nucl. Tci. Technol., 2023;60:1−60.
10) Takata S, Suzuki J, Shinohara T, Oku T, Tominaga T, et al. The design and *q* resolution of the small and wide angle neutron scattering instrument (TAIKAN) in J-PARC. Proc. 2nd Int. Symp. Science at J-PARC, JPS Conf. Proc. 2015;8:036020(1−6).

Acknowledgements

This work was conducted by the Industry-Academia Collaboration between Shimizu Corporation and Hokkaido University.

31. Feasibility test of cavity exploration using a prototype muography detector

Ayumu Okuda[1], Shoichiro Kawase[1#], Naoya Okamoto[1], Yukinobu Watanabe[1]

[1]Department of Interdisciplinary Engineering Sciences, Kyushu University,
6-1 Kasuga-koen, Kasuga, Fukuoka 816-8580, Japan
Email: kawase@aees.kyushu-u.ac.jp

Abstract

We aim to develop a disaster prevention system for cave-ins caused by underground tunnel construction using muography technique. As a first step, we have developed a dedicated prototype muography detector capable of determining the direction of incoming cosmic rays and performed a feasibility test to detect a simulated cavity created inside piled clay bricks. The location and size of the cavity were estimated from the transmittance obtained from the measured muon fluxes both with and without cavity. The estimated results were consistent with the actual location and size and were well reproduced by the PHITS simulation.

1 Introduction

In recent years, demand for underground tunnel construction has increased due to the growing use of underground space in urban areas. Shield tunneling methods are widely used to construct large underground tunnels. Although the methods are considered safe, subsidence accidents have occurred due to underground cavities created during tunnel excavation [1]. To prevent such accidents, it is necessary to detect the cavities during tunnel construction and take some preventive measures. Various exploration methods, such as ground-penetrating radar and boring surveys, have been used for this purpose. However, ground-penetrating radar cannot detect deep underground cavities. In addition, the locations where boring surveys can be conducted are limited and are not suitable for comprehensive surveys. Therefore, those traditional methods face limitations in continuously detecting cavities deeper than ten meters underground during tunnel construction. To overcome these limitations, we propose a new exploration method using the muography technique [2]. Muography is a noninvasive exploration method that utilizes cosmic ray muons.

Cosmic ray muons, a kind of environmental radiation, constantly reach the ground with a flux of approximately 1 /cm^2/s. High-energy muons, whose energy spectrum spans from a few MeV to TeV, can penetrate several kilometers of rock, and their flux is attenuated by the density of the material they pass through. Measuring the variation in muon flux at multiple locations allows us to obtain the spatial density distribution of soil and bedrock by the muography technique. Our proposed exploration system, depicted in Fig. 1, incorporates a dedicated detector installed behind a shield machine to continuously measure the muon flux. Thanks to the high penetrating power of muon, the measurement can be conducted 20 to 30 m underground where the shield tunneling method is used, addressing the limitations of conventional exploration methods.

The goal of our study is to develop a disaster prevention system for cave-ins by using muography technique as shown in Fig.1. As a first step, we have developed a prototype detector capable of determining the direction of incoming cosmic rays. This paper reports the results of a feasibility test using the prototype detector.

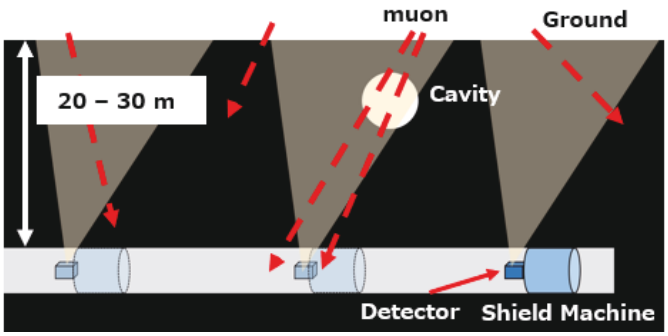

Fig. 1. Schematic drawing of a disaster prevention system for cave-ins using muography

2 Material and Methods

2.1 Muography detector and prototype detector

A proposed muography detector for detecting underground cavities is shown in Fig. 2. The detector is composed of several 1D detector modules and each 1D detector consists of a plastic scintillator and two photomultiplier tubes (PMTs) attached on both sides of the scintillator. Using these 1D detectors, two points on the muon's track are measured and the direction can be estimated. In the present work, we have developed a prototype detector consisting of four 1D detectors (PS1, PS2, PS3 and PS4) as shown in Fig. 3. Each 1D detector consists of a plastic scintillator (Eljen Technology EJ-200) and PMTs whose details are listed in Table 1, and they were assembled by optical cement EJ-500.

Table 1. Configuration of the 1D detectors

	Plastic scintillator size [mm^3]	PMT model number
PS1	100 × 1500 × 57	Hamamatsu H6410
PS2	100 × 1500 × 57	Hamamatsu H6410
PS3	100 × 1500 × 20	Hamamatsu H6410
PS4	100 × 1500 × 20	Hamamatsu H10828

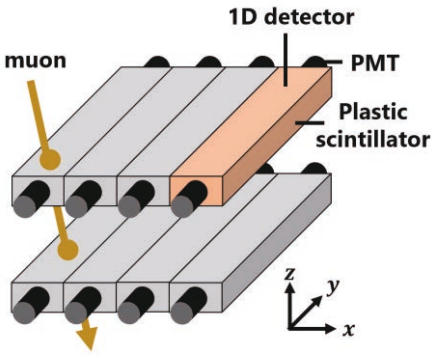

Fig. 2 The proposed muography detector

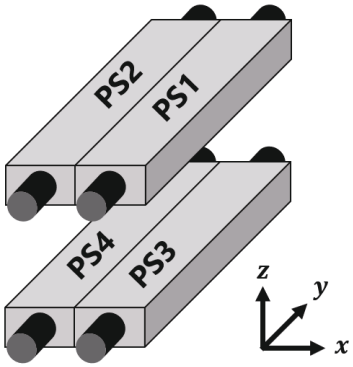

Fig. 3 Schematic view of the prototype detector

2.2 Principle of passing position and direction measurement

In this section, methods for measuring the passing position and direction of a muon through the 1D detector are explained. The position is determined from the time difference between the signals from the two PMTs attached on both sides of the detector. The y-axis is the longitudinal direction of the detector, with the origin at its center. If a muon passes through at $y = y_{\mathrm{m}}$ at times t_0, the arrival time of scintillation light at the left and right PMTs, $t_{\mathrm{L,R}}$, are expressed by

$$t_{\mathrm{L}} = t_0 + \frac{L/2 + y_{\mathrm{m}}}{v}, \tag{1}$$

$$t_{\mathrm{R}} = t_0 + \frac{L/2 - y_{\mathrm{m}}}{v}, \tag{2}$$

where L is the length of the plastic scintillator, and v is the effective speed of light in the plastic scintillator. Using Eqs. (1) and (2), the time difference Δt is given by

$$\Delta t \equiv t_{\mathrm{L}} - t_{\mathrm{R}} = \frac{2y_{\mathrm{m}}}{v}, \tag{3}$$

Therefore, y_{m} can be obtained by measuring Δt as follows:

$$y_{\mathrm{m}} = \frac{v}{2}\Delta t, \tag{4}$$

If two passing positions of muons (y_1, y_2) are measured by using the upper and lower 1D detectors as shown in Fig. 4, the passing position (y') of muons at h above the top surface of the upper 1D detector can be calculated by

$$y' = y_2 + \frac{h}{d}(y_2 - y_1), \tag{5}$$

where d is the distance between the top surfaces of upper and lower 1D detectors.

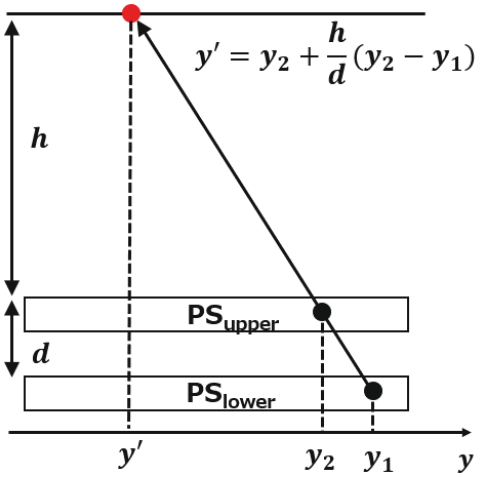

Fig. 4 The system of calculating the passing position y'

2.3 Data Acquisition System

In the data acquisition system, the output signals from both PMTs are converted to timing signals using a constant fraction discriminator (CFD, ORTEC CF8000) and the output signals from CFD serves as the

START signal input to a time-to-digital converter (TDC, CAEN V775). The data acquisition process is triggered by the coincidence of signals from the upper 1D detector (PS1 or 2) and the lower one (PS3 or 4), which acts as the COMMON STOP signal. The measurement data from the TDC is then transmitted via the VME bus to the computer for recording.

3 Feasibility test

To assess the feasibility of muography exploration method, we performed a test experiment to detect a simulated cavity created inside piled clay bricks.

3.1 Experiment setup

In this experiment, clay bricks were piled above the prototype detector to form a cavity as shown in Fig. 5. The size of each brick is $10 \times 21 \times 6$ cm^3 and the density is 2.0 g/cm^3. The distance between the two 1D detectors is 206 cm and the base of the brick pile is 162 cm above the top surface of the upper 1D detector. Figure 6 shows a photograph of the piled clay bricks. The plied bricks have a total size of $45 \times 126 \times 54$ cm^3. A cavity was simulated in the piled bricks by removing some bricks as shown in Fig. 7. The cavity size is $40 \times 42 \times 48$ cm^3. The horizontal center of the prototype detector was aligned with the central position of both the brick pile and the cavity. In this experiment, measurements were conducted under three different conditions: with the cavity, with no cavity, that is, no bricks were removed, and with no bricks at all. The measurement time is two weeks for each condition.

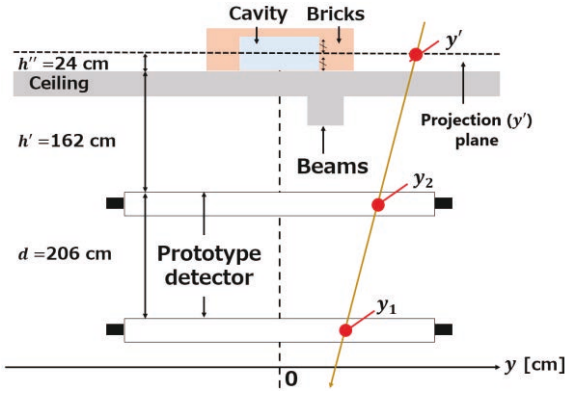

Fig. 5. Experimental setup

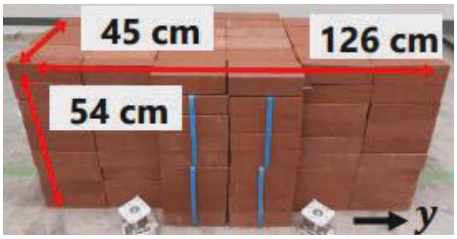

Fig. 6. Piled clay bricks

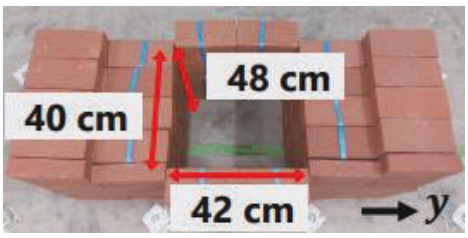

Fig. 7. A simulated cavity inside the brick pile

3.2 Data analysis

The two positions (y_1 and y_2) on the muon track were measured with the upper and lower 1D detectors by measuring Δt as described in section 2.2. To convert Δt to y_m, a linear function $y_m = a\Delta t + b$ was used.

The values of a and b were determined from a preliminary measurement and are summarized in Table 2. Muon tracks were reconstructed by using y_1 and y_2, and y' was calculated at the height of the cavity center by substituting 206 cm for d and 186 cm for h in equation (5). In addition, transmittance T was calculated to quantitatively evaluate the difference of muon flux due to the cavity:

$$T = \frac{n_{\text{with cavity}}(y', y' + \Delta y')}{n_{\text{without cavity}}(y', y' + \Delta y')}, \tag{6}$$

where $n(y', y' + \Delta y')$ is the number of muons passed through the interval $[y', y' + \Delta y')$. If the cavity exists, T is expected to be larger than 1.

Table 2. Parameters of the linear relational expression between y_m and Δt

	PS1	PS2	PS3	PS4
a [cm/ns]	13.55	13.58	14.82	15.01
b [cm]	1.74	1.02	-5.61	-5.61

3.3 Results

Figure 8 shows the y' distribution at the height of the cavity center measured in this experiment. The count exhibits significant increase around y'=0 in the measurement with the simulated cavity, compared to that without the cavity. To quantify the difference, T was calculated and presented in Fig. 9. In the distribution, T is significantly larger than 1 within the range of $-21\ \text{cm} \leq y' \leq 21\ \text{cm}$ where the cavity is located. This indicates that the low-density area is consistent with the known position and size of the cavity. One notices that muon counts are low around $y' = 20$ in the y' distribution. A possible reason for this will be discussed using simulation in the following chapter.

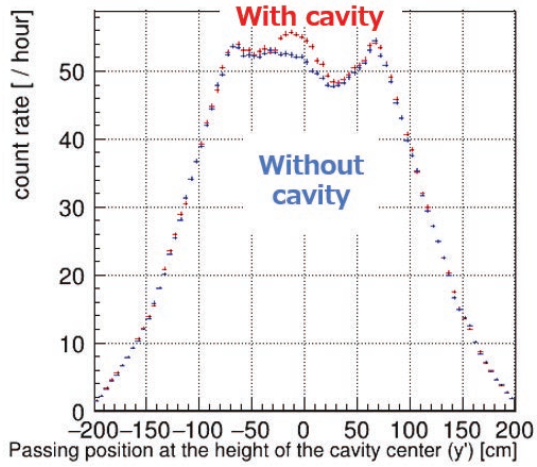

Fig. 8. y' distribution

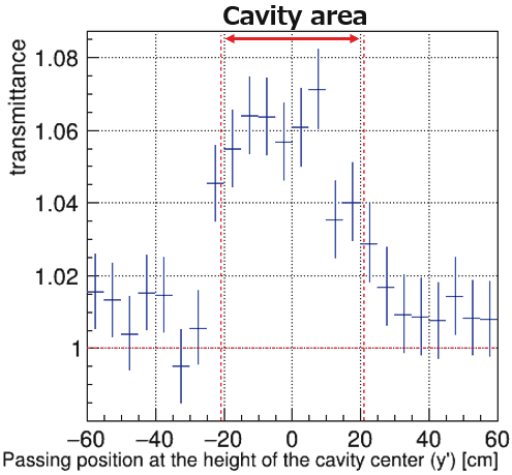

Fig. 9. transmittance distribution

4 Comparison with PHITS simulation

The experimental result is compared with simulations using a Monte Carlo particle transport code PHITS [3]. In the simulation, a realistic building structure including ceilings and beams was considered as shown in Fig. 10 (a). The incident muons were generated using the PARMA model [4] implemented in PHITS, assuming the number of incident muons equivalent to a four-month measurement on the ground. The

simulation results are presented in Fig. 10 (b). The histograms were normalized by integral value for comparison. The calculated transmittance is compared with the experimental result in Fig. 11. The simulation results show a good agreement with the experimental result. In the y' distribution shown in Fig. 10 (b), the PHITS simulation exhibits a dip around $y' = 20$ cm. This dip is expected to be generated by the attenuation of muons in the thick beam shown in Fig. 10 (a).

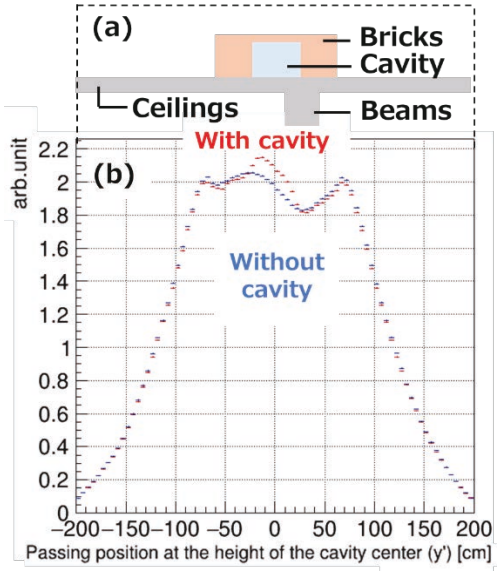

Fig. 10. (a) Placement of beams and bricks (b) y' distribution (PHITS result)

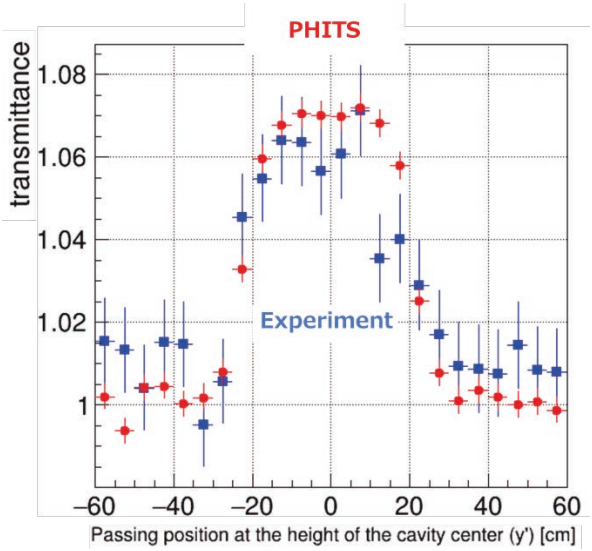

Fig. 11 Transmittance distribution

5 Summary and outlook

We proposed a new exploration method with muography for the cave-ins caused by underground tunnel construction. To demonstrate the feasibility, we developed a prototype muography detector and performed a test experiment to detect a simulated cavity. The experimental result shows that the location and size of the cavity can be estimated with the required accuracy. As a next step, we plan to estimate of 3D location and size of cavities by reconstruction of 3D density distribution information using multi-point measurement data.

Reference

[1] https://www.e-nexco.co.jp/news/cms_assets/news/2021/04/02/01.pdf (accessed 2024-01-04)

[2] L. Bonechi, R. D'Alessandro, A. Giammanco, Atmospheric muons as an imaging tool, Reviews in Physics, 5,100038 (2020)

[3] T.Sato, Y. Iwamoto, S. Hashimoto et al., Niita, Recent improvements of the Particle and Heavy Ion Transport code System – PHITS version 3.33, J. Nucl. Sci. Technol. DOI:10.1080/00223131.2023.2275736

[4] T. Sato, Analytical Model for Estimating Terrestrial Cosmic Ray Fluxes Nearly Anytime and Anywhere in the World: Extension of PARMA/EXPACS, PLOS ONE 10(12). (2015)

32. Study on Neutron Induced Charged Particle Emission Reactions Using Sample-Added Scintillator

Gengchen LI[1*a], Tatsuya KATABUCHI[1], Hiromi KONDO[1], Rovira GERARD[2],
Atsushi KIMURA[2], Shoji NAKAMURA[2], and Shunsuke ENDO[2]
[1]Laboratory for Advanced Nuclear Energy, Tokyo Institute of Technology, Tokyo, Japan
[2]Japan Atomic Energy Agency, Tokai, Ibaraki, Japan
[*]Email: li.g.aj@m.titech.ac.jp

A new measurement technique for neutron-induced charged-particle emission reactions was developed. The new method employed plastic scintillator added with sample material for measurement. Scintillators including sample materials were fabricated. The fabricated scintillators were tested in irradiation test experiments conducted with the Accurate Neutron Nuclear Reaction Instrument of the Japan Proton Accelerator Research Complex. Boron nitride and lithium fluoride were chosen as sample materials to mix with scintillator for the test experiments. To identify charged particles, the pulse shape discrimination technique was employed. As a result, charged-particles were detected and identified successfully.

1. Introduction

Data of neutron capture cross sections are important for fundamental studies and applications in nuclear science and engineering. The total cross section, capture cross section and scattering cross section of many substances have been widely measured. But the cross sections of neutron-induced charged-particle emission reactions have not been measured as systematically as total or capture cross sections. For example, chlorine constitutes coolant material in some types of molten salt reactors, but the lack of comprehensive data on neutron-induced charged-particle reactions limits the accuracy of criticality calculation of such reactors [1-4]. It is important to conduct further measurements of these cross sections for various materials.

In the present work, a new measurement technique for neutron-induced charged-particle emission reactions was developed. The new method uses plastic scintillator added with sample material for measurement. The purpose of the present study is to detect charged-particle emission reactions particles with the sample-added scintillation detector.

2. Experiments

The plastic scintillator used in the present work was UV-curable resin-based scintillator which consisted of UV-curable resin (M-211B), luminous agent (PPO), wavelength shifter (Bis-MSB), and

[a] Present address: Laboratory for Advanced Nuclear Energy, Tokyo Institute of Technology, 2-12-1 Ookayama, Meguro-ku, Tokyo, 152-8550, Japan

photo initiator (TPO) [5]. The mixing weight ratios of M-211B, PPO, Bis-MSB, and TPO were 79%, 21%, 0.1%, and 0.02%, respectively.

Sample materials for measurement were added to the scintillator resin. After mixing the sample material and scintillator resin, the mixture was poured into a ring-shaped frame followed by UV irradiation to cure the resin. For the present test experiments, the sample materials to add to the scintillator resin were boron nitride (BN) and lithium fluoride (LiF). A pure scintillator attached with a gold foil was also fabricate to calibrate time-of-flight measurement using resonances of the ^{197}Au(n,γ)^{198}Au reaction.

The fabricated scintillators were tested in irradiation test experiments conducted with the Accurate Neutron Nuclear Reaction Instrument (ANNRI) of the Japan Proton Accelerator Research Complex (J-PARC). The scintillator was placed at a flight distance of 28.75 m. The signal from the photomultiplier tube was fed into CAEN waveform digitizer V1720. The TOF and pulse height (PH) of detected events were recorded. In addition, the pulse shape discrimination (PSD) technique [6-8] was employed to separate charged-particle events from γ-ray background. The PSD technique is based on the fact that decay constant of light emission from organic scintillator depends on linear energy transfer. To perform the pulse shape discrimination, two different time gates, long gate and short gate, were set to integrate areas of the signal. The long gate covered whole time region of the signal and the short gate covered only the rising part of the signal. To identify particles, the quantity PSD was defined by the following Equation (1):

$$PSD = \frac{\text{(Total Gate Area)} - \text{(Short Gate Area)}}{\text{Total Gate Area}} \qquad (1)$$

When the signal has a longer falling tail, PSD becomes higher. Heavier charged particles have longer falling tail, thus showing higher PSD.

3. Results

Figures 1, 2 and 3 show two-dimensional plots for PH vs PSD, TOF vs PSD and TOF vs PH. As seen in Figure 1, the charged-particle emission reactions ^{6}Li(n, t)^{4}He and ^{10}B(n, α)^{7}Li were clearly observed with the LiF and BN-added scintillators. These charged-particle events appeared around 0.3 in PSD while the background events observed in both the pure and sample-added scintillators were 0.2 in PSD. The observed events for the pure scintillator measurement are attributed to **γ**-rays and protons, which were not separated well in the present work. The scintillator resin contained nitrogen, which can introduce proton events through the ^{14}N(n,p)^{14}C reaction.

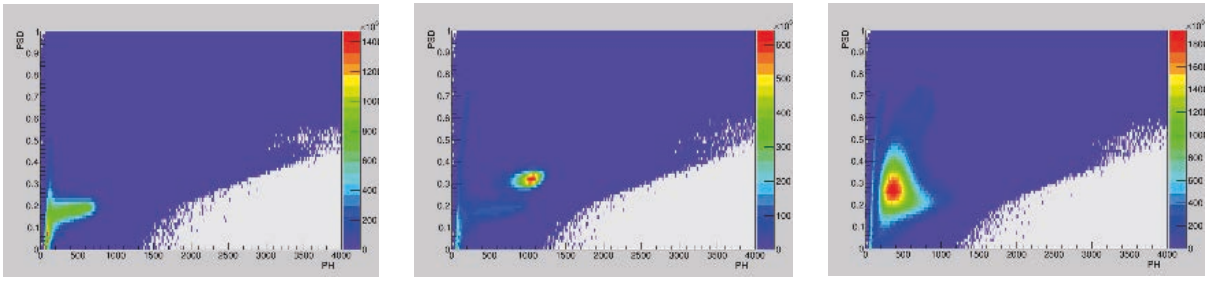

Figure 1. 2D histogram of PH vs PSD for (a) pure, (b) LiF and (c) BN-added scintillators.

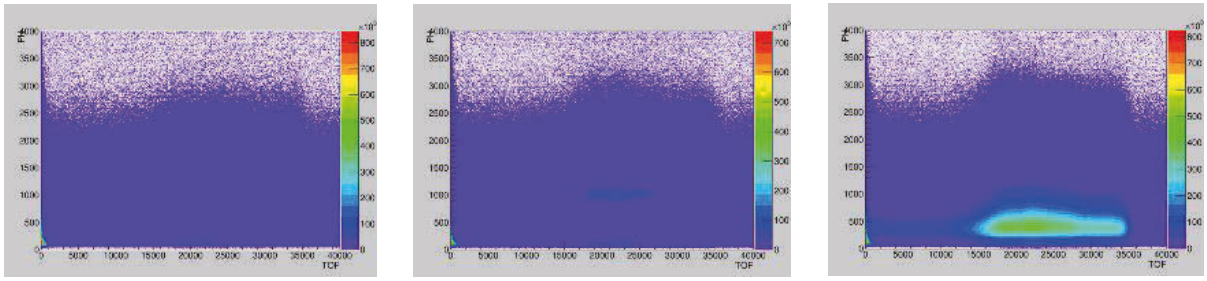

Figure 2. 2D histogram of TOF vs PH for (a) pure, (b) LiF and (c) BN-added scintillators.

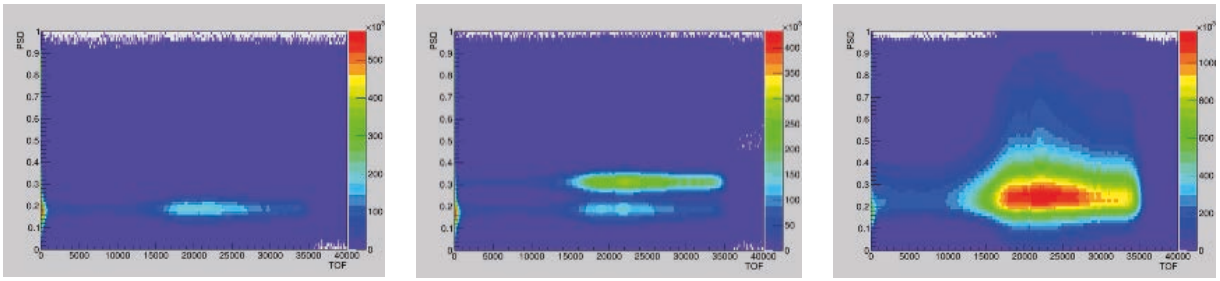

Figure 3. 2D histogram of TOF vs PSD for (a) pure, (b) LiF and (c) BN-added scintillators.

4. Conclusion

A new measurement technique for neutron-induced charged-particle emission reactions were developed. The new method employed plastic scintillator added with sample material for measurement. Scintillators including sample materials were fabricated. The fabricated scintillators were tested in irradiation test experiments conducted with ANNRI of J-PARC. Boron nitride and lithium fluoride were chosen as sample materials to mix with scintillator for the test experiments. To identify charged-particles, the pulse shape discrimination technique was also employed. As a result, charged-particles were detected and identified successfully.

References

1) S. A. Kuvin , H. Y. Lee , Nonstatistical fluctuations in the ^{35}Cl(n, p)^{35}S reaction cross section at fast-neutron energies from 0.6 to 6 MeV, Physical Review C 102, 024623 (2020).
2) E. Sansarbayar , Yu. M. Gledenov et al., Cross sections for the ^{35}Cl(n, α)^{32}P reaction in the 3.3–5.3 MeV neutron energy region, Physical Review C 104, 044620 (2021).
3) E. Sansarbayar , Yu. M. Gledenov, Erratum: Cross sections for the ^{35}Cl(n, α)^{32}P reaction in the 3.3–5.3 MeV neutron energy region [Phys. Rev. C 104, 044620 (2021)], Physical Review C, 105, 049902(E) (2022).
4) Y. Tahara, H. Hirano, S. Chiba, H. Mochizuki, T. Katabuchi, Request for ^{35}Cl(n,p) reaction cross-section measurements and re-evaluations from the standpoint of molten chloride salt fast reactor design, Journal of Nuclear Science and Technology, published online, doi.org/10.1080/00223131.2023.2282553, (2023).
5) Y. Shinjo, T. Kin, A. Nohtomi, Advancement of plastic scintillator made with 3D printer, Ionizing Radiation, 46, 39-48 (2020).

6) R. A. Winyard, J.E. Lutkin, and G. W. McBeth, Pulse shape discrimination in inorganic and organic scintillators. I, Nuclear Instruments and Methods 95, 141 (1971).
7) S. Pai, W.F. Piel Jr., D.B. Fossan , M.R. Maier, A versatile electronic pulse-shape discriminator, Nuclear Instruments and Methods. A 278, 749-754 (1989).
8) P.-A. Södertsröm, J. Nyberg, and R. Wolters, Digital pulse-shape discrimination of fast neutrons and γ-rays, Nuclear Instruments and Methods A 594, 79 (2008).

33. Study on Neutron Activation Method Using UV-Curing Resin Scintillator

Hiromi KONDO†[1], Tatsuya KATABUCHI[1], Li GENGCHEN[1],
Han JIAMO[1], Maxwell Clark MALONEY[1], and Yuta ARIKAWA[1]
[1]Laboratory for Advanced Nuclear Energy, Tokyo Institute of Technology, 2-12-1
Ookayama, Meguro-ku, Tokyo, 152-8550, Japan

†Email: kondo.h.af@m.titech.ac.jp

Abstract

A new method to detect β-rays in neutron activation measurement was developed. The method employed UV-curable resin-based plastic scintillator. In neutron irradiation test experiments, β-rays from an activated gold foil were successfully detected. The derived half-life of the observed decay curve was in good agreement with the half-life of ^{198}Au. It is concluded that the new method was proven to be feasible for detecting β-rays in activation measurement.

1 Introduction

Neutron activation analysis is used in a variety of many fields, such as geology, medicine, and archaeology. In the neutron activation method, a sample is irradiated with neutrons and activated via neutron-induced reactions. The elemental composition is determined from the radioactivity of the sample. In measurement of radioactivity, gamma-rays are often detected with a Ge detector which provides high enough energy resolution to identify gamma-rays from the radioactive sample. If the resultant radioactive nuclides emit only β-rays, β-rays are detected with a β-ray detector such as gas counter for high energy β-rays or liquid scintillator for low energy β-rays. In particular, low-energy β-rays have a very short range in material. This requires the sample to be thin enough for β-rays to emerge from the sample or to be dissolved into solvent of liquid scintillator, which needs bothersome sample preparation including chemical processing. Thus, measurement of pure β nuclides, which do not accompany γ-rays, is not as easy as that of γ-ray emitting radionuclides. To make neutron activation analysis for pure β nuclides easier, a new technique of activation method is being developed in the present research.

2 Methodology

In the new method, sample material for analysis is added to plastic scintillator and the scintillator including the sample is irradiated with neutrons. The irradiated scintillator is attached to a photomultiplier tube to count β-rays to determine the radioactivity. This technique does not require complicated chemical process before or after irradiation.

The plastic scintillator selected for the present work was UV-curable resin-based scintillator which consisted of UV-curable resin (M-211B), luminous agent (PPO), wavelength shifter (Bis-MSB), and photo initiator (TPO) [1]. The mixing weight ratios of M-211B, PPO, Bis-MSB, and TPO were 79%, 21%, 0.1%, and 0.02%, respectively.

The fabrication process is as follows and is shown in Fig. 1. (1) A square-shaped frame of 20 mm × 20 mm with a thickness of 10 mm was fabricated with a 3D printer. (2) A thin Mylar film was glued to the frame as the bottom part. (3) Scintillator resin was poured into the frame. (4) The upper side of the frame was covered with another Mylar film as the top part. (5) The scintillator sandwiched with the Mylar films in the frame was irradiated with UV light to cure.

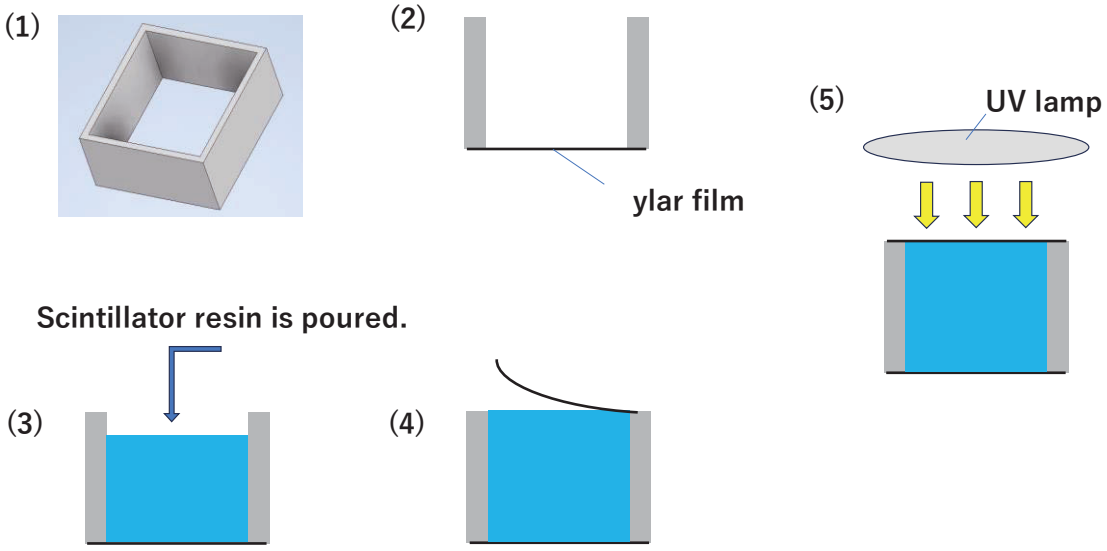

Fig. 1. The fabrication process of scintillator

3 Experiment

Test irradiation experiments were carried out with a Pelletron accelerator in the Tokyo Institute of Technology. The fabricated scintillators were irradiated with neutrons.

Neutrons were generated via the $^{7}Li(p,n)^{7}Be$ reaction induced by a proton beam from the Pelletron accelerator. The purpose of the experiment was to investigate if the scintillator fabricated in the present work can be used to detect β-rays from radioactive samples. The experimental setup is shown in Fig. 2 schematically. A gold foil with a thickness of 10 μm and an area of 20 mm × 20 mm sandwiched with aluminum plates was irradiated with neutrons for 3 hours. The incident proton beam current was around 5.0 μA. After irradiation, the gold foil was attached to the scintillator and β-rays from the activated gold foil were counted.

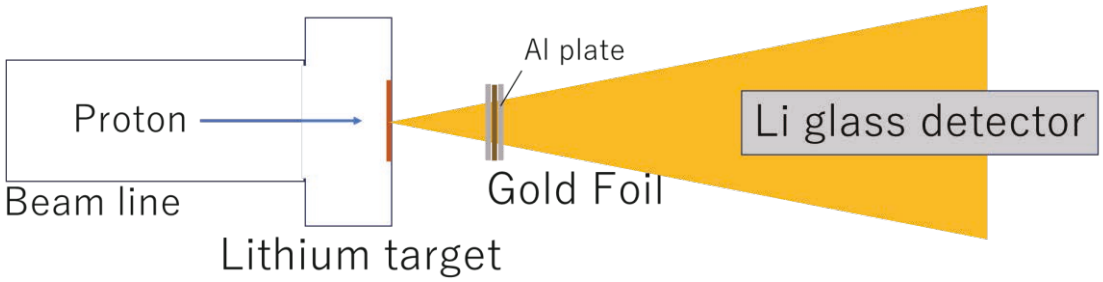

Fig. 2. Experimental Setup

4 Result

The obtained β-ray spectrum is shown in Fig. 3. The continuous β-ray energy distribution is observed well below 900 ch. Measurements were repeated and the time evolution of detected β-ray counts are plotted in Fig. 4. The results were fitted with an exponential curve, deriving the half-life of the decay curve. The derived half-life was 2.72 days, which agrees with the evaluated half-life of ^{198}Au (2.695 days).

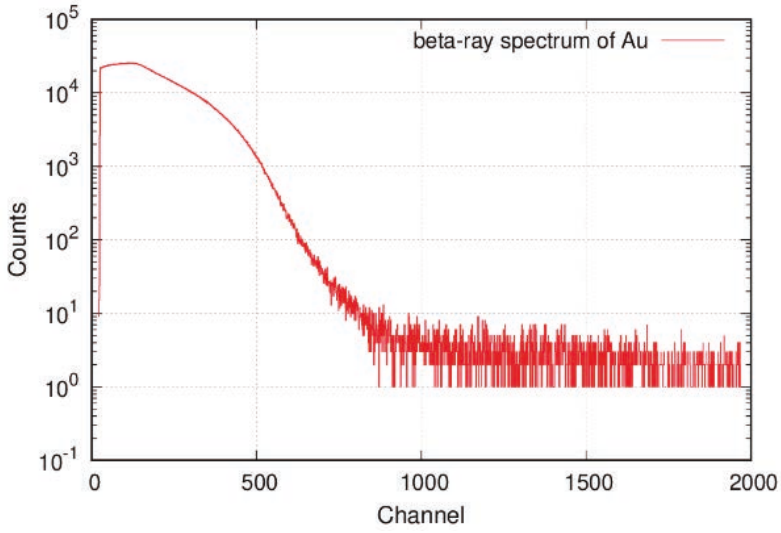

Fig. 3. Beta-ray spectrum of ^{198}Au

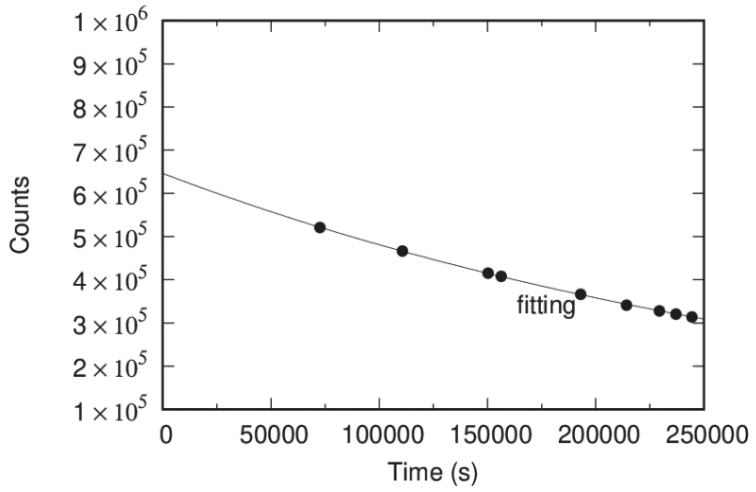

Fig. 4. Time evolution of the counts of detected β-ray

5 Conclusion

A new method to detect β-rays in neutron activation measurement was developed. The method employed plastic scintillator which used UV-curable resin. A neutron irradiation test experiments were carried out. Beta-rays from an activated gold foil were successfully detected and derived half-life of the observed decay curve agreed with the evaluated value. We conclude that the present plastic scintillator resin can be used for β-ray counting. Further irradiation experiments using sample-added plastic scintillators will be conducted as the next step in future work.

References

[1] Yuji Shinjo, Tadahiro Kin, Akihiro Nohtomi, Advancement of plastic scintillator made with 3D printer, Ionizing Radiation, 46, 39-48 (2020)

[2] Robert R. Greenberg, Peter Bode, Elisabete A. De Nadai Fernandes, Neutron activation analysis: A primary method of measurement, Spectrochimica Acta, Part B, 66, 193-241(2011).

34. Performance evaluation of an EJ-276 plastic scintillator using ^{252}Cf neutron source

Teppei KAWATA[1], Shoichiro KAWASE[1*] Yukinobu WATANABE[1], Nobuhiro SHIGYO[2]
[1]Department of Interdisciplinary Engineering Sciences, Kyushu University
6-1 Kasuga-koen, Kasuga, Fukuoka 816-8580, Japan
[2]Department of Applied Quantum Physics and Nuclear Engineering, Kyushu University
744 Motooka, Nishi-ku, Fukuoka 819-0395, Japan
[*]Email: kawase@aees.kyushu-u.ac.jp

We evaluated the performance of EJ-276 plastic scintillator for detecting fast neurons from a ^{252}Cf neutron source, in comparison with that of EJ-301. Both the neutron energy spectrum and the energy-dependent response functions were measured. The experimental response functions were in good agreement with those simulated using SCINFUL. The neutron energy spectrum measured using EJ-276 was consistent with that using EJ-301. Both the measured energy spectra using EJ-276 and EJ-301 were in good agreement with the JIS-recommended spectrum of ^{252}Cf neutron source.

1. Introduction

Fast neutron measurements are an indispensable technique in the field of experimental nuclear physics and nuclear data measurement. Nuclear reactions generating neutrons also yield gamma rays, which are difficult to shield, and thus form a significant background in neutron measurements. Therefore, it is necessary to use a detector capable of discriminating between gamma rays and fast neutrons. As a typical detector for fast neutron measurements, organic liquid scintillators are widely used. Although liquid scintillators are housed in metal containers, there is a problem that the volume decreases over time due to evaporation or leakage. Furthermore, their toxic and flammable nature complicates import and export processes required for overseas experiments. In contrast, plastic scintillators are convenient due to their physical hardness, non-toxicity, and lower flammability. One of the latest pulse-shape discriminating plastic scintillators is EJ-276, but there are few measurements of detector characteristics. Laplace et al. [1] reported the relationship between the energy of recoil protons and the light output in EJ-276, and Ngo et al. [2] extended the energy range of that relationship. Although the latter derived the experimental neutron response functions using monoenergetic neutron sources, they did not compare these with any simulations.

In this study, the response functions of EJ-276 and EJ-301 scintillators were measured using a ^{252}Cf neutron source and compared with simulation results using PHITS [3]. In addition, the n-γ discrimination performance was evaluated and the neutron energy spectrum was derived using the time-of-flight (TOF) method.

2. Experiment

Figure 1(a) shows a schematic diagram of the experimental setup. For comparison, we used EJ-301 organic liquid scintillators in addition to EJ-276. Figures 1(b) and (c) show the respective detectors. Table 1 summarizes the sizes of these detectors, the photomultiplier tubes (PMTs) attached to them and the voltages supplied to the PMTs. The signals from the PMTs were fed to a digitizer (CAEN V1730SB) to convert the analog waveforms into digital data. For each event, the TOF of neutrons emitted from the ^{252}Cf source was measured to derive the energy spectrum. The waveforms were also recorded for n-γ discrimination.

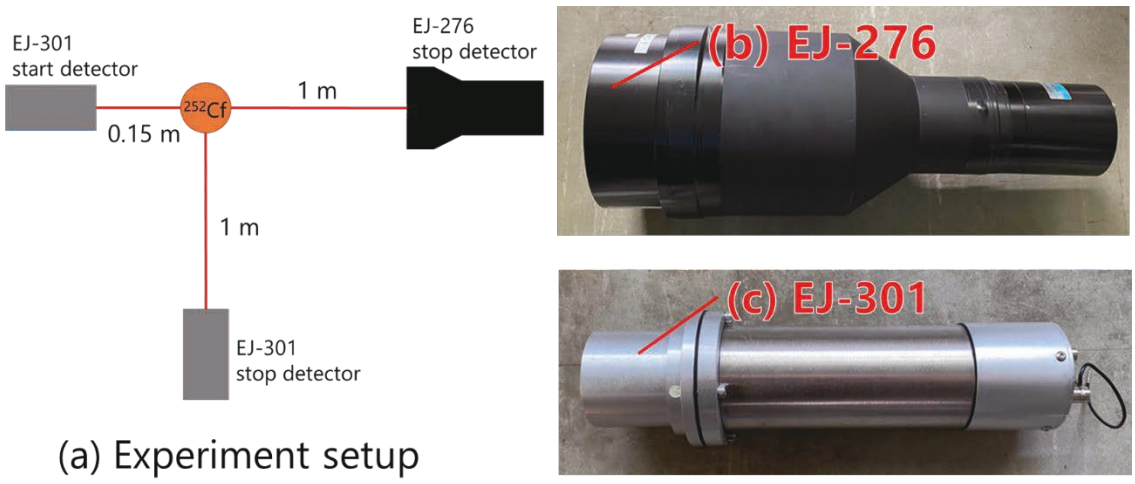

Figure 1 (a) Experimental setup, (b) EJ-276 scintillator and (c) EJ-301 scintillator.

Table 1 Detector sizes and PMTs attached.

	Diameter [cm]	Thickness [cm]	PMT	Voltage [V]
EJ-276	12.70	5.08	R1250	1800
EJ-301	5.08	5.08	R7724	1050

3. Analysis and Results

3.1. Light output calibration

The light output distributions of the EJ-276 and EJ-301 detectors were derived by integrating the waveform of each event over a specific time gate. This light output was calibrated in electron equivalent energy (eVee) using standard ^{137}Cs and ^{60}Co gamma-ray sources.

The calibration was performed using the same method as Dietze et al. [4]. They studied the relationship between light output resolution and the position of Compton edge through simulation. In this study, PHITS simulation was used to reproduce the results of gamma-ray measurements. The position of Compton edge was determined by simulating the energy deposition to the detector by the gamma ray and folding the light output resolution of the detector. Figure 2 shows the measurement results of the ^{137}Cs source of EJ-276 and the position of the Compton edge. The calibration lines for both EJ-301 and EJ-276 are shown in Figure 3.

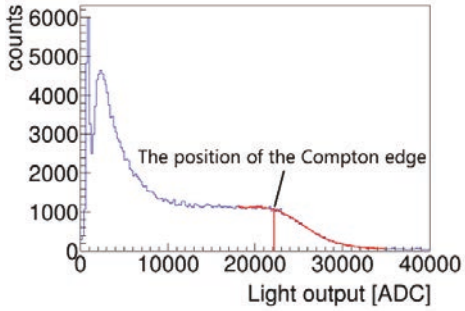

Figure 2 EJ-276 measurement result of ^{137}Cs and the position of the Compton edge.

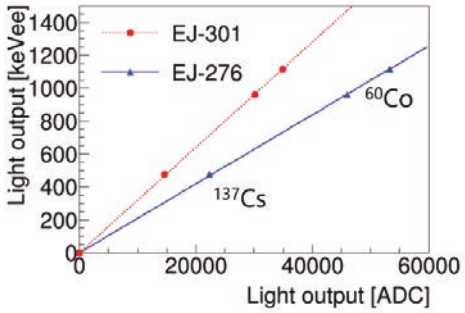

Figure 3 Calibration lines for EJ-276 and EJ-301.

3.2. Evaluation of n-γ discrimination performance

The n-γ discrimination was performed using that Pulse Shape Discrimination (PSD) method [5]. In this method, the ratio of the waveform component with a long decay time is larger in neutron emissions than in gamma-ray emissions. To apply the PSD method, the waveform data were integrated over two gates with different widths to obtain the total light output Q_{total} and the slow component of the light output Q_{slow}, respectively. Figure 4 illustrates the schematic diagram of the waveforms of a neutron and a gamma ray and the integral ranges of Q_{total} and Q_{slow}. The particle discrimination parameter PSD is defined as

$$\mathrm{PSD} = \frac{Q_{\mathrm{total}} - Q_{\mathrm{slow}}}{Q_{\mathrm{total}}}. \tag{1}$$

The PSD for neutrons is smaller than that for gamma rays. Figure 5 displays the results of the n-γ discrimination, where neutron and gamma-ray events are clearly distinguished. To quantify the n-γ discrimination performance, the figure of merit (FoM) is defined by

$$\mathrm{FoM} = \frac{|\mu_{\mathrm{n}} - \mu_{\gamma}|}{\mathrm{FWHM_n} + \mathrm{FWHM_\gamma}}, \tag{2}$$

where μ_{n} and μ_{γ} are the average values obtained from Gaussian fitting of the PSD distributions for neutrons and gamma rays, and $\mathrm{FWHM_n}$ and $\mathrm{FWHM_\gamma}$ are the full widths at half maximum of the neutron and gamma-rays peaks in the PSD distributions. The PSD distribution for specific light output ranges was derived. The PSD distribution at 500 keVee is shown in Figure 6. The FoMs of EJ-276 and EJ-301 are plotted against the light output in Figure 7. Each FoM was obtained for a ±10% window of the indicated light output. While the discrimination performance of EJ-301 was found to be superior to that of EJ-276 in whole light output ranges, it was demonstrated that EJ-276 has sufficient discrimination performance in measuring neutron energy spectra, as will be explained in section 3.4.

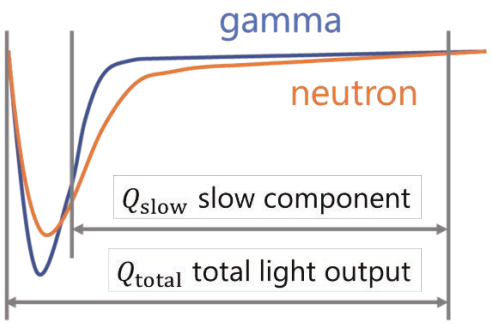

Figure 4 the schematic diagram of the waveforms and the integral ranges of Q_{total} and Q_{slow}.

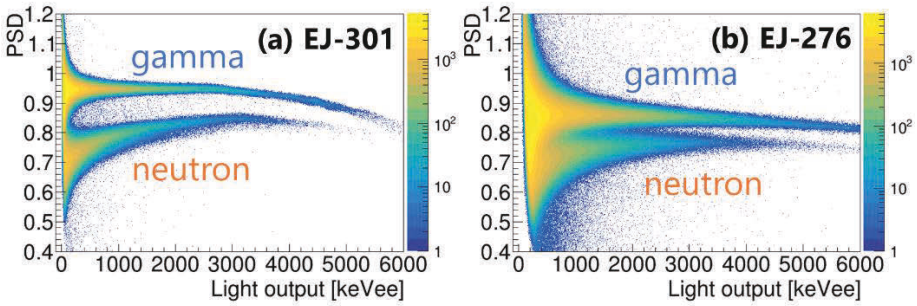

Figure 5 Two-dimensional plot of n-γ discrimination results using the PSD method (a) EJ-301, (b) EJ-276.

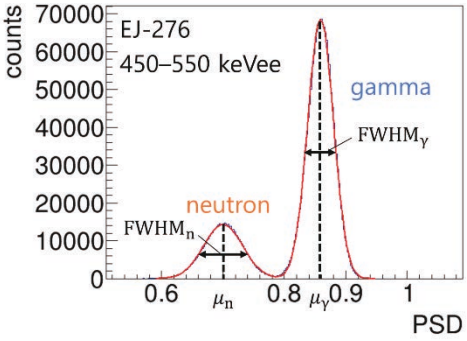

Figure 6 PSD distribution of EJ-276 around 500 keVee light output.

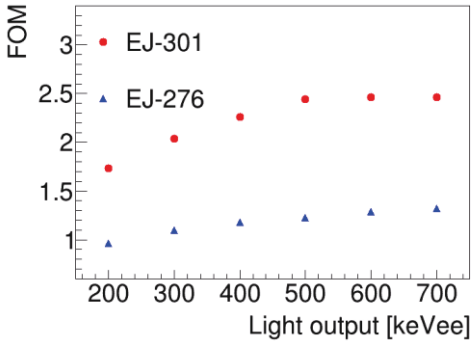

Figure 7 FoM values for different light output regions.

3.3. Response function

The response function, which is the light output distribution over a certain energy range of neutrons, was derived. The light output of EJ-301 was found to be larger than that of EJ-276, which is consistent with previous studies [1,2,6].

In addition to the measurements, the response functions were also simulated using SCINFUL [7] mode of PHITS. The following light output function (LOF) for recoil protons is used in SCINFUL:

$$L = a_1 E - a_2\{1.0 - \exp(-a_3 E)\}, \quad (3)$$

where L is the light output, E is the energy deposited by the recoil proton, and a_1, a_2, and a_3 are parameters. The LOFs for EJ-276 were obtained in the previous work by Laplace [1] and Ngo [2]. Figure 8 shows the LOFs for EJ-276 obtained by Ngo and Laplace, as well as the default LOF for EJ-301 [6] used in SCINFUL. Figure 9 presents the simulated response functions of neutrons in the 2.9–3.1 MeV range using Ngo's LOF, Laplace's LOF, and the mean of the two LOFs, in comparison with the experimental response function. The simulations with the Ngo and Laplace LOFs fail to reproduce the experimental response function, but the simulation employing the mean of the two LOFs reproduces the experimental one well. Figure 10 shows comparisons of other experimental response functions and simulations at three different energy ranges. The response functions for EJ-276 were simulated with the mean of the two of the LOFs. The simulation and experimental results for both EJ-276 and EJ-301 were in good agreement as shown in Figure 10.

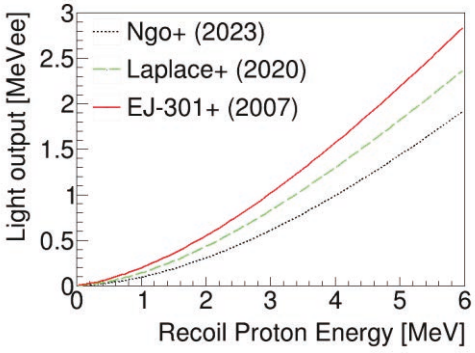

Figure 8 LOF for EJ-276 obtained in the studies of Laplace [1] and Ngo [2] and the LOF for EJ-301 [6].

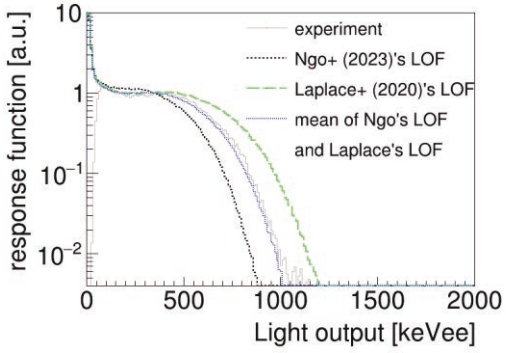

Figure 9 Experimental and simulated response functions of EJ-276 for neutrons in the 2.9–3.1 MeV energy range.

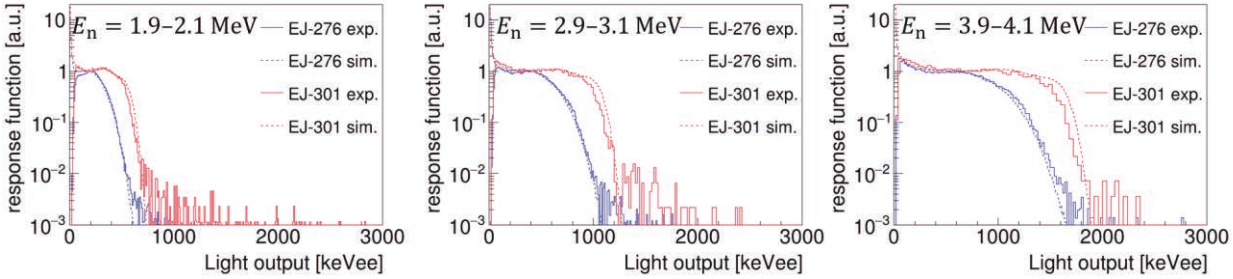

Figure 10 Experimental and simulated response functions.

3.4. Neutron Energy spectrum of ^{252}Cf derived by time of flight method

The TOF method [8] was used to derive the neutron spectrum. The neutron energy E_n was calculated by

$$E_n = \frac{m_n c^2}{\sqrt{1-\left(\frac{L}{L+ct_{n-\gamma}}\right)^2}} - m_n c^2, \quad (4)$$

where m_n is the neutron rest mass, L is the distance between the ^{252}Cf neutron source and the stop detector, c is the speed of light, and $t_{n-\gamma}$ is the time difference between the detection of gamma ray by the start detector and the neutron by the stop detector. Figure 11 shows the TOF spectrum plotted against $t_{n-\gamma}$. The $t_{n-\gamma}$ spectrum was offset so that $t_{n-\gamma} = 0$ corresponds to the peak at which both detectors detected gamma rays. The derived neutron energy spectrum after subtraction of gamma events is presented in Figure 12. The detection efficiency was calculated by SCINFUL. In the low energy range, the analysis was performed for neutrons with light output greater than 0.1 MeVee, and in the high energy range, the analysis was performed for neutrons with light output greater than 1.0 MeVee.

The measured energy spectrum using EJ-276 was found to be consistent with that using EJ-301, demonstrating the effectiveness of EJ-276 for the measurement of neutron energy spectrum. The derived energy spectra were also compared with the JIS-recommended neutron energy spectrum for ^{252}Cf neutron sources [9]. The JIS-recommended energy spectrum was normalized with the spectrum at 5 MeV. The experimental results were in fairly good agreement with the JIS-recommended energy spectrum in the range from 1 MeV to 12 MeV.

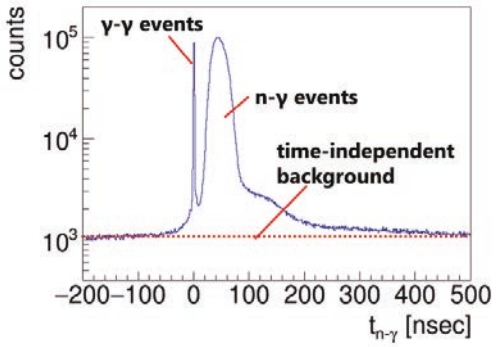

Figure 11 Measured TOF distribution for EJ-276.

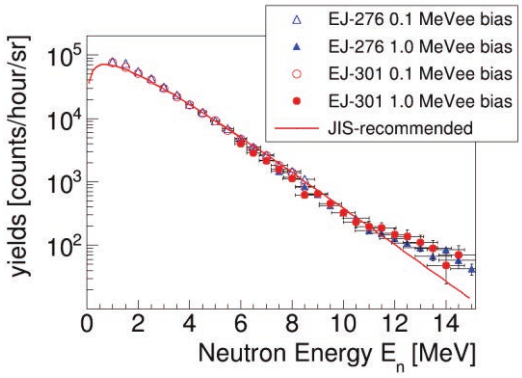

Figure 12 Energy spectra of ^{252}Cf.

4. Conclusion

The performance of EJ-276, which is one of the latest pulse-shape discriminating plastic scintillators, was compared with that of EJ-301, which is a conventionally used organic liquid scintillator. Neutron time-of-flight was measured to obtain the energy spectrum of neutrons emitted from ^{252}Cf. The n-γ discrimination performance of the EJ-276 detector was found to be satisfactory for neutron measurements but inferior to that of the EJ-301 detector. The measured response functions were well reproduced by SCINFUL simulation using the mean of Ngo's and Laplace's LOF. The TOF method was used to derive the neutron energy spectrum. The neutron energy spectra measured by both the EJ-276 and EJ-301 detectors were almost identical to the JIS-recommended energy spectrum in the range from 1 MeV to 12 MeV.

References

[1] T. A. Laplace, B. L. Goldblum, J. E. Bevins, et al., Comparative scintillation performance of EJ-309, EJ-276, and a novel organic glass, J. Instrum., vol. 15, Nov, 2020, P11020.

[2] K. D. Ngo, C. Cazzaniga, M. Paoletti, et al., Fast neutron response characterization of an EJ-276 plastic scintillator for use as a neutron monitor, Nucl. Instrum. Meth. Phys. Res., Sect. A, vol. 1051, Jun, 2023, 168216.

[3] T.Sato, Y. Iwamoto, S. Hashimoto, et al., Niita, Recent improvements of the Particle and Heavy Ion Transport code System – PHITS version 3.33, J. Nucl. Sci. Technol. DOI:10.1080/00223131.2023.2275736

[4] G. Dietze and H. Klein, Gamma-calibraiton of NE 213 scintillation counters, Nucl. Instrum. Meth. Phys. Res., vol. 193, Issue 3, 1982, pp. 549–556.

[5] M. Moszynski, G.J Costa, G. Guillaume, et al., Identification of different reaction channels of high energy neutrons in liquid scintillators by the pulse shape discrimination method, Nucl. Instrum. Meth. Phys. Res., Sect, vol. 343, Apr, 1994, pp. 563–572.

[6] D. Satoh, T. Sato, A. Endo, N. Matsufuji, et al., Extension of applicable neutron energy of DARWIN up to 1 GeV, Radiat. Prot. Dosim., vol. 126, no.1–4, May, 2007, pp. 555–558.

[7] D. Satoh and T. Sato, Improvements in the particle and heavy-ion transport code system (PHITS) for simulating neutron-response functions and detection efficiencies of a liquid organic scintillator, J. Nucl. Sci. Technol., vol. 59, no. 8, 2022, pp. 1047–1060.

[8] F. W. K. Firk, Neutron time-of-flight spectrometers, Nucl. Instrum. Methods, vol. 162, no. 1–3, Jun, 1979, pp. 539–563.

[9] Japanese Industrial Standards, JIS Z 4521, 2006.

35. Development of a PHITS simulation technique and a numerical method to optimize measures against radioactive sources

Naoya FURUTACHI[†1], Toru YOSHIDA[1], Hideaki YANAGI[1], Yukihiro HASEGAWA[1], and Masahiko MACHIDA[2]

[1]Research Organization for Information Science and Technology, 2-4, Shirakata, Tokai-mura, Ibaraki 319-1106, Japan
[2]Center for Computational Science and e-Systems, Japan Atomic Energy Agency, 178-4-4 Wakashiba, Kashiwa, Chiba 277-0871, Japan
[†]Email: furutachi@rist.or.jp

Abstract

We have developed a PHITS simulation technique that accounts for variations of a geometrical model efficiently. The equations to estimate the dose distribution after the incorporation of the measures against radioactive sources are presented. We have also developed a numerical method to optimize the decontamination rate of radioactive sources. By solving the constrained optimization problem, the decontamination rate that achieve a certain dose condition with the minimum cost is obtained.

1 Introduction

The leakage of radioactive materials from the reactor has resulted in numerous hot spots in the Fukushima Daiichi Nuclear Power Station (1F) building. To estimate the distribution of the leaked radioactive sources and plan measures against them, we have developed the radiation dose evaluation system for indoor environments: 3D-ADRES-Indoor [1, 2]. 3D-ADRES-Indoor uses Particle and Heavy Ion Transport code System (PHITS) [3] for the radiation dose calculation. In this article, a PHITS simulation technique and a numerical method to optimize measures against radioactive sources implemented in 3D-ADRES-Indoor are presented.

2 Technical details

2.1 A PHITS simulation technique for planning of measures against radioactive sources

For a better planning of measures against radioactive sources, it is necessary to repeat simulations with different geometrical models that incorporate various measures. However, it generally takes long computational times to execute whole new PHITS simulations with different geometrical models. Therefore, we have developed a PHITS simulation technique to construct the dose rates with specific models using those obtained from the smaller scale simulations that only account for the difference of models. The point of the technique is the decomposition of

dose rates using the “counter” feature and the simulation using the “dump source” feature. While this technique requires the decomposed dose rates and the dump data obtained by a normal simulation with a prior model, the computational times of the simulations with the models that incorporate various measures to the prior model are significantly reduced compared to the normal simulations. We consider four kinds of measures against radioactive sources: the decontamination, removal, relocation of contaminated structures, and shielding.

The purpose of the present technique is to obtain the dose distribution D', which varied from D after the incorporation of the measures against radioactive sources. First of all, a normal PHITS simulations is executed to obtain D and the decomposed dose distributions, and the dump data. The dump data is made for the particles entered to the structures or regions where the measures may be applied. Then D' is calculated using the equations presented below.

The dose distribution after the decontamination is easily calculated without additional simulations by

$$D' = D - \sum_{i \in A} u_i D_i^{\mathrm{src}}, \tag{1}$$

here D_i^{src} is the dose distribution caused by the i-th contaminated structure, and u_i is the decontamination rate. A is a set of structures or regions where the measure is applied. It is known that this kind of operations are often executed using the PHITS sumtally or anatally feature. The calculations of the dose distributions after the incorporation of the other measures require the additional simulations using the dump sources. First we consider the most simple case: the removal of one contaminated structure, for which D' is calculated by

$$D' = D - D_i^{\mathrm{src}} - D_i^{\mathrm{sct}} + D_i^{\mathrm{dmp}}, \tag{2}$$

here D_i^{sct} is the dose distribution caused by the particles scattered with the i-th structure, and D_i^{dmp} is the dose distribution obtained by the dump source simulation using the geometrical model in which the i-th contaminated structure is removed. If we try to calculate the dose rate after the removal of two contaminated structure exactly, it is necessary to consider the particles scattered among two structures,

$$\begin{aligned} D' = D \quad &- \quad (D_i^{\mathrm{src}} + D_j^{\mathrm{src}}) \\ &- \quad (D_i^{\mathrm{sct}} + D_j^{\mathrm{sct}} - D_{ij}^{\mathrm{sct}}) \\ &+ \quad (D_i^{\mathrm{dmp}} + D_j^{\mathrm{dmp}} - D_{ij}^{\mathrm{dmp}}), \end{aligned} \tag{3}$$

here D_{ij}^{sct} is the dose distribution caused by the particles scattered with both structures. While it is not impossible to distinguish such events by the counter feature, the calculational procedure becomes more complex. Therefore, we approximate the equation as

$$D' \simeq D - \sum_{i \in A} (D_i^{\mathrm{src}} + D_i^{\mathrm{sct}}) + \sum_{i \in A} D_i^{\mathrm{dmp}}, \tag{4}$$

where the scattering term D_{ij}^{sct} and the corresponding D_{ij}^{dmp} are neglected. Simirally, the equation for the shielding is given as

$$D' \simeq D - \sum_{i \in A} (D_i^{\mathrm{src}} + D_i^{\mathrm{pas}}) + \sum_{i \in A} (D_i^{\mathrm{dmp}}). \tag{5}$$

In this equation, D_i^{sct} of the removal is replaced by D_i^{pas}, which is the dose distribution caused by the particles passed through the target region where the shielding appears. Finally, the equation for the relocation is given as

$$D' \simeq D - \sum_{i \in A} (D_i^{\mathrm{src}} + D_i^{\mathrm{sct}} + D_i^{\mathrm{pas}}) + \sum_{i \in A} (D_i^{\mathrm{src}'} + D_i^{\mathrm{dmp}}). \tag{6}$$

Different from the removal and the shielding, the radiation from the relocated contaminated structure must be taken into account by $D_i^{\mathrm{src}'}$.

2.2 A numerical method to optimize decontamination rate

As for the decontamination, a numerical method to optimize the decontamination rates of the radioactive sources that achieve a certain dose condition with the minimum cost has been developed. Similarly with the technique presented in the previous subsection, a normal PHITS simulation is executed to obtain the decomposed dose rate D_i^{src} at first. Then a constrained optimization problem with the evaluation function composed of the cost function and the penalty function to suppress the dose rate under the target value D_{tag} is solved. The evaluation function is given as

$$L = f_{\mathrm{cost}}(\boldsymbol{u}) + \frac{C_{\mathrm{c}}}{M}\sum_{r=1}^{M}\left[max\left(\log\frac{D'_r}{D_{\mathrm{tag}}}, 0\right)\right]^2, \tag{7}$$

here D'_r is the dose after decontamination that is calculated by Eq. 1, the suffix r is the index of the spatial mesh, and M is the number of the mesh elements included in the target region where the dose rate is to be suppressed under D_{tag}. C_{c} represents the magnitude of the penalty and set at properly large value. While it is desirable that $f_{\mathrm{cost}}(\boldsymbol{u})$ represents a realistic financial cost of the decontamination, it is not obvious how to design such a function. Therefore, we suppose following simple expression for the cost function in the demonstration presented in the next section,

$$f_{\mathrm{cost}}(\boldsymbol{u}) = \frac{1}{N}\sum_{i=1}^{N}\frac{1}{(1-u_i)}, \tag{8}$$

where N is the number of radioactive sources.

To solve this numerical optimization problem, we have employed Particle Swarm Optimization (PSO) method [4] instead of a usual gradient decent method to make any kinds of cost function available. In PSO method, the parameters of the group g at k-th step are updated by

$$\boldsymbol{u}_g^{(k+1)} = \boldsymbol{u}_g^{(k)} + \boldsymbol{V}_g^{(k+1)} \tag{9}$$

$$\begin{aligned}\boldsymbol{V}_g^{(k+1)} &= w\boldsymbol{V}_g^{(k)} + C_p C_{\mathrm{rand}}(\boldsymbol{u}_g^{pbest} - \boldsymbol{u}_g^{(k)}) \\ &+ C_q C_{\mathrm{rand}}(\boldsymbol{u}^{gbest} - \boldsymbol{u}_g^{(k)}),\end{aligned} \tag{10}$$

here $\boldsymbol{u}_g^{pbest}$ is the best parameters in the group g that give the minimum value for the evaluation function and $\boldsymbol{u}^{gbest}$ is the best parameters among all the groups. w, C_p, and C_q are the hyper parameters of PSO, and C_{rand} is uniform random numbers.

3 Results

Figure 1 illustrates the operation of the present technique. In this example, we aim to obtain the dose distribution after the removal of the contaminated structure placed at left bottom of the room, which is indicated by the red dotted circle in the left panel. First we execute a normal PHITS simulation with the prior model to obtain the dose distributions D, D_i^{src}, D_i^{sct}, and the dump data. Then we execute the dump source simulation to obtain D_i^{dmp} using the geometrical model in which the contaminated structure is removed. The obtained dose distributions are operated according to Eq. 2, as shown in the right part of the figure. Practically, the operation

among the dose distributions is executed using the PHITS anatally feature. The left top panel of Fig. 1 shows the obtained D'. We can see a natural dose distribution around the region where the removed structure existed. As explained in 2.1, there is no approximation in Eq. 2 if only one structure is removed. We confirmed that D' obtained in the present technique perfectly agree with that obtained by the normal PHITS simulation.

Table 1 displays the number of histories in the present PHITS simulations. The computational time of Monte Carlo simulations almost proportional to the number of histories in general. It is clear that the histories of the dump source simulations required for the present technique are far smaller than that of the normal simulation. We note that the number of histories for the dump source simulation is equal to the number of the particles entered to the contaminated structure during the first simulation. Therefore, the number of histories for the dump source simulation increases as the removed structure increases. In the case of the shielding or relocation, the dump data is made for the particle that entered to the target region where the shielding or the relocated structure appears. In this case, the number of histories increases as the target region extends.

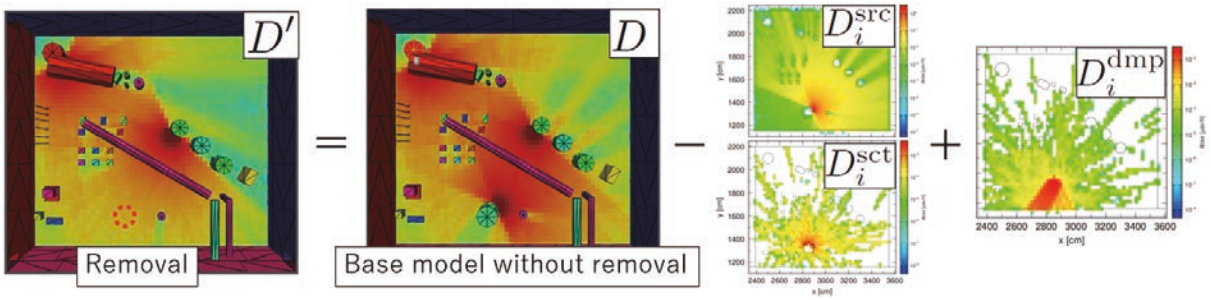

Figure 1: Operation of the present technique for the removal of the contaminated structure.

Table 1: Numbers of PHITS simulation histories.

	number of histories
normal simulation	1000000
removal × 1	6025
removal × 2	12699
removal × 3	14179

Figure 2 shows an example of more complicated operations using 3D-ADRES-Indoor. While the present technique requires complicated PHITS input descriptions, the PHITS input file for the present technique is automatically generated by the GUI operation of 3D-ADRES-Indoor. In this example, the removal, relocation, and shielding are considered at the same time. In the left top panel, the contaminated structures with 100 [Bq/cm^2] radiation are indicated by the red arrows. As measures against these radioactive sources, one of the contaminated structure is removed, and the other is relocated at right top region of the room, and the shielding is set to prevent the radiation from the relocated structure. The target region where the measures appear is set at right top of the room indicated by the white box prior to the normal simulation. The right bottom panel shows D' obtained after the dump source simulation with the geometrical model shown in the left bottom panel. While D' is drastically changed from D, the distribution seems natural. This result demonstrates that the present technique successfully work even if multiple measures are combined.

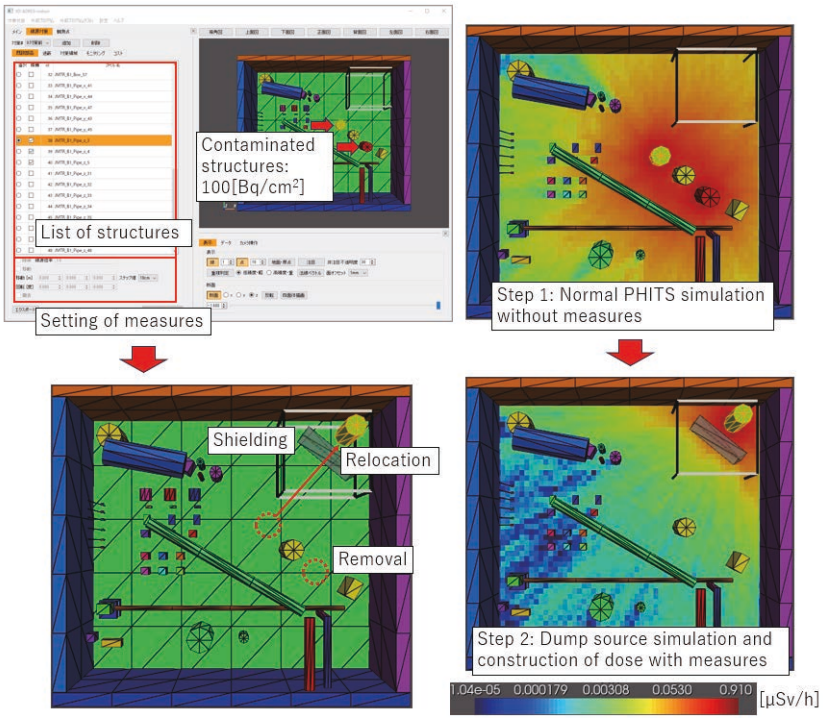

Figure 2: GUI operations in 3D-ADRES-Indoor to obtain the dose distribution after incorporating the measures. Settings of the measures are shown in the left panels. Dose distributions before and after the incorporation of the measures are shown in the right top panel and the right bottom panel, respectively.

Figure 3 shows an example of the application of the present numerical method to optimize the decontamination rate. In this example, the contamination is widely spread as shown in the left top panel. The number of sources N in Eq. 1 is ten, and each source has 100 [Bq/cm^2] radiation. At first, a normal PHITS simulation is executed to obtain D_i^{src} and D shown in the right top panel. Then the constrained optimization problem is solved to obtain the decontamination rates that suppress the dose under $D_{\mathrm{tag}} = 0.1$ [μ Sv/h] for all spatial meshes included in the target region that is indicated by the white dotted line in the right panels. The obtained decontamination rates for ten sources are shown in the left bottom panel. Since D_{tag} is approximately one-tenth of D in the target region, it is reasonable that the decontamination rates converge around ~ 0.9. We confirmed that the dose in the target region is suppressed under D_{tag} by applying the obtained decontamination rate as shown in the right bottom panel.

4 Summary

A PHITS simulation technique to obtain the dose distribution after the incorporation of the measures against radioactive sources was presented. The technique was demonstrated using 3D-ADRES-Indoor. We found that the technique is very efficient if the change in the geometrical model is small. A numerical method to optimize the decontamination rate was also presented. The decontamination rates that achieve a certain dose condition can be obtained without additional simulations by the present method.

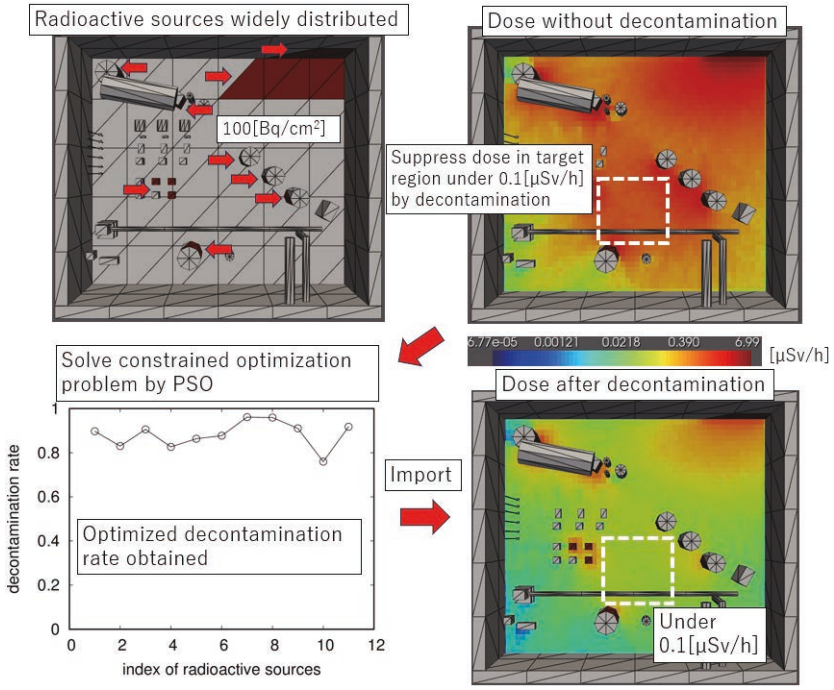

Figure 3: Application of the present numerical method to optimize the decontamination rate. In the left top panel, the radioactive sources are shown by the red arrows. In the right top panel, the dose distribution before the decontamination is shown. Dose distribution after the application of the decontamination rates shown in the left bottom panel is plotted in the right bottom panel.

Acknowledgments

This work was partially carried out in a subsidy program of "Project of Decommissioning and Contaminated Water Management", entitled "Development of Technologies for Work Environmental Improvement in Reactor Building (Development of Exposure Reduction Technologies by Improved Functional Digitalization of Environment and Radioactive Source Distribution)". One of authors (M.M.) is indebted to Prof. K. Okamoto, the leader of this project, and all other members, and would like to express our gratitude to the staffs in JMTR for their supports.

References

[1] Machida, M. et al., R&D of Digital Technology on Inverse Estimation of Radioactive Source Distributions and Related Source Countermeasures - R&D Status of Digital Platform including 3D-ADRES-Indoor -, RIST news No. 69, 2023, pp.2-18.

[2] Machida, M. et al., R&D of Digital Technology on Inverse Estimation of Radioactive Source Distributions and Related Source Countermeasures - R&D Status of Digital Platform including 3D-ADRES-Indoor -, RIST news No. 68, 2022, pp.3-19.

[3] Sato, T. et al., Recent improvements of the Particle and Heavy Ion Transport code System – PHITS version 3.33, J. Nucl. Sci. Technol. 61, 2024, pp.127-135, DOI: 10.1080/00223131.2023.2275736.

[4] Kennedy, J. and Eberhart, R., Particle swarm optimization, IEEE International Conf. on Neural Networks, 1995, pp. 1942-1948.

36. Design of new brachytherapy source using PHITS code

Ayano MAKINAGA[1*], Kideaki OTSU[1] and Yoshiharu HIRABAYASHI[2]
[1]RIKEN Nishina Center, 2-1 Hirosawa, Wako, Saitama-ken, 351-0198, Japan
Hokkaido University Information Initiative Center, Kita-11, Nishi-5, Kita-ku, Sapporo, Hokkaido, 060-0811, Japan
[*]Email: ayano.makinaga@a.riken.jp

The purpose of this research is to design new radionuclides suitable for brachytherapy sources. Currently, a limited number of nuclides such as ^{60}Co, ^{90}Sr, ^{106}Ru, ^{125}I, ^{137}Cs, ^{192}Ir, ^{198}Au are used in clinical practice. In this study, we simulate the dose properties of some radionuclides for brachytherapy based on the AAPM TG-43 method using PHITS code to suggest other possible treatment methods and tools for brachytherapy.

1. Introduction

Brachytherapy is a radiation therapy technique in which radionuclides sealed in capsules are inserted in to the body. After the discovery of ^{226}Ra by the Curies, brachytherapy began in 1903 for the treatment of skin cancer. In Japan, brachytherapy using ^{226}Ra radiation sources began in 1934 at Cancer Research Hospital. In 1965, the remote after – loading system (RALS) was developed at Hokkaido University [1] to solve the problem of radiation exposure for surgeons, and now it is popular technique all over the world as a method of radiotherapy. Brachytherapy uses photons, electrons and alpha rays from a radiation source, and can be applied to various diseases by controlling the placement method, irradiation time, and dose rate. While it is invasive method because the radiation source is placed directly near the tumor, the biological effects of high dose rate irradiation are often superior to external beam irradiation [2,3]. Currently, only limited nuclides such as ^{60}Co, ^{90}Sr, ^{106}Ru, ^{125}I, ^{137}Cs, ^{192}Ir and ^{198}Au are used in clinical settings. Typical treatment areas include the oral cavity, skin, uterus, prostate, and esophagus and so on. The requirements for a radiation source for brachytherapy are appropriate radiation energy (dose concentration on the target, reduction of exposure to non-targets), ease of handling (shielding, half-life, control aspects, etc.), and decay properties. The produced nuclide should not be gaseous [2-4].

Nuclides for brachytherapy are usually produced by a neutron capture reaction using reactor neutrons, but there are limits to the production and distribution of sources because of the number of nuclear reactors and their location. In addition, when using a radiation source in clinical practice, it is necessary to measure the source intensity and replace the source because of its half-life. In order to solve these problems, it is necessary to reconsider not only the therapeutic effect but also the handling and production method of the source. Recently, new designs of the size and shape of brachytherapy capsules, which has ultra-compact collimators in it or magnetic field to bend the secondary particles, has been developed actively all over the world. [5-13].

In recent years, highly accurate nuclear databases such as JENDL series [14] become a bridge between fundamental radiation science and the applied to the industrial field. In particular, the RI Beam Factory (RIBF) at the RIKEN Nishina Accelerator Center has actively measured nuclear data using unstable nuclides for that purpose of transmutation technology or medical isotope production [15,16]. In this study, we focus on the investigation of further possible candidate of brachytherapy sources using RIBF nuclear data.

2. Procedure of computational simulation using PHITS code

2.1. Radiation source properties for brachytherapy

The classical method of calculate the absorbed dose in brachytherapy was based on the fact that the source intensity is the inverse square of the distance. Classical method is well known that the correction accuracy of the scattering and attenuation effect are not enough for the high precision dose calculation of clinical use. Nowadays, Monte Carlo and model-based calculation parameters such as the geometric function $G_{\mathrm{L}}(r,\theta)$ and the radial dose function $g_L(r)$, which are related to the scattering and attenuation effects, are included to the treatment system [2]. In this study, a formula referred in AAPM TG-43U1 [10,11] is used to estimate the dose as follows.

$$D(r,\theta) = S_k \cdot \Lambda \cdot \frac{G_{\mathrm{L}}(r,\theta)}{G_{\mathrm{L}}(r_0,\theta_0)} \cdot g(r) \cdot F(r,\theta) \tag{1}$$

Here, S_k $(\mu Gy m^2 h^{-1})$ is the air kerma strength, Λ $(cGy h^{-1} U^{-1})$ is the dose rate constant, $G_{\mathrm{L}}(r,\theta)$ is the geometric function, $g_L(r)$ is the radial dose function for linear sources, and $F(r,\theta)$ is the anisotropic function. We note that $S_k \cdot \Lambda$ means the absorbed dose rate for $P(r,\theta)$ which is shown in figs.1 (left). $G_L(r,\theta)/G_L(r_0,\theta_0)$ means geometric distance parameter, $g(r)$ corrects for absorption and scattering effect in the medium and $F(r,\theta)$ corrects for anisotropy in dose distribution around the source. P(r_0,θ_0) is used as the reference point for the dose calculation. Each formula is shown as follows, respectively.

$$G_{\mathrm{L}}(r,\theta) = \begin{cases} \dfrac{\beta}{L \cdot r \sin\theta} & if \quad \theta \neq 0 \\ (r^2 - L^2/4)^{-1} & if \quad \theta = 0 \end{cases} \tag{2}$$

$$g(r) = \frac{D(r,\theta_0) \cdot G_X(r_0,\theta_0)}{D(r_0,\theta_0) \cdot G_X(r,\theta_0)} \tag{3}$$

$$F(r,\theta) = \frac{D(r,\theta) \cdot G_{\mathrm{L}}(r,\theta_0)}{D(r,\theta_0) \cdot G_{\mathrm{L}}(r,\theta)} \tag{4}$$

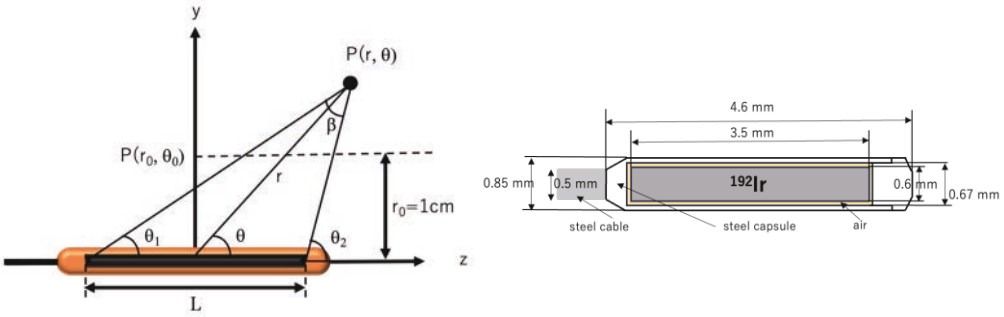

Fig. 1 The left figure shows the coordinate system for the brachytherapy dose calculation in polar coordinate. For P(r,θ), r = 1 and $\theta = 90^{\circ}$ are used as the reference point. The right figure shows a cross-sectional view of the flexisource [10,11] used as the PHITS geometry.

2.2. Geometry of PHITS

The geometric coordinates of the source characteristics used in the PHITS code and the cross-sectional view of the flexisource are shown in Fig.1 (right). As a test study, the source characteristics were calculated using a flexisource capsule container that has been used in recent years. ^{192}Ir, ^{60}Co, ^{198}Au, ^{137}Cs, ^{96}Tc, ^{106}Ru radiation sources placed inside the capsule container, respectively. The dose calculation was performed by changing the distance from the source in 2 cm increments and the angle in 10 degrees increments. Fig.2 (a) and (b) show the result of comparing the PHITS calculation and evaluated AAPM result for $g(r)$ and $F(r,\theta)$. Although fundamental trends were reproduced in each quantity, differences between PHITS calculation and evaluated result appear because of the precision of the geometric settings. Fig.3 (a) and (b) are obtained by changing the radiation source inside the capsule. It can be seen that $F(r,\theta)$ has different characteristics for each radiation source on the left and right sides around $\theta = 90°$. This is because when the angle changes, the amount of attenuation changes depending on the energy of gamma rays and the distance across the material.

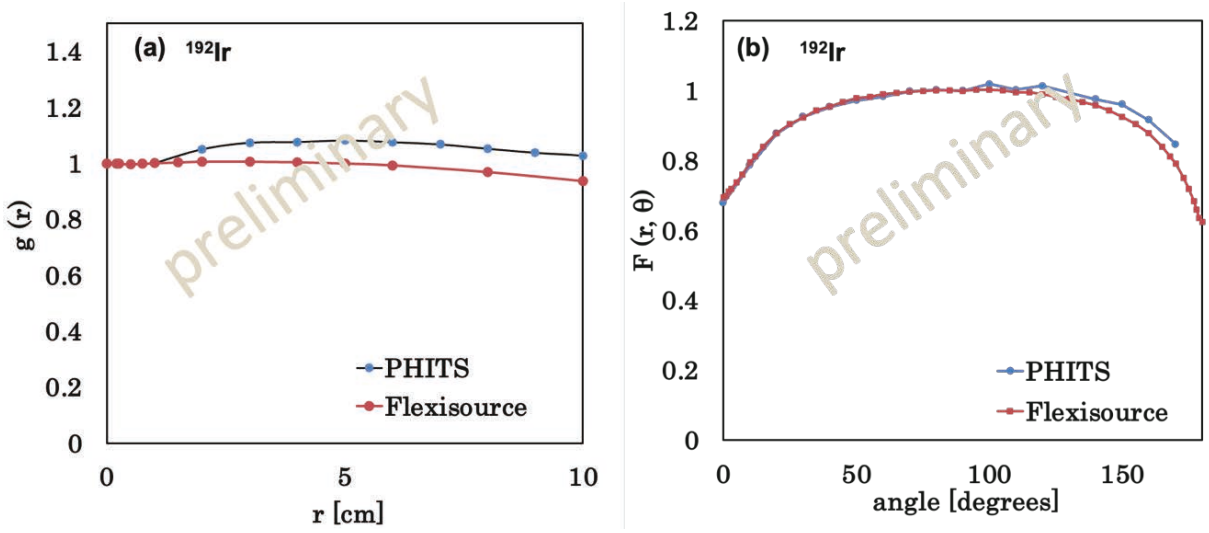

Fig. 2 The left panel (a) shows the geometric function g(r) of ^{192}Ir and right panel (b) shows the anisotropic function $F(r,\theta)$ of ^{192}Ir. In each graph, blue dotted data shows the result of PHITS and red dotted data shows the data of flexisource referred in TG-43U1 [10,11].

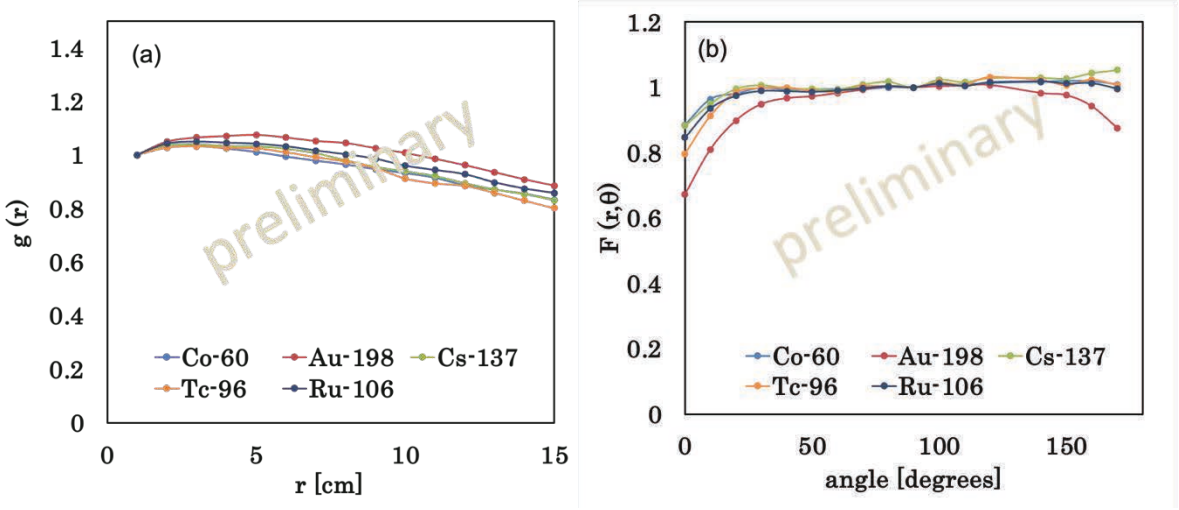

Fig. 3 The left panel (a) shows the geometric function g(r) and right panel (b) shows the anisotropic function $F(r,\theta)$. As test studies, ^{192}Ir, ^{60}Co, ^{198}Au, ^{137}Cs, ^{96}Tc, ^{106}Ru radiation sources are used in the simulation.

3. Summary

To design new radionuclides suitable for brachytherapy sources, we simulate the dose properties of some radionuclides for brachytherapy based on the AAPM TG-43 method using PHITS code. We simulate the dose properties of $g(r)$ and $F(r,\theta)$ for ^{192}Ir, ^{60}Co, ^{198}Au, ^{137}Cs, ^{96}Tc, ^{106}Ru radiation sources and compared with the AAPM result. Although the details of the $g(r)$ and $F(r,\theta)$ differ due to geometric precision, it was confirmed that they generally showed good agreement. In the future, further various nuclides and capsule shapes will be attempt to calculate for the brachytherapy simulation.

References

1) Wakabayashi, M. et al., High Dose rate Intracavitary radiotherapy using the RALSTRON, Japanese Journal of Radiology, vol.31, no.4, 1965, pp.340.
2) Dosimetry of Absorbed Dose to Water in Brachytherapy (Dosimetry in Brachytherapy 18), Japan Society of Medical Physics, 2018, Tsushosangyokenkyusha.[in Japanese]
3) Brachytherapy Medical treatment・Physics QA manual, JASTRO Japanese Society for Radiation Oncology Japanese Group of Brachytherapy, 2022,Kanehara & Co., LTD.[in Japanese].
4) Nishio, M., Brachytherapy General Remarks on Brachytherapy, Nippon Acta Radiologica, vol.65, 2005, pp.207-215. [in Japanese].
5) IAEA, The Transition from 2-D brachytherapy to high dose rate brachytherapy, IAEA HUMAN HEALTH REPORTS No.12, 2015.
6) IAEA, Implementation of high dose rate brachytherapy in limited resource settings, IAEA HUMAN HEALTH REPORTS No.30, 2015.

7) Rivard, M.J., et al., Supplement to 2004 update of the AAPM Task Group No. 43 Report, Medical Physics, vol.34, no.6, 2007, pp.2187-2205.
8) Rivard, M.J., et al., Spplement2 for the 2004 update of the AAPM Task Group No. 43 Report: Joint recommendations by the AAPM and GEC-ESTRO, Medical Physics, vol.44, no.9, 2017, pp.e297-e338.
9) Prisciandgro, J., et al., AAPM task group report 303 endorsed by the ABS: MRI implementation in HDR brachytherapy – Consideration from simulation to treatment, Medical Physics, vol.49, 2022, pp.e983-e1023.
10) Nath, R., et al., Dosimetry of interstitial brachytherapy sources: Recommendation of the AAPM Radiation Therapy Committee Task Group No. 43, Medical Physics, vol.22, no.2, 1995.
11) Rivard, M. J., et al., Updated of AAPM Task Group No. 43 Report: A revied AAPM protocol for brachytherapy dose calculations, Medical Physics, vol.31, no.3, 2004.
12) Nath., R., et al., Guidelines by the AAPM and GEC-ESTRO on the use of innovative brachytherapy devices and applications: Report of Task Group 167, Medical Physics vol.43, no.6, 2016.
13) Adams, Q. E. et al., Interstitial rotating shield brachytherapy for prostate cancer, Medical Physics vol.41, no.5, 2014.
14) Iwamoto, O., et al., Japanese evaluated nuclear data library version 5: JENDL-5, Journal of Nuclear Science and Technology, vol.60, no.1, 2023, pp.1-60.
15) Wang, H., et al., Spallation reaction study for the long-lived fission product Pd-107, Progress Theoretical and Experimental Physics, 2017, 021D01.
16) Wang, H., et al., Spallation reaction study for fission products in nuclear waste: Cross section measurements for Cs-137 and Sr-90 on proton and deuteron, Physics Letteres B, vol.54, 2016, pp.104-108.
17) Sato, T., et al., Particle and Heavy Ion Transport Code System PHITS, Version 2.52, Journal of Nuclei and Science Technology, vol.50, no.9, 2013, pp.913-923.

Acknowledgements

This research is partly supported by the collaborative research program 2023 information initiative center, Hokkaido University, Sapporo, Japan.

37. Estimation of deposition positions of α-emitters in the body by L X-ray analysis

Koki HOKAZONO[1], Nobuhiro SHIGYO[1], Keisuke MAEHATA[2]
[1]Kyushu University, [2]Teikyo University
Email : hokazono.koki.993@s.kyushu-u.ac.jp

In the case of accidents involving inhalation of radioactive materials, there is a need for rapid evaluation of the amount of transuranium (TRU) nuclides such as Pu ingested in the body by measurement from outside of the body. In the measurement, L X-rays, which have energies of 10 to 30 keV and are emitted by internal conversion electrons following α-decay, are used. In order to measure the L X-ray energy spectrum of TRU, the use of a transition edge sensor (TES)-type microcalorimeter with an energy resolution of less than 100 eV is being considered. In this case, the attenuation of L X-rays in body tissues must be taken into account, and information on the position of deposition in the lungs is important. The deposition positions of α-emitters are estimated by the radiation transport code PHITS with a tetrahedral mesh phantom model published by ICRP and a TES-type microcalorimeter using a Sn absorber. The energy spectra deposited to the absorber are calculated. As a result, it was found that the deposition position in the lung was estimated from the intensity ratio of each L X-ray peak in the energy spectrum.

1. Introduction

In order to fundamentally reform the evaluation method of transuranium (TRU) nuclides such as Pu and Am, which has been a bottleneck in the rapid evaluation of human doses, we aim to realize rapid and reliable dose evaluation. The purpose of this study is to contribute to the enhancement of protective measures against radiation exposure in nuclear fuel reprocessing plants and against radioactive dust generated during fuel debris treatment.

When evaluating internal exposure due to TRU by in vitro measurement methods, it is difficult to measure the α-rays emitted from TRU, which are α-decay nuclides, from outside the body because the range of the α-rays is less than several tens of micrometers. On the other hand, L X-rays with energies of 10 keV to 20 keV, which are emitted from the daughter nuclides due to the energy transition of the outer orbital electrons caused by the internal conversion electrons associated with the α-decay of TRU, can be used. In the case of internal exposure in actual nuclear fuel cycle facilities, the L X-ray peaks emitted from multiple TRUs are adjacent to each other in the range of 10 to 30 keV, making clear peak discrimination difficult. Recently, a nondestructive analysis of transuranium elements has been demonstrated through spectral analysis using a Transition Edge Sensor (TES)-type microcalorimeter, which has high energy resolution below 100 keV.(1)

In the evaluation of internal doses from TRU by in vitro methods, it is necessary to consider attenuation in body tissues, and information on the position of deposition in the lungs is important. In LX-ray spectra measured in vitro with a TES-type microcalorimeter, which enables clear peak discrimination, it is expected to estimate the position of lung deposition by analyzing the intensity of several major peaks. Therefore, we investigated the estimation of TRU deposition position by a TES-type microcalorimeter using Sn absorbers, using Particle and Heavy Ion Transport code System (PHITS)(2) and the human body structure based on the tetrahedral mesh phantom model published by the ICRP(3).

2. Simulation

2.1 Simulation code

The simulation code is PHITS ver. 3.27(2), a three-dimensional Monte Carlo particle transport code was used for the simulation of L X-ray induced reactions in the complex geometry. The Electron-Gamma

Shower version 5 (EGS5)[4] model was adopted for electron-photon coupling transport above 100 keV. The EGS5 code deals with the transport of electrons/positrons or photons in any element, compound, or mixture.

2.2 L X-ray Source

Three L X-rays emitted from ^{237}Np a daughter nuclide of ^{241}Am, one of the TRU, were set as the source of L X-rays for the simulation. The energy, natural width, and emission probability of the LX-rays are the values in Table 1, and the energy distribution is represented by the following Lorenz distribution with energy E, energy position E_0, and natural width Γ.[5][6]

$$\mathrm{L}(E) = (\Gamma/2\pi)/((E - E_0)^2 + (\Gamma/2)^2) \quad (1)$$

Table1. Energy, Natural width, and Emission probability of L X-ray emitted from ^{237}Np. [5][6]

L X-ray peak	Energy E_0 [keV]	Natural width Γ [eV]	Emission probability [%/decay]
Lα1	13.946	11.8	14.9
Lβ1	17.751	13.4	8.37
Lγ	20.784	15.9	1.92

The energy spectrum of L X-ray emitted from the source is shown in Fig. 1.

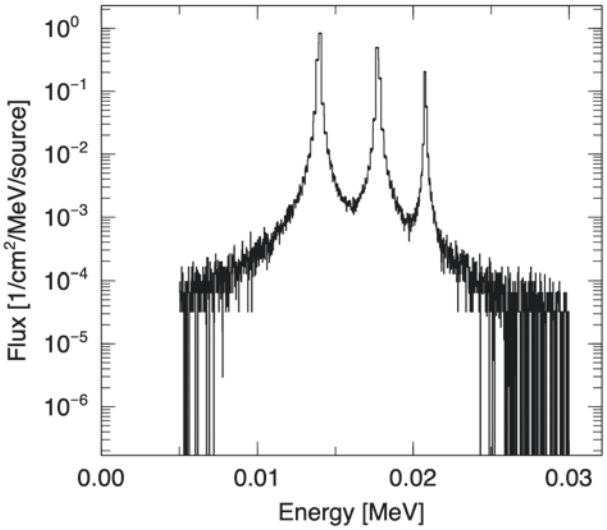

Figure 1. L X-ray energy spectrum.

2.3 Geometry of simulation

Fig. 2 shows the geometry of simulation. To use a more realistic human anatomy, we used the adult male model of Adult Mesh-Type Reference Computational Phantom published by the ICRP. This phantom model was released as a continuous tetrahedral mesh phantom model for use in Monte Carlo simulations to calculate dose conversion coefficients, etc., necessary for radiation protection. In the simulation calculation, the L X-ray source described earlier was set as a point source in the lungs, and

a TES-type microcalorimeter, a cubic Sn absorber with a cube with 0.5 mm per side[7], was placed in front of the lungs of the human body. The energy imparted to the absorber was calculated by varying the position of the source within the lung and irradiating from the source with a narrow beam covering the absorber.

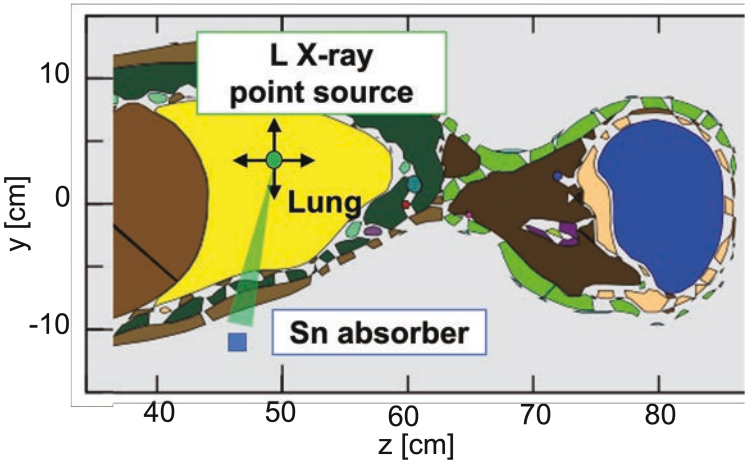

Figure 2. Simulation geometry.

3. Result

3.1 Movement of the source in the lung depth (y) direction

The z-coordinate of the source in Fig. 2 was fixed at z = 45.5 [cm] and changed to the y-coordinate of the source to irradiate the absorber. Fluence of X-rays is shown in Fig. 3, and as an example, the energy distribution given to the absorber when the y-coordinate of the source is y=0 [cm] is shown in the Fig. 4. To reduce calculation time, the source particles were irradiated only in the direction of the TES.

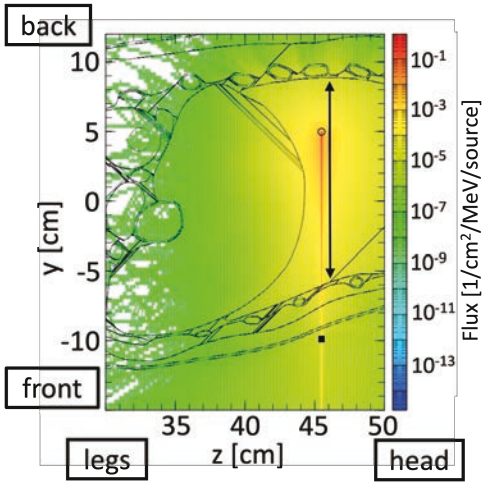

Figure 3. Appearance of fluence of X-rays. (Source particles are irradiated only in the direction of the TES to reduce calculation time.)

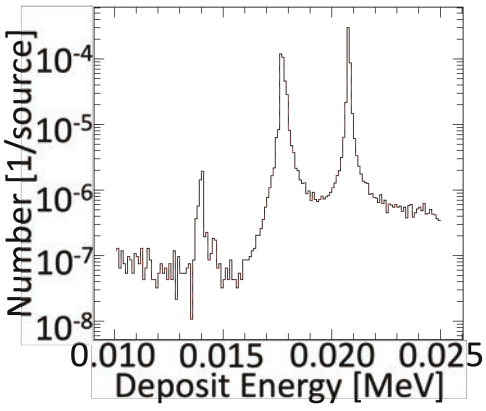

Figure 4. Energy spectrum assigned to Sn absorber when the source coordinate is y=0 [cm].

The relative intensities for each of the three peaks of energy imparted to the absorber are shown in Fig. 5, and the ratios of the relative intensities are shown in Fig. 6. It was found that all ratios can be used for position estimation within a deposition depth of 10 cm (In Fig. 3, the y-coordinate of the source is y=4[cm]).

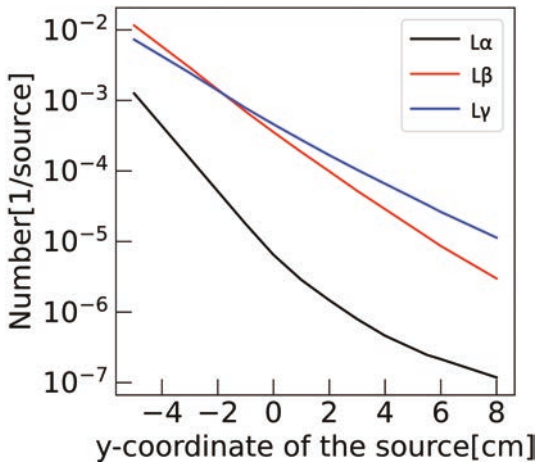

Figure 5. Relative intensities of the three L X-rays.

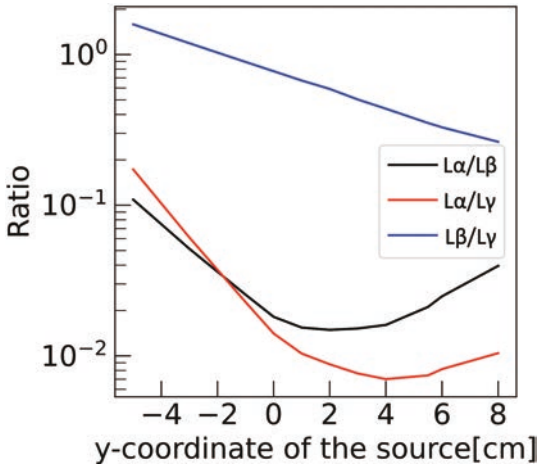

Figure 6. Ratio of the relative intensities.

3.2 Movement of the source in the lung height (z) direction

The y-coordinate of the source in Fig. 2 was fixed at y = -1.0 [cm] and the z-coordinate of the source was changed to irradiate the absorber. Fluence of X-rays is shown in Fig. 7. To reduce calculation time, the source particles were irradiated only in the direction of the TES.

The relative intensities for each of the three peaks of energy imparted to the absorber are shown in Fig. 8, and the ratios of the relative intensities are shown in Fig. 9. It was found that the ratio of the relative intensities changed significantly as the irradiation beam passed through the bone. The point where the change is particularly large is when the irradiation beam passes through dense tissue such as cortical bone.

3.3 Comparison of γ-ray from ^{241}Am and L X-rays from ^{237}Np

The γ-ray (energy 59.54 keV, emission probability 35.9%/decay) emitted from ^{241}Am, the parent nuclide of ^{237}Np, was also added as a source. As in section 3.1,The z-coordinate of the source in Fig. 2 was fixed at z=50[cm], and the y-coordinate of the source was changed to irradiate the absorber. The relative intensities of the three peaks of energy imparted to the absorber are shown in Fig. 10, and the ratios of the relative intensities are shown in Fig. 11. It was found that the use of γ-rays enabled the estimation of even deeper deposition positions.

4. **Conclusion**

PHITS and continuous tetrahedral mesh phantom models were used to estimate the deposition position of TRU nuclides when measured with a TES-type microcalorimeter using Sn absorber. As a result, it was found that the depth of deposition can be estimated by taking the ratio of relative intensities between L X-ray. Even the low energy Lα1 can be used to estimate the deposition depth if it is within 10 cm in the

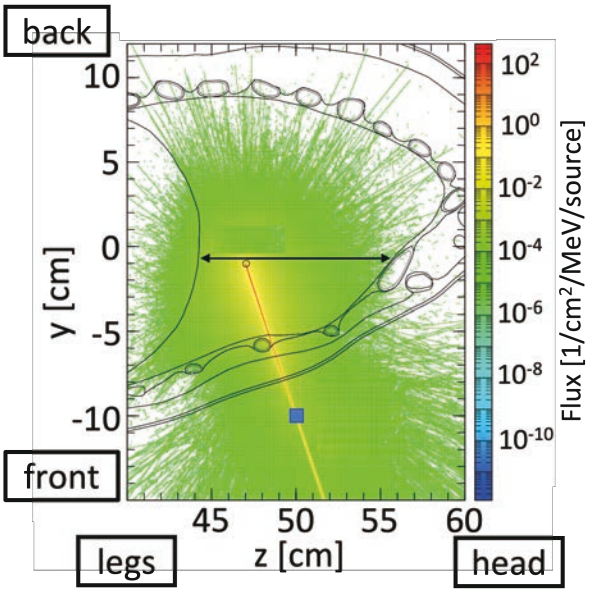

Figure 7. Appearance of fluence of X-rays.
(Source particles are irradiated only in the direction of the TES to reduce calculation time.)

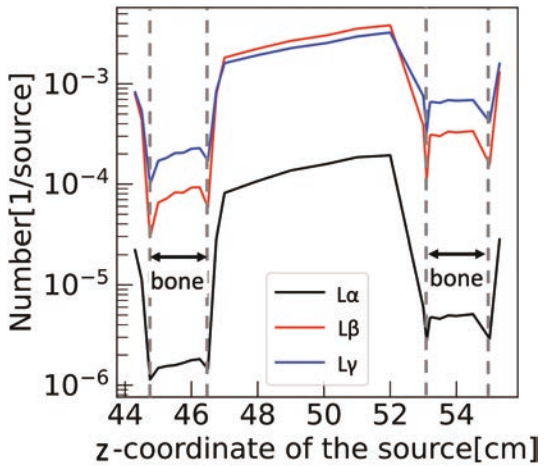

Figure 8. Relative intensities of the three L X-rays.

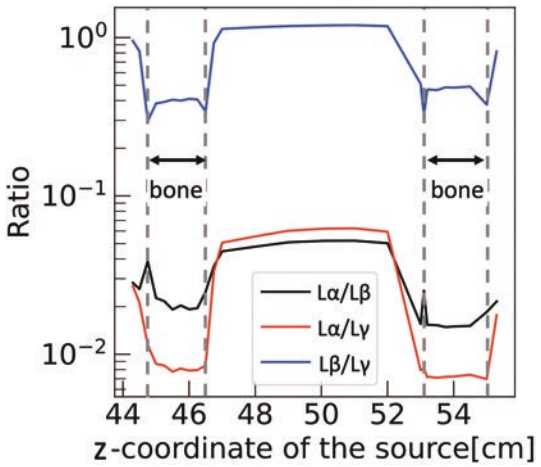

Figure 9. Ratio of the relative intensities.

body. In addition, it was found that the presence of bone between the source and the absorber can be useful information for estimating the deposition position, because the relative intensity is extremely low when bone is present. Furthermore, it was found that adding γ-ray to the evaluation method enables the estimation of the position of deeper deposition.

References

(1) K. Maehata et al., Response of a superconducting transition-edge sensor microcalorimeter with a mushroom-shaped absorber to L X rays emitted by transuranium elements, IEICE Trans. Electron., E98.C, (2015), p. 184.
(2) T. Sato, et al., Recent improvements of the Particle and Heavy Ion Transport code System – PHITS

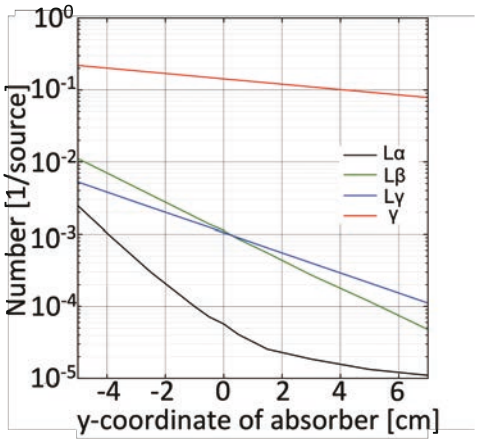

Figure 10. Relative intensities of the three L X-rays and the γ-ray.

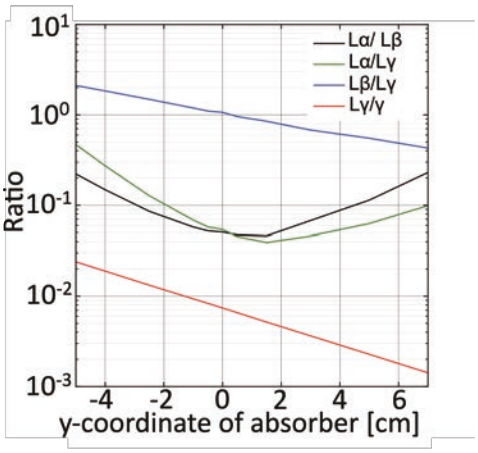

Figure 11. Ratio of the relative intensities.

version 3.33, J. Nucl. Sci. Technol. 61 (2024) 127-135.
(3) C. H. Kim, et al., ICRP Publication 145: Adult mesh-type reference computational phantoms, Ann. ICRP, 49 (2020) 13-201.
(4) H. Hirayama, et al., The EGS5 Code System KEK Report, 2005-8 (2005).
(5) K. Maehata et al., Development of a TES microcalorimeter for spectroscopic measurement of Lx-rays emitted by transuranium elements, J. Nucl. Sci. Technol., vol.47, no.3. pp.308-313, Jan.2010.
(6) BNM-LNHB/CEA Table de Radioneucléides, (http://www.nu-cleide.org/DDEP_WG/DDEP-data.html).
(7) R. Smith et al., Optimization for Device Structure of Superconducting Transition Edge Sensor Coupled With Heavy Metal Absorber, IEEE Transactions on Applied Superconductivity, Volume: 31, No. 5, August 2021, 2100704.